Measurement and qualification of the local heat transfer and pressure losses in high turbulent gas flows in channels with different artificial surface structures

Zur Erlangung des akademischen Grades eines

Doktor der Ingenieurwissenschaften

von der Fakultät für

Maschinenbau

des Karlsruher Instituts für Technologie (KIT)

genehmigte

Dissertation

von

Rodrigo Gomez de Leija

Tag der mündlichen Prüfung: 17.01.2018

Hauptreferent: Prof. Dr.-Ing. Robert Stieglitz (KIT)
Korreferent Prof. Dr.-Ing. Leo Bühler (KIT)

2018

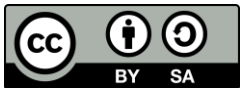

Acknowledgments

First and foremost, I would like to express my deep gratitude to Professor Dr. Robert Stieglitz and Professor Dr. Leo Bühler, Dr. Wolfgang Hering and Dr. Frederik Arbeiter, my research supervisors, for their patient guidance, encouragement, and useful critiques of the research work.

I also wish to express my gratitude to the Karlsruhe Institute of Technology for the travel and support grants they have given to me during the PhD study and research as well for providing me with a good environment and facilities to complete this project.

My special acknowledgement goes also to the 7th European Framework program GoFastR (European Gas-Cooled Fast Reactor) and THINS (Thermal-Hydraulics of Innovative Nuclear Systems) for the financial support provided to this experimental thesis work.

I would like as well to express my gratitude to Dr. Regina Krüssmann, Jürgen Aberle, Dr. Angela Jianu, Sarah Scherrer, Dr. Uwe Imke and Dr. Michael Böttcher, for their technical support during the design, construction and improvement of the L-STAR facility at the Institute for Neutron Physics and Reactor Technology (INR) at Karlsruhe Institute of Technology (KIT).

I am glad to name my KIT/INR friends and colleagues: Dr. Javier Jimenez, Nerea Diez de los Rios Ramos, Dr. Armando Gómez, Dr. Manuel Calleja, Dr. Wadim Jäger, Dr. Markus Schlenker, Ana Berkhan, Dr. Christoph Hartmann, Cristian Garrido and Dr. Aleksandar Ivanov for all the good memories they have brought me during these years at INR-KIT.

Lastly, but most important, I would like to thank my family, especially Mom and Dad, for the continuous support they have given me throughout this entire process. I would like as well to express my gratitude to the Jösel family for their continued support and encouragement, without such a team behind me and their love; I doubt that I would be in this place today.

Abstract

Heat transfer enhancement through turbulence augmentation has been recognized as a key factor for improving heat decay removal issue in innovative Gen-IV Gas-cooled Fast Reactors (GFR) and many other engineering systems. The artificial structuring of fuel rod assemblies in GFR's would allow the increase the operational heat flux densities in the core, keeping the temperature of the cladding wall within acceptable levels, thus reducing the pumping power considerably.

In the present experimental research, a series of investigations have been performed to investigate the effects on friction factors, heat transfer coefficients, velocity distribution, as well as cladding axial temperature distributions in smooth and structured rod channels have been conducted. For the structured channel cases, two different structures types in form of metallic rings (solid and perforated type) with a square cross-sectional shape, fixed to a *relative roughness height-to-hydraulic diameter ratio* e/D_h of 0.084 and a *pitch-to-rib height ratio* P/e= 10 are investigated. The experiments are carried out for a wide Reynolds number range of $2000 \leq Re_i \leq 70000$ and heating rates q_i^+ =0.0015 – 0.003.

For this purpose, an experimental facility "L-STAR" has been designed and erected at the Institute for Neutron Physics and Reactor Technology (INR) at the Karlsruhe Institute of Technology (KIT), within the framework of two European research projects, namely Thermal Hydraulics of Innovative Nuclear Systems (THINS) and European Gas Cooled Fast Reactor (GoFastR). The experimental facility consists of annular hexagonal cross-sectional flow channel instrumented with an electrically heated rod element (smooth and artificially structured) placed concentrically in the flow channel the test section. The geometry of the flow channel, as well as the investigated flow parameters range are chosen relevant for the thermal-hydraulic study of the gas-cooled reactor demonstrator ALLEGRO.

The first part of the experimental results is dedicated to the comparison and validation of the smooth channel against well-known analytical correlations. The evaluated friction factors, heat transfer coefficients, as well as velocity distributions for the smooth rod channel are in a very good agreement with the corresponding analytical predicted values. Furthermore, excellent experimental data reproducibility, within the measurement errors, is achieved with the experimental setup of the L-STAR facility. Based on these results, the feasibility of the experimental setup, as well as the used methodology was demonstrated. The second part of the results, the discussion of the structured rod channels conducted at isothermal and three different heating rate boundary conditions is presented. In contrast to the smooth channel test, the structured rod channels exhibit considerably higher heat transfer enhancement coefficients. The highest heat transfer coefficients, in the order of 2.3 to 5.1 times, are attained with the perforated ring structures compared to the smooth channel cases. In the cases of intense heating q_i^+ =0.002 – 0.003, the axial cladding temperature distribution for both structured channels remain considerably lower, without exceeding the axial temperature distribution of the smooth rod cases, conducted at lower heating rates q_i^+ =0.0015. The experimental results

provide an important contribution to the study of the decay heat removal, considered one the main safety related issues of Gen-IV GFR system.

The higher heat transfer enhancement obtained with the structured channels is accompanied by an increase in the pressure losses along the test section of about 3.9 to 5.9 times higher compared to the smooth channel cases. However, as the ring structures are changed from solid to perforated type, pressure losses were considerably decreased, up to ~37%, for the investigated Reynolds number range. As a result, the thermo-performance index η is thereby increased. The experimental results of the structured rod channels have been compared to literature heat transfer and friction factor correlations proposed by Webb and Rashkovan. In general, the experimental data is overpredicted by the correlations, whereas the trends are correctly predicted. These results highlight the need for new experimental data, which could allow a better thermal-hydraulic analysis for this type of structured flow channels.

The effects on the mean velocity and turbulence intensity distributions between two consecutive ring structures have been investigated by means of a two-component Laser Doppler Anemometry (LDA) system for a single Reynolds number $Re_i \cong 16477$. Compared to the smooth channel case, the surface structures induced a strong flow separation at the leading edge of the ring structures, causing the formation of several recirculation zones (in form of close vortices), as well as flow reattachment at the inner-spacing of the ring structures. Furthermore, the multiple holes on the of perforated rings lead to the formation of a jet-like flow system downstream the wall, inducing stronger flow mixing motions very close to the wall. As a result, higher convective heat transfer coefficients between the heated wall and the cooling gas flow are attained compared to the solid rings and smooth channel cases. At the outer region of the flow channel, the mean velocity and turbulence intensity distributions for all studied cases (smooth and structured) show a remarkable similarity. This result provides a strong support to the current understanding of *roughness sub-layer* concept.

Finally, a qualitative study of the particle deposition which might be caused by abrasive friction between components and gas impurities has been conducted for both smooth and structured rod channels. For the smooth rod channel case formation of a fine homogeneous particle deposition layer all along the cladding is observed. In the case of the structured rod channels, local particle deposition regions are identified downstream and top of the ring structures, as well as in the region in which the secondary recirculation zones occur. In the cases of the perforated rings, the amount of particles deposited on the wall is considerably reduced into small narrow region of the wall, in which the jet-flow system is located. This decrease can be explained due to the reduction of the secondary recirculation zones in the inner-spacing of the structures.

The comprehensive experimental data for friction factor, heat transfer and velocity distribution on smooth and artificially structured channels conducted in this thesis, provides a valuable and accurate database for the further development, verification and validation of advanced models and numerical tools, supporting the numerical study of turbulence, as well as the safety design studies of Gen-IV GFR.

Zusammenfassung

Die Verbesserung der Wärmeübertragung durch den Einsatz strukturierter Oberflächen wurde als ein wichtiger Faktor für die Verbesserung der Nachwärmeabfuhr zwischen der Brennelementoberfläche und dem Kühlmittelgas in Gen-IV Gasgekühlten schnell Reaktoren (GFR) und vielen anderen technischen Systemen erkannt. Die Verbesserung der Wärmeübertragung von Brennelementen führt zu einer niedrigeren Oberflächentemperatur und somit zu einer geringeren thermischen Beanspruchung. Dadurch kann mit höheren Wärmestromdichten gearbeitet werden, was den Wirkungsgrad nachfolgender thermischer Prozesse optimiert, bei gleichen Geometriedaten und Materialen.

Im Rahmen dieser Arbeit wurden der Wärmeübertragungs-und Reibungskoeffizienten, die zeitgemittelten Geschwindigkeitsverteilung und die axialen Temperaturverteilungen an hydraulisch glatten und künstlich strukturierter gasgekühlte Kanäle sowohl experimentell als auch theoretisch untersucht. Bei den strukturierten Kanälen wurden zwei verschiedene Oberflächenstrukturtypen in Form von metallischen Ringen (Solide und Perforierte) mit einer quadratischen Querschnittsform untersucht. Die bedeutendsten geometrischen Parameter wie z.B. dem *relative roughness height-to-hydraulic diameter ratio* e/D_h of 0.084 and a *pitch-to-rib height ratio* P/e= 10 wurden konstant gehalten. Die Untersuchung erstreckt sich für Reynoldszahlen im Bereich $2000 \leq Re_i \leq 70000$ und Dimensionslose Heizraten von q_i^+ =0.0015 – 0.003.

Zu diesem Zweck, wurde am Institut für Neutronenphysik und Reaktortechnik (INR) am Karlsruher Institut für Technologie (KIT) eine Versuchsanlage "L-STAR" konzipiert und errichtet. Die L-STAR Versuchseinrichtung besteht aus einem Kreislauf mit einer hexagonalen Teststrecke, die direkt mit einem zylindrischen Elektrische Heizstabelement (glatt und künstlich strukturiert) betrieben wird. Die Geometrien des Strömungskanals, sowie der untersuchte Bereich der Strömungs-Parameter, orientieren sich an den Eigenschaften des gasgekühlten schnell Demonstrationsreaktors ALLEGRO.

Der erste Abschnitt der experimentellen Ergebnisse widmet sich der Diskussion und dem Vergleich des glatten Kanals mit bekannten analytischen Korrelationen. Die gemessenen Reibungsfaktoren, Wärmeübergangskoeffizienten sowie die Geschwindigkeitsverteilungen für den glatten Kanal zeigen eine sehr gute Übereinstimmung mit den entsprechenden berechneten analytischen Werten. Darüber hinaus wurde eine hervorragende Reproduzierbarkeit der Messdaten mit der L-STAR Versuchseinrichtung erreicht. Basierend auf diesen Ergebnissen wird die Machbarkeit des experimentellen Aufbaus sowie der verwendeten Auswertungsmethode demonstriert. Im zweiten Abschnitt wird die experimentelle Untersuchung der strukturierten Kanäle bei isothermen und drei verschiedenen Heizraten dargestellt. Im Gegensatz zu dem glatten Kanaltest führen die strukturierten Kanäle zu erheblich höhere Wärmeübertragungskoeffizienten. Die höchsten Wärmeübergangskoeffizienten werden mit den Ringstrukturen erhalten. Diese sind um den Faktor 2.3 bis 5.1 größer als bei den glatten Kanälen.

Der axialen Wandtemperaturverteilung für beide strukturierten Kanäle, die bei höheren Wärmestromdichten $q_i^+ = 0.002 - 0.003$ durchgeführt wurden, überschreiten nicht die axiale Temperaturverteilung des glatten Kanal Referenzfalls, die bei niedrigerer Wärmestromdichte $q_i^+ = 0.0015$ durchgeführt sind. Basierend auf diesen Ergebnissen wurde gezeigt, dass die Strukturierung der Wand den Betrieb bei höheren Wärmestromdichten im System ermöglicht, ohne die maximale Wandtemperatur des glatten Kanals zu überschreiten. Dieses Ergebnis kann als ein wichtiger Beitrag zum Studium der Nachwärmeabfuhr betrachtet werden, der als eins der wichtigsten und sicherheitsrelevanten Themen des Gen-IV-GFR-Systems gilt.

Die höheren Wärmeübertragungskoeffizienten der strukturierten Kanäle, die durch höhere erzeugte Turbulenz verursacht wurden, sind von einer zunehmenden Erhöhung des Druckverlusts Entlang der Teststrecke begleitet. Die Druckverluste für die strukturierten Kanäle sind im Vergleich zu den glatten Kanalfällen etwa 3.9 bis 5.9-mal höher. Durch einen Wechsel der Oberflächenstruktur vom festen zum perforierten Ringtyp, wurden die Druckverluste für den untersuchten Reynolds-Zahlenbereich deutlich verringert (bis zu ~37%). Dadurch wird der der thermische Performance Index η erhöht. Die Versuchsergebnisse der strukturierten Kanäle wurden mit den von Webb und Rashkovan vorgeschlagenen Literaturwärmeübertragungs- und Reibungsfaktorgleichungen verglichen. Im Allgemeinen werden die experimentellen Daten durch die Korrelationen deutlich Überschätz, während ein einheitlicher Trend beobachtet wird. Die Ergebnisse bezeichnen die Notwendigkeit neuer experimenteller Daten, die eine bessere thermohydraulische Analyse für diese Art von strukturierten Strömungskanälen ermöglichen.

Die zeitgemittelte Strömungsgeschwindigkeit und die statistischen Momente der Geschwindigkeitsverteilung wurden mit einem Zweikomponenten- Laser Doppler Anemometrie System (LDA) für die Reynoldszahl $Re_i \cong 16477$ untersucht. Durch den Vergleich der experimentellen Daten der strukturierten Kanäle mit denen des glatten Kanals wird beobachtet, dass die Oberflächenstrukturen eine starke Trennung und Beschleunigung der Strömung an der Vorderkante der Ringstrukturen induziert, was zur Bildung von mehreren Sekundärströmungen in Form geschlossener Wirbel im Bereich zwischen den Ringstrukturen führt. Zusätzlich zeigt das Vorhandensein von perforierten Ringen die Bildung eines jet-artigen Strömungssystems stromabwärts der Ringstruktur. Die höhere Strömungsmischung sehr nahe an der Wand verringert die Entstehung der geschlossenen Wirbel und dadurch werden die konvektiven Wärmeübergangskoeffizienten zwischen der erwärmten Wand und dem Kühlgasstrom erhöht. Im äußeren Bereich des Strömungskanals zeigen die mittleren Geschwindigkeits- und Turbulenzintensitätsverteilungen für alle untersuchten Fälle (glatt und strukturierte) eine bemerkenswerte Ähnlichkeit. Die Ergebnisse unterstützen das aktuelle Verständnis des *roughness sub-layer* Konzepts.

Schließlich wurde eine qualitative Untersuchung der Partikelablagerung auf glatten und strukturierten Kanälen durchgeführt. Für den glatten Stabkanal zeigt sich die Bildung einer feinen homogenen Partikelablagerung. Bei den strukturierten Kanälen werden lokale Partikelablagerungsbereiche stromabwärts und oberhalb der Ringstrukturen sowie in dem Bereich, in dem die sekundären Rezirkulationszonen auftreten, identifiziert. Der Ergebnisvergleich zeigt, dass

der niedrigste Partikelabscheidungsgrad mit den perforierten Ringstrukturen erhalten wird. Die Abnahme kann zur Verminderung die Sekundärströmungen im Bereich zwischen den Ringstrukturen erklärt werden.

Die umfangreichen experimentellen Daten für die Reibungskoeffizienten, Wärmeübertragung und Geschwindigkeitsverteilung auf den glatten und künstlich strukturierten Kanälen bieten eine wertvolle und genaue Datenbank für die Weiterentwicklung, Verifikation und Validierung von fortgeschrittenen Modellen und numerischen Werkzeugen, die die Turbulenzstudie unterstützen, sowie die Sicherheitsdesignstudien von Gen -IV GFR

Nomenclature

A_c	Total flow cross section area, [m^2]
$A_{w,h}$	Nominal heated rod wall surface area, [m^2]
A_s	Area of the ring structure, [m^2]
B	Smooth wall logarithmic law constant, [-]
C_f	Fanning friction factor, [-]
c_p	Heat capacity, [J/kg K]
D_h	Hydraulic diameter, [m]
d_L	Beam waist diameter, [µm]
d_F	Diameter of focused laser beams, [µm]
d_w	Reference rod outer diameter, [m]
d_{MV}	Diameter measuring volume, [µm]
e	Surface structure height, [mm]
e^+	Roughness Reynolds number, [-]
e/D_h	Relative roughness height-to-hydraulic diameter ratio [-]
E	Expansion factor, [-]
h_{hex}	Hexagonal flow channel width, [m]
H	Channel height, [m]
$G0$	Smooth rod channel
$G1$	Solid rings
$G2$	Perforated rings
$G(e^+)$	Heat transfer similarity law
f	Friction factor, [-]
F_L	Optic focal length
F_b	Frequency laser beam
F_d	Doppler frequency
F_D	Darcy-Weisbach friction factor, [-]
$f_{D,s}$	Friction factor smooth rod channel, [-]
$f_{D,r}$	Friction factor structured rod channel, [-]
k_s	Equivalent sand grain roughness, [m]
L_h	Total heated length, [m]
L_s	Heated sections length, [m]
$\dot{m}_{CFM}$	Coriolis flow meter mass flow, [kg/s]
Ma	Mach number, [-]
Nu	Nusselt Number, [-]
Nu_i	Simplified Nusselt number, [-]
$Nu_{i,s}$	Simplified Nusselt number for smooth rod channel, [-]
$Nu_{i,r}$	Simplified Nusselt number for structured rod channel, [-]
P	Surface structure pitch, [mm]
P_i	Pressure inlet, [Pa]
P_c	Center line of the perforations with respect to the wall, [mm]
P_d	Perforation diameter of the optimized ring structures, [mm]

P_{dyn}	Dynamic pressure, [Pa]
P/e	Relative roughness pitch-to-height ratio, [-]
Pr	Prandtl number, [-]
q_1^+	Dimensionless heat up ratio, [-]
$\dot{q}_w$	Wall heat flux, [W/m^2 · K]
$\dot{q}_{w6}$	Local heat flux heated section number six, [W/(m^2 · K)]
$q_{(z)}$	Quotient function, [-]
$\dot{Q}_H$	Electric input power, [kW]
$\dot{Q}_{wr}$	Radiation heat losses rod to wall, [kW]
r_p	Ring perforation radio, [m]
r_{hex}	Hexagonal channel corner radius, [m]
Ra_{rod}	Average wall surface roughness of the channel, [µm]
Ra_{hex}	Average wall surface roughness of the heater rod, [µm]
Re	Reynolds number, [-]
Re_i	Reynolds number as a function of the inlet flow conditions, [-]
$R(e^+)$	Roughness function, [-]
S_w	Wetted perimeter, [m]
St	Stanton Number, [-]
TD	Turndown; i.e., ratio of the upper range limit to the set span
T_i	Temperature as function of the initial conditions, [K]
T_o	Temperature at the outlet, [K]
T_g	Gas temperature, [K]
TT	Test Section
TS	Thermocouple
T_w	Cladding wall temperature, [K]
u_i	Time series velocities, [m/s]
u^+	Dimensionless velocity, [-]
u_τ	Friction velocity or shear velocity
U	Mean axial velocity, [m/s]
U_s	Mean axial velocity smooth rod channel, [m/s]
U_r	Mean axial velocity structured rod channel, [m/s]
$U'_{r,rms}$	Velocity fluctuations structured rod channel, [m/s]
$U'_{s,rms}$	Velocity fluctuations, [m/s]
U_m	Bulk velocity, [m/s]
W	Surface structure width, [mm]
w/e	Relative roughness width
w_i	Transit time weighting
y^+	Dimensionless wall distance, [-]
Y_w	Radial wall distance from the rod to the channel [mm]
X	Coordinate in the radial against direction of the flow, [m]
Y	Coordinate in the radial direction of the flow, [m]
Z	Coordinate in the axial direction of the flow, [m]
Z_r	Axial position between two consecutive structures, [m]

Greek symbols

α	Flow angle of attack of the surface structures
$\alpha_{TC,i}$	Angular coordinate of the thermocouples position
Φ	Angular coordinate for the LDA measurements
$\emptyset_p$	Separation angle between centerlines of each perforation G2, [m]
β_o	Open area ratio of the perforated rings
δ_f	Fringe distance in measuring volume, [m]
δ_L	Boundary layer thickness, [m]
Z	Total loss coefficient, [-]
ϵ	Material emissivity
ε	Surface roughness of the channel for Eq. [5.3], [m]
η	Thermo-performance index, [-]
σ	Uncertainty error
σ_{SB}	Stefan–Boltzmann constant, [$W \cdot m^{-2} \cdot K^{-4}$]
ρ	Density, [kg/m^3]
λ	Thermal conductivity, [W/(m · K)]
κ	von Kármán constant, [-]
τ	Total shear stress, [Pa]
τ_w	Shear stress, [Pa]
u_t	Friction velocity
υ	Kinematic viscosity, [m^2/s]
ΔU^+	Roughness function

Acronyms

AOMs	Acoustic Optic Modulators
ALLEGRO	Gen IV Gas-cooled reactor demonstrator
CCD	Cross-correlation sensor
CFD	Computational Fluid Dynamics
DACS	Data Acquisition and Controller System
DGV	Doppler Global Anemometry
DHR	Decay Heat Removal
EC	European Commission
EIR	Swiss Federal Institute for Reactor Research
ESNII	European Sustainable Nuclear Industry Initiative
HWA	Hot-wire and film anemometry
INR	Institute for Neutron Physics and Reactor Technology
KIT	Karlsruhe Institute of Technology
KfK	Kernforschungszentrum Karlsruhe
GoFastR	European Gas Cooled Fast Reactor
GFR	Gas-Cooled Fast Reactor
GEN IV	Generation IV reactors
GIF	Generation IV International Forum
HTGR	High Temperature Gas-cooled Reactor
FP7-Euratom	Seventh Framework Program of the European Atomic Energy Community
LDA	Laser-Doppler Anemometry
LDV	Laser-Doppler Velocimetry
LFR	Lead-cooled Fast Reactor
L-STAR	Luft – Stab, Abstandshalter, Rauheiten, (air – rod, spacer, and roughness)
LWR	Light-water reactor
MOX	Mixed oxide fuel
MSR	Molten Salt Reactor
NBK	Fused silica glass windows
PCI	Peripheral Component Interconnect
PIV	Particle Image Velocimetry
PBMR	Pebble Bed Modular Reactor
SCWR	Supercritical Water-cooled Reactor
SNETP	Sustainable Nuclear Energy Technology Platform
SFR	Sodium-cooled Fast Reactor
THINS	Thermal-hydraulics of Innovative Nuclear Systems
UKAEA	UK Atomic Energy Authority
VHTR	Very High Temperature Reactor
UKAEA	UK Atomic Energy Authority
VHTR	Very High Temperature Reactor
UK	United Kingdom
WDM	Wave Division Multiplexing

Table of contents

1. Introduction

1.1. Motivation and necessity of this study

Among the most efficient techniques for the heat transfer enhancement in numerous engineering applications such as, gas turbines blades, heat exchangers, concentrated solar power receivers, Nuclear reactors and other several aerospace applications, has been the improvement of the convective turbulent mixing through the artificial structuring of the heated zone in form of small protuberance or cavities uniformly distributed along the streamwise direction to the flow, also known as *artificial surface structures*.

This particular passive enhancement technique has become an important technologically feasible option for innovative gas cooling systems, as gases, in comparison to liquids are characterized by inherently lower thermal conductivity and specific heat capacity rates, since the density of the gas decreases as the temperature increases [1]. In the nuclear field, gases have been considered as a primary coolant medium for the Gen-IV innovative nuclear reactors, such as the High Temperature Gas-cooled Reactor (HTGR), the Pebble Bed Modular Reactor (PBMR) and most recently for Gas-cooled Fast Reactor (GFR) [2]. The choice of gases as cooling medium (such as Helium) is dictated by the desire to introduce the smallest amount of neutron absorption and moderation, while still being able to reliably remove the heat from this high-power density configuration [3]. Furthermore, gases offer a number of advantages compared to the liquid cooling reactor designs. Gases as helium do not interact with neutrons and do not become radioactive; however, some impurities might be present. This simplifies the reactor physical design as the coolant has no significant effect on the moderation of neutrons, compared to liquid coolants. Gases coolants are also chemically inert; therefore do not contribute to corrosion degradation of reactor materials. The other common coolant choices for gas-cooled fast reactors are CO_2, and steam. Moreover, as gases are mostly transparent, the maintenance of the reactor is easier, thereby making the reactor more cost-efficient. The innovative gas-cooled Fast Reactors are being investigated by Generation IV International Forum (GIF) with the main focus on demonstrating their technical feasibility, economic competitiveness and improved safety characteristics. The Gen-IV GFR reactors are foreseen as an extension to overcome the limitation of the water-cooled reactors systems and are expected to substantially contribute to close the fuel cycle, characterized by a better utilization of the fuel and reduction of radioactive waste [4]. For these energy systems, a high overall efficiency is envisaged, leading to operate at high temperatures between 700 and 1000 °C, which generally translates into higher power densities in the reactor [3].

Despite the many advantages there are also challenges in using gases as a reactor coolant. As it widely recognized one of the major design challenges of this type of cooling system is to ensure sufficient decay heat removal under depressurized conditions and loss of coolant, while ensuring sufficient cooling of the fuel rods. This issue has led to an increased effort to investigate how the thermal-hydraulic performance could be optimized, which would allow the development and implementation of more efficient cooling systems capable of operating at higher heat flux rates. The artificial structuring has been recently taken into consideration for its implementation in GFR fuel rod

assemblies. The improvement of the heat transfer by surface structures is achieved by disturbing the boundary layer, caused by the separation and reattachment of the flow promoting higher local turbulent mixing of the flow in the vicinity of the heated wall, which significant contributes to a better transport of momentum, heat and mass transfer rates in the system. However, the heat transfer augmentation generated by the artificial surface structures is generally accompanied by higher pressure losses; which in terms lead to an increase of the pumping power in the system. Therefore, an optimization between the heat transfer efficiency and the pressure losses is needed if additional artificial structures are to be used. The thermal-hydraulic enhancement by artificially structured fuel rod elements in GFR could contribute to the thermal-hydraulic design and safety assessment of either critical or subcritical systems, allowing the increase of the heat flux densities over a wide range of Reynolds numbers, reducing potentially the thermal loading on the cladding material keeping the temperature of the cladding within acceptable levels. Despite the fact, that there have been numerous studies dedicated to investigate the general thermal-hydraulic performance of artificially structured walls in the past decades (see section 2.4) in terms of friction factor and Nusselt number characteristics, there is still the necessity of investigating in the local transport mechanism and associated stream and spanwise transfer quantities. Moreover, the wide variety of artificial structures and channel geometries can influence in different ways the flow across the channel, making this subject even more challenging to study [5]. On the other hand, the improvement of the measurement methods and numerical simulation tools has led to an increased effort to produce more detailed and accurate data, which can be used as a benchmark for the validation and verification of different numerical tools such as Computational Fluid Dynamics (CFD) and system codes. However, the successful modeling and prediction of turbulent flows over artificially structured walls is mainly limited by the empirical physical base models used in the numerical tools, such as the eddy viscosity and Reynolds stress models [6], as well as to their high computational cost and their rather poor agreement with experimental data.

The analysis and study of such problems requires further and more detailed investigation by means of experimental research, with emphasis on local parameters such as the wall temperatures, pressure losses and high spatial resolution velocities distributions, for the knowledge improvement of the thermal-hydraulic aspects relevant for advanced gas-cooling systems, is the key feature of this thesis.
For this, the Seventh Framework Programme of the European Atomic Energy Community (FP7-Euratome) launched in 2010 two cooperation projects, GoFastR (Gas-Cooled Fast Reactor) THINS (Thermal-Hydraulics of Innovative Nuclear Systems), with the main focus of improving the understanding of the challenging thermal-hydraulic scenarios present in innovative Gas-cooled reactor systems. Within the EU FP7 projects, an experimental gas loop test facility (L-STAR) was designed and erected at the Karlsruhe Institute of Technology (KIT), with the main objective of conducting experimental and numerical investigations on pressure loss penalties and improvement of turbulent convective heat transfer over artificially structured rods compared to smooth ones. The test section of the L-STAR experimental facility was designed and scaled to assure similar thermal-hydraulic characteristics as a sub-channel with a single fuel rod of a GFR. Furthermore, this experimental thesis seeks to provide an accurate set of data for the further development, validation, and verification of more advanced deterministic models and system codes.

1.2. Challenges in turbulent flows research

Deterministic description of turbulent flows remains one of the phenomena, which poses some of the most difficult and fundamental problems in classical mechanics, characterized mainly by its ability to transport and mix fluid at higher velocity fluctuations compared to laminar flows [7], as well as to complex fields and three-dimensional dissipation all over the flow. So far, there is no universal model that predicts the behavior of turbulent flows. Recently direct numerical simulation (DNS) has made considerable improvement by the study of turbulent flow; however, the computational cost of DNS is very high, even at low Reynolds numbers. This complicates the design and optimization of the heat transfer systems in which turbulent flows occur [8]. In turbulent flows, the physical quantities such as the pressure, temperature and velocity profiles present an irregular and complex behavior, which makes a challenging task to obtain reliable and accurate information of it. Since these key parameters are implemented in the governing equations in the deterministic models used to describe the flow behavior mechanism and heat momentum transfer [9], it is essential to make sure that the numerical tools include suitable deterministic models. One of the main key issues in fundamental studies of turbulence in fully developed flows is the challenging measurement of the velocity components, due to the multi-scales motions and unsteady aperiodic motions. To overcome these issue different authors have proposed the implementation of measurement techniques with high spatial and temporal resolution capable of detecting both large and smaller scales, especially near the wall surface, since the turbulence near the wall region has a direct influence on friction and heat transfer processes [10]. The spatial resolution is important to identify the turbulence levels behavior, whereas, the temporal resolution is required to identify and resolve the turbulence fluctuations.

1.3. Background and objectives

The design of high temperature gas cooled systems is mainly limited by the properties of the fluid and the limitation of the wall materials. For high efficiency cooling systems, optimization of the heat transfer and pressure drop are pre-required for the design assessment, in order to allow a higher power density operation. Hence, both values and their uncertainties have to be precisely known. It is essential to make sure that the numerical analysis tools and system codes used to predict and analyze these phenomena include a validated set of data, based on accurate experimental measurements, which promotes to the further development and validation of suitable deterministic models for turbulent flows. As described above; one of the key safety issues of the advanced Gas-cooled reactor systems is the decay heat removal under normal operational and depressurized conditions. Therefore, it is the aim of this thesis to investigate and contribute to the existing knowledge of the underlying physical phenomena in single-phase flows in the field of internal turbulent flows over smooth and artificially structured single rod geometries (similar to the fuel rod elements in GFR), in particular study the frictional losses, heat transfer coefficients and velocity field distribution. Furthermore, the particle agglomeration caused by gas impurities or material wear, as well as the intensive heating of the cladding wall effects on the thermal-hydraulic performance is investigated and compared to the smooth channel design. The work has been done within the frame of the Seventh Framework

Programme projects THINS and GoFastR founded by the European commission. This research may be then viewed as a direct contribution to the study of turbulent flows and thermal-hydraulic performance of GFR and other innovative cooling systems.

The specific goals and tasks of this experimental research are summarized below:

- Establish an accurate database for the development of new physical computational fluid dynamics (CFD) models, in order to improve and validate the numerical analysis in the vicinity of the wall for its application to innovative nuclear systems.

- Investigate the thermal-hydraulic influence and optimization of smooth and artificially structured walls in hexagonal annular flow channels.

- Design and optimization of a vertical internally heated annular test section suitable for the investigation of thermal-hydraulic issues related to GFR rod geometries.

- Investigate the velocity distribution in the vicinity of the wall, in order to provide more detailed information of the enhancement mechanism of turbulent flows.

- Analyze and gain knowledge on the particle deposition patterns caused by the implementation of different artificial structures on turbulent gas flows, as well as advance the knowledge of experimental gas loops by means of a benchmark contribution.

1.4. Gas-cooled reactors systems

During the 50's and 60's several Gas-cooled reactors were studied; the most remarkable programs were carried out by the UK Atomic Energy Authority (UKAEA), the Swiss Federal Institute for Reactor Research (EIR) and the former Kernforschungszentrum Karlsruhe (KfK) now known as Karlsruhe Institute of Technology (KIT). During that period, the GFR concept was expected to increase the thermal efficiency of a nuclear power plants and mitigate some of the issues associated with liquid–metal coolant based rectors. In the 1970's the situation for fast reactors changed. The technological advances made enrichment cheaper; uranium turned out to be more abundant than originally thought and the nuclear power industry did not grow at the expected high rate [3]. In the 1980's, almost all major fast reactor programs in the world were either cancelled or significantly downsized. Nevertheless, the benefits of the gas cooling technology were recognized, mainly their high number of excess neutrons available in a fast reactor allows their application as actinide transmutation reactors and thus reducing the long-term radiotoxicity of nuclear waste, if higher gas temperatures could be achieved [4]. These goals, coupled with the constant effort of designing more efficient nuclear applications, motivated the further investigation and development of the gas cooling technologies [11]. Figure 1.1 provides a schematic representation of the worldwide Gas-cooled reactors technology evolution.

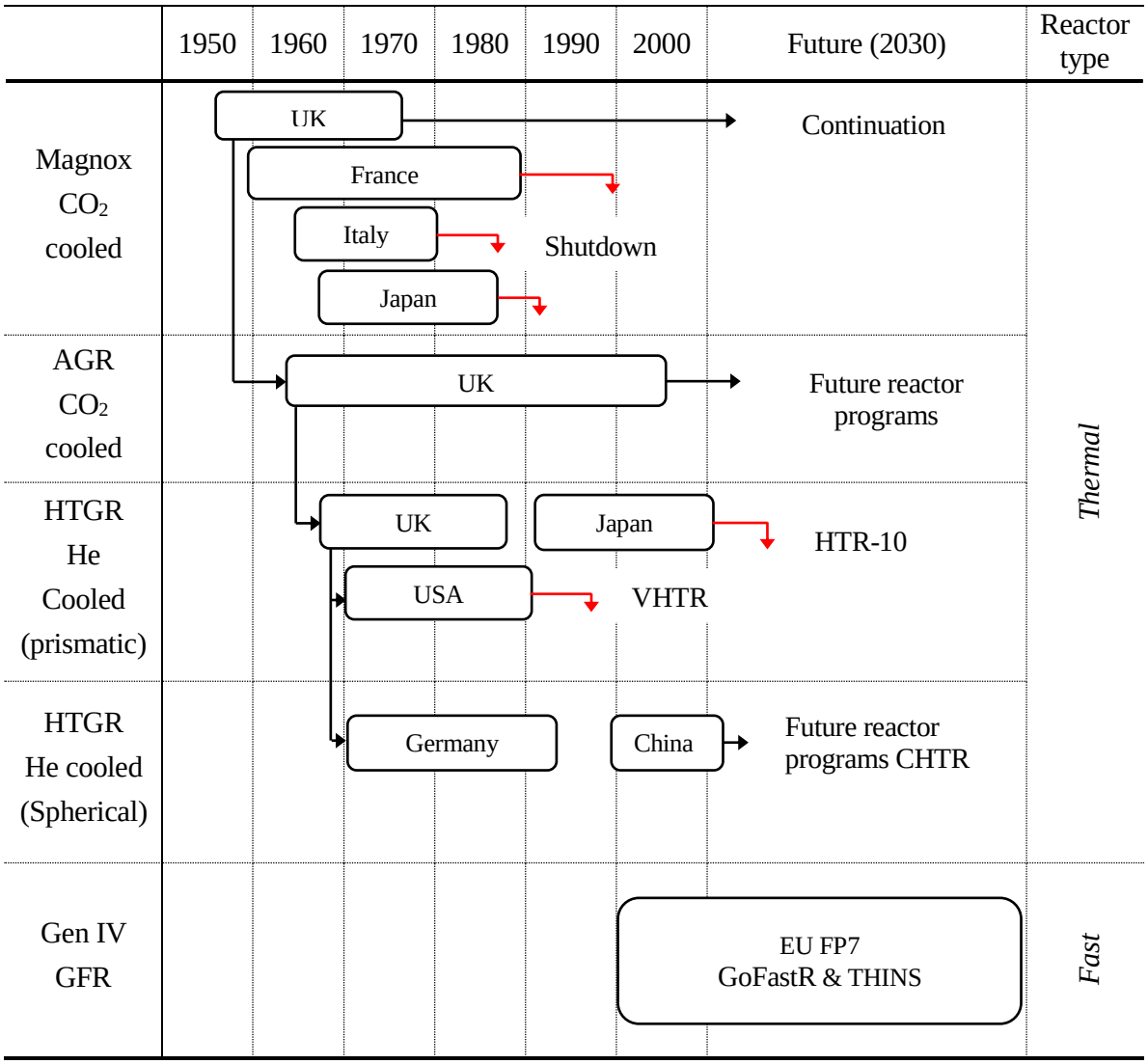

Figure 1.1: Evolution of Gas-cooled reactors technology.

1.4.1. Gen-IV GFR Demonstrator: ALLEGRO reactor

The Gas-cooled reactors have been subject of constant research and development improvement during the last decades. However, given the current state of GFR development several issues still need to be studied and solved. In order to demonstrate the technical feasibility and viability of Gen IV Gas-cooled technologies, an experimental demonstrator reactor called ALLEGRO, is recently being planned in Europa, within the European Commission's framework (FP6 and FP7) [12]. The ALLEGRO reactor project was launched in 2010 as part of the ESNII[1] initiative with the aim of building a low power experimental helium Gas-cooled reactor of about 50 to 80 MW_{th} (no electrical generation), originally designed in France by CEA[2] in 2009 within the contribution of several

[1] ESNII acronym stands for European Sustainable Nuclear Industrial Initiative
[2] CEA acronym stands for French Alternative Energies and Atomic Energy Commission.

European entities. Two different core configurations have been proposed by the developers, namely a standard MOX fuel core covered by a stainless-steel cladding, whereas the second design concept takes into consideration the use of a ceramic fuel, which could allow operating the GFR at the higher temperatures. A detailed description of the ALLEGRO design concept can be found in [12, 13]. Under the main objectives of the ALLEGRO demonstrator, are:

- *Qualification of the GFR fuel and subassembly concept.*
- *Study the decay heat removal function.*
- *Demonstration of core operation and control with the appropriate instrumentation.*
- *The establishment of a first GFR safety reference framework.*
- *Acquisition of GFR operational experience, providing the overall system viability.*

The ALLEGRO demonstrator is foreseen to function not only as a demonstration reactor hosting GFR technological experiments, but also as a test pad by using the high temperature coolant of the reactor in a heat exchanger extracting heat for industrial applications and a research facility which, thanks to the fast neutron spectrum, makes it attractive for fuel and material development and testing of some special devices or other research works [14]. The original CEA design of ALLEGRO is described in Figure 1.2.

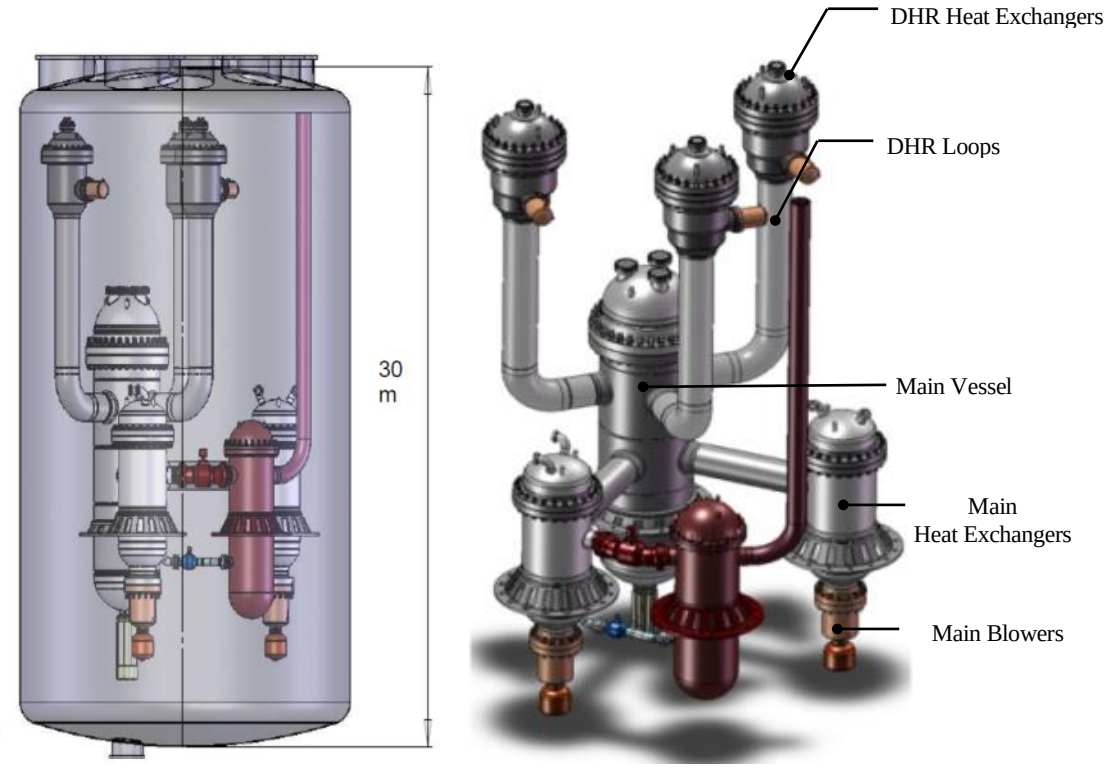

Figure 1.2: Main concept design of the ALLEGRO reactor by CEA; Primary circuit enclosed in a guard vessel [16].

1.5. Experimental approach

The experiments are conducted in a gas loop facility "L-STAR[3]" design and erected at the Institute for Neutron Physics and Reactor Technology (INR) at the Karlsruhe Institute for Technology (KIT) for the investigation of the heat transfer and pressure drop issues in single rod geometries. Among the state of art instrumentation, one of the key elements of the L-STAR experimental facility is the possibility to acquire the velocity distribution by means of Laser Doppler Anemometry (LDA), within a measurement volume in the order of ≥1 mm and a spatial resolution of ~78 µm (near to the vicinity of the wall) and ~189 µm (for the outer glow region of the channel) [15]. The flow field data are complemented by measurements of the wall temperature profiles and pressure losses to provide a comprehensive understanding of the velocity distribution. Furthermore, the optical access of the L-STAR enables the simultaneous monitoring of particle deposition by turbulent gas flows over smooth and artificially structured single rod channels. A detailed description of the facility, test section, and instrumentation is given in section 3. The experimental work presented in this thesis strives to expand the knowledge regarding the study of thermal-hydraulic issues of Gen IV Gas-cooled fast reactors, such as the ALLEGRO demonstrator reactor, which features a cylindrical fuel pins and hexagonal flow arrangement [12]. An elementary geometric cell representation of the ALLEGRO ceramic pin core is shown in Figure 1.3. In this figure, the edges of a hexagon are drawn (green), for which the wetted perimeter is equivalent to the sum of the six arcs sections (120°) of the neighboring rods. For the virtual hexagonal geometry, the measured h_{hex}/d_w results on 0.91, whereas for the L-STAR a h_{hex}/d_w =0.95 was chosen (see Figure 3.5), to obtain a proxy for the situation of neighboring rods.

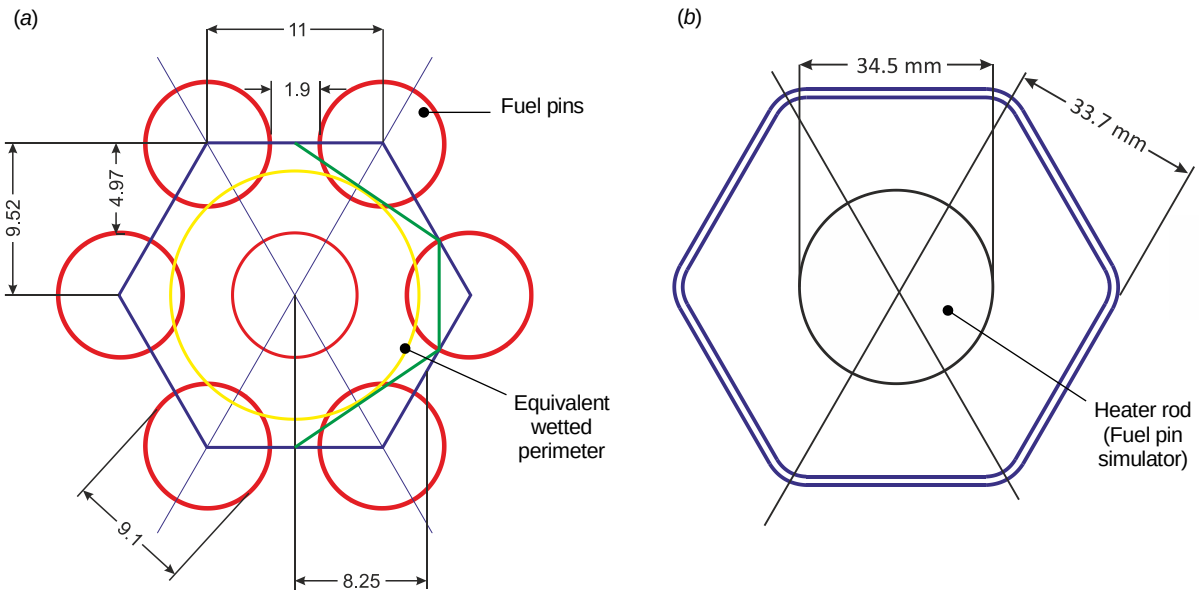

Figure 1.3: Sketch of the elementary geometric fuel bundle cell inside the ALLEGRO ceramic pin core (*a*) and (*b*) L-STAR hexagonal flow channel at INR-KIT.

[3] L-STAR (the acronym stands for the German words Luft – Stab, Abstandshalter, Rauheiten, which means air – rod, spacer, and roughness)

As reported in [15], it is obvious that reactor flow and temperature conditions cannot be reproduced 1:1 in the L-STAR experimental facility. The most relevant deviations are the different geometries (single rod in experiment vs. rod bundle in reactor), and the different coolant media (low pressure air in experiment vs. high pressure helium in reactor). The main working parameters are summarized in Table 1.1. A meaningful way to transfer the experiment results to reactor analyses can be done by using a set of dimensionless similarity parameters. Under the most common dimensionless parameters to characterize the thermal-hydraulic behavior of a system are $Re, Pr, Gr,\ Nu,$ and q^+. Whereas the Nusselt number Nu, friction factor f, dimensionless velocity $u^+(y^+)$ are used to describe the heat transfer, friction factor and mean velocity distribution near the walls, respectively. Since it is usually not possible to simultaneously match exactly more than one parameter between experiment and application, it is necessary to identify the most dominant quantities in the given cases. In the case of forced convective flows, Reynolds number is usually the dominant characterizing quantity for the heat transfer transport, since the Reynolds number determines the transversal turbulent exchange of momentum and energy in the boundary layer [16]. For intensive heating, additional (usually secondary but compared to the Reynolds number) effects may occur by the local variation of the gas properties (density, viscosity). Furthermore, in this case the effect on the turbulence structures is a relevant mechanism, for example the effect of the viscosity on dampening terms, and the effect of the density on the acceleration terms in the conservation equation for the turbulent kinetic energy [17]. Furthermore, buoyancy can play a role, either promoting or deteriorating the heat transfer. Moreover, there is no universal parameter describing the effect of intensive heating on the heat transfer. However, engineering correlations and criteria quantities such as T_w, T_g or q^+ are well suited for experiments planning and design tasks, since these can be computed from a-priori set point values only (mass flow, heating power) and do not rely on quantities, which will emerge a-posteriori as results from the experiments [15]. With the above argumentation, the Reynolds number (see Eq.[4.7]) is used to scale the mass flow between experiment and reactor conditions, while the heating power is scaled by using the dimensionless heating rate q_i^+ (see Eq.[4.15]).

Parameter	ALLEGRO MOX	ALLEGRO Ceramic Pin	L-STAR facility
Coolant	Helium, 7 MPa	Helium, 7 MPa	Air, 0.3 MPa
Core power	75 MW	75 MW	0.024 MW
Fuel element geometry	Bundle 169 pins	Bundle 109 pins	Annulus, 1 pin
Dimensional			
Hydraulic diameter [mm]	4.2	5.4	35.4
Heated length [mm]	860	860	2500
Gas inlet temp. [°C]	260	400	20
Gas Outlet temp. [°C]	530	940	Up to 250
Gas velocity, bulk [m/s]	25.9	20.9	4.7
Wall temperature, max [°C]	562	863	181
Wall heat flux [kW/m²]	477	557	3.7
Non-dimensional			
Inlet Reynolds number, Re	24000	**16 550**	**16 550**
Heat up ratio, q_i^+	0.001	**0.0015**	**0.0015**

Table 1.1: Comparison of working condition between the ALLEGRO reactor and the L-STAR experimental facility at INR-KIT [15].

If we knew what we were doing, it
wouldn't be called research, would it ……...!

Albert Einstein (1879-1955)

2. Background and literature review

This chapter deals with the general background and detailed literature review of the present experimental research effort. First, a brief description of enhancement techniques used to reduce the temperature difference between heated walls and the working fluids is given in section 2.1; followed by a short description of the major factors affecting the enhancement mechanisms on smooth and structured walls is provided. Section 2.4 summarizes the previous studies carried out in this field for the last past decades, describing experimental and numerical results on heat transfer enhancement, friction factor and velocity distributions by using different artificial surface structures on heated walls. Finally, a small description of the current project activities in the frame of Gen-IV GFR is given.

2.1. Heat transfer augmentation techniques

Heat transfer augmentation techniques for single and two-phase flows is classified into two broad categories (*i*) *active techniques,* that require an external power source and (*ii*) *passive techniques,* which does not need external power source to generate an enhancement. Convective heat transfer enhancement techniques have been widely investigated by many different researchers, among others e.g. Bergles et al., 1985 [18] or Dewan et al., 2004 [19].

The basis of any active heat transfer enhancement technique is in the utilization of an external energy inducing turbulent mixing into the working fluids; destabilize the thermal boundary layer, thereby substantially increasing the heat transfer coefficient between the wall and the fluid [20]. However, this external power is not easy to provide, due to the complicated arrangement. Some examples of active methods require for example, pulsation mechanical aids, surface vibration or the use of an electromagnetic field to disturb the seeded light particles in a flowing stream. On the other hand, passive techniques do not require any direct input or external source of power; rather they use and convert the kinematic energy of the main flow towards the interface, however ultimately leading to a pressure drop increase. Some examples of such passive techniques are the use of small metallic fins, wires wraps, dimples, artificial surface structures or geometrical modifications incorporated to the wall. Both active and passive techniques have been used to increase the heat transfer coefficient in several commercial engineering applications.

However, for the present thesis study only passive augmentation with artificial surface structures is considered, this mainly since no other additional active systems are feasible to be implemented inside a GFR fuel pin.

2.2. Artificial surface structures

The artificial surface structures are basically a passive technique, which is becoming quite important in commercial applications, as means of augmenting the heat transfer in forced convective single-phase flows. Artificial surface structures or turbulence promoters have been described, as well-defined small protuberances or cavities placed at regular and controlled intervals along the fluid wall interface, contrary to sand-grain roughness, where the surface topology is stochastically distributed along the wall [21]. Considering the success achieved in the commercial systems, the use of artificial surface structures on the cladding material of GFR fuel rod assemblies has been recently proposed, to improve the heat decay removal in the systems. The primary mechanisms of surface structures are the disturbance and break-up of the boundary layer creating various secondary motions, promoting local streamwise and spanwise turbulent mixing close to the roughened wall, thus increasing the velocity gradients between the structures, as shown in Figure 2.1. As a result, a larger energy and heat momentum exchange between the fluid and the heated wall is achieved [22]. The performance of the artificial surface structures depends significantly on the Reynolds number as well as the geometrical characteristics, such as the structure height (e), width (w), spacing (P), flow angle of attack α with respect to the flow and the structure shape. These key geometrical parameters of the surface structures are frequently presented in their dimensionless parameters, as follows:

- *Pitch-to-height ratio,* (P/e)
- *Roughness height ratio,* (e/D_h)
- *Roughness width,* (w/e)
- *Roughness structure shape*
- *Flow angle of attack,* (α)

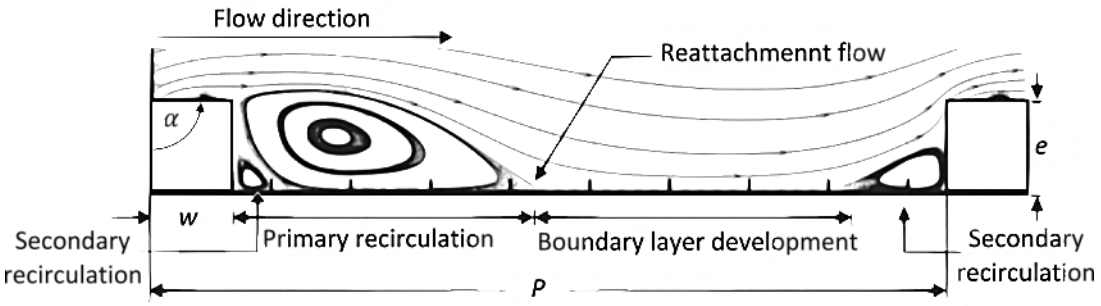

Figure 2.1: Streamline distribution of a horizontal flow over two square shaped consecutive surface structures and assignment of the individual flow domains characteristic induced by the geometry parameters [23].

Many authors have classified the artificial structures, depending on their distribution, mainly into two-dimensional and three-dimensional surface structures. Three-dimensional surface structures are characterized by a continuous distribution in the direction of the fluid flow, whereas, three-dimensional structures are periodically interrupted, a detailed report can be found by Bergles et al., 1985 [18].

2.3. Boundary layer concept

The first step to understanding heat transfer augmentation in forced convective flows is the boundary layer concept. The boundary layer concept was first introduced by Prandtl et al., 1904 [24] who defined it as a thin layer close to a solid surface, where viscous effects are dominant. The boundary layer thickness δ_L is normally defined, as the distance from the solid surface at which the fluid experiences no appreciable frictional influence; frequently given as the point where the velocity reaches approximately 99% of the main flow, u [25, 26]. Hence, the velocity near the wall is smaller than at a larger distance of the surface. The boundary layer is normally subdivided into four regions as is shown in Figure 2.2: (*1*) viscous sub-layer is thin layer next to the boundary $y^+ \leq 5$ across only a limited number of turbulent fluctuations and associated inertial effects can be expected compared to viscous effects. In this layer, the mean velocity profile has a universal form, which follows the relationship $u^+ = y^+$; (*2*) transition layer $5 \leq y^+ \leq 30$, the viscosity and turbulent forces are equally important and the flow is turbulent; (*3*) turbulent logarithmic layer $y^+ \geq 30$, where the viscous shear stress can be neglected and the turbulent shear stress is constant and equal to the bottom shear stress and (*4*) turbulent outer layer $y^+ \geq 50$, where mean velocities are almost constant because of the presence of large eddies, which produce strong mixing of the flow and shear stress gradually reducing to zero at the freestream flow [27].

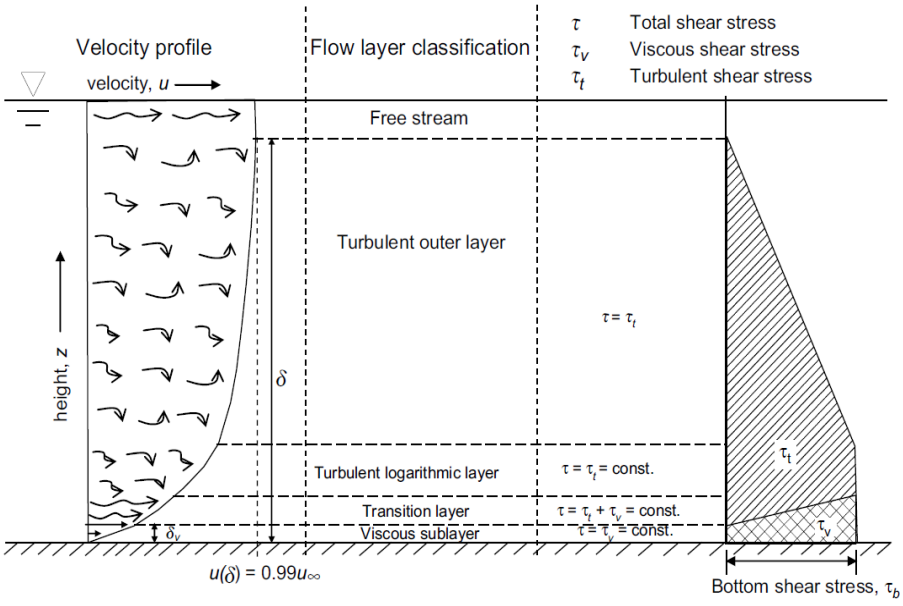

Figure 2.2: Boundary layer velocity profiles and shear stress distribution within different flow regions of the boundary layer [28].

2.3.1. Boundary layer on smooth walls

Even though this study aims to study the turbulent flows over artificially structured walls, it seems appropriated to provide a brief introduction overview to smooth surfaces. If the surface structure geometry is relatively smaller than the viscous sub-layer, such that the sub-layer is not significantly disturbed by the surface, then the surface is considered to be hydraulically smooth [26]. The boundary layer over hydraulically smooth walls can be sub-divided mainly in two regions; the inner region *viscous layer,* in which the viscosity is an important parameter and *outer region*, where the flow is independent of the viscosity [29]. In the inner region of the smooth wall boundary layer, the velocity distribution can be correlated in terms of the dimensionless velocity u^+ and dimensionless y^+, as followed:

$$u^+ = y^+ \tag{2.1}$$

where $u^+ = u/u_\tau$, $y^+ = y \cdot u_\tau/v$ and the friction velocity or turbulent velocity u_τ can be defined as,

$$u_\tau = \sqrt{\frac{\tau_w}{\rho}} \tag{2.2}$$

Further from the wall the velocity distribution can be determined by the *logarithmic law of the wall*, as followed:

$$u^+ = \frac{1}{\kappa} ln(y^+) + B \tag{2.3}$$

where, κ refers to the universal von Kármán constant equal to 0.418 and B represents an integration constant. In fluid dynamics, the von Kármán constant refers to the dimensionless distribution of the longitudinal velocity in the wall-normal direction of a turbulent fluid flow near a boundary [30, 31]. The corresponding value of B could variate in the literature from 5.0 to 5.45 from author to author, which might be connected with lack of information about turbulent boundary layer [32].

2.3.2. Boundary layer over artificially structured walls

Investigation of the flow passing over artificially structured walls has gained a very important role in the development of turbulent theory, specifically with regard to engineering type flows, where surface structures are often encountered. Turbulent boundary layers have been continuously studied over the last decades and despite the knowledge on turbulent boundary layers over smooth and structured walls, still numerous questions regarding the structural characteristics and nature of

turbulent flows over artificial surface structured walls remain open [33]. One of the first experimental studies of surface roughness began with the studies performed by Nikuradse et al., 1933 [34], who conducted a systematic and extensive investigation of the effects of Reynolds number, friction factor and velocity distribution of fully developed flow over very uniform roughness pattern of sand grains, wire meshes and perforated pipes.

The introduction of the surface structures yields a modification of the boundary layer leading to an increase of the wall shear stress and a change on the mean velocity profile, due to enhanced turbulent energy diffusion, increasing significantly the friction factor compared to the smooth walls [35, 36]. The modification of the boundary layer has a significant impact on the momentum, heat, and mass transfer rates, since they are controlled by the turbulent mixing in the vicinity of the wall. The lack of this information is critical not only in understanding the basic flow mechanisms, but also affects the capacity to accurately model the flow parameters such as, the friction factor and heat transfer coefficient in complex flows configurations.

The effect of the artificial surface structures on the velocity profiles was first studied by Clauser et al., 1954 [31]. He established that the inner layer for structured walls had a similar logarithmic region with a similar slope compared to the smooth walls. According to this and taken into to account the terms of a modification of the logarithmic law proposed by Clauser, the local mean velocity of in the inner region can be calculated as described in Eq.[2.4]:

$$u^+ = \frac{1}{\kappa} ln(y^+) \; + \; B \; - \Delta U^+ \qquad [2.4]$$

The coefficient κ and B are assumed to be invariant for smooth and structured walls [30, 31]. The ΔU^+ represents the roughness function, which gives the downward shift of the mean velocity distribution compared to smooth walls, caused by the wall condition change [37]. The roughness function ΔU^+ (zero for a smooth wall) described in Eq. [2.5] depends on the roughness Reynolds number $e^+$and the geometry nature of the surface structure [31].

$$\Delta U^+ = e^+_{smooth} - e^+_{rough} = \left(e/D_h \sqrt{\frac{f}{2}} Re \right)_{smooth} - \left(e/D_h \sqrt{\frac{f}{2}} Re \right)_{rough} \qquad [2.5]$$

Most recently, Tachie et al., 2001 [9] and Jimenez et al., 2004 [5] reported that an accurate determination and interpretation of turbulent flows over artificially structured walls depends on how accurately the mean velocity distribution are measured, particularly very close to the wall. For this reason, more experimental investigation for the accurate determination of such phenomena continues to be an important issue until present day.

2.4. Literature on artificial surface structures

The turbulent flow over artificially structured tubes, ducts, and channels has been a subject of studies since the beginning of the 20th Century in the areas of fluid dynamics and heat transfer. Flows of this nature can be found in engineering systems of significant technological interest such as turbine blade internal cooling, heat exchangers, aerospace and solar heaters. As a result of the constant development and improvement of the available technologies, the subject has significantly gained relevance in the recent years. As a result of this, the artificial structuring of the fuel rod cladding in GEN IV Gas-cooled reactors has been recently proposed by the Generation IV International Forum. The literature survey is divided into three sections, concerning the first pioneer works in section 2.4.1, followed by most recent investigations outcomes concerning the general aspects for structured heated walls in section 2.4.2 and finally first experimental implementation attempts in Gas-cooled systems in section 2.4.3.

2.4.1. Early Investigations

One of the first pioneers who attempted to understand the influence of surface roughness on friction factor was Darcy et al., 1858 [38], who conducted sensitive pressure drop measurements in water conduits over 21 pipes with different materials and roughness surfaces, mainly made of cast iron, asphalt and glass. With the exception of glass, all pipes were 100 m long with a varying diameter between 1.2 and 50 cm. As a result of his experiments, he established that the flow distribution depended on the type of surface roughness, pipe diameter and its inclination with respect to the flow. In addition, he observed that the resistance coefficient for a relative roughness height e/D_h varied with the Reynolds number, concluding that the friction factor decreases as the Reynolds number increases, however within a certain range, the friction factor becomes almost independent of the Reynolds number [39]. Years later Fanning et al., 1877 [40] proposed a correlation for the pressure drop as a function of surface roughness.

Stanton, 1911 [41] conducted experimental measurements on roughened pipes with different diameters to compare the influence of different surface roughness parameters. Stanton varied the depth and space of the roughness geometry proportional to the pipe diameter. He compared for the same pipe the largest and the smaller Reynolds numbers to achieve fully developed velocity profiles for different pipe diameters. As result of his experiments, Stanton obtained a good agreement for the dimensionless velocity profiles; however, he observed small discrepancies in the close vicinity of the wall, which proved a similarity of the flow through different roughened pipes.

Schiller, 1923 [42] conducted further experimental researches regarding the effects on friction factor on conventional macroscopic rough pipes at various depths, inclinations and Reynolds numbers, similar as those conducted by Stanton. His results also indicated that for a fixed Reynolds number range, the friction factor increases with increasing surface roughness. Schiller indicated that for fully developed turbulent flows, the friction factor is independent of the Reynolds number, but nevertheless

is fully determined by the relative roughness height-to-hydraulic diameter ratio e/D_h. He established that the law of resistance for circular tubes could be used for non-circular cross section geometries, if the hydraulic diameter is used as a characteristic value of the cross-section area [43].

A more exhaustive research of the impact of rough surfaces on pressure drop as a function of the geometrical parameters and Reynolds number was conducted by Nikuradse, 1933 [34], who studied the effect of sand grain roughness on the friction factor and velocity profiles of fully developed pipe flow by means of experimental measurements in a series of circular roughened pipes using six different sand grains configurations between $0.002 \leq e/D_h \leq 0.06$ and a Reynolds range of 600 to 10^6, respectively. He found, that the internal boundary layer flow can be distinguished in four primary flow regimes: laminar, smooth, transitionally rough, and fully rough. These regimes are highly Reynolds number dependent. Therefore, he established a relationship for the friction factor behavior expressed as a function of Reynolds number for each value of relative roughness height e/D_h, also known as the roughness Reynolds number e^+.

With his results, he defined three regions for fully developed flows in terms of the roughness Reynolds number e^+. The hydraulically smooth flow region ($0 \leq e^+ \leq 5$), where the roughness has no effect in the friction factor because the roughness height e lie entirely within the laminar sub-layer. In the transitional rough flow regime ($5 \leq e^+ \leq 70$) the size of the roughness elements is in the order of the thickness of the boundary sub-layer. As the roughness height e/D_h and Reynolds number further increases, the surface roughness elements begin to produce more projections passing through the sub-layer causing the reduction of its thickness, increasing the energy losses. The fully rough regime ($e^+ \geq 70$) the roughness function e/D_h is considered to be independent of the roughness Reynolds number. In this regime, the friction factor attains its maximum value without any remarkable augmentation by increasing the Reynolds number, since the boundary layer is nearly eliminated [44].

Moreover, his remarks showed that for small Reynolds numbers the friction factor is the same for rough and smooth pipes. Furthermore, he observed that at higher Reynolds number the friction factor increases. However, for any given relative roughness the friction factor eventually becomes constant at higher Reynolds numbers. Based on these findings Nikuradse developed a friction similarity law for sand grain roughness surfaces.

Schlichting, 1936 [45] following the results obtained by Nikuradse and Prandtl, conducted a series of experimental studies on a variety of surface roughness elements with various height, shapes and spaces in fully developed turbulent flows in rectangular channels, with the aim of determining the friction factor effects. As a result, Schlichting proposed the *equivalent sand grain roughness*, k_s concept. The equivalent sand grain roughness concept is a simplified empirical model used for the prediction of the friction factor effects of well-defined roughness structures, which can be compared to the Nikuradse and Prandtl experimental results on friction factor over sand grains for internal flows.

Later on, Colebrook and White, 1939 [46] published their findings of the variation of surface roughness and its effects on the pressure drop. Colebrook and White experiments consisted of six

concrete lined pipes with an inner diameter of 53.5 mm and a total length of 6 m. The six different roughness types were formed by combining several sand grains sizes fixed to the pipes by bituminous paint. The average relative roughness values ranged from 0.043 mm to 0.254 mm. These experiments were conducted under transitional and fully developed turbulent flow regimes. As a result, they were able to determine, that the friction factor rises as the flow velocity increases for all roughness types. However, once the velocity reaches the power law, the friction factor remains constant for all further higher velocities.

Cope, 1941 [47] conducted simultaneous measurement on heat transfer and friction coefficients over a series of smooth and internally roughened pipes. The inner surface roughness elements were mechanically produced by a special knurling process, which produced a series of pyramids geometrically similar in form but varying in absolute size from pipe to pipe. The roughness ratios (pipe radius/height of roughness elements) were set approximately to 8/1, 15/1, and 45/1. The experiments were conducted by using water as working fluid in a Reynolds number range from 2.0×10^3 to 6.0×10^4. His results indicated that when fully turbulent conditions are established, the surface roughness has a very low effect on the heat transfer coefficient, however, in the transitional regime (between laminar and fully turbulent flow), the surface roughness may considerably increase both friction factor and heat transfer coefficients, compared to the smooth walls.

Sams, 1952 [48] was probably one of the first who conducted combined experimental investigations on convective forced heat transfer and pressure drop associated to the thermal-hydraulic improvement of single rod geometries associated to gas-cooling flows in GFR. The experiments were conducted with air flowing through electrically heated Inconel tubes having various different square-thread-type fins, with a conventional relative roughness height-to-hydraulic diameter ratio e/D_h of 0.016, 0.025, and 0.037. The experiments were carried out for Reynolds numbers up to 350 000 at average wall temperature up to 800 °C and heat flux density up to 362 kW/m^2. His experimental data showed that both heat transfer and friction increased with increasing surface roughness e/D_h, becoming more pronounced with an increasing Reynolds number. The isothermal friction data for the roughened tubes resulted in curves similar to those obtained by other experimental studies; that is, that the curve for a given roughness deviates from the line representing turbulent flow in smooth walls at lower Reynolds number values. Good correlation for the heat transfer data was obtained for all investigated tubes, by making a modification of the conventional Nusselt correlation parameters, wherein the mass velocity in the Reynolds number was replaced by the product of air density evaluated at the average temperature and the so-called friction velocity; in addition, the physical properties of air were evaluated at the average temperature. A fair correlation for the frictional losses was obtained for each tube with different heat fluxes by incorporating the roughness parameter into the correlation.

Morris, 1955 [49] studied the effect of flow structures by varying the roughness heights and spacing. The experiments were conducted by using a surface roughness with a relative roughness pitch-to-height ratio P/e smaller than 0.7 m and relative roughness heights e/D_h of 0.05 m. He concluded that the separation between ribs i.e. the relative roughness pitch P/e parameter has an important influence on the heat transfer enhancement in roughened channels, caused by a wake formation downstream the

surface roughness, resulting in a turbulent mixing and the dissipation of energy. Based on the spacing of the roughness elements Morris defined three kinds of flows: (*i*) quasi-smooth (dense elements), (*ii*) isolated obstacles (wide spacing) and wake-interference (intermediate conditions). Years later and based on the results of Morris, 1955, Perry and Hoffmann, 1969 [50] reclassified the surface roughness elements into two basic categories; *k-type roughness*, which presents a large space between each other and *d-type roughness* with a small pitch separation. They conducted flow visualizations of the mean velocities and temperature profiles over *d-type* and *k-type* roughness. They found that the flow over *k-type* roughness produced eddies on a scale comparable to the roughness height, which are shed into the flow and then diffused into the shear layer, whereas *d-type* roughness generates stable eddies between two consecutive structures, without any strong diffusion into the boundary layer flow.

Nunner, 1958 [51] performed a series of experiments over smooth and rough pipes. As artificial roughness Nunner used a set of four split rings with a square cross section and a set of three of semicircular shape inserted into the pipe. He concluded that the heat transfer coefficient was significantly increased for the roughened pipes, due to the reduction of the thermal resistance layer on the turbulent domain. Nunner proposed one of the first flow models to explain the increase of heat transfer and friction factor effects of different geometrical shapes. He noticed that for a fixed pitch-to-height ratio P/e, both the friction factor and heat transfer coefficients tend to decrease for the semicircular shapes compared to the sharp edge geometries.

Several years later Dipprey and Sabersky, 1963 [52] conducted experimental studies on the relationship of the heat transfer and friction factor characteristics for various granular types of surface roughness sizes on demineralized water flows through electrically heated circular pipes at various Reynolds and Prandtl numbers. They confirmed the Reynolds number dependency on heat transfer and friction factor, as previously observed by other researchers. As for the heat transfer coefficient, an increase up to 270% at high Re and Pr numbers compared to the smooth tubes were reported, however, the enhancement was accompanied by a larger friction factor. For a very high Reynolds numbers up to 10^6 a maximum increase on the friction factor was observed for all combination of Re and Pr. Furthermore, Dipprey and Sabersky extended Nirkuradse´s work [34], assuming that the similarity law applies to both temperature and velocity profiles and developed the *heat transfer similarity law*. This model is based on the momentum heat transfer analogy, applied to a two-flow region model namely; *(a)* roughness influenced viscous wall region and *(b)* turbulent outer region, which is insensitive to the roughness.

2.4.2. Recent experimental activities

Several experimental studies have been conducted to provide more information regarding the heat transfer, pressure drop and velocity distribution for complex turbulence structured flows over well-defined artificial surface structures in different flow channel configurations [53]. Most of the activities were conducted to specifically understand the influence of the geometrical parameters, as a function of the pitch-to-height ratio P/e, relative roughness height-to-hydraulic diameter ratio e/D_h, shape, angle of attack (α), on the global thermal performance. Perhaps one of the most important experimental studies has been conducted by Webb et al., 1971 and 1972 [22, 54] who carried out extensive experimental activities over rectangular two-dimensional roughened flow pipes, focusing on the effect of the geometrical parameters and their effects on heat transfer and pressure drop at different Reynolds and Prandtl numbers for different type of fluids. The experimental data of Webb covered a wide range of relative roughness heights e/D_h and pitch to high ratios P/e between 10 and 40. As a result of their experimental investigation, they were able to describe the flow patterns between the ribs structures as function of the relative roughness height e/D_h and the relative pitch-to-height ratio P/e. They observed, that when the surface roughness elements are placed too close to each other, i.e. a pitch-to-height ratio P/e less than $\leq$5, a negative influence of the reattachment process of the flow is observed meaning that the reattachment of the free shear layer does not occur. On the other hand, for a roughness pitch-to-height ratio between $5 \leq P/e \leq 8$ results in excessive increase on pressure drop in the channel without any heat transfer exchange between the heated wall and the cooling fluid flow. Moreover, if the relative pitch-to-height ratio P/e is larger than 15, the boundary sub-layer may grow too much, reducing also the heat transfer enhancement between the fluid and the heated wall. Furthermore, they found that the local heat transfer coefficient between two consecutive surface roughness geometries is attained close to region were the flow reattaches (reattachment point, see Figure 2.1).

Additionally, Webb and Eckert extended the *law of the wall* and *momentum transfer analogy* from Dipprey and Sabersky work and developed a friction and heat transfer correlation for periodic two-dimensional structures in annular channels. Using these expressions, they introduced the concept of thermo-performance index η, as a form of comparing the thermal performance between the smooth and structured walls, as a function of Nusselt and the friction factor.

Lewis, 1975 [55] carried out an elementary analytical analysis to predict the momentum heat transfer and pressure drop characteristics for structured channels, in order to find the optimum flow configuration for different rectangular structure geometries. In his study, equally spaced rectangular ribs were considered. He introduced new efficiency parameter for optimization of the thermal-hydraulic performance of roughened surfaces with respect to smooth walls. For the calculation method, the exact shape and distribution of the roughness elements are required together with the friction factor magnitudes and a characteristic separation length i.e. the relative pitch-to-height ratio P/e. Although the experimental data for two dimensional roughened surfaces were fairly well predicted, the method did not predict any differences on the thermal-hydraulic performance over different width to high ratios (w/e).

Further experimental studies regarding the effects of the surface structures arrangement and shape configuration on the heat transfer and pressure losses have been performed by Williams et al., 1970 [56], Han et al., 1978 [57], Webb et al., 1980 [58], Sparrow and Tao, 1983 [59], Vilemas and Simonis,1985 [60] Hijikata, 1987 [61], Liou and Hwang, 1992 [62], Taslim & Wadsworth, 1997 [63], Rau et al., 1998 and most actual studies and reviews have carried out by [64], Leonardi et al., 2003 [65], Jimenez et al., 2004 [5] and Saini et al., 2008 [66].

Wilkie, 1966 [67] performed studies of the effect of the rib shape, the rib height, rib with and angle of attack on heat transfer and pressure drop for several rod elements in cylindrical channels. From his experiments, he concluded that the optimum heat transfer performance with transverse ribs occur at pitch to high ratio (*P/e*) greater than 7.2 and less than 15, as later confirmed by Webb et al, 1980 [58] . The optimal separation between ribs depends on the rib height relative to the channel. He found that the pressure drop generated was greater than the proportional increase of heat transfer for all tested artificial surfaces structures, when the coolant is a gas. Furthermore, he concluded that a slight chamfering of sharp edges resulted in a decrease on the friction factor by almost 10%, while the complete rounding of the structure had not more effects.

Williams and Watts, 1970 [68] conducted experimental tests on heat transfer and pressure drop performance over three basic surface structure geometry shapes. The experiments were conducted using different types of transverse structure, namely rectangular, chamfered, helically shape geometries placed in a rectangular flow, using water. Their results show than that the optimum thermal performance for all studied shapes was obtained at a pitch to high ratio (P/e) of 7. Furthermore, they observed that the thermal performance of chamfer ribs was superior when compared to the transverse and helical ribs, due to the creation of more vigorous vortex between ribs resulting in more frequently shedding of the boundary layer. The highest thermal performance was reported to be attained with a chamfer angle of 13° degrees, observing a slight decrease with the increase of the chamfer angle with respect to the flow. They report almost a 37 % higher heat transfer coefficient and a rather low increase on the friction factor of approximately 10 % compared with all the other structures shapes.

Han et al., 1978 [57] conducted experimental studies on the rib shape, angle of attack and pitch-to-height ratio effects in rectangular channels with two opposite rib roughened walls to determine the effects on heat transfer and friction factor. The channel was instrumented with two dimensional geometries simulating a rib roughened pipe. The experimental results showed that the rib shape and angle of attack (α) with respect to the flow had a significant effect on the pressure drop and rather a lower influence in the heat transfer enhancement. The performance comparison of the studied rib roughness elements, showed that the ribs with an angle of attack of 45° and sharp edges at a relative roughness pitch-to-height ratio P/e of 10 have a superior heat transfer performance at a given friction factor compared to the 90° transverse ribs and sand grain roughness. Additionally, based on the law wall and the application of the heat-momentum analogy developed by Dipprey and Sabersky, Han was able to develop a general correlation for the friction factor and heat transfer, which accounts for the rib shape effects, angle of attack and spacing.

Webb et al., 1980 [58] repeated the experiments in single-phase flows in circular flow channels instrumented with two-dimensional rib structures in form of a wire wrap arranged at different angles of attack to fluid flow. The purpose of his study was to understand and establish the effect of the angle of attack with respect to the flow, the angles that were studied in this experiment were 30°, 45°, 70° and 90° all with a pitch-to-height ratio P/e of 15. He concluded that helical arrangement yielded a greater heat transfer per unit friction than the transverse ribs, obtaining the best performance at angle 45° degrees. The result reported by Webb proved the experimental activities of Han et al., 1978 [57] on the benefits of implementing a helically arrangement.

Hijikata and Mori, 1987 [61] conducted measurements on local heat transfer coefficients for different transverse surface roughness shapes (square, semi-circular and arc shaped) placed along some rectangular and cylindrical channels with air and water as a working fluid, respectively. All the experimental measurements were carried out with the same e/D and P/e ratios. As a result of their study, they indicated that the thermal performance was highly dependent of the roughness shape. Furthermore, they indicated that the recirculation zone (located just upstream roughness), as well as the reattachment point were significantly affected by the shape of the surface roughness [69]. Moreover, their results showed that the transverse ribs attained the highest heat transfer enhancement, whereas the arc and semi-circular shapes attained similar lower heat transfer coefficients. However, the arc-shaped shape was found to have the lowest pressure loss compared to the transverse and semi-circular shapes.

Ichimiaya K, 1987 [70] performed a series of force convective heat transfer experiments in a narrow concentric annulus, using two-dimensional surface roughness, to investigate the heat removal from high-temperature gas flows. Experiments were carried out on the local and mean heat transfer coefficient and friction factor by changing the height and pitch of two different surface roughness elements (rectangular and triangular) and the flow rate. Their examination of spacing effect showed that the local heat transfer coefficients approaches a developed behavior between the third to fifth pitch from the position of the first roughness element, reporting an improvement on local the heat transfer of about two times higher when compared to the smooth wall measurements. On the other hand, they indicated that the shape of the structure element had more remarkable effect on the friction factor compared to the size of the surface structure, which is in a good agreement with the reported results of Hijikata and Mori.

Liou and Hwang, 1992 [62] performed experimental studies on heat transfer and friction for fully turbulent flows through channel with two opposite walls roughened with semicircular, square and triangular shape ribs. They reported that the three types of surface roughness had comparable thermal performances. Among the three types of ribs, the square rib was found to yield the maximum thermo-performance index at similar Nusselt numbers. However, it is also noted that the semicircular and triangular ridge yielded 1 to 2 times lower friction coefficients, nevertheless, these geometries were less likely to yield the hot spots behind the ridges compared to the square geometries.

Taslim and Wadsworth, 1997 [63] studied the contribution of the rib angle of attack, relative roughness rib spacing P/e, and relative roughness height-to-hydraulic diameter ratio e/D_h to the overall heat transfer enhancement of rib roughened walls in square channels. As well as other researchers, they reported that pitch-to-height ratios P/e between 8.5 and 10 produced the highest thermo-performance index among all studied cases. Secondly, they observed that the rib average heat transfer coefficient was much higher directly upstream of the roughness geometry compared to the area between the ribs. Taslim reported a higher thermal performance with 90° degrees structures (parallel to flow), when compared to the 45° degrees' arrangement, thus contradicting the results reported by Han et al., 1978 [57] and Webb et al., 1980 [58]. As for the general effect of rounding of the roughness corners, he described a decrease in both heat transfer coefficient and channel pressure drop.

Investigation of the velocity distribution effects over structured wall has been also conducted by several experimental approaches; however just few of them have been carried out in fully turbulent developed channel flows [39]. The study of the velocity distribution is a one of the key factors that allows a better understanding of the heat and momentum transfer mechanism, and friction factor characteristics on well-defined artificially structured walls. The effects of surface structures on the mean velocity and temperature profiles were well reviewed by Raupach et al., 1991 [35] and Krogstad and Antoniaet, 1999 [71] who investigated the effects of the turbulent boundary layers over surface roughness by comparing measurements over two rough walls with measurements from a smooth wall boundary layer. The two rough surfaces have very different surface geometries, although designed to produce the same roughness function, i.e. to have nominally the same effect on the mean velocity profile. They observed different turbulent transport characteristics for the rough surfaces. Substantial effects on the stresses occur throughout the layer, showing that the roughness effects are not restricted to the wall region. Subsequently, they reported that the flow over roughness elements increases turbulent fluctuations, which leads to a highly-modified distribution for the turbulent energy production. However, at sufficiently high Reynolds numbers, rough and smooth walls have the same turbulence structure above the roughness. One may infer from these observations, that flow behavior for different rough walls will pose a significant challenge for turbulence modelling.

Yokosawa et al. 1989 [72] measured fully developed turbulent in a square duct, in which two opposite walls of which were roughened, using a hot-wire anemometer. Velocities and stresses are presented and compared with measurements taken in a square duct with four smooth walls. Symmetric results, with respect to the axes of symmetry of the duct cross-section, were obtained for every flow quantity measured [39].

Liou and Kao et al., 1998 [73] conducted an extensive study on the velocity distribution over symmetric and asymmetric turbulent flows in a rectangular channel over two-dimensional rib structures at different Reynolds numbers by means of Laser-Doppler velocimetry (LDV). The Reynolds number was varied in the range of 2.0×10^3 to 7.6×10^4, covering a relative roughness height-to-hydraulic diameter ratio e/D_h between 0.13 to 0.33 and a rib width to height ratio e/w from 1 to 10. From their measurement results of the mean velocity and turbulence intensity, the critical rib height

and the critical Reynolds number Re_c in which the flow patterns become asymmetric were determined. In addition, the effects of the rib width w and boundary layer thickness δ_L on the formation and size of the separation zones between two consecutive rib roughness structures were documented.

Martin and Bates 1992 [74] reported velocity field and turbulence structure in an asymmetrically ribbed rectangular duct at several rectangular channel heights. The velocity measurements were carried out by means of a Laser-Doppler Anemometry (LDA) over the two sides of the channel: one with a smooth wall and the opposite one with a rib-roughened wall plane. Their measurements along the plane wall agree well with existing classical sub-layer zones concepts. Moreover, they remarked from near wall LDA measurements that the reattachment of the flow to the channel floor does not take place in this type of channel configuration. Therefore, previous measurements on similar channels by using relatively large control volumes could therefore be misleading. In view of their observations they remarked that it is not surprising that the existing numerical models have difficulties in accurately predicting reattachment and separation points for these types of geometries.

Saini et al., 2002 [75] conducted a series of experiments to collect heat transfer and friction data for forced convection flow of air in solar air heater rectangular duct with one broad wall roughened by using wedge shaped transverse ribs. The experiments were conducted in Reynolds number range from 3000 to 18000; relative roughness height 0.015 to 0.033; the relative roughness pitch P/e<12; and rib wedge angle of 8, 10, 12 and 15°. The effect of parameters on the heat transfer coefficient and friction factor were compared with the result of smooth duct under similar flow conditions. From the experimental results they derived correlations for the Nusselt number and friction factor in terms of geometrical parameters of the roughness elements and the flow Reynolds number.

Leonardi et al., 2003 [65] carried out experimental and numerical simulation over fully developed turbulent channel flows over two-dimensional rib roughness. Circular and square cross section surface structures were considered over a wide relative pitch-to-height ratio (P/e) ranges. From these results, they observed that the best thermal performance was obtained at a pitch-to-height ratio of $7 \leq P/e \leq 8$ for both structure geometries. Furthermore, they indicated that the total drag for the round shapes was about 40% lower compare to the squared roughness shapes, thereby providing a more efficient means of increasing the exchange of momentum and heat between the wall and the external flow. Moreover, Leonardi also observed that the surface roughness strongly affected the near wall flow structures; due to the outward motion occurring, most of all, close to the leading edge of the elements. The previously mentioned effect causes the change of the mean velocity profile in the vicinity of the wall, which in consequence modifies the heat transfer and friction factor coefficients.

Most recent experimental work denoting the most important parameters, affecting the heat transfer enhancement at surface structured walls were carried out by Jimenez et al., 2004 [5]. They reported two important parameters; one of them was the roughness Reynolds number parameter e^+, which measures the effect of the roughness in the boundary layer. A second parameter, whose importance has been remarked, was the ratio of the boundary layer thickness to the roughness height, where most of the energy and shear are concentrated. They concluded that the effect of artificial surface structures

influenced the flow across the whole boundary layer near the wall on the bulk velocity profile. As well, Jimenez suggested the need of more extensively and careful experimental studies with higher spatial resolution techniques, which could give more detailed information on this phenomenon.

2.4.3. Artificial structures in Gas-cooled system

During the 50's and end of 80's several notable experimental programs regarding the study of Gas-cooled reactor systems were carried out, of which the most notable programs were conducted by the UK Atomic Energy Authority (UKAEA), the Swiss Federal Institute for Reactor Research (EIR) and the Karlsruhe Institute of Technology (KIT) former Kernforschungszentrum Karlsruhe (KfK). The programs aimed to provide an experimental basis of the fundamental effects on the heat transfer and friction factor distribution over smooth and artificially structured single rod and bundle geometries. Additionally, to the experimental test, the development of analytical models and correlations was also conducted.

In the frame of the Nordic Committee for Nuclear Safety Research (NKS) in 1956, the UKAEA conducted one of the first experimental research programs regarding the thermal-hydraulic issues relevant to gas-cooled reactors systems. The Magnox reactor (named after the magnesium-alloy used to encase the fuel) was a gas cooled graphite moderated reactor using carbon dioxide as a cooling medium [76]. The Magnox reactor was initially designed as prototype to study the increase of the heat flux from the cladding to the coolant by implanting small metallic fins placed along the cladding of fuel rods. As a result of the experimental program significant experience was obtained, in particular on the increase of cooling gas pressures, as well as the design of steam generators and material limitations. In the early 1980s, Hudina and Noetlinger [77] conducted several experimental test programs on the MEGAERE [78] and the ROHAN [79] annular air loops, at the Swiss Federal Institute for Reactor Research (EIR). The experiments were designed to investigate the heat transfer and friction factor coefficients for artificially structured and smooth surfaces in gas cooled flows, taking into consideration the optimal key dimensionless rib parameters, as suggested by other author's studies, in order to determine the empirical constants for turbulent flow modeling**.** The experiments were carried out for different structured single heated rods placed into smooth circular channel, varying the hydraulic diameter of the channel from 50 to 90 for the MEGAERE and from 8 to 16 for the ROHAN loop. All experimental tests were conducted using air as coolant at pressures of 1 to 1.2 bars, with a peak heating power of 1300 W. As the reference case for each of the tube diameters, heated and unheated tests with a smooth rod, i.e. without artificial roughness, were conducted. Friction factors and heat transfer coefficients were measured. Also, available for the different tests are inlet, bulk, and outlet temperatures [80]. Moreover, through the experimental and analytical investigation, Hudina was able to confirm the heat transfer and friction factor data of early studies; as well as, establishing a complex criteria matrix for the choice of the most suitable surface structure design, depending on the technological and operational variables [81].

Similar research and development programs to study the thermos-hydraulic performance of artificially structured single rods were independently carried out at the former Institute for Neutron Physics and Reactor Technology (INR) at the KfK between 1972 and 1983. The principal tests were conducted with structured rods containing, square, trapezoidal and rounded edges structures. The experiments at EIR were performed with CO_2, while the experiments test at the INR-KfK were performed by using different gasses, i.e. Helium, Nitrogen and Air, as cooling medium. The main results of these experimental researches are summarized in several publications and reports done by Sevatteri, 1972 [82], Dalle Donne et al., 1977-1979 [83, 84, 85, 86, 87, 88] and Meyer et al., 1979 [89, 90].

Sevatteri, 1972 [82], presented an experimental investigation to determine the friction factors and flow distribution in artificially structured rod bundles. The rod bundle consisted of 19 structured tubes, with an outer diameter of 18 mm and a pitch of 26.1 mm, in hexagonal arrangement. The structure elements of the bundle were made of small equal-sided triangle metallic protuberances with a reported high of 0.11 mm and a pitch-to-height ratio of 8.25. From his study, he derived a method for the calculation of the friction factor in structured rod bundles as an extension of Nikuradse's work [34]. Sevatteri also demonstrated how in the case of rod bundles the effects of the structured and smooth walls can be evaluated separately from each other.

Dalle Donne & Meyer, 1977 [84, 85, 86, 87] examined and summarized a number of experimental studies to analyze the friction factor and the turbulent heat transfer coefficients on smooth and structured single rod geometries. For the structured rods, small square rib structures were machined, with a relative roughness height-to-hydraulic diameter ratio (e/D_h) between 0.96 - 2.73 and pitch-to-height ratios (P/e) from 6.25 to 29.7, respectively. The experiments were carried out on ten different structured rods, each being tested subsequently in four different channel configurations under high heat flux conditions and Reynolds number up to 2×10^5. From their experimental data, they derived an empirical transformation method for the extrapolation of the experimental results obtained in single rod channels to bundle geometries.

In a later work, Dalle Donne et al., 1978 [88] repeated the heat transfer and pressure drop experiments conducted at the EIR. The tests were performed with the same geometrical arrangement used at the EIR (after conduction of the CO_2 tests at EIR, the test section and the rods were moved to the KfK so that, as mentioned, the test set-up was kept identical for all three gases). The experiments at the KfK were performed by using helium and nitrogen. Although their measurements showed, that the slope of the logarithmic temperature profiles differs from the standard value of 2.5, as reported in [34], they reported that above assumption does not significantly affected the transformed heat transfer data [91].

Meyer & Vogel, 1979 [89, 90] carried out experimental tests over two-dimensional surface structured cylindrical channels, in order to obtain information on the influence of structures shape on the velocity distribution and the momentum loss. Structures with round edged trapezoidal ribs similar to those used at the experimental program at EIR were compared to sharp edged rectangular

structures at similar high and pitch ratios. The time averaged velocity measurements were carried out by means of circular Pitot tube with an outer diameter of 0.6 mm. Their results showed that velocity distribution at the narrow channel is clearly limited to the inner region of the sub-layer. The velocity profiles over rectangular structures showed higher velocities than those over rounded edged structures, while no distinct differences were observed at the outer region for both geometries. The friction factor related to the average velocity measurements over both geometries were found to be lower for the trapezoidal structures gaining about 10% lower values with respect to rectangular shapes, at same pitch-to-height ratios (P/e). Additionally, they observed that recirculation zones and reattachment of the flow tends to be shorter for the rounded structures compared to the rectangular ones, which might explain the fact the of the lower friction factor values for the round edged structures.

Years later Meyer et al., 1981 [92, 93] conducted numerous experimental works on fully developed turbulent flows by using different configurations of two-dimensional and three-dimensional surface structures on seven different single rod geometries, with the objective to study the pressure losses and heat transfer enhancement characteristics for gas-cooled single rods. The measurements of the velocity and temperature distributions in the structured annuli were used to analyze data obtained from measurement of the pressure drop and heat transfer. Their results showed that three dimensional structures, within a certain range of rib parameters, produce higher friction factors and heat transfer coefficients when compared to the two-dimensional structures. The thermal performance of three-dimensional structures was found to vary between 8 to 15 % compared to the two-dimensional structures, as the Reynolds number increases. Moreover, they reported that three-dimensional surface structures were observed to be more sensitive to cross-sectional changes, due to the increased probability of suffering corrosion and higher particles deposition. Another valuable result was a simple transformation method for the extrapolation of the heat transfer coefficients measured in an annulus into an arbitrary annular cross section.

The Generation IV International Forum (GIF) and the European Commission (EC) initiated and supported the creation of the Seventh Framework Programme of the European Atomic Energy Community (FP7-Euratom). The FP7-Euratom project was formally adopted at the end of 2006, covering seven-year period 2006-2013. The overall aims of this European project were to address and research the major issues and challenges in nuclear fission research, such as the management of high-level/long-lived radioactive waste, promote the nuclear safety, resource-efficient, as well as to ensure a robust and socially acceptable system for the environment against the effects of ionizing radiation [94]. Furthermore, the project activities under the FP7 aim to achieve optimum usage of the available European resources in experimental facilities, numerical tools, and expertise to establish a new common platform of research results and infrastructure in Europe. Two projects within the 7th Framework under the topic research and development of advanced nuclear systems (Gen IV) were devised; European Gas Cooled Fast Reactor (GoFastR) and the Thermal-hydraulics of Innovative Nuclear Systems (THINS). This present thesis work contributed significantly to both European Framework programs activities namely under the GoFastR WP 1.5 (Methods Development & Qualification) and THINS WP 1.1.2 (gas-cooled fuel assemblies).

The European Gas-Cooled Fast Reactor (GoFastR) project was designed as contribution for the further development of the Gas-cooled reactor systems (GFR), one of the six Generation IV systems, within the 6th and 7th Framework Programmes project activities. The GoFastR project aimed to review, preserve and extend the knowledge associated to the basic design of the Gen IV GFR systems (including the core and fuel subassemblies), development (e.g. ceramic fuel pins), as well as achieving the necessary diversity and reliability of the safety systems. In parallel, the conceptual design and safety related issues for the demonstration reactor ALLEGRO, such as decay heat removal, were carried out and used for the further qualification and validation of different numerical tools [95]. Undertaken studies included neutronics, thermal-hydraulics and core mechanics, to demonstrate that ceramic core can be produced and will be sufficiently robust to withstand handling and operation in a commercial power reactor. Furthermore, the GoFastR activities also included cooperation with other European FP7 projects. The most important of these was the Sustainable Nuclear Energy Technology Platform (SNETP) - GFR features strongly in its roadmap and in the European Sustainable Nuclear Industry Initiative (ESNII), which is proposed as the vehicle via which fast reactor elements of the SNETP roadmap is to be implemented [96].

The Thermal-hydraulics of Innovative Nuclear Systems (THINS) project is a large-scale integrated research program launched in 7th Framework Program of European Union, designed to promote the further development and validation of new deterministic models, improvement and qualification of numerical analysis tools and their application to Gen IV innovative nuclear reactor systems [97]. The main goals and objectives of the THINS project were setup, thorough extensive review of the most significant thermal-hydraulic phenomena involved in different innovative nuclear systems was carried out, to identify the common thermal-hydraulic challenges that are important to the design of the nuclear systems and need further investigations. Several important, crosscutting thermal-hydraulic topics were identified, i.e. advanced reactor core thermal-hydraulic s, single-phase mixed convection, single-phase turbulence, two-phase flow and code coupling and qualification [98]. As a result of the THINS activities, advanced methodologies and modeling improvement of the numerical engineering tools (system analysis, sub-channel analysis and CFD codes) dedicated to simulate innovative reactor systems were developed and validated, supported by an experimental data base platform [99].

> Nothing tends so much to the advancement of knowledge as the application of a new instrument. The native intellectual powers of men in different times are not so much the causes of the different success of their labors, as the peculiar nature of the means and artificial resources in their possession.
>
> Humphrey Davy (1778 - 1829)

3. Experimental facility

In this chapter, the experimental facility and measuring equipment which are used in the present work are discussed. In section 3.1 the main components of the gas loop and a detailed description of the test section and heater rod design are given. Detailed information of the data acquisition system, the system instrumentation, as well as systematic instrumentation errors are discussed in section 3.1.3. Furthermore, in section 3.2 the set-up description of the laser-Doppler anemometry technique and auxiliary system are introduced.

3.1. Experimental Set-up

3.1.1. Overview

The L-STAR test facility depicted in Figure 3.1 and Figure 3.2 (The acronym comes from the German words; Luft – Stab, Abstandshalter, Rauheiten, which means air – rod, spacer, and roughness) was designed and erected at the Institute for Neutron Physics and Reactor Technology (INR) at the Karlsruhe Institute of Technology (KIT). The L-STAR facility was developed to allow the experimental investigation of gas cooling single rod geometries similar to the GFR fuel rod elements. The L-STAR facility is a low pressurized gas loop designed to work at maximum pressure of 0.3 MPa in the circuit and a maximum gas temperature of 180 °C, allowing a heated rod surface temperature of about 750 °C. The facility is operated with “air” as working fluid with a maximum operation flow rate of about 0.33 kg/s corresponding to a Reynolds numbers up to 2.0×10^5. The basic design conditions for the test loop are listed in Table 3.1.

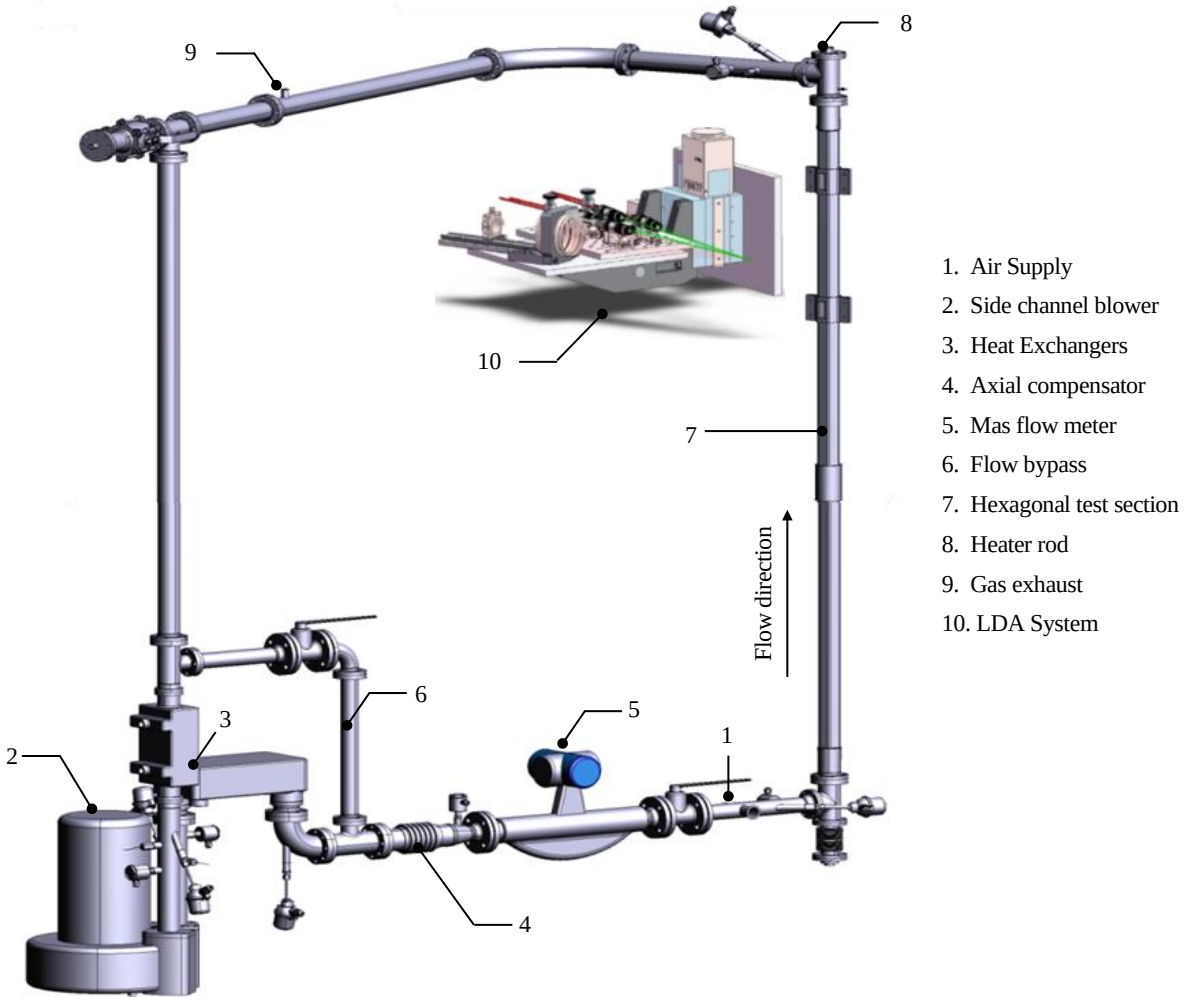

Figure 3.1: Schematic representation of piping in the L-STAR gas loop facility and its components.

The L-STAR test facility is composed mainly of a hexagonal test section (SL-TS-01) with an inner electrical heater rod element placed concentrically within the flow channel. A side channel driven blower (SL-CP-01) by Becker GmbH with an electronically controlled rotational speed up to 3000 rpm is used to regulate the flow velocity of the gas through the test section. The different set points for the mass flow are controlled by a frequency converter (SL-FC-01). Two air-water heat exchangers, (SL-HX-01) downstream of the blower are designed to lower the gas temperature raised by the gas compression of the blower, whereas the second heat exchanger (SL-HX-02) located upstream of the blower is used to cool down the gas coming from the heated test section, thus protecting the blower and the mass flow meter from being damaged by high temperatures, as well as helping to set and control the operating boundary conditions in the test section entrance. Immediately after the blower and the heat exchangers an axial compensator with an inner guidance sleeve (type ARN 06.0080.060.0) from Witzenmann® was mounted in order to reduce possible vibration disturbance effects on the test section.

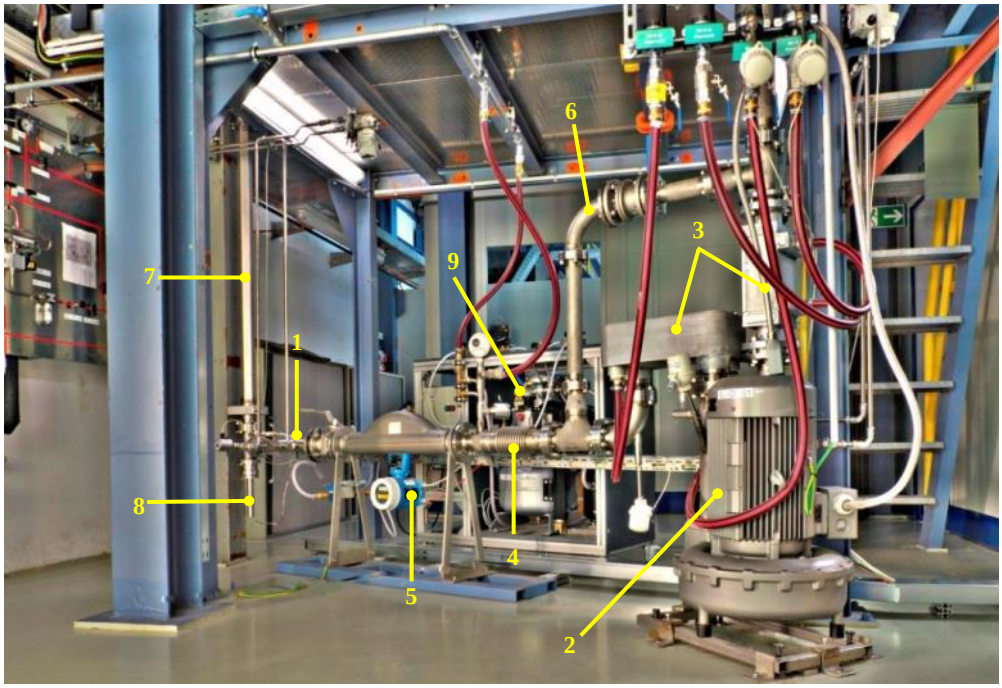

Figure 3.2: Picture of the L-STAR test facility and main components. (1) Air supply, (2) blower, (3) heat exchangers, (4) compensator, (5) flow meter, (6) bypass, (7) lower part test section, (8) heater rod and (9) particle generator.

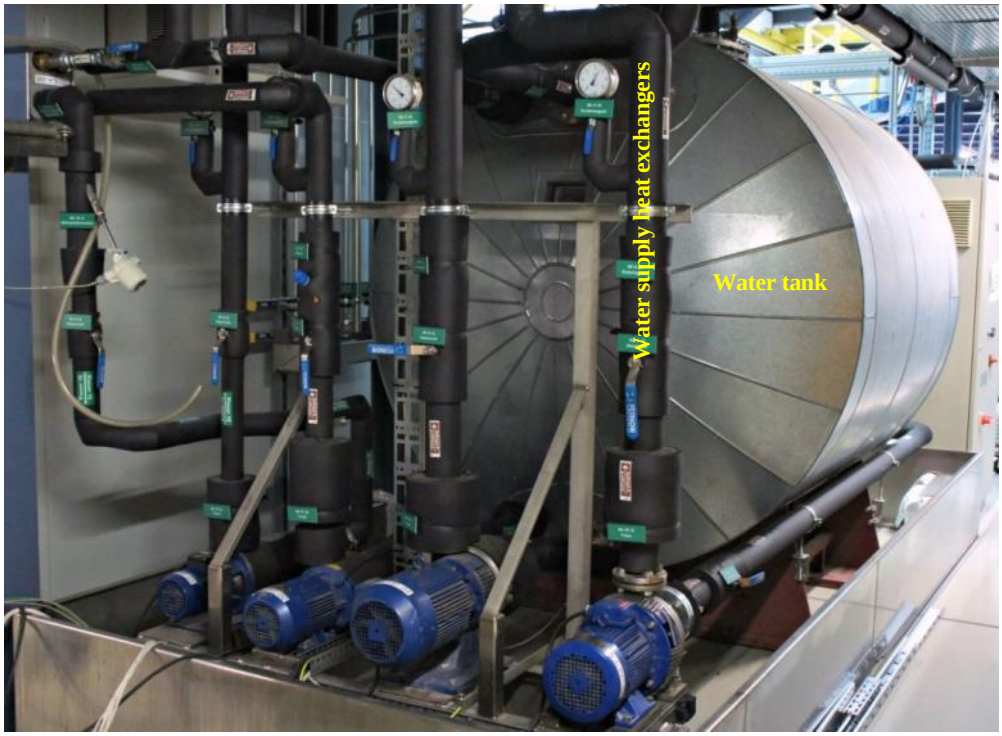

Figure 3.3: Picture of the auxiliary cooling system of L-STAR test facility use for temperature control of the air blower system.

Parameter	Value
Maximum mass flow rate	0.33 kg/s, turn-down-ratio > 30 possible
Gas pressure	0.1 – 0.3 MPa
Design electrical heating power	24 kW (up to 750 °C rod temperature)
Inlet temperature to test section	RT - (7-40 °C)
Outlet temperature from test section	< 200 °C

Table 3.1: Overview of the basic design conditions of the L-STAR gas loop facility.

The mass flow rate at the test section entrance is measured directly by a Coriolis mass flow meter (SL-FL-01), the measurement principle of this system delivers directly the mass flow rate. Two bypass valves were designed and installed in the loop; the first bypass valve (SL-VC-02) is designed to increase flexibility in mass flow rate and temperature regulation, namely allowing and increasing the stability of the facility at low Reynolds numbers. A second bypass valve (SL-VC-01) serves to feed the trace particle coming from the seeding generator unit during the flow velocity measurements. Additionally, the facility is protected by a safety valve (SL-VS-01) against overpressure, which is electrically controlled and directly connected to an exhaust pipeline, where air vented from the loop is collected to protect the working place of any contamination by seed particles. The full P&I diagram of the gas loop facility is shown in Figure 3.4. Additional to the basic instrumentation components, the L-STAR facility was equipped with Laser Doppler Anemometry (LDA) system and a seeding aerosol generator (AG) to provide a comprehensive description of the velocity distribution, evidencing detailed information of the enhancement mechanism of turbulent flows on smooth and single structured rod geometries. A detailed description of basic instrumentation and LDA systems is given in section 3.1.3 and section 3.2. An auxiliary cooling water system was designed and used for the temperature control of both air–water heat exchangers. The water-cooling system shown in Figure 3.3, consist mainly of a storage tank of about 5200 l fill up with a demineralized water and 34% ethylene glycol mixture plugged to two water pumps used to induce the flow into the heat exchangers (SL-HX-01/02). Two control valves and one pressure reducing valve from Danfoss® are installed to allow the temperature regulation by adjusting the valves openings, whereas a pressure reducing valve is used to avoid pressurization damage in the storage tank and reduce the flow noise in the installation. A pressure transmitter is used to determine the liquid level in a tank. The cooling water is circulated through an air cooler (McQuay chiller) to regulate the temperature of fluid during long measurement campaigns. A detailed description of the water system is reported in [100].

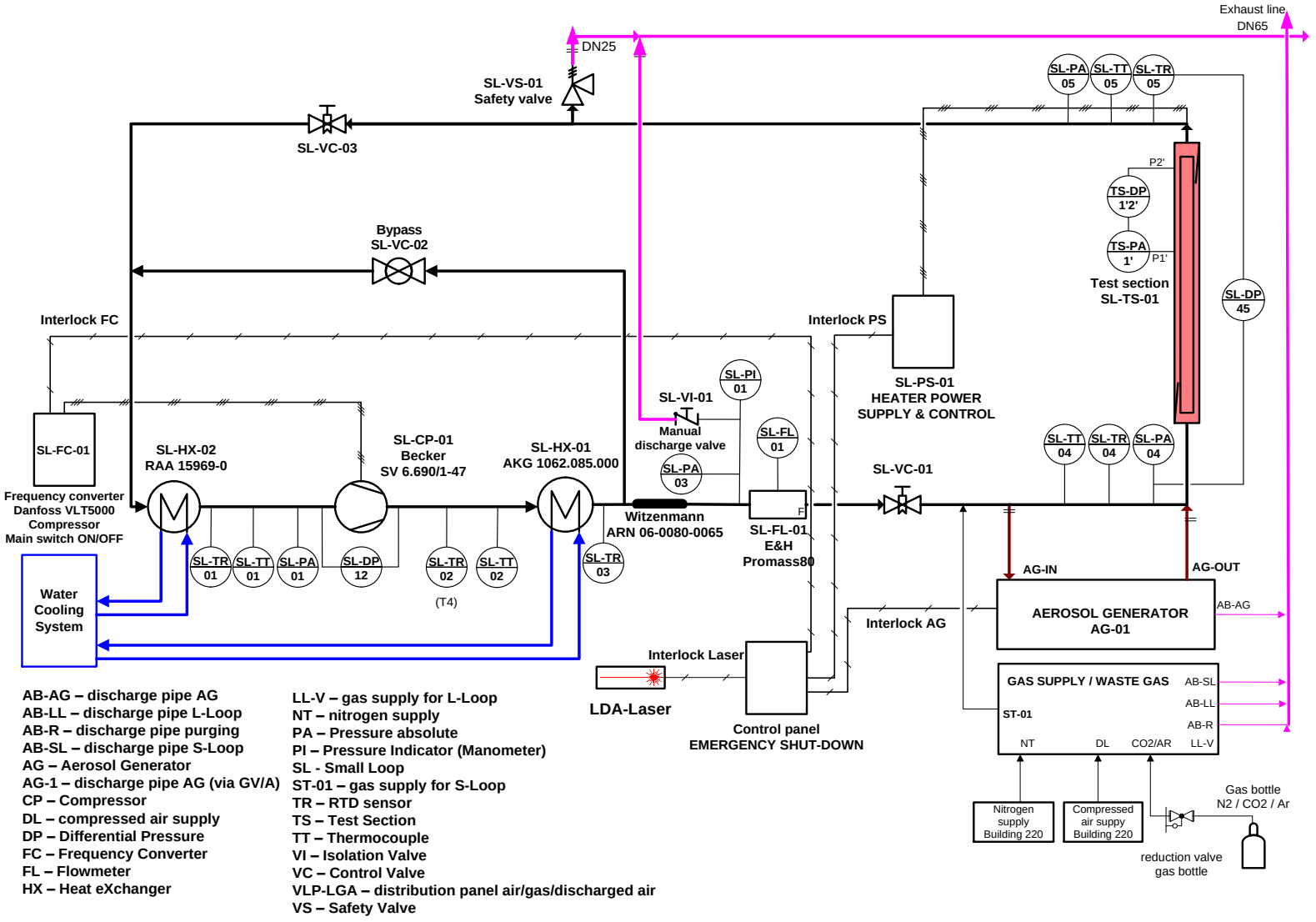

Figure 3.4: Process and instrumentation layout (P&ID) of the experimental L-STAR facility at the INR-KIT.

3.1.2. Test section

Flow channel

The test section of the flow channel is composed of hexagonal cross-section tube, made of AISI 304 stainless steel segments (with a wall thickness of 1.5 mm), with an inner electrical heater rod (smooth and structured) placed concentrically at the test section, which approximately simulates the scaled flow area of a GFR fuel rod element. The hexagonal test section channel has a total flow cross section area A_c about 2.9 ×10^{-3} m^2 and a hydraulic diameter D_h of 35.46 mm, as shown in Figure 3.5. This figure indicates the main Cartesian coordinate system (X, Y and Z) and the angular coordinate (ϕ) used for later the evaluation of the experimental results in chapter 5. On the lower and the upper ends of the test section, two T-junctions are used to connect the flow channel inlet and outlet to the vertical piping system. The T-junctions are joined by a transition piece, which allows the cross-section change from circular to hexagonal form. The central heated rod assembly has its mechanical fix point at the upper end cap, where the test section coordinate system Z= 0 (*Zero Point*) is defined, as indicated in Figure 3.6. The origin and orientation have been chosen, so that the thermal expansion of the rod can be expressed in a straight forward way. For the maximum theoretical working temperature of 750 °C, an elongation of approximately 29 mm could be expected in the heated rod [101]. To accommodate this elongation, the lower part of the test section has been equipped with a feedthrough gland (see Figure 3.7), through which the rod can axially expand, thus avoiding the axial bending of the heater rod during the experimental test. The technical roughness of the test section inner wall, measured with a HOMMEL tester T1000, has approximately an average wall surface roughness $R_{a,hex}$ of 1.06×10^{-6} m (±0.1 µm) and therefore considered as hydraulically smooth. In Figure 3.5, the main Cartesian coordinate system (X, Y and Z) and the angular coordinate ϕ used later for the evaluation of the experimental results in chapter 5 are also described.

Channel flow domain:

d_w = 34.55 mm
h_{hex} = 33.77 mm
r_{hex} = 6.55 mm
A_c = 2999.3 mm^2
S_w = 338.3 mm

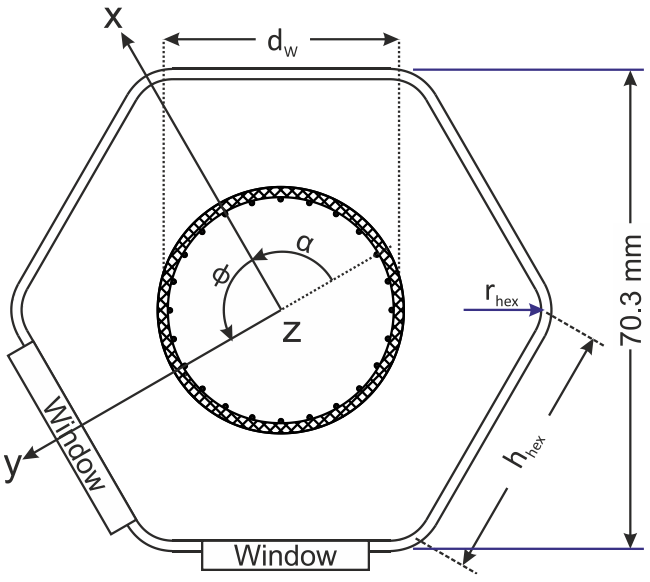

Figure 3.5: Schematic cross-sectional representation of the L-STAR test section with flow domain coordinate system, and optical accesses for velocity measurements.

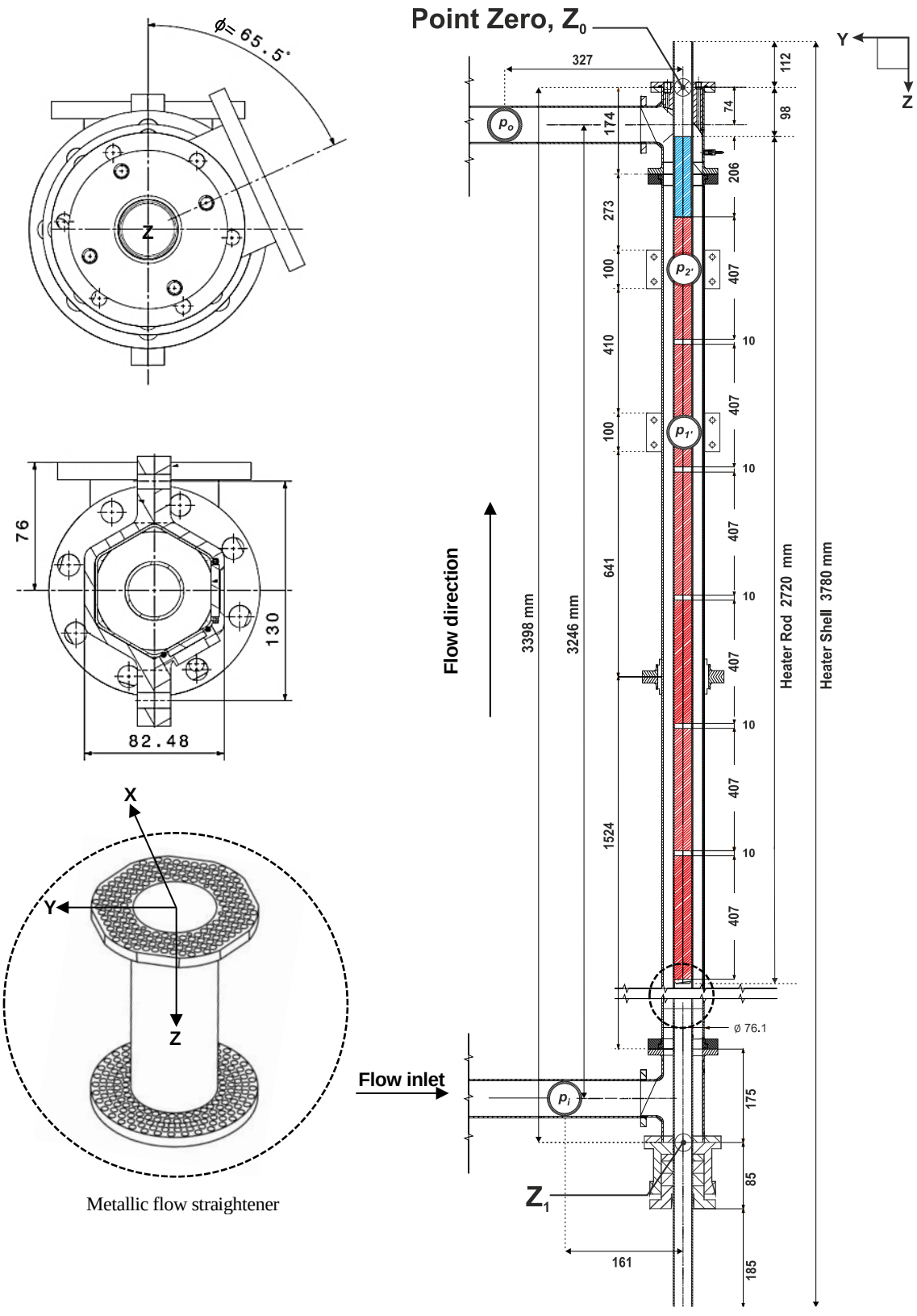

Figure 3.6: Schematic representation of axial partitioning (single heated sections 1 to 6 from the bottom to the top) of the heater rod and flow straightener installed in the L-STAR test section. Flow inlet ϕ= 0° and the outlet at the top at an (approx.) angle of ϕ= 65.5°. Dimensions are given in mm.

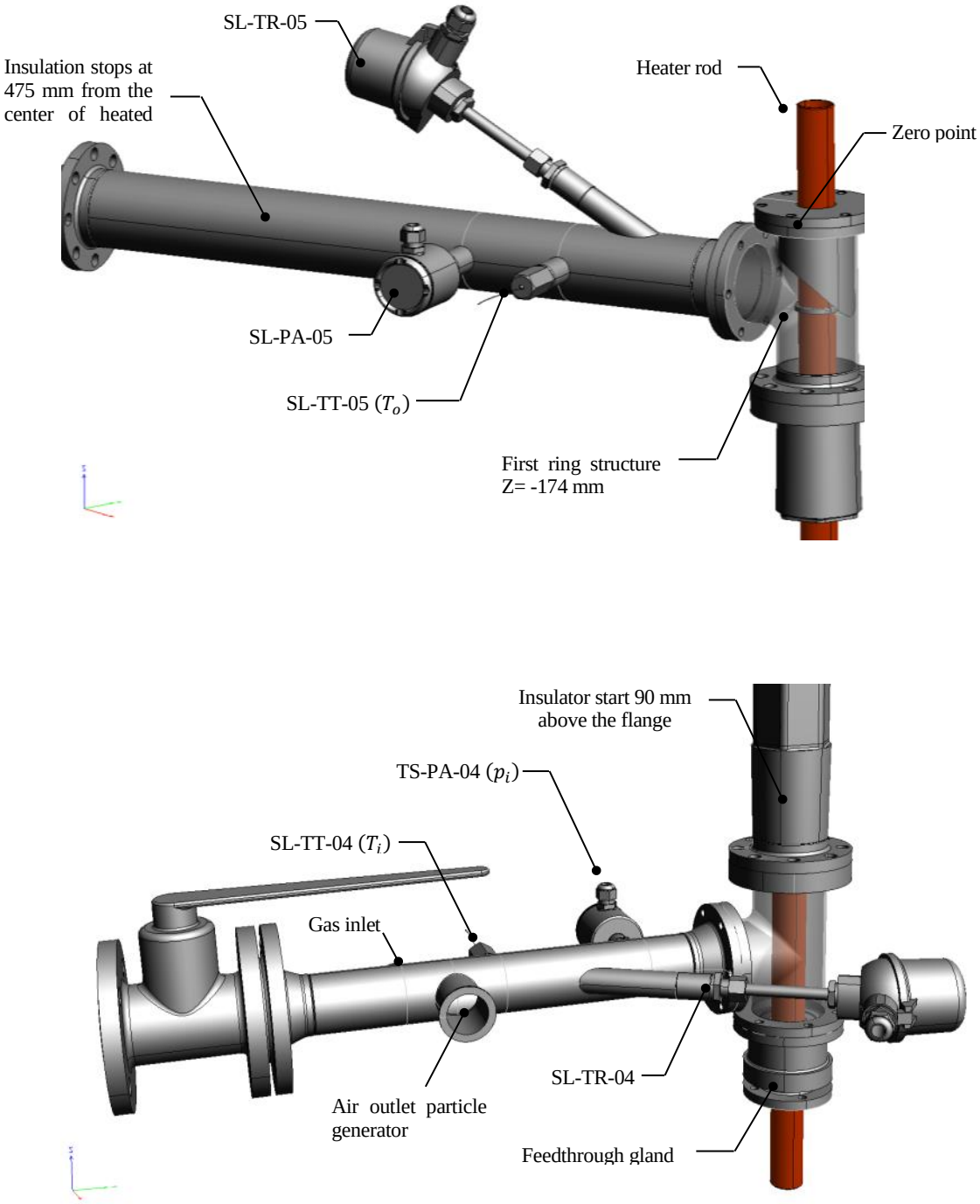

Figure 3.7: Overview of the main instrumentation for temperature and pressure measurements at the inlet (lower) and outlet (upper) of the test section.

The test section is equipped with several absolute and differential pressure transducers, used to attain the total and local pressure losses across the test section, as well as to control the boundary condition at the entrance and outlet of the flow channel. The bulk and wall temperature profiles are obtained by means of several Pt-100 ports and Type-K thermocouples located at the in-and outlet, as well as at different axial positions of the test section, respectively. A detailed description of system instrumentation is given in section 3.1.3.

A flow straightener device consisting of two perforated metallic plates was designed and integrated to the bottom part of the test section to reduce the flow effects of the T-junction and improve the uniformity of the flow field in the measurement region where the LDA measurements were to be performed. The flow device was designed to obtain a flow blockage rate of approximately 50%. The metallic plates were made of a stainless steel 1.4571 (5 mm wall thickness) with a total length of 100 mm. The perforations of the metallic plates have a nominal diameter of 2.0 mm at the inner region and 3.0 mm at the edges, respectively. The lower end of the flow straightener is located approximately 10 mm upstream the lower T-junction (inlet region) of the test section, as shown in Figure 3.6. To allow the flow visualization, the upper part of test section was equipped with two high quality Fused silica glass windows (NBK-7) located at an axial high of $Z = 486$ mm and $Z = 1007$ mm, allowing the access for optical flow measurement methods, such as Laser Doppler Anemometry (LDA) and Particle Image Velocity (PIV). The test section length is considered to be sufficient to ensure fully developed turbulent flow conditions before reaching the optical measurement regions and far enough from the channel inlet (including the flow straightener) and outlet T-junctions to ensure no disturbances to the flow. The hexagonal test section is entirely thermally insulated with two layers (19 mm each) of Armaflex–HT with a thermal conductivity k of 0.042 $Wm^{-1}K^{-1}$ (temperature range -50 °C to +200 °C) placed between the lower and upper T-junctions, reducing the heat loss to a minimum level. Estimations of the relative heat losses between insulated test section and the room environment based on one-dimensional heat transfer calculations resulted in less than 1% of the total supplied electrical heating power for all analyzed cases obtained during the steady-state phase [101].

Heater rod design

The test section is internally heated by means of an electrically heated rod assembly with a total length ~3780 mm and outer diameter $d_w = 34.55$ mm (±0.1 mm), where approximately a total length L_h of ~2500 mm ($Z = 307$ mm and ends at $Z = 2799$ mm) is uniformly heated. The heater rod is composed of five different layers, namely the heater cartridge and wires, ceramic glue, ceramic filler, compression shells and cladding, as depicted in detail in Figure 3.8. The core of the heater rod is composed of six industrial high-performance cartridges made of stainless steel delivered by Türk + Hillinger Group, each one with a total length L_s of ~407 mm. On each end of the heated sections, there is a length of about 2.5 mm without heating, followed by a 5 mm ceramic gap disk made of C230 (Porous steatite) separating the heater sections; effectively, there is a nominal distance of about 10 mm between each heated zone. The axial segmentation of the heater rod assembled in the test section is schematically depicted in Figure 3.6. A detailed design specification attained by X-ray analysis is given in Appendix A. The heater cartridges are protected and electrically isolated by Ø20 mm ceramic filler layer made of compressed MgO powder, followed radially by a ceramic support layer with an outer diameter Ø25 mm, onto which a band of NiCr 8020 resistive material is coiled in a spiral. The heater coils, with an outer diameter of about Ø27.7 mm, are fixated to the ceramic support by using ceramic glue, which is also used to fill up the gap between the ceramic support and the heater shell. Finally, the heater and ceramic components are covered by two metallic layers, namely the heater shell and compression shell.

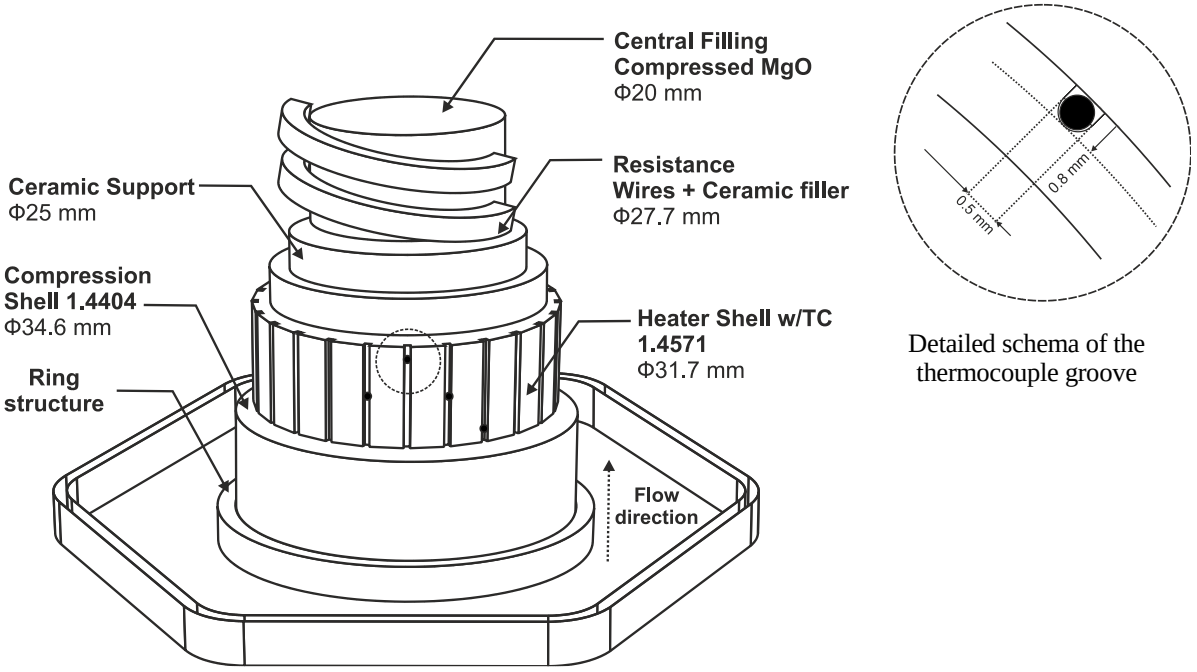

Figure 3.8: Schematic representation of the inner structure composition of the L-STAR heater rod element.

The heater shell of the heater rod (first metallic layer) is made of stainless steel 1.4571 with a wall thickness of 2.0 mm and an outer diameter of Ø31.7 mm (±0.15 mm). In this region 24 mini-channels (grooves) with a 0.8 mm depth were manufactured, into which a total of 48 type-K thermocouples, with an outer diameter Ø0.5 mm, are embedded. The thermocouples on the heater rod (TS-TT-00 – TS-TT-47) cover a total axial length from $Z = 74$ mm to 3320 mm. Furthermore, the thermocouples beneath the heater shell were installed in a specific pattern to resolve both global and local temperature distributions on the heater rod, since higher temperature differences between the structures may occur. Therefore, a high density of temperature measurement points, with a total amount of 19 thermocouples equally spaced, at about 5 mm (±0.1 mm) and $\alpha_{TC,i} = 15°$ degrees, was arranged at location height of both optical access regions. A detailed overview of the thermocouples pattern is given in Table 3.2. This pattern configuration enables to combine insights from flow structure measurements and from thermal measurements in a common interpretation. Finally, the heater shell with thermocouples is covered by hammering a compression shell (rod cladding) made of stainless steel 1.4404 with a wall thickness of 1.5 mm and a total outer nominal diameter of Ø34.55 mm. The average wall surface roughness of the cladding material $R_{a,rod}$, measured with a HOMMEL tester T1000, was determined to be 0.29×10^{-6} m.

TC [ID]	Angle [°] $\alpha_{TC,i} = \phi_{TC,i} + 90°$	$Z_{TC,i}$ [mm]	TC [ID]	Angle [°] $\alpha_{TC,i} = \phi_{TC,i} + 90°$	$Z_{TC,i}$ [mm]
TS-TT-00	0	472.5	TS-TT-24	0	478
TS-TT-01	15	982.5	TS-TT-25	15	988
TS-TT-02	30	472.5	TS-TT-26	30	983
TS-TT-03	45	74	TS-TT-27	45	1798
TS-TT-04	60	484	TS-TT-28	60	489
TS-TT-05	75	993	TS-TT-29	75	999
TS-TT-06	90	483	TS-TT-30	90	995
TS-TT-07	105	307	TS-TT-31	105	2175
TS-TT-08	120	494	TS-TT-32	120	500
TS-TT-09	135	1005	TS-TT-33	135	1012
TS-TT-10	150	494	TS-TT-34	150	1005
TS-TT-11	165	690	TS-TT-35	165	2558
TS-TT-12	180	504	TS-TT-36	180	509
TS-TT-13	195	1016	TS-TT-37	195	1021
TS-TT-14	210	505	TS-TT-38	210	1016
TS-TT-15	225	826	TS-TT-39	225	2928
TS-TT-16	240	515	TS-TT-40	240	520
TS-TT-17	255	1026	TS-TT-41	255	1031
TS-TT-18	270	517	TS-TT-42	270	1026
TS-TT-19	285	1419	TS-TT-43	285	3320
TS-TT-20	300	526	TS-TT-44	300	532
TS-TT-21	315	1038	TS-TT-45	315	1043
TS-TT-22	330	526	TS-TT-46	330	1037
TS-TT-23	345	532	TS-TT-47	345	1044

Table 3.2: Angular ($\alpha = \phi + 90°$) band axial distribution (Z-Axis) of the forty-eight thermocouples placed onto the electrically heated rod in the L-STAR test section.

A Cartesian coordinate system X, Y and Z axis, as well as, an angular coordinate ϕ were defined in Figure 3.5. The Z-axis originates in the upper fixation flange of the heater rod, which is oriented geodetically upward to the flow direction. The Y-axis is perpendicular to the main optical access window, while the angle ϕ is counted zero at the X-axis and increases counter-clockwise, so that the y-axis indicates the angle $\phi = 90°$. With the given relation of α and ϕ and the above defined parameters can be comprehended, that the thermocouple with $\alpha = 180°$ ($\phi = 90°$) is directly facing the optical window. With this configuration, the thermocouples with $\phi = \{0°, 60°, 120°, 180°, 240°, 300°\}$ face the edges of the hexagonal flow channel, while the thermocouples with $\phi = \{30°, 90°, 150°, 210°, 270°, 330°\}$ are facing the flat sides of the hexagonal flow channel. This could be important to explain the temperature variation, which can be originated by the formation of secondary flows at the edges of the hexagonal channel. The thermocouples TS-TT-03, TS-TT-39 and TS-TT-43 are soldered inside of the compression shell, located outside the heater cartridge region. Some important factors are summarized in Table 3.3.

Point/Object	*Z* coordinate [mm]
Axis of test section gas outlet	74
Pressure port for p2’	486
Center of upper window LDA	497
Center of lower window LDA	1007
Pressure port for p1’	1022
Axis of test section gas inlet	3320
Upper end of heater cartridge	101
First position of the structure element	174
Upper end of heater 6 (upper end of heated zone)	307
Lower end of heater 6	714
Upper end of heater 5	724
Lower end of heater 5	1131
Upper end of heater 4	1141
Lower end of heater 4	1548
Upper end of heater 3	1558
Lower end of heater 3	1965
Upper end of heater 2	1975
Lower end of heater 2	2382
Upper end of heater 1	2392
Lower end of heater 1 (lower end of heated zone)	2799
Lower end of heater cartridge, incl. footer	2821
Cold upper end thermocouple (TS-TT-03)	74
Heated upper end thermocouple (TS-TT-07)	307
Upper end of upper densely instrumented zone	472.5
Lower end of upper densely instrumented zone	532
Upper end of lower densely instrumented zone	982.5
Lower end of lower densely instrumented zone	1044
Heated lower end thermocouple (TS-TT-35)	2558
Cold lower end thermocouple (TS-TT-43)	3320
Heater rod safety control thermocouple	732
Upper (below the upper T-junction)	187.7
Middle (visible in upper window)	467.7
Lower (visible in lower window)	977.7

Table 3.3: Axial position of internal components in the L-STAR test section

3.1.3. Surface structure characterization

As discussed in section 2.4, implementation of artificial surface structures has been devoted to improve the convective turbulent heat transfer on many engineering applications. In the particular case of Gas-cooled Fast Reactors (GFR) the increase of the thermal-hydraulic performance of the fuel rods assemblies has been envisaged, with main focus of increasing the core power heat flux densities, keeping the temperatures of the fuel rod cladding at an acceptable level, which could reduce the electrical power generating costs [84]. For this particular thesis work two different types of artificial surface structures with a simple geometry have been studied. A schematic view of the two used structure elements is given in Figure 3.9. The structure elements are manufactured in form of metallic rings made of stainless-steel 1.4404 with a square cross section and sharp edges. A total number of 89 metallic rings are fixed and placed periodically into the cladding layer of the heater rod within an angle of attack α of 90° with respect to the direction of the main flow, covering the complete heated rod section. The metallic rings have an inner diameter of Ø34.2 mm (±0.1 mm), a height *e* and width *w* of 3.0 mm (±0.1 mm), equivalent to relative roughness height-to-hydraulic diameter ratio e/D_h of 0.084 m. The separation between each ring structure, also known as pitch P, is kept constant at about 30 mm (±0.2 mm), corresponding to a pitch to rib height-to-hydraulic diameter ratio P/e of 10, as suggested by former studies in the literature survey [102, 58, 63, 57, 103]. A cross-section representation of the ring structures is given in Figure 3.10 a,b. The upstream face of the first ring structure is set at about an axial length of Z= 174 mm (±0.2 mm), as depicted in Figure 3.10 c. To overcome this particular drawback, an optimized surface structure in the form of a perforated metallic ring has been designed and manufactured. The perforated ring structures consist of metallic rings with a total number of 23 drilled holes, with an outer diameter of P_d of 1.5 mm (±0.1 mm), separation angle $\emptyset_p$ of 15° degrees between the centerline of each perforation and a total open area ratio β_O of ~12%.

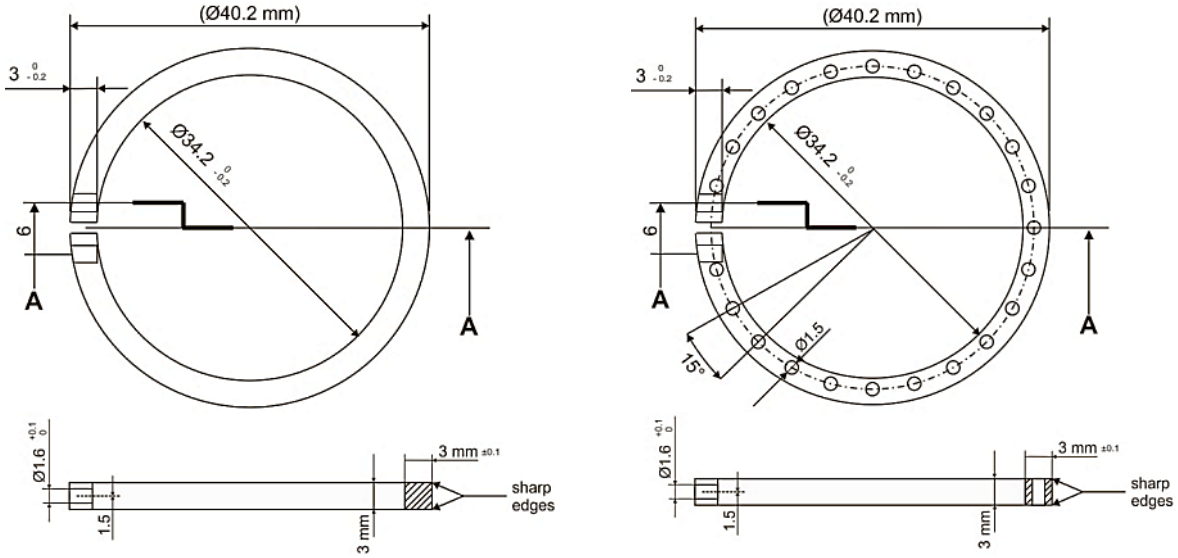

Figure 3.9: Schematic view of the investigated structure elements: solid (*left*) and straight perforated (*right*).

These can be found in nomenclature sections, as the sum ratio area of the perforated section in a single surface structure [104], and can be calculated as shown in Eq.[3.1]:

$$\beta_O = (n \cdot \pi \cdot r_p^2)/A_s \qquad [3.1]$$

where, n is the number of perforations drilled in a single ring structure, r_p the ring perforation radius and A_s represents the total ring area.

The center line of the perforations is located at about a wall distance P_c of 1.25 mm from the heater rod cladding, as depicted in Figure 3.10 c. The average technical roughness $R_{a,r}$ (outer face) for both ring structures elements have been measured to be about 2.25 µm for the solid and 2.18 µm for the perforated rings, respectively. The perforated ring structures have been designed to reduce the blockage ratio of the main flow, thus decreasing the local frictional losses. Furthermore, heat transfer might be increased as a result of the higher local mixing near the surface structure wall, generated by the flow jets at each perforation. Likewise, particle deposition onto the wall, between the surface structures, might be improved compared to solid ring geometry cases.

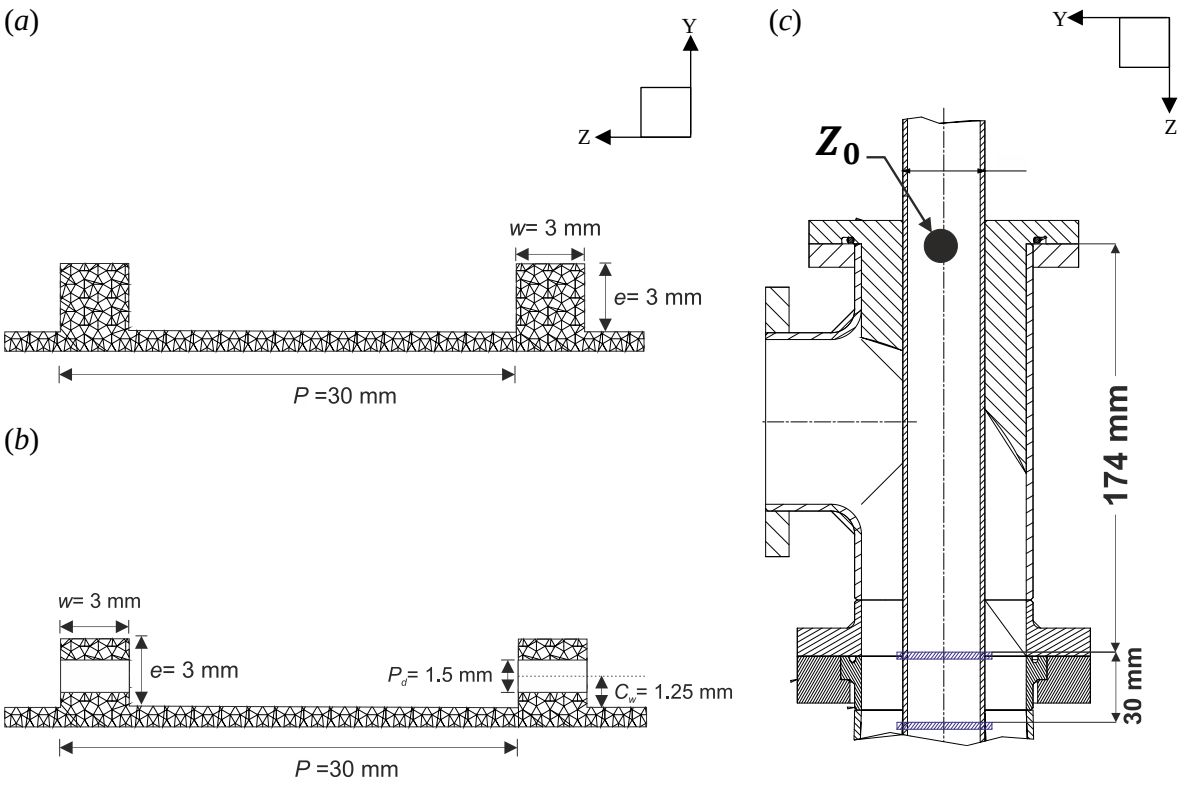

Figure 3.10: Cross-section details of the solid (*a*) and perforated (*b*) ring structures and axial location of the first metallic ring on the heater rod (*c*).

3.2. Laser Doppler anemometer

The velocity measurements are carried out by a two-component Laser Doppler Anemometry system. The LDA measurement technique, also known as Laser Doppler Velocimetry (LDV) is a widely accepted measurement technique which has been used for about four decades for fluid dynamic investigation in gases and liquids, providing information about flow velocity and turbulence fields in one measuring point. One of the advantages of LDA is that it is non-intrusive technique and therefore does not disturb the flow. It has a high spatial and temporal resolution, no user calibration is needed, and it has a high accuracy. The fact that the measuring device is not in contact with the flow has the further advantage that it is possible to measure in hazardous environments, e.g. obtaining velocity components in a flame.

The LDA measurement technique is based on Doppler shift effect of the light scattered from moving tracer particles seeded into the flow [10]. The Doppler principle is illustrated in Figure 3.11, where vector U represents the particle velocity, and the unit vectors $e_{1,2}$ and e_s describes the direction of the incoming and scattered light, respectively. According to the Lorenz-Mie scattering theory, the light is scattered in all directions at once, however only the light reflected in the direction of the LDA receiver is considered [105]. The light reflected from the moving particles act as a moving transmitter reaching the receiver. The incoming light has the velocity c and the frequency F_b (subscript b for beam), but due to the particle movement the seeding particle "sees" a different frequency F_p (subscript p for particle), which is scattered towards the receiver. From the receiver point of view, the seeding particle acts as a moving transmitter, and the movement introduces an additional Doppler-shift in the frequency of the light reaching the receiver [106, 107].

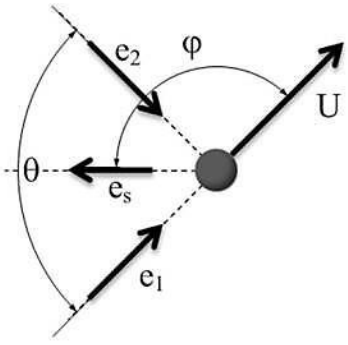

Figure 3.11: Light scattering of two incoming laser beams [108].

When two wave trains of slightly different frequency are superimposed, the beat frequency phenomenon emerges. The beat frequency corresponds to the difference between the two wave-frequencies. Since the two incoming waves originate from the same laser, they also have the same frequency at the intersecting point $F_{s,1} = F_{s,1} = F_{insident}$ [106]. This gives the general equation expressing the Doppler shift F_d in the frequency of the scattered light as a function of the particle velocity U. According to the Doppler-theory the Doppler frequency is given by:

$$F_d = F_{b,1} - F_{b,2} = F_{incident} \quad [3.2]$$

$$F_d = F_{b,1}\left[1 + \frac{U}{c}\cdot(e_s - e_1)\right] - F_{b,2}\left[1 + \frac{U}{c}\cdot(e_s - e_2)\right]$$

$$F_d = F_{incident}\left[1 + \frac{U}{c}\cdot(e_1 - e_2)\right]$$

$$F_d = \frac{F_{incident}}{c}|\,e_1 - e_2|\cdot|U|\cdot cos(\theta)$$

$$F_d = \frac{1}{\lambda}\cdot 2sin\cdot cos\left(\frac{\theta}{2}\right)\cdot\ u_x$$

$$F_d = \frac{2\sin(\theta/2)}{\lambda}\cdot u_x$$

where, c represents the speed of light, θ is the angle between the intersected laser beams, λ is the wavelength of the light and u_x denotes the velocity components in the x-axis.

Another practical approach to determine the relation between the detected signal and the measured velocity is the implementation of a fringe system model. The principle of the fringe model is the splitting and intersection two coherent laser beams into a common volume, thus generating parallel planes of light and darkness, known as fringe pattern [108], as shown in Figure 3.12.

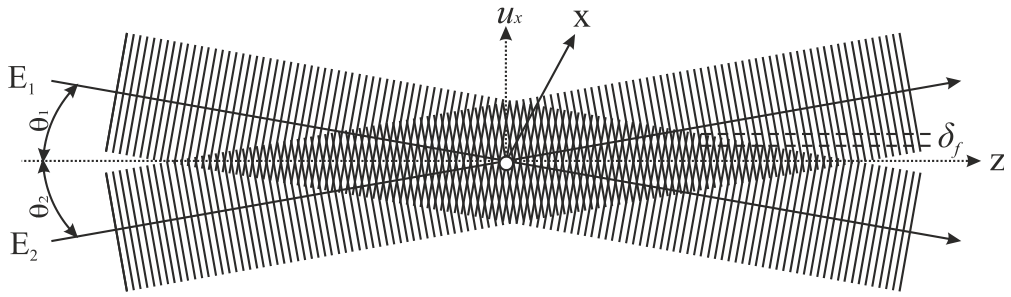

Figure 3.12: Fringe system at the point of beam waist of two coherent laser beams [109].

The fringe distance δ_f is proportional to the wavelength of the laser λ and the angle of the incidence between the beams θ [108]. The fringe distance can be obtained as given in Eq.[3.3].

$$\delta_f = \frac{\lambda}{2\ sin(\theta/2)} \quad [3.3]$$

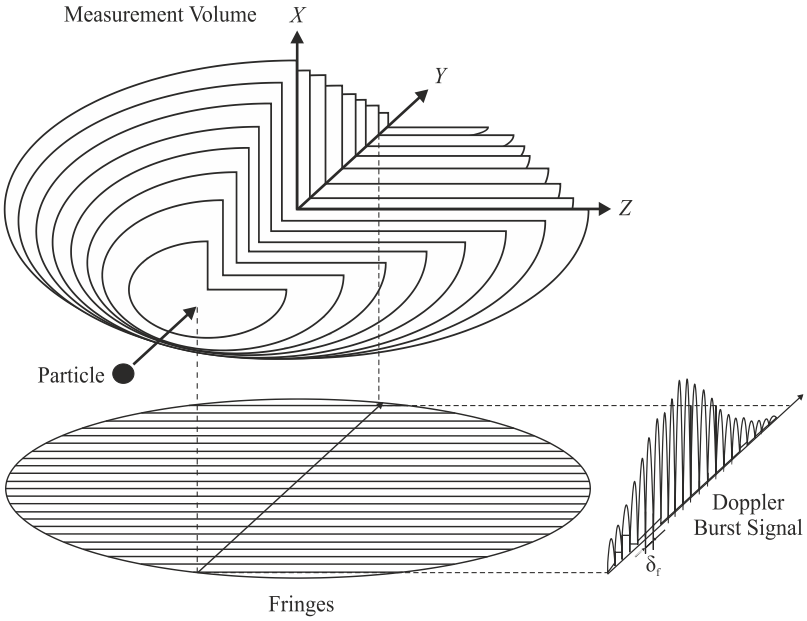

Figure 3.13: Schematic of the measurement volume and Doppler burst signal of a laser Doppler anemometry system [53].

When the seeding particles passes though the fringe pattern scatters the light of the incident beams generating a Doppler burst signal, as shown in Figure 3.13. The intensity of light reflected from a particle moving through the measuring volume will vary with a frequency proportional to the velocity component u_x of the particle velocity, as described in Eq.[3.4]:

$$F_d = \frac{u_x}{\delta_f} = \frac{2\,sin(\theta/2)}{\lambda}\,u_x \qquad [3.4]$$

Both the measurement volume size and the specified optical performance determine the quality of flow measurements [108]. The size of the measuring volume d_{MV} can be calculated from the beam waist diameter of the focused laser beams d_F and the angle θ. In addition, the focal length F_L of the front lens, laser wavelength λ, beam expansion factor E and beam waist diameter of the laser beam before passing the front lens d_L.

$$d_F = \frac{4F_L\,\lambda}{\pi E d_L} \qquad [3.5]$$

$$d_{MV,x} = \frac{d_F}{cos(\theta/2)} \qquad [3.6]$$

$$d_{MV,y} = d_F \qquad [3.7]$$

$$d_{MV,z} = \frac{d_F}{sin(\theta/2)} \qquad [3.8]$$

3.2.1. LDA setup

The velocity flow measurements are conducted by using a conventional LDA backscattering system from DANTEC Dynamics® “type Fiberflow 2D. The LDA set-up consist mainly of a 400 mW air-cooled Argon-ion laser linked to a FiberFlow transmitter unit and a FiberFlow probe [110], as shown in Figure 3.14. The beam produced by the laser source is split into two laser beams, where one of the two existing beams is shifted with a fixed 40 MHz with respect to the other one, by acousto-optic modulator (AOM), also known as Bragg cell. This frequency is inserted to handle the directional ambiguity, i.e. distinguish between positive and negative flow directions or measure zero velocity. The two laser beams are then split into six beams by a colour splitter, attaining three different laser wavelengths (476.5 nm, 488 nm and 514.5 nm). Nevertheless, for the current work only the 488 nm (blue) and 514.5 nm (green) laser beams have been used. The resulting laser beams are conducted then by single mode polarization preserving fibres into the measurement probe. The LDA probe is instrumented with two different optic sets, namely a 160 mm focal objective (for the measurements close to the rod wall) and AF-S NIKKOR 85 mm f/1.4 lens [111] (for the outer flow region of the channel), used to focus both laser beams into a single point to build a measurement volume. The main proprieties for the used focal lengths are given in Table 3.4. The total output power at the fibres is about 40% of the supplied power of the laser source. The light which is scattered by particles within the measurement volume is collected in the same optics in backscatter and conducted by a multimode fibre to a colour splitter, where the wavelengths are identified, dived and filtered and sent to a photomultiplier (PM) [107]. The electrical signals of the photomultiplier are then processed by a Burst Spectrum Analyzer (BSA) transmitter, also manufactured by DANTEC. The signal is analyzed by a Fast Fourier Transform (FFT) and a post processor, capable of handling and validating Doppler bursts at rates of up to 100 kHz. The user interface and data acquisition of the measured velocity distribution is conducted by scripting tools based on C#, Java and Visual Basic languages (BSA Flow software v5.0) [112].

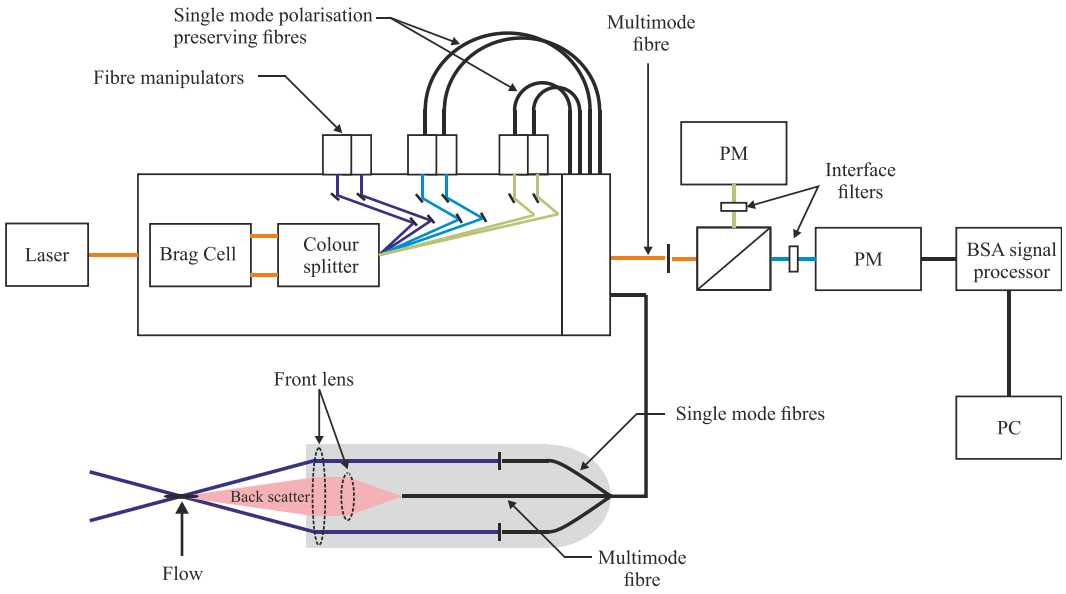

Figure 3.14: Simplified representation diagram of the DANTEC LDA measuring System [113].

Table 3.4: Characteristics of measuring volume with focal objectives 160 mm and 85 mm.

	θ[°]	$d_{MV,y}$ [µm]	$d_{MV,x}$ [µm]	$d_{MV,z}$ [µm]	δ_f [µm]	N_F
F160 mm	13.4	77	78	650	2.1	35
F85 mm	25.2	39	41	189	1.1	35

The measurement probe of the LDA system is mounted into a three translate and one rotation traverse system, located between the two optical window accesses of the test section, as shown in Figure 3.15. The traverse system was designed to achieve precise positioning of the measurement volume within a minimal vibration disturbance, especially important for the velocity measurements in the vicinity of the wall, where a larger precision is needed. The traverse system is composed of a X-Y stages stepping motors, as well as a 180° rotatory stage motor plates from the company LINOS®. The first motor stage allows the horizontal and lateral positioning of the LDA head component with respect to the test section, while the rotation stage maximizes the LDA access through the limited area of the sidewall windows, increasing the accurate alignment of the measurement volume near the rod wall, respectively. The traverse system has a total resolution positioning of about ±1 µm for the XY-axis and ±0.2 degrees for the rotatory stage motor [114]. The axial positioning along the test section, i.e. Z-axis, was achieved by a third step motor system from IEF Warner® (type PA-CONTROL Single) integrated to the traverse system. All components are computed controlled by M50-PCI[4] bus card integrated to the main computer, which allowed the remote control of the traverse system.

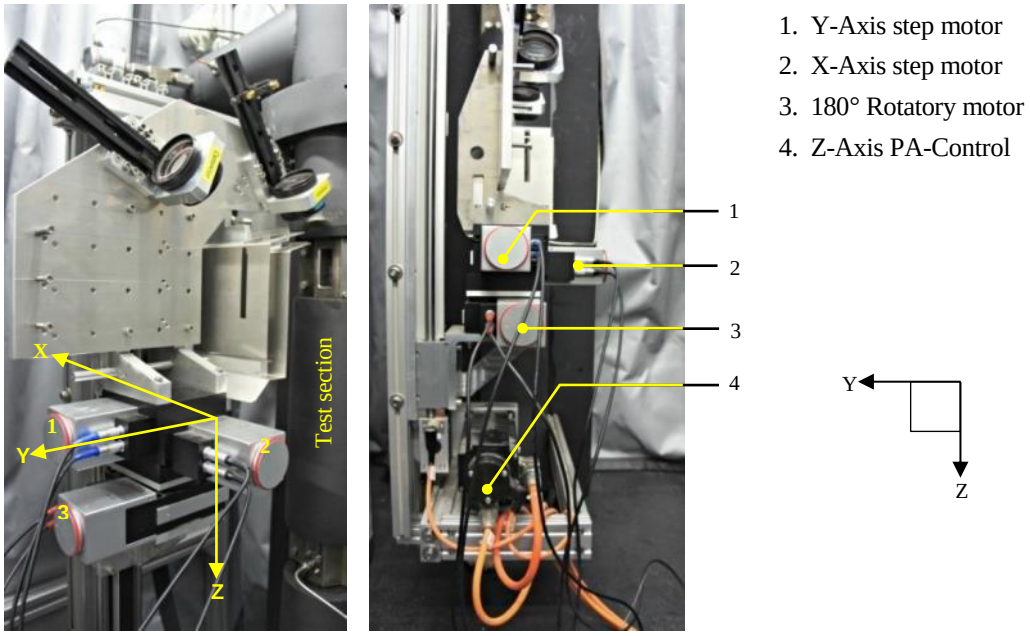

Figure 3.15: Picture of the stepping motor (*X*, *Y*, *Z* and rotation ϕ angle) LINOS® traverse system, coupled with an LDA system.

[4] PCI acronym stands for Peripheral Component Interconnect

The traverse system was aligned to the flow direction of the flow (Z-Axis) using an aluminum profile construction with a ±0.1 deg. The alignment of the traverse system to the test section was verified by marking their path on the test section wall, as the system was traversed in the stream-wise direction.

The LDA measurement system requires the use of seeding particles in the main flow to produce light scattering in the measurement volume and consequently reproduce the velocity and turbulence levels of the flow. The seeding particles are required to be small with low mass density such that they accurately follow the flow. Moreover, a high number of seeding particles is necessary to provide sufficient information on the flow dynamics. For the current experimental work fine titanium dioxide (KEMIRA L530 Ultrafine TiO_2) with a crystal grain size of 30 nm are used as flow tracers. The TiO_2 seeding particles can be used at high gas temperatures; moreover, they have a good backscattering light output (high refractive index). The selection of particles, as well as the basic concept of the seeding unit was conducted by Arbeiter et al., 2008 [115] and Hering et al., 2008 [116]. The seed particles are compressed and introduced by a brush type aerosol particle generator system RBG 1000 SL (AG-1) from PALAS®. The particle generator system is connected to the loop forming a secondary bypass, as shown in Figure 3.16. The air required for the particles injection is extracted from the loop before the test section and pressurized by a piston compressor (type "Dental" KAESSER T1). In order to minimize the pulsation caused by free piston compressor, two vessels (vessel-1 and vessel-2) of 10 and 24 liters are attached before and after to produce the driving pressure head. The air is then forced through a brush driven particle disperser, where fine TiO_2 particles are injected into the main flow through a metallic nozzle located directly after the flow straightener to avoid a possible flow blockage by the particle agglomeration on the straightener. The seeding generator is generally operated at particle feed of 2310 mg/h at an absolute pressure of 1.5 bars. All air vented from the loop is collected through an exhaust gas pipe, in order to protect the workplace from possible contamination by TiO_2 dust during the LDA experimental runs.

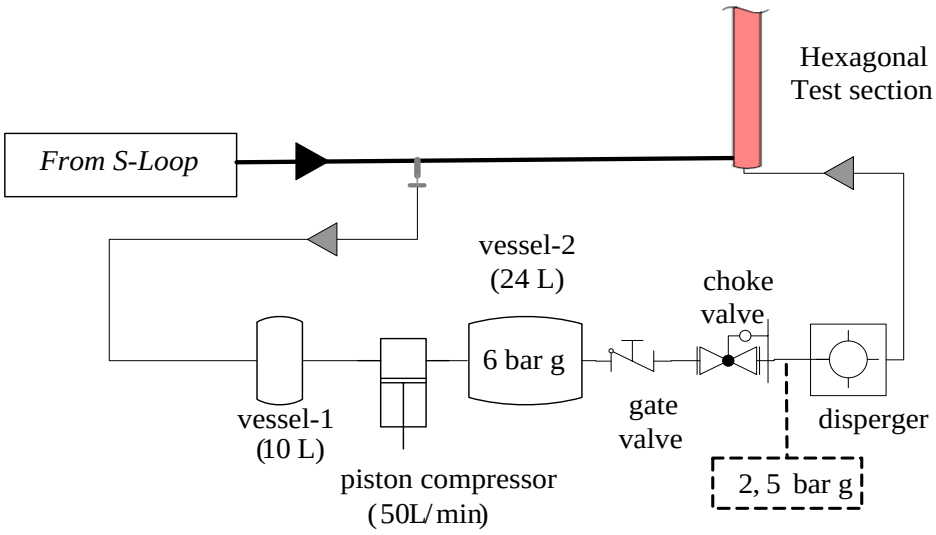

Figure 3.16: Schematic layout of particle seeding generator used for LDA measurements in the L-STAR test facility [101].

4. Data reduction and experimental procedure

In this chapter, the methodology and experimental procedure for evaluation of the measurement campaign using a smooth and two different structured rod channels is presented. In section 4.1, the experimental methodology, definitions, and equations used for the thermal-hydraulic analysis of the results is discussed. Section 4.2 describes the experimental procedure, as well as the main considerations for the evaluation of the experimental results. Section 4.3 outlines a detailed overview of the experimental program carried out in this research work.

4.1. Data reduction

4.1.1. Total loss coefficient and friction factor

In order to facilitate the comparison of obtained experimental results (for the smooth and structured rod channels), all parameters are expressed in terms of their dimensionless form according to the equations described in the following sections. Quantities with the index "*i*" are referred to the fluid state conditions at the inlet of the test section. Since absolute values and deviations may be misleading, the relative deviations of the dimensionless results are more appropriate. Furthermore, the dimensionless parameters allow a fair a comparison with others experimental and numerical analyses. This is necessary, since the numerical analyses are performed under exactly nominal boundary conditions, while each experiment slightly deviates from the exact nominal values. Furthermore, the comparison of the dimensionless parameters allows transferring the experiment results to the ceramic pin core gas-cooled fast reactor demonstrator ALLEGRO, according to the EU-Projects GoFastR and THINS [101]. The pressure losses in the current experimental work are evaluated by using the loss coefficient ζ and Darcy friction factor f_D. The pressure loss coefficient ζ is used for evaluation of dimensionless total pressure losses between the inlet and outlet sections (TS-DP-45), which includes the pressure loss effects at the upper and lower bends (see Figure 3.4), scaled by the dynamic pressure p_{dyn}, as shown in Eq.[4.1]:

$$\zeta = \frac{\Delta p_{4,5}}{p_{dyn}} \qquad [4.1]$$

where P_{dyn} is obtained from Eq.[4.2]:

$$p_{dyn} = \frac{\dot{m}_{CFM}^2}{\rho_{air}(p_i, T_i)} \cdot \frac{1}{2{A_c}^2} \qquad [4.2]$$

The local pressure losses are expressed by in form of Darcy – Weisbach friction factor f_D, a dimensionless quantity used for the description of friction losses along a pipe, as well as open-channel flow, to the average velocity of the fluid flow [16], as given in Eq.[4.3]:

$$f_D = \frac{D_h}{0.5 \cdot \rho_{air}(p_i, T_i) \cdot {U_m}^2} \cdot \frac{\Delta p_{1',2'}}{\Delta_z} \quad [4.3]$$

where $\Delta p_{1',2'}$ is the differential pressure obtained by the pressure transducer (TS-DP-1'2'), Δ_z the central axial distance between the pressure ports p_1' and p_2' of 0.536 m, δ_{air} is the density of air as function of the pressure and temperature at inlet conditions, and where U_m is the mean flow velocity extracted from a direct measurement of the mass flow rate $\dot{m}_{CFM}$.

This dimensionless quantity is not to be confused with the friction coefficient, sometimes called the Fanning friction factor C_f, as shown in Eq.[4.4], defined as the ratio between the local shear stress and local flow kinetic energy density [117].

$$C_f = \frac{\tau_w}{1/2 \, \rho U_m^2} = \frac{f_D}{4} \quad [4.4]$$

The effective diameter of the flow in non-circular tubes or channels can be characterized by the hydraulic diameter D_h, as shown in Eq.[4.5]. The hydraulic diameter is also used to determine Reynolds number Re and Nusselt number Nu.

$$D_h = 4 \cdot \left(\frac{A_c}{S_w}\right) \quad [4.5]$$

where A_c and S_w are the channel cross-sectional area of 2.99993×10^{-3} m^2 and the wetted perimeter 338.3×10^{-3} m, respectively.

The flow pattern of a fluid passing through a flow channel can be determined by the Reynolds number Re. The Reynolds number is defined as the ratio of convective to viscous momentum transport, defining the transition from laminar to turbulent flow [118]. It is given by the following relation in Eq.[4.6]:

$$Re = \frac{U_m \cdot D_h}{\nu} \quad [4.6]$$

However, several different definitions of the Reynolds number analogy have been used by different authors for the study of diverse engineering applications, in particular in the case of single-phase flows in annular channels [17]. The Reynolds number Re_i according to Eq.[4.7] is formulated by employing the gas inlet flow conditions at the test section, scaled to the nominal geometry of the flow channel D_h and A_c, respectively. The entrance Reynolds number Re_i is used as a variable for setting and controlling the fluid flow boundary conditions during the experimental test cases.

$$Re_i = \frac{\dot{m}_{CFM}}{\mu_{air}(T_i, p_i)} \cdot \frac{D_h}{A_c} \quad [4.7]$$

4.1.2. Heat transfer and temperature distribution

The heat transfer coefficient for single-phase fluid is usually defined by the dimensionless form of the Nusselt number Nu, as given in Eq.[4.8]. It describes ratio of the convective heat transport to conductive heat transfer of the fluid across the boundary layer [117].

$$Nu = \frac{\dot{q_w}}{(T_w - T_g)} \cdot \frac{D_h}{\lambda_{T_g}} \quad [4.8]$$

The evaluation of the heat transfer coefficients in Eq.[4.8], is limited in this particular experimental approach, due to the lack of an exact measurement of the local bulk gas temperature T_g inside the test section in order to avoid unwanted flow modifications. When compared with the convective heat transfer results obtained from this experimental work, it should be noted that a more approximate method was used for the evaluation of the local Nusselt number. A simplified Nusselt number definition Nu_i was considered, as described in Eq.[4.9]. The simplified Nusselt number is estimated at a reference point $Z = 826$ mm (see Figure 3.6), where flow conditions are assumed fully developed.

$$Nu_i = \frac{\dot{q}_{w,5}}{T_{TS,15(Z=826\,mm)} - T_{g,15(Z=826\,mm)}} \cdot \frac{D_h}{\lambda_{T_g}(T_{g15(Z=826\,mm)})} \quad [4.9]$$

where, $\dot{q}_{w,5}$ is the local wall heat flux at the fifth heated segment of the heater rod (724 mm $\leq Z \leq$ 1131 mm), $T_{TS,15}$ represents measured wall temperature T_w of the heater rod at axial height (Z =826 mm) corresponding to the thermocouple (TS-TT-15) located on sixth heated section, as shown in Table 3.2. For constant surface heat flux condition, the bulk gas temperature is a linear function of the position [117]. Therefore, the bulk gas temperature $T_{g,15}$ is determined assuming a linear behavior along the rod as given in Eq.[4.10]:

$$T_{g,15(Z=826\,mm)linear} = T_i + \frac{P_H \cdot \omega}{\dot{m}_{CFM} \cdot c_p(T_i)} = T_i + \frac{P_H \cdot [(1131 - 826)/6/407]}{\dot{m}_{CFM} \cdot c_p(T_i)} \quad [4.10]$$

where, ω=0.7916 is the heated ratio delivered to the gas up to the position of thermocouple $T_{TS,15}$ located at the fifth heated rod segment with respect to the total input power P_H.

The cladding wall temperatures are obtained from the thermocouples sensors embedded in the heater shell of the heater rod (see Figure 3.8). To obtain an accurate reading, the temperature measurements must be corrected for the temperature drop between the thermocouples and the cladding wall. Assuming steady-state conditions with uniform electrical power the temperature of the cladding wall can be obtained using Eq. [4.11].

$$T_{w,(z)} = T_{TC,(Z)} - \left[\frac{\dot{q}_{w,(z)}}{\lambda_w} \cdot \frac{d_w}{2} \cdot \ln\left(\frac{d_w}{2r_{TC}}\right)\right] \quad [4.11]$$

Where $T_{w,(z)}$ is the well temperature with respect to the Z-axis, d_w is the rod outer diameter equal to 34.55×10^{-3} m, λ_w represents the thermal conductivity of the cladding and r_{TC} is the radius where the thermocouples are located 15.3×10^{-3} m.

As a representative variable for comparing the local temperature distributions at different operating conditions, the non-dimensional temperature Θ_w was defined as described in Eq.[4.12]. The heater rod temperatures are referenced to T_i and scaled with the heat flux density and the heat resistivity of the channel. The non-dimensional temperature $\Theta_{w,i}$ quantity has the character of an inverse Nusselt number, as can be seen comparing with Eq.[4.8].

$$\Theta_{w,i} = \frac{T_{TS} - T_i}{P_H} \cdot \frac{A_{w,h} \cdot \lambda_{air}(T_i)}{D_h} \quad [4.12]$$

where, T_{TS} represents the wall temperature at a selected axial position and $A_{w,h}$ denotes the nominal heater rod wall surface of 0.2713 m^2.

The heat flux sometimes also referred heat flow rate intensity is a flow of energy per unit of area and time, normal to the direction of heat flow. The heat flux in the test section $\dot{q}_{w.5}$ is considered to be constant and uniform in all six heated sections. The heat flux rate $\dot{q}_{w,5}$ is then obtained by Eq.[4.13]:

$$\dot{q}_{w,5} = \frac{P_H/6}{L_s \cdot \pi \cdot d_w} \quad [4.13]$$

where, P_H denotes the nominal electric input power, corrected only with the electric losses of the cables and d_w is the rod outer diameter and L_s is the length of one heated section of ~407 mm.

For the heated experiments, the heating intensity is quantified by the dimensionless heating ratio q^+ defined in Eq.[4.14], which defines the ratio of the temperature increase as function of the flow cross-section area of the flow channel.

$$q^+ = \frac{\dot{q}_w \cdot A_c \cdot \beta}{\dot{m} \cdot c_p} \quad [4.14]$$

where, A_c is the channel cross-sectional area of the channel and β denotes the coefficient of thermal expansion $\beta = 1/T$ defined as the change in the density of a substance as a function of temperature at constant pressure. The parameter q^+ in Eq.[4.14] can be obtained based on the gas conditions at the

inlet of the test section, as well as the geometrical variables of the flow channel, as described in Eq.[4.15].

$$q_i^+ = \frac{\dot{q_w} \cdot A_c}{\dot{m}_{CFM} \cdot c_{p,}(T_i) \cdot T_i} = \frac{P_H}{\dot{m}_{CFM} \cdot c_{p,}(T_i) \cdot T_i} \cdot \frac{A_c}{A_{w,h}} \quad [4.15]$$

where, $A_{w,h}$ represents the heated wall surface area, which can be obtained by Eq.[4.16]:

$$A_{w,h} = L_h \cdot \pi \cdot d_w \quad [4.16]$$

where, L_h is the total heated length of the heater rod (including gaps) of ~2500 mm, covering about an axial length $Z = 307$ mm – 2799 mm.

A common way to evaluate the convective heat transfer enhancement between a smooth and structured flow channels is the evaluation of the thermo-performance index η, proposed by Webb et al., 1981 [119]. This concept describes the heat transfer enhancement and friction factor ratios between artificially structured and smooth channel walls, based on the equal pumping power. The thermo-performance index η can be determined as shown in Eq.[4.17]:

$$\eta = \frac{Nu_r/Nu_s}{\left(f_{D,r}/f_{D,s}\right)^{1/3}} \quad [4.17]$$

where, the subscripts r and s denote the results of the structured and smooth channel, respectively.

The analytical equation for radiation heat exchange between an infinite rod, inside a closed domain, is used to estimate the radiation losses $\dot{Q}_{wr}$, as shown in Eq. [4.18]:

$$\dot{Q}_{wr} = \frac{\sigma_{SB}}{\left(\frac{1}{\epsilon_{rod}}\right) \cdot \left(\frac{A_{w,h}}{S_w \cdot L_h - A_{w,h}}\right) \cdot \left(\frac{1}{\epsilon_{hex}} - 1\right)} \cdot A_{w,h} \cdot \left({T_{rod}}^4 - {T_{hex}}^4\right) \quad [4.18]$$

Where, σ_{SB} represents the Stefan–Boltzmann constant (5.67×10^{-8} $W\cdot m^{-2}\cdot K^{-4}$), ϵ_{rod} and ϵ_{hex} are literature values for the emissivity of a slightly oxidized steel and a non-oxidized steel surface. Literature values of ϵ_{rod} =0.6 and ϵ_{hex} =0.25 were used [120]. However, it has to be remarked that the emissivity values cannot be precisely assessed; therefore, an additional uncertainty of ±30% should be taken into consideration.

4.1.3. Velocity distribution

The statistical evaluation integrates the measurements to reduce the systematic errors, which are inherent to the burst-mode data acquisition. However, under certain circumstances the LDA velocity measurements may produce some systematic error, which can mainly be associated to specific instrumentation effects. The most common cause for this deviation arises from the probability, that high velocity particles are proportionally more frequently sampled than the slow velocity particles, thus the arithmetic average of the velocity components are shifted to higher values [121]. This systematic deviation is known in the literature as *velocity bias*. To minimize this systematic deviation, several different methods have been developed and implemented for the data processing of the LDA velocity measurements, as shown in detailed by Zhang et al., 2010 [108]. However, the most common method to avoid the so-called *velocity bias* is the use of the time residence or transit time t_j of individual particle crossing through the measurement volume by introducing a weighting factor w_i, as described in Eq. [4.19]. The transit time weighting method is based on the assumption that a statically uniform flow passes through the measurement volume, i.e. no velocity gradients within the measurement volume are considered [122]. The bias–corrected time-averaged mean velocities and velocity fluctuations for the turbulent flow measurements are calculated and corrected automatically by the BSA Flow Software V5 [112] as follows:

The weighting factor for the velocity bias correction is calculated as:

$$w_i = t_i / \sum_{i=0}^{N-1} t_j \qquad [4.19]$$

The time averaged mean particle velocities are obtained as:

$$\overline{U} = \sum_{i=0}^{N-1} u_i \, w_i(t_i) \qquad [4.20]$$

The time averaged mean particle velocity fluctuations are obtained as:

$$U'_{rms} = \sqrt{\sum_{i=0}^{N-1} w_i \, [u_i(t_i) - \overline{U}]^2} \qquad [4.21]$$

Additionally, to compensate the small variations of the boundary conditions between each measurement test, the velocity profiles are normalized by using the reference velocity U_m, as a function the flow properties ($\dot{m}_{CFM}$, ρ_{air}, p_i and T_i) across the channel, as described in Eq.[4.22]:

$$U_m = \frac{\dot{m}_{CFM}}{\rho_{air}(p, T_i) \cdot A_c} \qquad [4.22]$$

4.2. Experimental procedure

This section describes the experimental procedure and test configurations for the study of the local heat transfer coefficients, pressure losses, and velocity distribution for both smooth and surface structured rod channels.

Before starting of each measurement campaign, the tightness of the experimental loop is carefully verified. Subsequently, the offsets of the primary variables $\dot{m}_{CFM}$, T_i, p_i and P_H are obtained by fitting a linear function from the time series data and then after removed from the raw experimental data in order to reduce the contributions effects caused by the instrumentation errors. After this procedure, the gas loop is pressurized by using dry compressed air (working fluid) coming from the site network and kept at constant pressure level of 0.15 MPa (abs). Immediately after the flow rate conditions $\dot{m}_{CFM}$ and the electrical power P_H of the heater rod geometry are gradually set and regulated until the specified experimental conditions are reached and maintained constant. For the experimental set of tests conducted at lower flow rates than 25.3 g/s, i.e. Reynolds number lower than 10 000, the bypass section (SL-CV-02) is opened up to 50% in order to allow a better regulation of the main flow into the test section. Preliminary calculations are conducted to estimate the electrical input required for each experimental case in order to achieve the chosen heat-up ratios q_i^+ (see Table 4.2 and Table 4.3). The inlet gas temperature T_i is maintained approximately about 291.15 K (±5 K) for all studied cases. The gas temperature is regulated by using the two heat exchangers, connected to the auxiliary water-cooling system, placed before and after the side blower (sees Figure 3.4). The most relevant operational parameters of the L-STAR test are listed in Table 4.1.

Experimental parameters [Units]	Nominal value
Inlet gas temperature [K]	291.15
Mass flow rate [g/s]	6.32 to 105.5
Inlet pressure [MPa.]	0.15
Thermal power [kW]	0.58 to 5.5

Table 4.1: Nominal boundary condition of the L-STAR experimental program.

During the experimental measurement campaigns, the DAQ system constantly monitors the mass flow rates, pressures, temperatures and thermal power conditions in the test section. Once the test section attained thermal steady-state conditions, inlet-and outlet pressures and temperatures, as well as the axial cladding wall temperature distributions are simultaneously recorded. The experimental data is recorded for a period time of 660 s, with a sampling rate of 15 Hz for the inlet-and outlet pressures, flow temperatures and mass flows (over 10000 data points) and 2 Hz (over 1000 data points) for the cladding wall temperatures, respectively. The stationary conditions for pressure losses and the cladding wall temperatures on the test section are considered to be reached, once their standard deviation is less than 0.5% and 0.2 K, for a time period of 300 s. Finally, the resulting time-

averaged mean values and the corresponding friction factors, heat transfer coefficients and cladding wall temperature distribution are recorded and evaluated.

One of the fundamental ideas to study the measurement reliability of turbulent flows is that any statistical quantities (e.g. U, U'_{rms} or Reynolds stress) measured at any Reynolds numbers should collapse to a single profile, when normalized by the proper velocity and length scales [109]. The mean velocity distribution described by *law of the law* located between the inner and outer layers is a good example of this idea [123]. The axial velocity distribution for both smooth and structured are carried out at the fully developed flow region of the test section, by means of Laser-doppler anemometry for a single Reynolds number $Re_i \cong 16447$. A two-component LDA system (Dantec Dynamics) operated in back-scattered mode is used. The mean velocity distribution is obtained in form of a discretized time series $u_i(t_i)$, in which each measurement is triggered by an individual particle passing through the measurement volume at a random time (burst mode). Taking the recommendation made by Arbeiter et al., 2008 [116] and Hering et al., 2008 [115], ultra-fine Titanium dioxide (TiO_2) particles are used as flow tracer. For the discussion of the velocity distribution a Cartesian coordinate system (ϕ, X_w, Y_w,Z) is defined, as described in Figure 4.1. Where, ϕ denotes the angular coordinate with respect to the heater rod, X_w and Y_w are the distance from the rod element to the channel wall in the radial flow direction (with an approximate length of 20.59 mm and 16.5 mm), and Z represents the axial position with respect to the test section. The velocity distributions are obtained from two different reference cross-sections LDA_{A-A} and LDA_{B-B}. The origin of the coordinate Y_w for both reference cross-sections is visually obtained by gradually moving the LDA measurement volume towards the heater rod by using LDA transverse system.

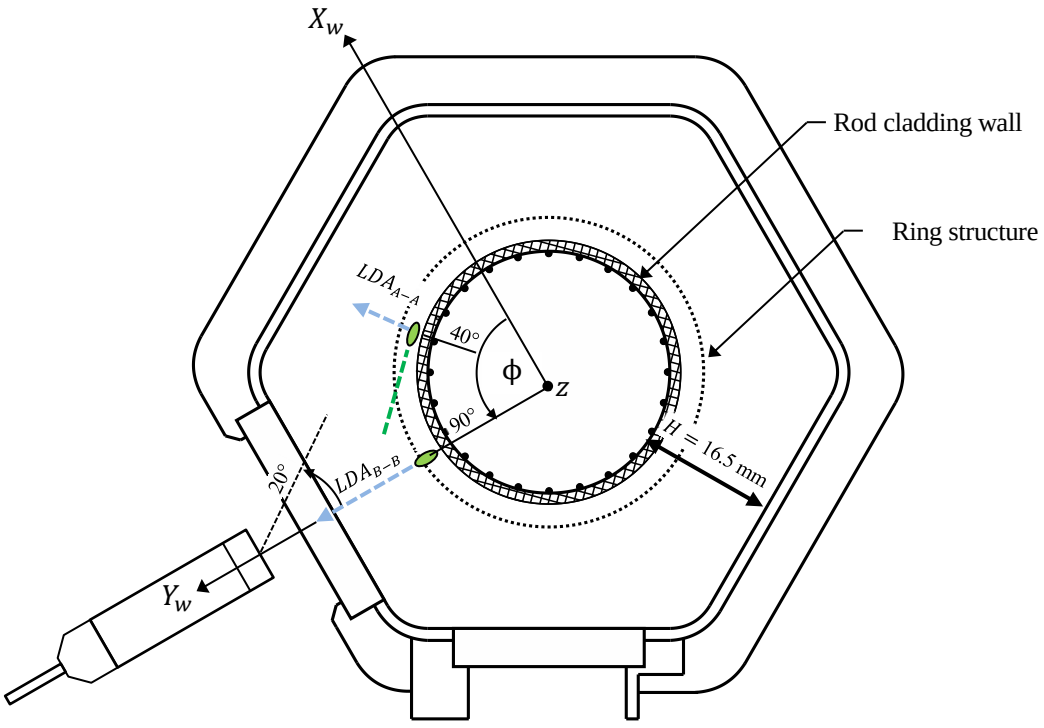

Figure 4.1: Cartesian coordinate system (ϕ, X_w, Y_w, Z) used for LDA velocity measurements in the L-STAR test section.

The origin of the coordinate Y_w for both reference cross-sections is visually obtained by gradually moving the LDA measurement volume towards the heater rod using the transverse system. For this task, a low laser voltage of 500 V is used, in order to reduce undesired light scattering effects coming from the channel wall. Furthermore, to find the origin of the cross-section LDA_{A-A} the LDA probe is moved about ~20° degrees with respect to cross-section LDA_{B-B}. The position, in which the maximum intensity level from the back-scattering signal on the heater rod wall is obtained, is considered as the origin of the coordinate $Y_w = 0$ mm. After the origin at the heater rod wall is obtained, the measuring volume is moved along the coordinate Y_w in the direction of the optical access (glass window), where a second maximum is attained at about a wall distance Y_w =16.486 mm. The variation of Y_w length with respect to the designed value of 16.5 mm might be attributed to the slightly higher thickness of the glass windows with respect to the channel wall. The two-component probe is oriented in such a way, that the beam system with wavelength 514 nm (green) is arranged in the X_w, Z_r– plane, measuring the axial velocity components U, while the beam system with wavelength 488 nm (blue) is arranged in the Y_w, X_w–plane, measuring the tangential velocity components V.

Through the above described arrangement of the beam systems, the ellipsoid LDA measurement volume is oriented with its long axis along Y_w and with the two short axes along X_w and Z_r, thus allowing velocity measurements in the close vicinity of the rod surface at the cross-section LDA_{A-A}. The velocity measurements at this region are conducted by using the F160 mm optic probe, attaining a spatial resolution of about 78 μm, up to a wall distance 0 mm $\leq Y_w \leq$ 5.0 mm. Furthermore, this arrangement allows the reduction of undesirable light scattering contributions from the heater rod. At the outer region of the flow channel (from wall distance 5.0 mm $\leq Y_w \leq$ 16.5 mm) the velocity distributions are obtained at the cross-section LDA_{B-B} (perpendicular to the rod). In this region the NIKKOR 85 mm focal objective is used, with a spatial resolution of 189 μm.

4.3. Experimental Matrix

The experimental program conducted at the L-STAR facility for the investigation of the heat transfer enhancement, frictional losses and mean velocity distribution characteristics with a special focus close to the wall, were conducted in two phases, mainly experimental test with smooth rod channel (*i*) and structured rod channel (*ii*), both under unheated and heated conditions. A detailed matrix of the performed experimental cases in terms of the primary nominal parameters ($\dot{m}_{CFM}$, T_i, p_i and P_H) is given in Table 4.2 and Table 4.3.

i. Steady-state tests under unheated (L-STAR-G0-DP) and heated conditions (L-STAR-G0-TX) with a hydraulically smooth rod channel. These tests were foreseen to establish the feasibility of the L-STAR facility and used methodology, as well as to record data for baseline comparison for the structured rod channel experiments.

ii. Steady-state tests under unheated (L-STAR-G1/G2-DP) and heated (L-STAR-G1/G2-TX conditions, by using two different types of metallic ring structures, namely solid (G1) and perforated (G2) covering the heated section of the cladding wall.

L-STAR-G0	**Mass flow $\dot{m}_{CFM}$ [g/s]**	**T_i [K]**	**p_i [MPa]**	**Heated tests**	**Reynolds Re_i**	**Heater power, P_H [W]**
						q_i^+ =0.0015
-DP/TX-01	6.32	291.15	0.15	+	4108.6	256.1
-DP/TX-02	9.48	291.15	0.15	-	6162.9	-
-DP/TX-03	12.6	291.15	0.15	+	8191.3	508.0
-DP/TX-04	18.9	291.15	0.15	-	12286.9	-
-DP/TX-05	25.3	291.15	0.15	+	16447.6	1016.0
-DP/TX-06	31.8	291.15	0.15	-	20673.2	-
-DP/TX-07	37.9	291.15	0.15	+	24638.9	1523.0
-DP/TX-08	44.2	291.15	0.15	-	28734.5	-
-DP/TX-09	50.5	291.15	0.15	+	32830.2	2022.0
-DP/TX-10	56.9	291.15	0.15	-	36990.8	-
-DP/TX-11	63.52	291.15	0.15	+	41294.5	2543.4
-DP/TX-12	69.92	291.15	0.15	-	45455.1	-
-DP/TX-13	77.1	291.15	0.15	+	50122.9	3087.1
-DP/TX-14	83.5	291.15	0.15	-	54283.5	-
-DP/TX-15	90.86	291.15	0.15	+	59068.3	3638.1
-DP/TX-16	97.26	291.15	0.15	-	63229.0	-
-DP/TX-17	105.27	291.15	0.15	+	68436.3	4215.0
-LDA-G0	25.3	291.1	0.15		16447.6	LDA Velocity profiles

Table 4.2: Nominal boundary conditions for the smooth rod channel experiments (L-STAR-G0) conducted for q_i^+ = 0.0015 in a Reynolds range $4\times10^3 \leq Re_i \leq 7\times10^4$.

L-STAR-G1/G2	Mass flow $\dot{m}_{CFM}$ [g/s]	T_i [K]	p_i [MPa]	Heated tests	Reynolds Re_i	Heater power, P_H [W]		
						q_i^+ = 0.0015	q_i^+ = 0.002	q_i^+ = 0.003
-DP/TX-01	6.32	291.15	0.15	+	4108.6	256.1	337.4	506.1
-DP/TX-02	9.48	291.15	0.15	+	6162.9	382.6	506.1	759.2
-DP/TX-03	12.6	291.15	0.15	+	8191.3	508.	672.6	1009.0
-DP/TX-04	18.9	291.15	0.15	+	12286.9	759.8	1009.0	1513.0
-DP/TX-05	25.3	291.15	0.15	+	16447.6	1016.0	1350.6	2026.0
-DP/TX-06	31.8	291.15	0.15	+	20673.2	1276.0	1697.7	2546.6
-DP/TX-07	37.9	291.15	0.15	+	24638.9	1523.0	2023.3	3035.1
-DP/TX-08	44.2	291.15	0.15	+	28734.5	1769.8	2359.7	3539.6
-DP/TX-09	50.5	291.15	0.15	+	32830.2	2022.0	2696.0	4044.1
-DP/TX-10	56.9	291.15	0.15	+	36990.8	2278.0	3037.7	4556.6
-DP/TX-11	63.52	291.15	0.15	+	41294.5	2543.4	3390.0	5085.1
-DP/TX-12	69.92	291.15	0.15	+	45455.1	2799.6	3731.7	5597.6
-DP/TX-13	77.1	291.15	0.15	+	50122.9	3087.1	4116.1	-
-DP/TX-14	83.5	291.15	0.15	+	54283.5	3343.4	4457.8	-
-DP/TX-15	90.86	291.15	0.15	+	59068.3	3638.1	4847.5	-
-DP/TX-16	97.26	291.15	0.15	+	63229.0	3894.3	5189.2	-
-DP/TX-17	105.27	291.15	0.15	+	68436.3	4215.0	5605.6	-
LDA-G1/G2	25.3	291.15	0.15	+	16447.6	LDA Velocity profiles		

Table 4.3: Nominal boundary conditions for the structured rod channel experiments (L-STAR-G1 and G2) conducted for q_i^+= 0.0015 – 0.003 in a Reynolds range 4×103≤ Re_i ≤ 7×104.

From the above mentioned experimental matrix, two experiments are mainly subject of discussion in this experimental thesis. The experimental case (-DP/TX-01) has been chosen to reproduce the effects of the ALLEGRO emergency decay heat removal using pony motor powered circulation. On the other hand, the experimental case (-DP/TX-05)**,** hereafter referred as *Base case scenario*, has been chosen to emulate the basic flow and thermal power operational conditions of ALLEGRO reactor, by working at the similar Reynolds number Re_i and dimensionless heating rate q_i^+ [12].

Base case scenario parameters	[Units]	Value
Mass flow (air), $\dot{m}_{CFM}$	[g/s]	25.3
Inlet gas temperature, T_i	[K]	291.15
Inlet pressure, p_i	[MPa]	0.15
Thermal power, P_H	[kW]	1.016
Reynolds number, Re_i	[-]	~16 447
Dimensionless Heat-up ratio, q_i^+	[-]	~0.0015

Table 4.4: Nominal boundary conditions for the L-STAR-*Base case* (DP/TX-05).

The experimental boundary conditions for the studied matrix may deviate from the specified set point within a tolerance range of ±6% for the mass flow, 0.5 hPa for the pressure, ±5 °C for the inlet temperature and 5% for thermal power, respectively.

Each set point is repeated up to three times to prove stability and feasibility of the experimental main results. Despite the fact, that the facility was not designed to work at very low flow rates, three extra measurement points with an approximate flow rate from 3.1 to 5.1 g/s – covering a small region of the laminar and transitional flow regime between a Reynolds number $2000 \leq Re_i \leq 3500$ – were conducted, as described in Table 4.5. It has to be remarked, that the inlet boundary conditions during the measurement campaigns showed higher deviations compared to the specified exact set points given in the experimental program.

L-STAR-G0/G1/G2[5]	**Mass flow $\dot{m}_{CFM}$ [g/s]**	**T_i [K]**	**p_i [Mpa]**	**Heated tests**	**Reynolds Re_i**
-DP-1’	3.1	291.15	0.15	-	2015.3
-DP-2’	4.1	291.15	0.15	-	2665.4
-DP-3’	5.1	291.15	0.15	-	3315.5

Table 4.5: Nominal boundary conditions for the smooth rod channel cases (L-STAR-G0) conducted in a Reynolds range $2\times10^3 \leq Re_i \leq 3.5\times10^4$.

[5] G0 = smooth rod, G1= solid structured rod and G2 =perforated structured rod

5. Experimental results

In this chapter, the experimental results characterizing the friction factors f_D, heat transfer coefficients Nu_i and mean axial velocity distribution for the smooth and structured rod channels are presented. This chapter is divided in two sections. In section 5.1, the experiment results for the smooth rod channel and their comparison with well-established analytical models are discussed. Section 5.2, focuses on the attained experimental results for both structured channels, instrumented with periodically placed solid and perforated ring structures. The main outcomes of the experiment campaigns are given in their dimensional and dimensionless form, as described in section 4.1.

5.1. Smooth rod channel investigation

Before conducting the experimental measurements for the structured rod channel, a series of heated and unheated experiment tests with a smooth rod channel geometry have been performed, covering a wide range of Reynolds numbers. The smooth rod channel experiments have been conducted to verify the feasibility of the experimental results, as well as serve as direct comparison baseline against the structured rod channel measurements. Furthermore, the study of the smooth rod channel is important; since smooth surfaces are currently the base case envisaged for the GEN IV fuel rod elements. The experimental results of the smooth rod channel are divided in three sections, namely frictional losses, heat transfer coefficients and mean axial velocity distribution under heated and unheated conditions.

5.1.1. Total loss coefficient smooth rod channel

The experiment results for the total loss coefficients ζ in Eq.[4.1] are calculated from the total pressure losses over the whole test section $\Delta p_{4,5}$ (including the bends at the inlet and outlet). Figure 5.1 depicts the total loss coefficient results of the smooth rod channel ζ_s for both unheated (L-STAR-G0-DP) and heated (L-STAR-G0-TX) cases at different Reynolds numbers Re_i. No significant differences are obtained between the unheated and heated cases, which may be explained by the lower heating impact of the bulk at the end of the upper T-junction. Furthermore, it can be noticed that the total loss coefficients start to decrease significantly, as the Reynolds number increases, tending asymptotically towards to a constant value at about a $Re_i \geq 50000$. As previously mentioned in section 3.1.2, optimization of the flow by means of a metallic flow straightener, located at the lower bend of the test section inlet (see Figure 3.5) was conducted.

A detailed analysis of the pressure losses attributed to the flow straightener is given in Figure 5.2. The analysis shows that the flow straightener induces the highest pressure losses in the test section. The total pressure losses $\Delta p_{4,5}$ in the test section are observed to increase about 3.4 times more, compared to the corresponding experimental runs without the flow straightener.

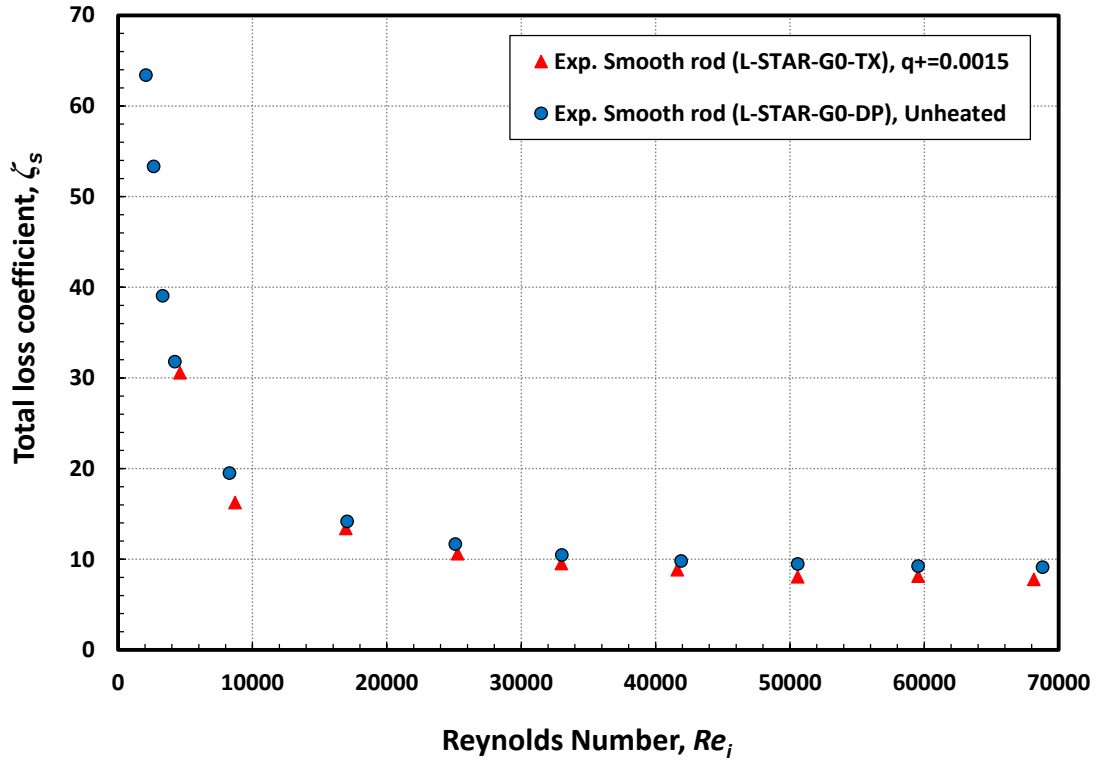

Figure 5.1: Total loss coefficient over the test section for the unheated and heated smooth rod channel experiments (including the upper and lower bends) as function of the Reynolds number Re_i.

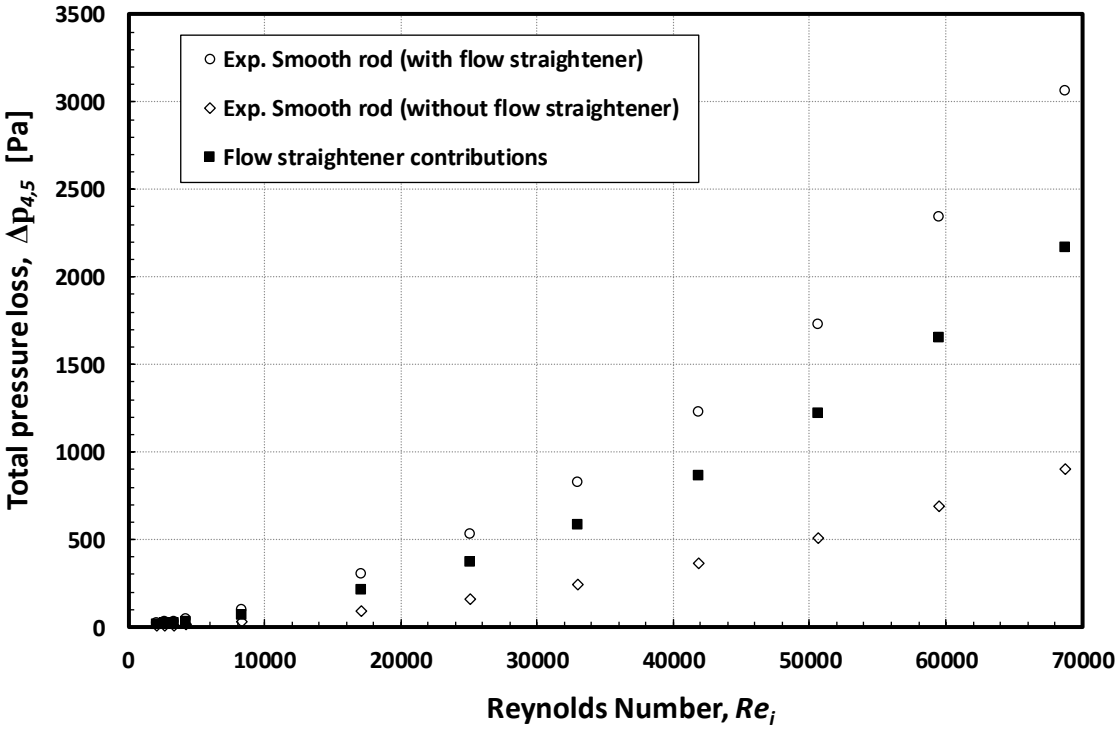

Figure 5.2: Analysis of the pressure losses contributions with and without flow straightener in the test at different Reynolds numbers Re_i.

5.1.2. Friction factor smooth rod channel

The friction factor results f_D are based on the increase of the pressure differences $\Delta p_{1'2'}$ at the straight part of the test section and then evaluated by using the Darcy-Weisbach Eq. [4.3]. As well as for the loss coefficients, a total of twelve experimental set points are conducted. An overall view of the calculated local friction factors for the smooth rod channel $f_{D,s}$ under heated and unheated conditions is shown in Figure 5.3. The calculated friction factors for the smooth channel experimental tests are additionally compared to analytical and empirical correlations suitable for smooth channels. For the single-phase laminar flow regime ($Re_i \leq 2300$) the Hagen–Poiseuille equation Eq. [5.1], also known as the Hagen–Poiseuille law [120] is used.

$$f_{lam} = \frac{64}{Re} \tag{5.1}$$

In the case of the fully developed turbulent flow regime, the frictional losses are compared to the explicit correlation suggested by Chen et al., 1979 [124] for circular channels, shown in Eq. [5.2]. The correlation is reported to be valid for a Reynolds number range between ($4000 \leq Re_i \leq 10^5$) and a $2\times10^{-8} \leq \varepsilon/D_h \leq 0.1$ within an average deviation error of approximately ±3% compared to the Moody's equation.

$$f_{Chen} = \left[-2 \cdot \log\left(\frac{\varepsilon/D_h}{3.7065} - \frac{5.0452}{Re}\log\left(\frac{\varepsilon/D_h{}^{1.1098}}{2.8257} + \left(\frac{7.149}{Re}\right)^{0.8981}\right)\right)\right]^{-2} \tag{5.2}$$

The empirical correlation developed by Churchill et al., 1977 [125] in Eq.[5.3] is also used. In contrast to Chen's correlation, Churchill proposed a more complex expression for the engineering calculation of the frictional losses in single-phase flows covering all three flow regimes: laminar, transitional, and fully developed, within an average deviation error of 10% at low Reynolds numbers.

$$f_{Churchill} = 8 \cdot \left[\left(\frac{8}{Re}\right)^{12} + \left(\frac{1}{(A)^{3/2}}\right)\right]^{1/12} \tag{5.3}$$

where,
$$A = \left[2.475 \cdot \ln\left[\left(\frac{7}{Re}\right)^{0.9} + 0.27\left(\frac{\varepsilon}{D_h}\right)\right]^{-1}\right]^{16} + \left(\frac{37530}{Re}\right)^{16}$$

where, ε represents the effective roughness of the pipe. For hydraulically smooth channels ε (i.e. the roughness on the wall is smaller than the thickness of the laminar sub-layer of the turbulent flow) can be changed to equivalent sand-grain roughness. As reported by Arbeiter et al. 2013 [101] the effective sand-grain roughness $k_{s,eff}$ can be obtained, as described in Eq. [5.4]:

$$\varepsilon = k_{s,eff} = 5.0 \cdot R_{a,weighted} \tag{5.4}$$

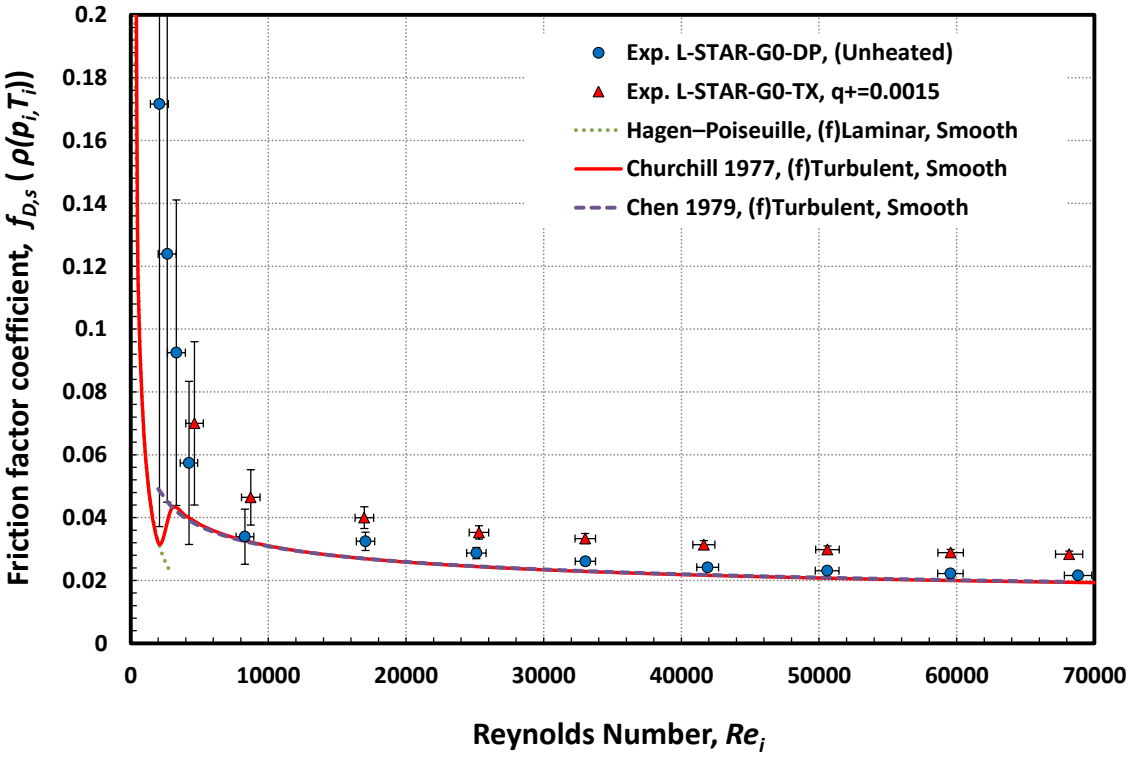

Figure 5.3: Friction factor for the unheated and heated smooth rod channel cases as a function of Reynolds number Re_i and inlet flow conditions T_i and p_i.

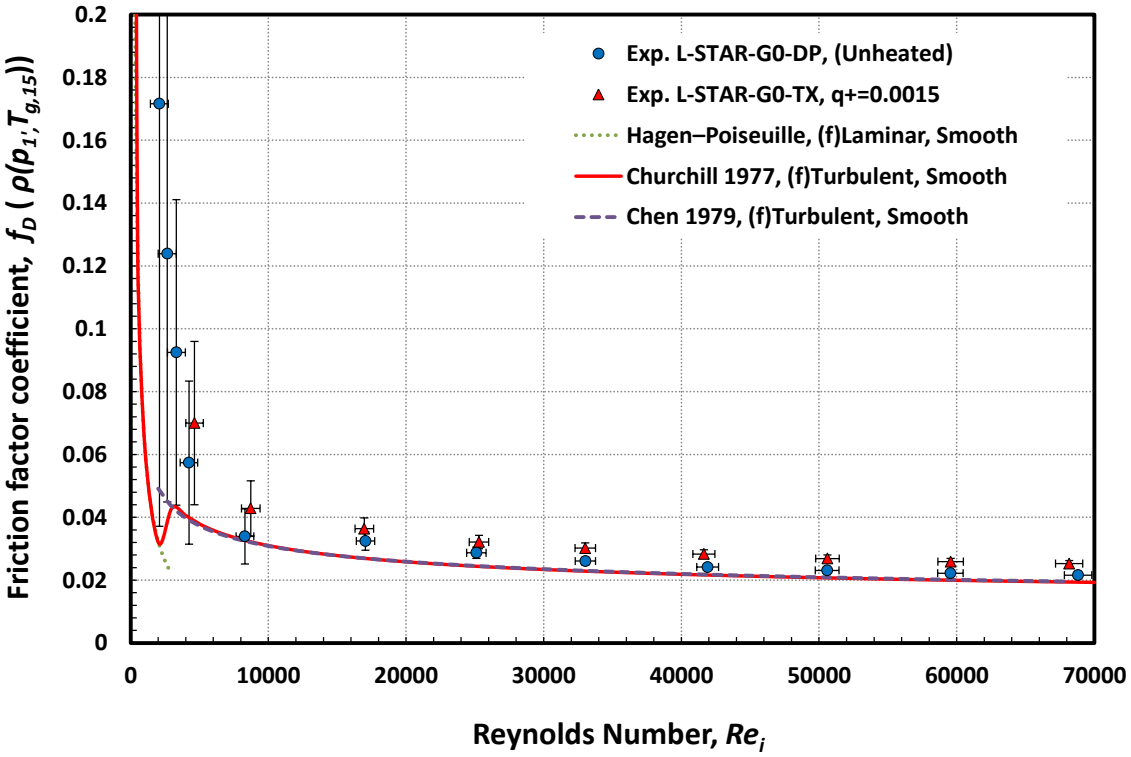

Figure 5.4: Friction factor for the unheated and heated smooth rod channel cases as a function of Reynolds number Re_i and local flow conditions $T_{g,15}$ and $p_{1'}$ at the test section.

where, $R_{a,weighted}$ is the average roughness value of the heater rod $R_{a,rod}$ and flow channel surface $R_{a,hex}$, weighted by the wetted perimeter of each component. The weighting factors are 0.325 for the rod and 0.675 for the hexagonal flow channel, yielding a $R_{a,weighted}$ =0.81 μm and $k_{s,eff}$ = 4.05 μm.

The characteristic dependence of the friction factor as a function of the Reynolds number can be clearly seen for both heated and unheated experimental cases. The heating of the test section causes an increasing effect on the friction factors of about ~25%, compared to the unheated results. This difference is mainly attributed to pressure and temperature variation effects between the inlet and the upper part of the test section conditions, affecting the pressure port (SL-DP-1'2') placed directly at the fully developed flow region of the test section. However, this increase on the friction factor for the heated cases is significantly reduced to ~9%, by using the derived local test section flow conditions $T_{g,15}$ and $p_{1'}$ at the fully developed flow region, as shown in Figure 5.4.

For the conducted experimental cases at lower Reynolds number 2000≤ $Re_i \leq$ 3500, a significantly higher deviation and uncertainty magnitudes can be observed with respect to the predicted values of Eq.[5.1] and Eq.[5.3]. The high uncertainty magnitudes for the lower Reynolds number cases are mainly attributed to the assumed constant uncertainty contribution from instrument non-linearity and offset correction affecting the pressure measurements $\Delta p_{1'2'}$, causing the exponential increase of the uncertainty by an order of magnitude of the values. However, for the area of interest of this experimental work, mainly the study of high turbulent flows, the friction factor values show a good agreement with respect to the predicted values obtained by Chen and Churchill proposed correlations, with an average deviation error of about ~11% with respect to the experimental data.

As the Reynolds number increases beyond $Re_i \geq$ 9000, the friction factor values tend to attain almost an asymptotic distribution value for all studied Reynolds numbers. This can be explained by the fact that the shear stress τ_w in fully developed turbulent flows becomes proportional to the dynamic pressure. The friction factor coefficients $f_{D,s}$ and their estimated uncertainty magnitudes $\sigma_{f_{D,s}}$ and σ_{Re_i} for the Reynolds number, are summarized in Table 1.D in Appendix D. Experimental uncertainties for the friction factor and Reynolds numbers are estimated following the methodology of Kline and McClintock [126], as described in Appendix B.

5.1.3. Heat transfer in smooth rod channel

For the heat transfer study of the smooth rod channel, a series of seventeen different experiments have been conducted and compared to analytical and empirical correlation. With the considerations described in section 4.1.2, the local wall heat flux, the average gas temperature and the thermo-physical proprieties of the gas, and ultimately dimensionless heat transfer coefficient in term of Nusselt number Nu_i and dimensionless heat-up rate q_i^+ for the smooth rod channel has been obtained. Since the heating of the cladding surface plays an important role in the evaluation of the convective heat transfer enhancement, the discussion of the heat transfer results for the smooth rod channel are led by a short analysis of the cladding wall temperature along the heated rod.

The temporal evolution of the cladding wall temperatures for the *Base case* scenario ($Re_i \cong 16447$ and $P_H \cong 1016$ W) at several axial positions through the heat-up transient is shown in Figure 5.5. From this figure, it is observed that the cladding temperature of the smooth rod channel begin to increase immediately after the electrical power supply is provided. The thermal equilibrium between the gas flow and the heated rod cladding wall has been reached and maintained constant approximately after two hours, without any significant changes over a long-time period. Although, uniform electrical power has been supplied, a lower axial temperature progress variation on the cladding temperatures can be observed at an axial position 0.09 ($Z = 307$ mm), measured by thermocouple TT-TS-07, compared to other axial positions. This particular delay can be explained by the fact that, this thermocouple is placed between the upper end of the sixth heated section at the beginning of the unheated zone (dead zone) close to the flow outlet of the test section, as be seen in Figure 3.6. The steady-state results of the axial cladding temperature distribution along the whole heated smooth rod channel are shown in Figure 5.6. The experiments have been carried out for different Reynolds numbers Re_i under constant inlet pressure P_i =0.15 MPa and heat flux q_i^+=0.0015 conditions, as described in Table 4.2. The temperature profiles of the cladding are obtained by means of 48 type-K thermocouples placed just underneath the cladding layer (see Figure 3.8). As a first observation, it can be seen that the temperature distribution of the smooth heater rod increases, as the flow develops from the inlet along the test section, attaining almost a uniform temperature profile at about an axial position 0.32 ($Z = 1.1$ m). The cladding wall temperatures at the fully developed flow region of the test section are the result of the heat conduction, as well as, convective effects of the transported heated gas along the channel. The reference gas bulk temperatures $T_{g,15}$, at the fully developed flow region at about an axial position 0.11 – 0.32 (400 mm $\leq Z \leq$ 1100 mm) are found to vary from 303 K to 322 K for the studied cases, respectively. Furthermore, the influence of the ceramic gaps, located between all six heated sections (see Figure 3.6) on the axial cladding temperature distributions is clearly depicted at an axial position 0.20 ($Z = 690$ mm, TT-TS-11). In this region, the cladding temperatures are about ~3% (~7 K) lower, with respect to the nearest thermocouple (TT-TS-23) located at an axial position 0.15 ($Z = 532$ mm), for all studied cases. The *base case* scenario (black and dotted lines) is used as a reference to demonstrate the accuracy and reproducibility of the cladding temperatures measurements.

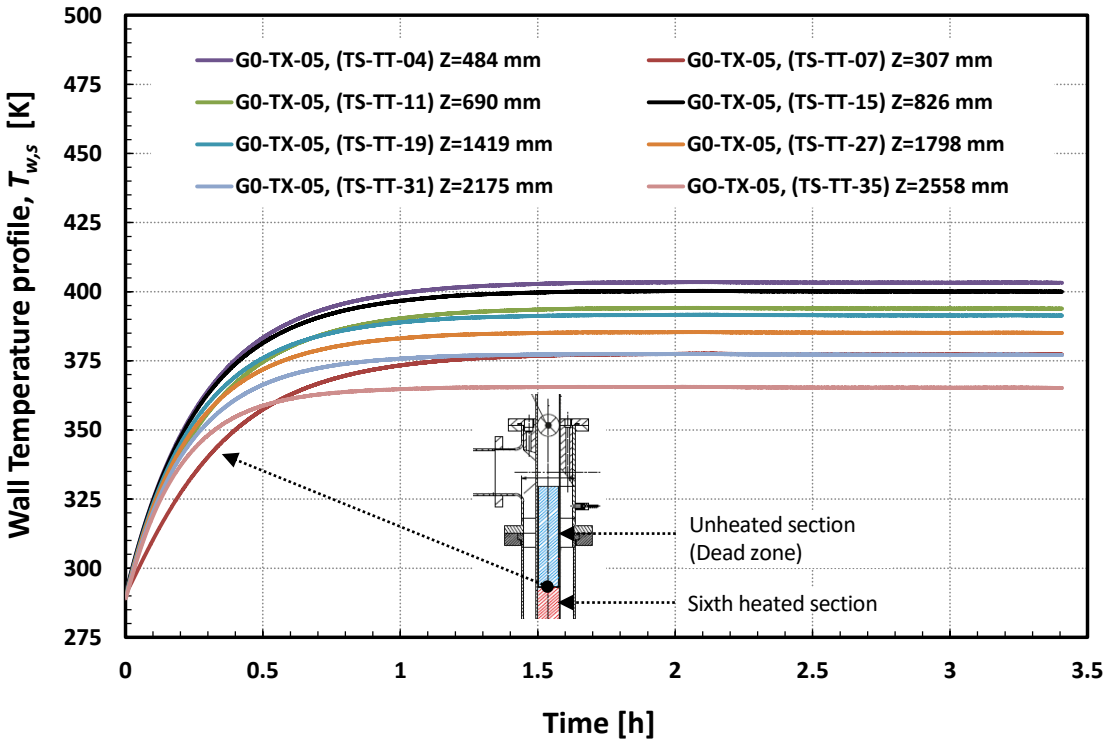

Figure 5.5: Wall temperature development for the smooth rod channel along eight axial positions during the heat-up transient of the *Base case* ($Re_i \cong 16447$ and $P_H \cong 1016$ W), as function of time in hours.

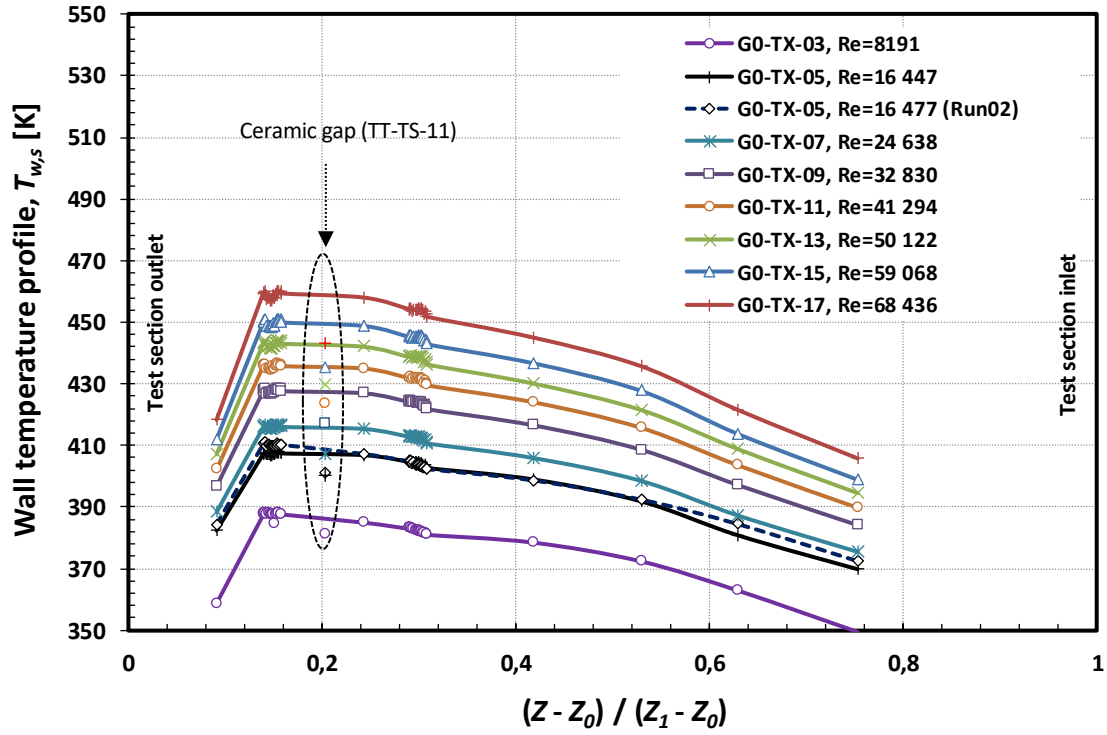

Figure 5.6: Axial wall temperature distribution $T_{w,s}$ for the heated smooth rod experiments along forty-eight thermocouples. *Base case* (*dotted line*) used as reference to demonstrate reproducibility of the temperature profiles.

A very good reproduction of the axial cladding temperature distribution is obtained for the *Base case* scenario, with a maximal deviation error between (Run01 and Run02) of about ~3.1 K. The small deviations are attributed mainly to the thermocouples uncertainty errors, as well as slight difference of the experimental boundary conditions during each test. As a comparison reference, the heat transfer coefficients of the smooth rod channel are compared by to analytical and empirical correlations for smooth wall channels. Petukhov and Kirillov,1958 [127] in Eq.[5.5], developed a theoretical calculation of the convective heat transfer for fully developed flows in circular pipes with constant heat flux boundary conditions, based on an algebraic turbulence model. Their correlation is valid in the Reynolds numbers in the range of $4000 \leq Re \leq 5{\times}10^6$ and a Prandtl numbers between $0.5 \leq Pr \leq 10^6$, within an uncertainty of approximately ±6%.

$$Nu_{Petukhov} = \frac{(f/8)\, Re\, Pr}{C + 12.7\,(f/8)^{1/2}\,(Pr^{2/3} - 1)} \qquad [5.5]$$

where, $C = 1.07 + 900/Re - \ [0.63/(1 + 10Pr)]$

Gnielinski et al., 1976 [128] proposed a correlation, in Eq.[5.6], for single-phase turbulent flows (gas and liquids) passing through circular pipes, under both uniform surface heat flux and constant temperature, obtained by the modified equation of Petukhov and Kirillov. According to this equation a wide range of experimental data for heat transfer in circular pipe flows has been well predicted. The correlation can be used in a Reynolds number range $2300 \leq Re \leq 5{\times}10^6$ and Prandtl number between $0.5 \leq Pr \leq 2000$, within an uncertainty of ±15% for most non-circular ducts [118, 129].

$$Nu_{Gnielinski} = \frac{(f/8)(Re - 1000)Pr}{1 + 12.7\,(f/8)^{1/2}\,(Pr^{2/3} - 1)} \cdot \left[1 + \left(\frac{D_h}{L}\right)^{2/3}\right] \qquad [5.6]$$

where, f represent in both correlations the friction factor of a smooth pipe. According to several authors in [129], the friction factor f can be calculated from the equation developed by Filonenko (for $10^4 \leq Re \leq 5{\times}10^7$), as described in Eq.[5.7]:

$$f_{Filonenko} = (1.82 \cdot \log Re - 1.64)^{-2} \qquad [5.7]$$

Additionally, to the above described correlations, a simpler expression for the comparison of Nusselt number developed by Dittus and Boelter et al., 1930 [130], based on the heat and momentum transfer is also used. The heat transfer correlation in Eq.[5.8] can be applied to gases and liquid fluids with Prandtl number ($0.7 \leq Pr \leq 120$) and within a Reynolds number range ($2300 \leq Re \leq 1.2 \times 10^5$) exhibiting a general standard deviation of ±12%.

$$Nu_{Dittus-Boelter} = 0.024 Re^{0.8} Pr^n \qquad [5.8]$$

where, n represents a parameter of the flow proprieties under heating and cooling conditions (0.4 for heating and 0.3 for cooling). According to Kakac et al., 1987 [16], the equation developed by Dittus-Boelter is found to predict about 13.5% to 17.1% higher values for gas flows compared to the Gnielinski correlation.

The heat transfer coefficients $Nu_{i,s}$ as a function of the Reynolds number Re_i and the dimensionless heating rate q_i^+ for the smooth rod channel are shown in Figure 5.7. As a first observation, it can be seen that the Nusselt numbers increases as the Reynolds number increases, caused by the reduction of the thermal boundary layer thickness and the increase of the axial transport, as the mass flow is increased [131]. As well as the frictional losses, a very good reproduction of the local heat transfer coefficients is obtained, as shown by the results of the conducted (Run01) and (Run02) tests, within an average variation error between the two experimental runs less than ±3%. Furthermore, it can be observed that the experimental and predicted Nusselt numbers are in very good agreement with the Gnielinski correlation, whereas for the Petukhov equation an underestimation about ~5% is attained. On the other hand, it can be noticed that the Dittus-Boelter correlation tends to overestimate the experimental data, especially at higher Reynolds number $Re_i \geq 3\times10^4$ by an average deviation error about +20%.

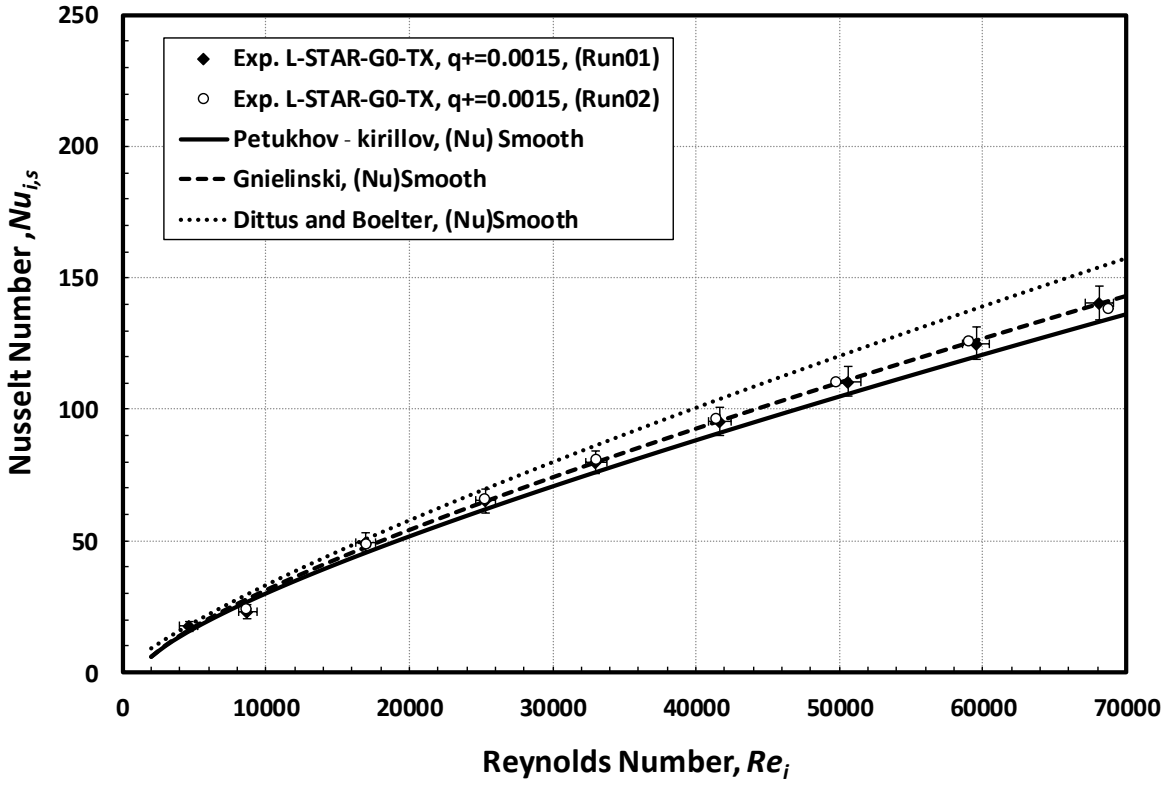

Figure 5.7: Heat transfer coefficients distribution $Nu_{i,s}$ as function Reynolds number for the smooth rod channel cases, compared against the correlations developed by Dittus-Boelter, Gnielinski, and Petukhov.

The small discrepancies between the experimental and the predicted heat transfer coefficients results can be accounted by the heat losses especially in the non-isolated parts of the test section, as well for the geometrical facts, since the geometrical characteristics of the L-STAR facility differ from those of the cylindrical annular geometries for which these types of correlations were developed. The radiation losses are estimated to be about 110 W $\leq \dot{Q}_{wr,s} \leq$ 300 W of the applied heating power P_H. The experimental and predicted mean Nusselt numbers results for the smooth rod channel $Nu_{i,s}$ with their estimated uncertainty magnitudes $\sigma_{Nu_{i,s}}$ and σ_{Re_i} are summarized in Table 2.D in Appendix D.

5.1.4. Velocity distribution smooth rod channel

The mean axial velocity distribution profiles for the smooth rod channels are obtained at the upper optical access (Z= 497 mm) of the test section, in which fully developed flow conditions are assumed to be reached. A total number of 37 radial measurement set points along the plane Y_w are carried out to reproduce each velocity profile. It needs to be highlighted; that a high density of measurement points equally distributed are set-up close to the heater rod wall, covering a wall distance from 0 mm $\leq Y_w \leq$ 3.0 mm (11 measurement points between 0 mm $\leq Y_w \leq$ 1.0 mm and 8 measurement points between 1.0 mm $\leq Y_w \leq$ 3.0), in order to allow the accurate capture of large velocity gradients in this region. The visualization of the mean axial velocity components U_s, the average normalized velocity U/U_m and normalized velocity fluctuations U'_{rms}/U_m, are given in Figure 5.8. The mean results are obtained from a series of time instantaneous velocity values $u_i(t_i)$ – using a data set of approximately 100 000 points acquired for time period between 100 s to 150 s at a sample rate higher than 1 kHz. All velocity measurements are calculated and corrected from bias errors by applying the time weighted average correction scheme, as described in Eq.[4.19].

The mean axial velocity distribution U_s in Figure 5.8 a, exhibits the typical flat profile shape for fully developed turbulent flows on hydraulically smooth walls, caused by the constant shear stress in this region. Even though the thickness of boundary layer is relatively thin, with an estimated value δ_{lam}= 15 µm, a slight asymmetry of the velocity profiles can be noticed. The maximum velocity values are attained close to the center of the flow channel $Y_w/H = 0.44$ (between the hexagonal channel and the heater rod) with an average value of 5.48 m/s for both test runs. The asymmetric shape of the velocity profiles U_s is attributed to the unequal drag and average wall roughness R_a, between the heater rod wall and the inner wall of the test section. Furthermore, the wall distance of the rod and the hexagonal channel varies circumferentially, thereby inducing circumferential pressure differences which translate to into a non-symmetric velocity profile. To compensate these effects and since identical inlet conditions cannot always be maintained during a large LDA measurement campaigns, the average velocities for the smooth channel are normalized by the mean bulk axial velocity U_m as a function of the inlet flow properties ($\dot{m}_{CFM}$, ρ_{air}, P_i and T_i), as described in Eq.[4.22].

The normalized mean velocity distribution U_s/U_m in Figure 5.8 b, shows a slightly better symmetric profile for the two middle parts of the channel, attaining a nearly constant velocity ratio of 1.3 (at a wall distance about 0.30 $\leq Y_w/H \leq$ 0.66). This ratio is considered as a typical value for fully

developed turbulent flows through smooth wall channels [16]. Furthermore, a very good reproduction of the normalized velocity profiles is obtained for both individual experimental test runs (Run01 and Run02), with a maximum average deviation of a ~2% between them. The normalized axial velocity fluctuations for the smooth channel $U'_{s,rms}/U_m$, also known as turbulence intensity, are presented in Figure 5.8 c. It can be observed that the velocity fluctuations are characterized by two maximum peaks located close to the heater rod and channel wall, which then after starts to decrease with the increase of wall distance Y_w/H denoting the typical *M–shape* distribution for fully developed turbulent flows in smooth channels [16, 132]. The measured velocity fluctuation peaks at these region variates from 0.883 – 0.850 m/s at Y_w/H =0.02 and Y_w/H =0.96. The highest velocity fluctuation values obtained near the wall regions are attributed to the increase of the turbulent kinetic energy generated by the high velocity gradients near the wall, and then transported and dissipated into the center region of the flow channel [121], where the turbulence intensities attain their lowest values.

The *logarithmic law* is used as a qualitative comparison for the velocity measurements of the smooth rod channel. In the fluid dynamics, the logarithmic law of the wall is assumed that the average velocity of a turbulent flow at a certain point is a function only of the flow conditions at the wall and independent of the flow conditions far away the wall. The logarithmic representation of the mean velocity distribution was originally proposed by von Kármán et al., 1939 [133], based on similarity hypothesis of Prandtl et al., 1910 [134] using the mixing length theory using asymptotic analysis. The mean velocities are normalized by estimating the shear stress τ_w and friction velocity u_τ obtained from the pressure gradients $\Delta P_{1',2'}$ measured in the fully developed region of the test section, mainly by adopting the definition of the friction factor, as described in Eq.[5.9] and Eq.[5.10]:

$$\tau_w = f_D \cdot \frac{\rho}{8} \cdot {U_m}^2 \qquad [5.9]$$

$$u_\tau = U_m \cdot \sqrt{\frac{f_D}{8}} \qquad [5.10]$$

where, f_D represents the Darcy-Weisbach friction factor and U_m the mean bulk axial velocity of the flow channel. With the known values of the frictional velocity u_τ, the velocity profiles can be obtained in terms of the dimensionless velocity u^+ and the dimensionless wall distance y^+.

$$u^+ = \frac{u}{u_\tau} \qquad [5.11]$$

$$y^+ = \frac{y \cdot u_\tau}{\nu} \qquad [5.12]$$

In terms of the wall coordinates u^+ and y^+ the dimensionless profiles of the smooth rod channel are compared within the mathematical expressions obtained by Prandtl and von Kármán.

Laminar: $u^+ = y^+ \qquad y^+ \leq 5$ [5.13]

Turbulent : $u^+ = 1/\kappa \cdot ln(y^+) + 5.5 \qquad \kappa = 0.41 \qquad y^+ \geq 30$ [5.14]

Additionally, a more complex mathematical expression proposed by Reichardt et al., 1951 [135] Eq.[5.15], is used to describe the whole dimensionless velocity profile:

$$u^+ = 2.5 \cdot \ln(1 + 0.4y^+) + 7.8 \cdot \left[1 - e^{-y^+/11} - (y^+/11) \cdot e^{-0.33 \cdot y^+}\right] \quad [5.15]$$

Figure 5.9 shows the mean velocity distribution of the smooth rod channel at a Re_i ≅16477 in terms of the dimensionless velocity u^+ and the dimensionless wall distance y^+, compared to the mathematical expressions of Prandtl, von Kármán and Reichardt. The derived dimensionless velocity distribution for the two center sections of the hexagonal channel, namely the velocity distribution from the heater rod wall to center of the flow channel $u^+(y^+)_{RC}$ ($Y_w/H = 0 – 0.5$) and the velocity distribution from the optical access window to center of the flow channel $u^+(y^+)_{WC}$ ($Y_w/H = 1.0 – 0.5$), exhibit an acceptable agreement and a qualitative distribution with respect to the *logarithmic law* over the entire inner and outer regions. The discrepancies of the resulting velocity distribution, between both channel middle sections, might be attributed to the use of an average friction factor (between the heater rod and channel wall), for the estimation of the frictional velocity u_τ in Eq.[5.10]. In the laminar sub-layer $y^+ \leq 5$ and buffer layer $11.5 \leq y^+ \leq 30$ the experimental results $u^+(y^+)_{RC}$ are in a very good agreement within a maximal deviation of about 12%, whereas the velocity distribution $u^+(y^+)_{WC}$ exhibit some pronounced deviations in the buffer layer. The difference in this region can be additionally attributed to the higher light scattering near to the vicinity of the wall regions and the systematic measurement errors of the LDA system, as well as uncertainty contributions caused by visual positioning measuring volume. At the fully turbulent or logarithmic region, $y^+ \geq 30$, the velocity distributions collapse into a single line presenting a very good agreement, with a maximal deviation of ~6%, compared to the predicted values.

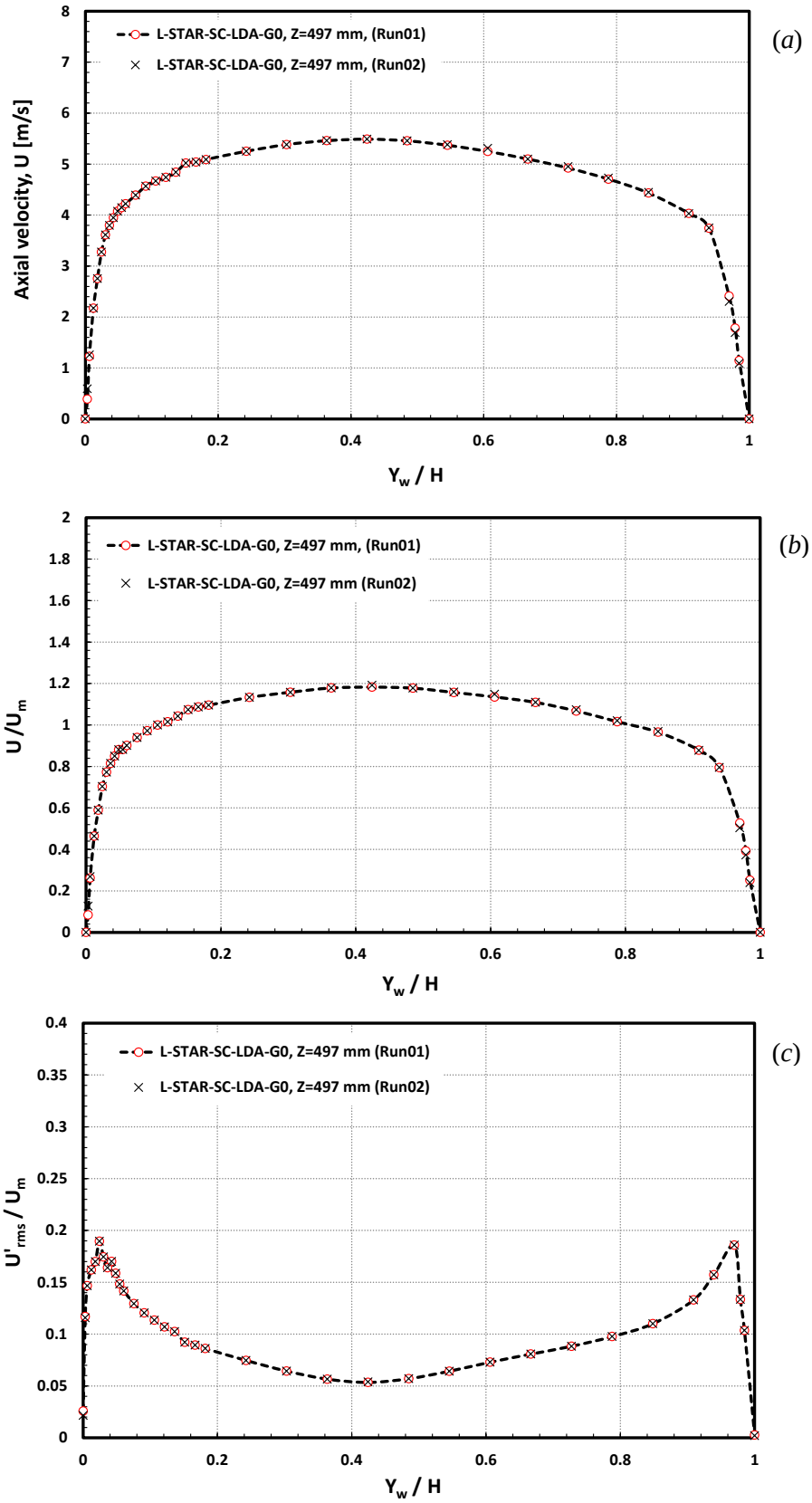

Figure 5.8: Mean axial velocities distribution U_s (*a*), normalized axial velocity U_s/U_m and normalized velocity fluctuations U'_{rms}/U_m (*c*) of the smooth channel cases (*G0*), obtained at an axial position Z= 0.497 mm and Re_i ≅16447.

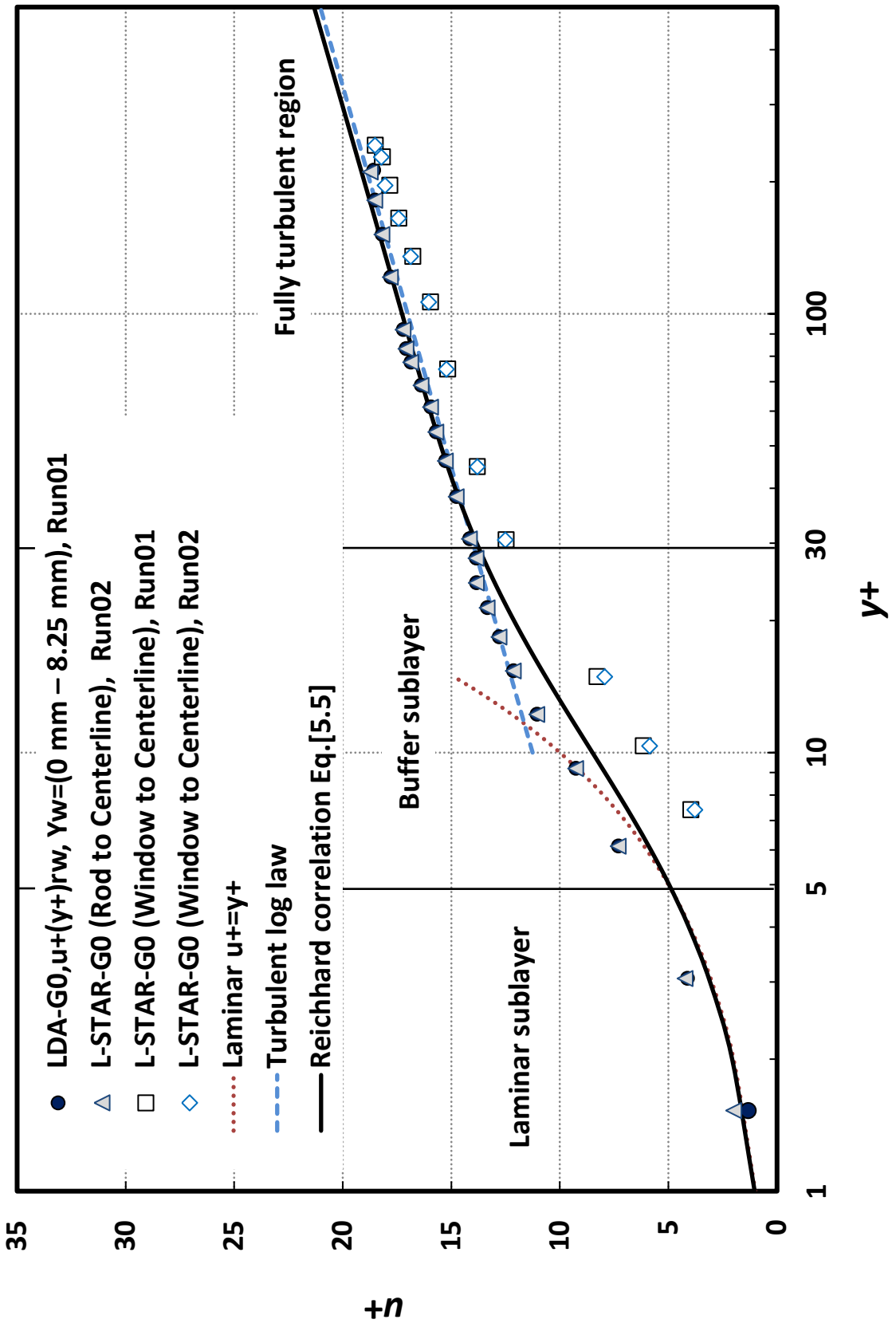

Figure 5.9: Comparison of the dimensionless axial velocity profiles for both center sections of smooth rod channel, as a function the logarithmic law $u^+(y^+)$ and Reynolds number Re_i ≅16447.

5.2. Structured rod channel

In this chapter, the experimental results for velocity distribution, friction factor and heat transfer enhancement of the structured rod channels are analyzed and compared to the smooth channel cases, as well as to empirical correlations. The structured rod channel measurements are carried out at similar Reynolds numbers Re_i and heating rates q_i^+. Additionally, the thermal-hydraulic performance by increasing the heat flux densities on the structured heated rod channels is investigated. In section 5.2.5 a small qualitative analysis for the particle deposition caused by the artificial structuring of the cladding walls is described.

5.2.1. Velocity distribution structured rod channels

The identification of separation and re-attachment of the flow can be interpreted as regions of a reduced or intensified heat transfer, while the secondary recirculation zones can be understood as the main factor for the increase of pressure penalties in the system [119]. The velocity distribution for the solid (L-STAR-LDA-G1) and perforated (L-STAR-LDA-G2) ring structured channels have been conducted between two consecutive ring structure elements, namely between the 11th and 12th ring structures. The selected domain is located at the upper optical access of the test section, covering an axial length about 474 mm $\leq Z \leq$ 504 mm, corresponding to a pitch to high ratio (P/e) of 10. The velocity distribution measurements for the structured rod channels have been conducted under similar inlet flow conditions, as those of the smooth channel tests, at a fixed Reynolds number $Re_i \cong$16447. A similar coordinates system (ϕ, X_w, Y_w, Z) is used, however, in order to simplify the positioning of the velocity distribution between the selected ring structures a fourth coordinate Z_r is introduced (pointing in the streamwise direction of the flow). The velocity distributions are acquired at thirteen representative axial positions $0 \leq Z_r/e \leq 9.3$, between the structured rod and the smooth channel wall, covering a channel height $H = 16.5$ mm, as described in Figure 5.10.

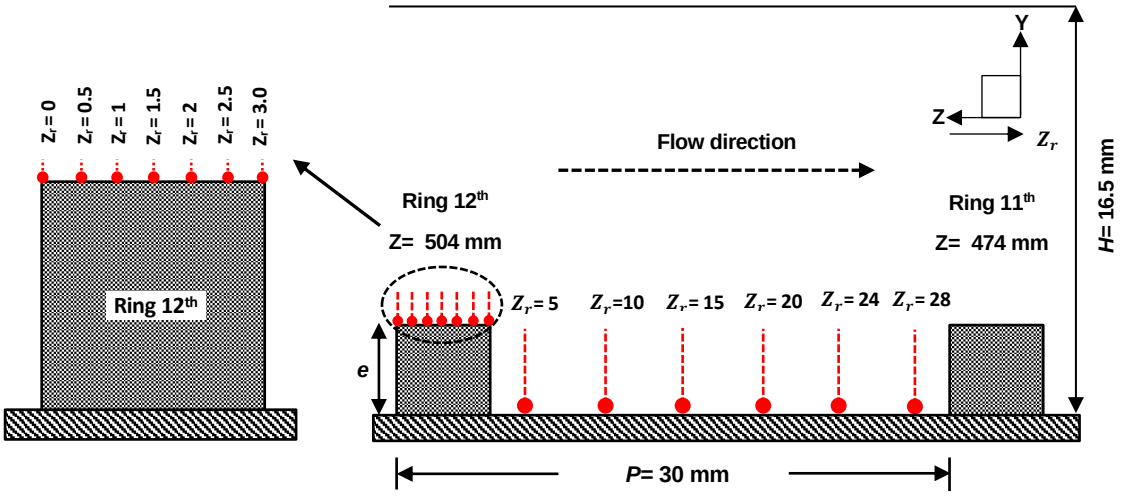

Figure 5.10: Coordinate system used for LDA measurements between two consecutive ring structures (rings 11th – 12th) at the fully developed region (Z = 474 mm –504 mm).

A total of 38 radial individual measurement points along the plane Y_w are recorded for each axial position Z_r. As well as for the smooth channel, a high-density distribution of measurement points close to the structured wall have been conducted to resolve the velocity distribution in this region. The statistics of the time-averaged normalized velocity magnitude and velocity fluctuations are obtained from a larger data set among 200 000 to 300 000 samples acquired approximately during 300 s. A recording sample rate of about 0.5 – 0.7 kHz has been achieved at the inner region of the structured rod wall up to a radial wall distance $Y_w/H \leq 0.18$, while up to a 10 kHz recording rate for the outer region is attained.

Figure 5.11 shows a general overview for the main results of the time-averaged normalized velocity U_r/U_m and normalized turbulence intensity distributions $U'_{r,rms}/U_m$ for both structured rod channels in the Y_w, Z_r – plane at a Reynolds number $Re_i \cong 16477$. The contour and vector representation of the axial velocities clearly highlight important features of the flow distribution, such as the separation and reattachment lengths of the main flow, as well as the development of several recirculation zones close to the structured rod walls, while the normalized velocity fluctuation distribution mainly describes the formation of different turbulent zones regions between surface structures. A single representation of the normalized velocity and normalized velocity fluctuations distribution for the structured rod channels is given in Figure 5.12 and Figure 5.13. Additionally, the main velocity results for the smooth rod channel are integrated for comparison.

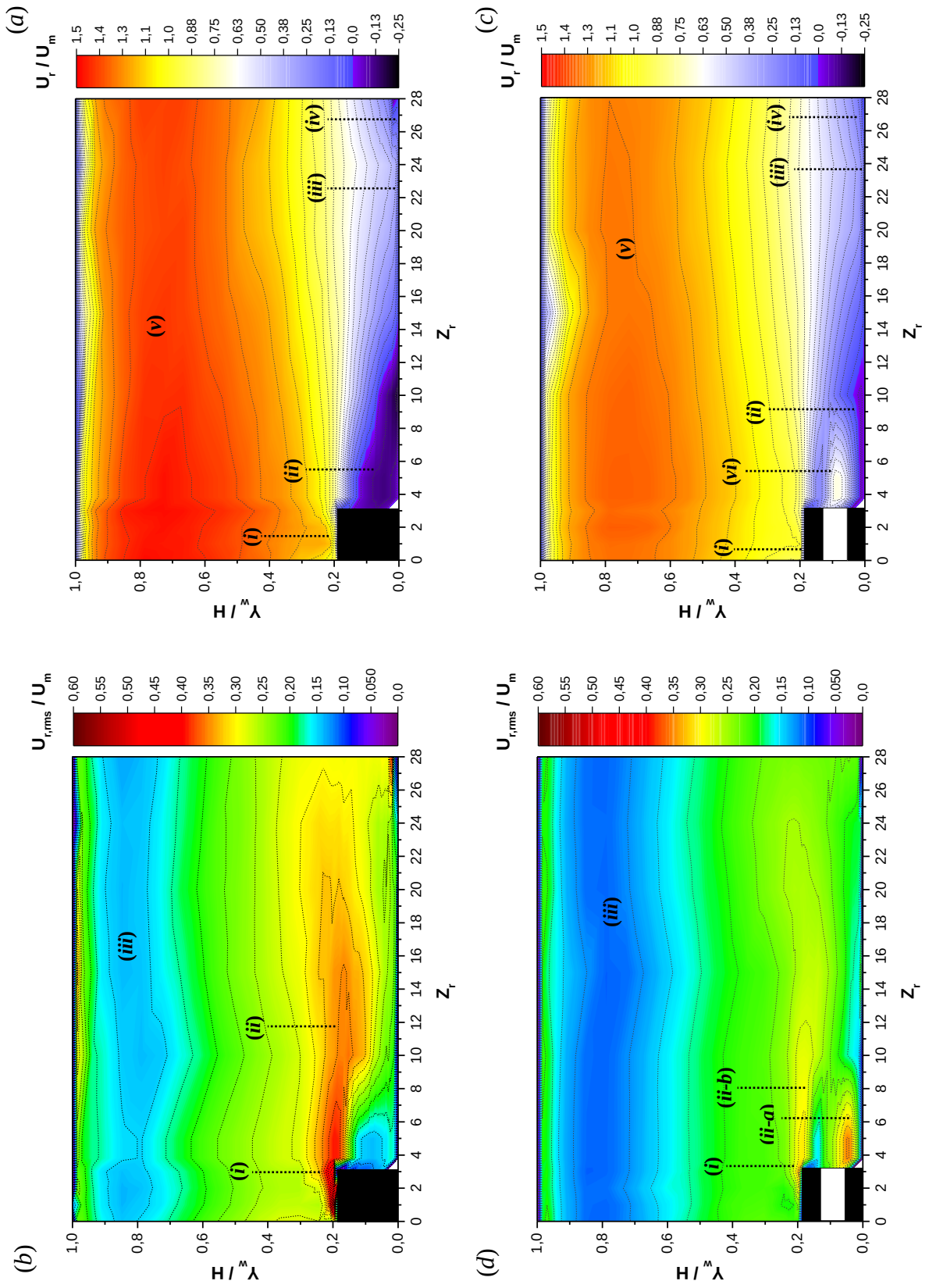

Figure 5.11: Contour representation of time normalized mean axial velocity U_r / U_m for the solid (*a*) and perforated rings (*c*) and turbulence intensity distribution $U_{r,rms} / U_m$ for the solid (*b*) and perforated rings (*d*), for a fixed $Re_i \cong 16477$.

Mean axial velocity distribution

Solid ring structures (G1)

As a starting point of discussion, it is noticed that in contrast to the velocity distribution in the smooth rod channel, the artificial structuring of the cladding, results in a significant displacement of the main flow toward the smooth outer wall of the channel, attaining higher velocity values in the vicinity of the structured wall. The normalized axial velocity distribution for the solid ring structured rod attained their maximum (v) just upstream to the center of the flow channel at about a wall distance $Y_w/H \leq 0.72$, as shown in Figure 5.11 a and Figure 5.12 (filled bullet points).

The axial velocity distributions at the top of the solid ring structures $0 \leq Z_r/e \leq 1.0$ are mainly dominated and characterized by an increase of the velocity components. At this region, the cross-section area of the flow channel is reduced by the presence of the ring structures, forcing the separation of main flow just above the leading edge of the 12th solid ring structure. A closer analysis of the velocity distribution at the top of the solid structures, denotes the formation of a small recirculation zone or *separation bubble* (i), at the upper face of the solid ring structure, expanding approximately about an axial position $0.16 \leq Z_r/e \leq 0.66$, and a wall distance $0.18 \leq Y_w/H \leq 0.21$. Similar results were reported by Rau et al., 1998 [136] and Coletti et al., 2014 [137]. This is effect is evidenced by the bimodal shape of the statistical distribution $u(t_i)$ attained during the LDA measurements, as depicted in Figure 5.14. According to Rau et al., 1998 [136], the recirculation zone at the top of the solid ring structures is associated to the interaction effects caused by the separation and flow shedding taking place downstream in each of the surface structures.

As the main flow crosses into the inner-spacing of the ring structures, the fluid experiences a deceleration and forward reattachment to the wall, caused by the increase of the cross-section area. As a result of this deceleration, the flow expands downstream leading to the development of a large clockwise recirculation zone, also known as *primary recirculation* (ii) located at the front face of the 12th solid ring structure. The primary recirculation zone is expressed by the negative velocities close to the wall, along the streamwise length from $1.0 \leq Z_r/e \leq 5.0$, extending up to a wall distance $Y_w/H \leq 0.12$. As the flow develops along streamwise direction of the inner-spacing Z_r, the primary recirculation zone seems to gradually shrink, causing that the main flow slowly reattaches to the structured rod wall. This effect can be observed by the progressive decrease of the negative velocity gradients in the streamwise direction of the flow, as the flow develops into the inner-space of the solid ring structures.

The reattachment of the flow (iii) for the solid ring structures is identified to take place within a narrow region close to the upcoming surface structure, at about an axial position $7.5 \leq Z_r/e \leq 8.0$. This result is found to be in a very good agreement within the experimental investigation made by Webb et al., 1981 [119] and several other experimental studies. The reattachment of the flow has been associated to the Coriolis force produced by the primary recirculation zone, dragging the freestream flow from the center of the channel into the inner-spacing of the surface structures [66]. Immediately after the flow

reattachment takes place, the main flow separates a second time from the wall, characterized by a well-defined increase of the axial velocity between $8.0 \leq Z_r/e \leq 0.93$. This effect has been associated to formation and growth of mixing turbulent boundary layer [138].

A second weak recirculation zone, also known as secondary recirculation (*iv*), is measured at the downstream end of the 11th ring structure, at an axial position $Z_r/e \leq 9.3$. In this area, small negative velocity region is observed in a wall distance of $0 \leq Y_w/H \leq 0.02$. This secondary recirculation zone may be explained by the impingement of a small fraction of the main flow downstream of the solid rings, which is then transported into the inner-spacing. Furthermore, the formation of secondary recirculation zones at the downstream region of the artificial surface structures has been recently related to cause a negative effect on the heat transfer enhancement, leading to the development of local hot spots, which in some cases could exceed the maximum design temperature of the materials [139]. This effect is consistent to the attained temperature distribution results, described in section 5.2.3.

Perforated ring structures (G2)

The time-averaged normalized axial velocity distributions for the perforated ring structures $U_{r(G2)}/\ U_m$ are given in Figure 5.11 c and Figure 5.13 (unfilled bullet points). From this figure, it can be seen that the flow distribution is considerably modified in the vicinity of the wall. In particular the recirculation zones between the ring structures, as well as the amount of flow separation at the leading edge of the perforated rings are altered. At the outer region of the channel $0.24 \leq Y_w/H \leq 0.90$, similar velocity distribution is observed between the perforated and solid ring structures, attaining their maximum value (*v*), close to the smooth wall side of the channel, at about wall distance Y_w/H =0.78. The axial velocity distributions for the perforated ring structures are noticed to be somewhat lower, about 10%, compared to the solid ring velocity distribution. These variations at outer region of the channel are associated to higher effective flow cross-section of the perforated rings. Furthermore, the contour representation in Figure 5.11 c, exhibits that the main flow does not fully separate at the upper edge of the ring structures, but rather a larger part of the fluid located within the structure height flows forward through the ring perforations and exit in form of a multiple jet-like flow system (v*i*), manly affecting the size, location and expansion of the recirculation zones between the surface structures.

In contrast to the solid ring cases, the primary recirculation (*ii*) is displaced further downstream into a narrow region in the vicinity of the wall. This is indicated by a smaller region of negative velocities, at an axial length $1.6 \leq Z_r/e \leq 5.0$, compared to the solid rings. The effects of the multiple jet-like flow system on the axial velocity distribution are concentrated in a small inner-spacing region close to the perforated ring structures, which is not exceed $Z_r/e \leq 3.3$. In this region, their characteristic flow pattern can be clearly observed, characterized by a sinus shape, covering a wall distance $0.01 \leq Y_w/H \leq 0.13$, attaining its maximum value upstream the ring perforations at about a wall distance Y_w/H =0.9. Despite the fact that the multiple jet-like flow system produces higher velocities gradients, about 7.4 times higher than the solid ring structures at wall distance $Y_w/H = 0.9$, the velocity distributions at the midpoint of the inner-spacing $5.0 \leq Z_r/e \leq 8.0$ exhibits a similar

qualitative flow pattern as the solid ring structures. On the other hand, the reattachment of the flow (*iii*) is not significantly affected by the displacement of the primary recirculation zone or the multiple jet-like flow system motions transported to the inner-spacing of the structures. The reattachment of the flow is found to take place at a similar axial distance, somewhere in between a pitch-to-height ratio 7.5 $\leq Z_r/e \leq$ 8.0.

The velocity profiles close to the rear side of the 11th perforated ring structure, at an axial length $Z_r/e \leq$ 9.3, indicated the absence of any secondary recirculation at the downstream region. This effect can be associated to the lower blockage and redirection of the main flow at the rear side of the perforated rings, as it is indicated by the lack of negative velocities in the vicinity of the rod wall. Furthermore, contrary to what was expected the development of a flow bubble (*iv*) at the top of the perforated ring structures is not completely avoided, nevertheless, a lower effect can be noticed compared to the solid ring, as indicated by the statistical velocity distribution in Figure 5.14.

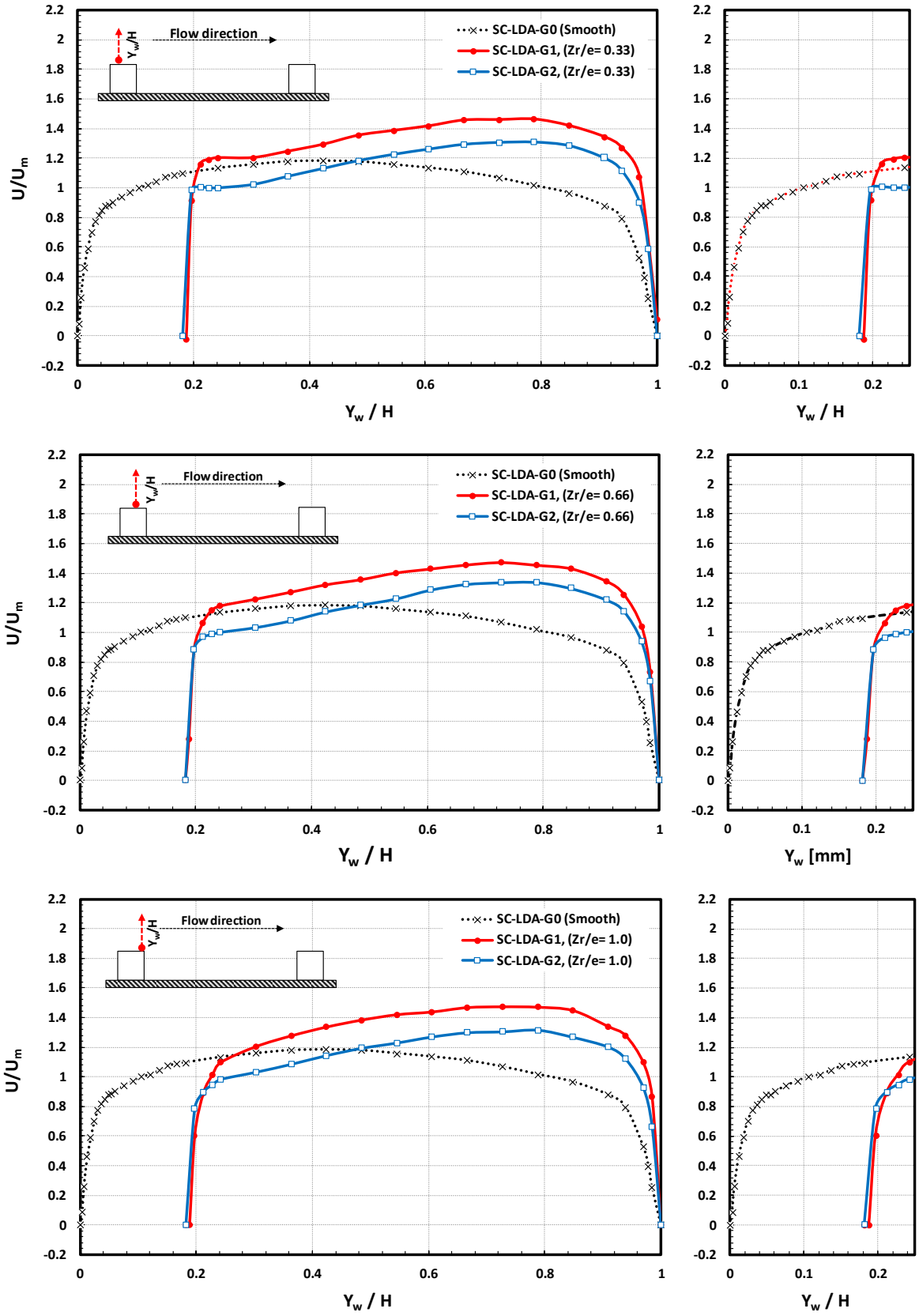

Figure 5.12: Mean normalized velocity results of the axial velocity components U/U_m for the solid (*G1*) and perforated (*G2*) ring structures, compared to the smooth rod channel results(*G0*), for a Reynolds number $Re_i \cong 16477$.

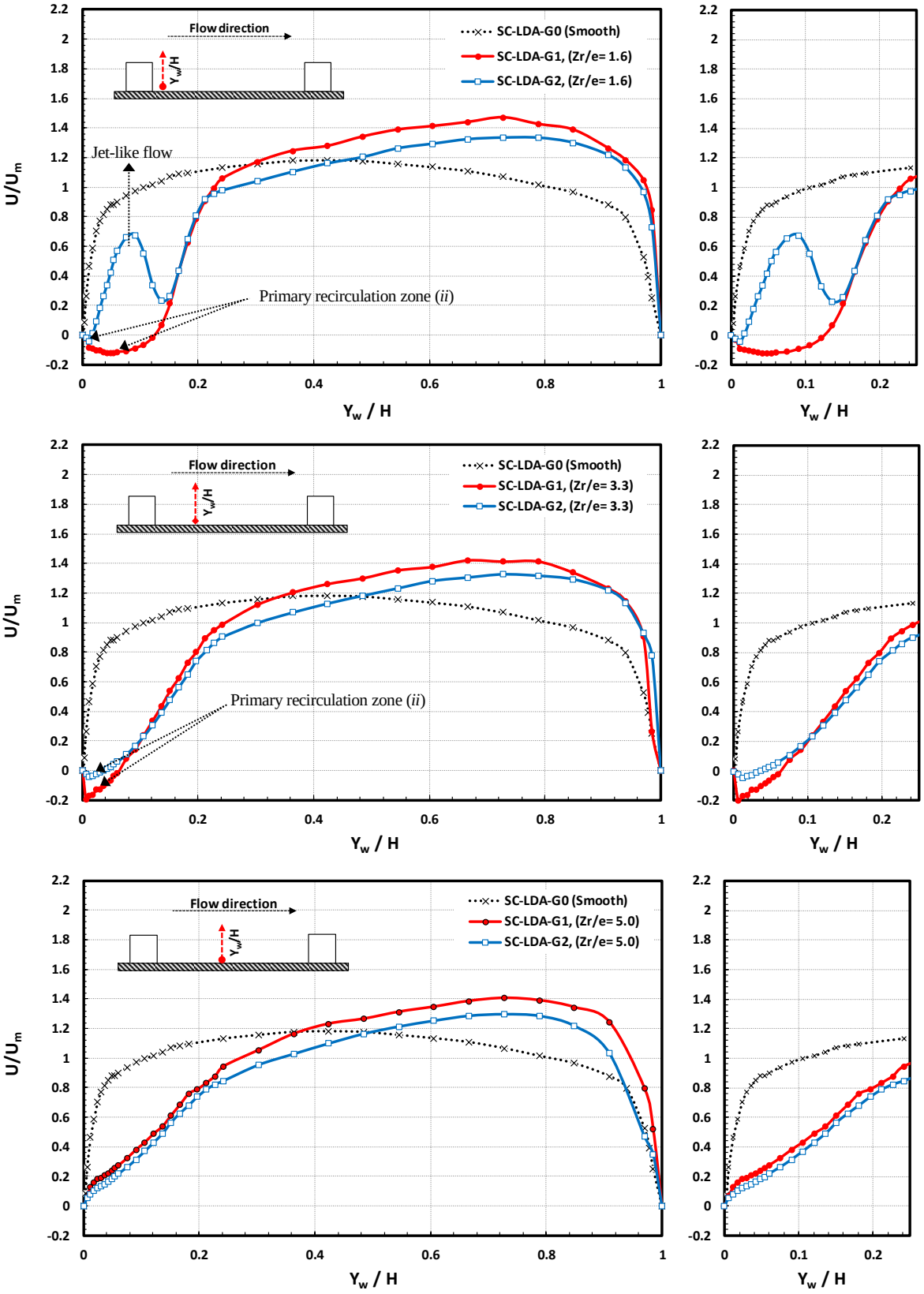

Figure 5.12 (Continuation): Mean normalized velocity results of the axial velocity components U/U_m for the solid (*G1*) and perforated (*G2*) ring structures, compared to the smooth rod channel results (*G0*), for a Reynolds number $Re_i \cong 16477$.

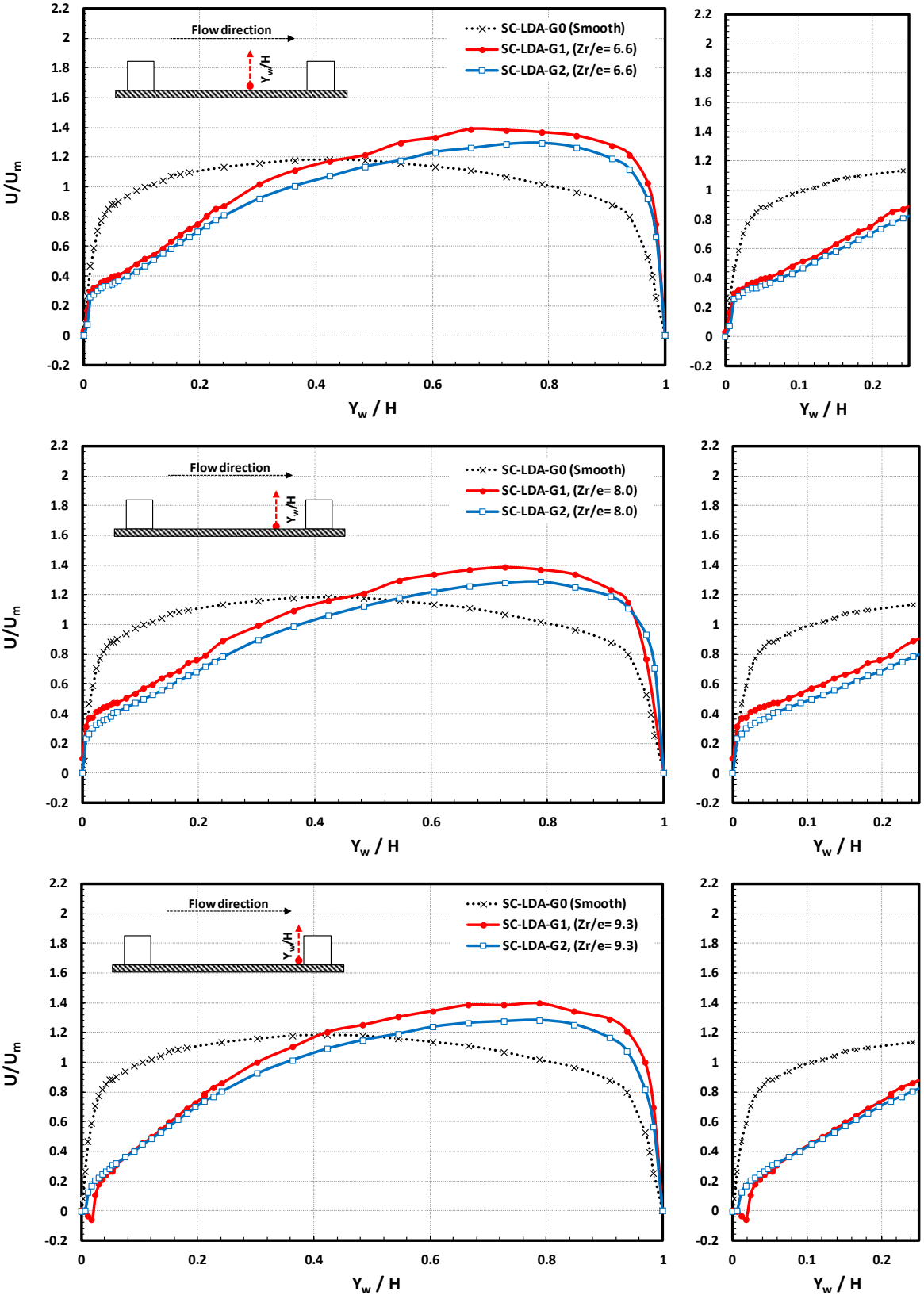

Figure 5.12 (Continuation): Mean normalized velocity results of the axial velocity components U/U_m for the solid (*G1*) and perforated (*G2*) ring structures, compared to the smooth rod channel results (*G0*), for a Reynolds number $Re_i \cong 16477$.

Mean turbulence intensity distributions *rms*

Solid ring structures (G1)

The development of the normalized velocity fluctuation distributions $U'_{r,rms(G1)}/U_m$ (also known as turbulence intensity) for the solid ring structures are given in Figure 5.13 (filled bullet points). Compared to the smooth rod channel, the solid ring structures generate much higher turbulence levels, particularly in the close to the vicinity of the wall. This near-wall region, in which the turbulence intensities are increased by the presence of the surface structures, is known as the *roughness sub-layer*. This sub-layer is generally assumed to have a height closer to $2 \sim 5$ times the roughness height (e) [140, 141] and it is limited to the point at which the turbulence statistics become spatially homogeneous and independent of the surface structure shape [140].

In the case of the solid rings cases, the highest turbulence intensity levels are measured at the top of the ring structures (*i*), $0 \leq Z_r/e \leq 1.0$ at a wall distance of about $0.18 \leq Y_w/H \leq 0.19$, as observed in the contour plot Figure 5.11 b. In this region, the velocity fluctuations are about 2.1 to 3.7 times higher, than those obtained for the smooth rod channel experiments under same flow conditions. The increase of the velocity fluctuations at the top region of the solid rings are caused by the development of an unsteady shear layer and the strong acceleration imposed by the separation of the flow at the leading edge of the ring structure, thus leading to the production of higher turbulent kinetic energy [138]. Furthermore, as shown in Figure 5.11 b a small shear of the turbulent kinetic energy produced at the top the 12th ring structure is transported into the inner-spacing, extending up to an axial length of about $Z_r/e \leq 5.0$.

Directly after the 12th ring structure, at an axial position $Z_r/e \leq 1.6$, the development of the primary recirculation causes a low mixing of the flow in the vicinity of the structured wall. Furthermore, inside in this region similarity between the solid rings and the smooth channel velocity fluctuation levels are observed up to a wall distance $Y_w/H \leq 0.75$. Directly above the recirculation zone, the velocity fluctuations start to increase with the distance from the structured wall, attaining a second local peak (*ii*), at a wall distance $0.18 \leq Y_w/H \leq 0.19$. This increase is attributed to the higher transport and dissipation of turbulent kinetic energy at the top of the ring into the inner-spacing, as well as the higher shear stress between the main flow and the surface structure, as the cross-section of the channel decreases [142]. As the flow develops into the midpoint of the inner-space $5.0 \leq Z_r/e \leq 8.0$, the velocity fluctuation distributions are dissipated in both span-and streamwise directions, describing a non-symmetric distribution in form of "*S*–profile" shape and attaining their lowest values (*iii*) near to the smooth wall side of the channel, at about a wall distance $0.78 \leq Y_w/H \leq 0.84$. A second region of low turbulence levels is measured downstream of the ring structure 11th, at an axial position $Z_r/e \leq 9.3$. Additionally, at this axial position the velocity fluctuation distribution exhibits an interesting flatted profile, which extends in the spanwise direction of the flow beyond the ring structure height e, up to a wall distance $Y_w/H \leq 0.24$. It is not entirely clear why such a distribution is obtained at this region; however, this flattened distribution might be explained by the strong spanwise dissipation of the flow downstream of the 12th solid ring structure. Similar results have been reported, that this type

of velocity distributions in this area are mainly originated, due to a high momentum region downstream the structures which is eventually captured by the main flow [143].

Perforated ring structures (G2)

The normalized velocity fluctuation distributions $U'_{r,rms(G2)}/\ U_m$ for the perforated ring structured rod channel cases are depicted in Figure 5.11 d and Figure 5.12 (unfilled bullet points). It can be noticed, that the velocity fluctuation levels at the top of the perforated ring structures (*i*), at about a wall $0.19 \leq Y_w/H \leq 0.21$ are significantly decreased compared to the solid ring experiments. In this region, the velocity fluctuations for the perforated ring cases are about 1.6 to 2.5 times lower compared to the solid ring experiments. This might be explained by the lower spanwise and streamwise transport of the turbulence fluctuations in the channel, as shown in contour representation. Furthermore, as well as for the solid ring cases the lowest turbulence levels are obtained close to the smooth wall, at a wall distance $0.78 \leq Y_w/H \leq 0.84$.

Close to the jet-like flow system, at an axial length $Z_r/e \leq 1.6$, the formation of two consecutive velocity fluctuations peaks are observed. The first local peak (*ii-a*) at the close vicinity of the wall $Y_w/H = 0.04$ is attributed to the higher shear magnitudes caused by the strong interaction between the jet-like flow system and the small primary recirculation in the vicinity of the structured wall. Quantitatively, the velocity fluctuation levels at the center of the jet-like flow are about 2.1 to 2.4 times higher compared to the solid ring and smooth channel cases. Immediately downstream the jet-like flow system, at about a wall distance $Y_w/H \geq 0.13$, the velocity fluctuation levels start to increase again attaining a second local peak (*ii-b*), at about a wall distance $Y_w/H = 0.18$. This second peak can be attributed to the acceleration of the main flow crossing at the top of the ring structure into the inner-spacing, as well as to small turbulence shedding produced by the multiple jet-like flow systems. As the flow develops beyond the jet-like flow system, between an axial position $3.3 \leq Z_r/e \leq 8.0$ can be observed that neither the different flow patterns generated by the jet-like flow system close to the perforated ring structure and/or the interaction of the small-scale structures deteriorate the velocity fluctuation levels with the increase of Z_r/e. At the rear of the 11th perforated ring structure, at an axial position $Z_r/e = 9.3$ the velocity fluctuations exhibit a decrease of the turbulence levels very close to the vicinity of the wall $Y_w/H \leq 0.01$, which is about 1.7 times lower, compared to the solid rings cases at the same wall distance, this may indicate a riddance of the secondary flow recirculation. Furthermore, as the distance with respect to the structured wall increases, about $0.024 \leq Y_w/H \leq 0.24$, similar velocity fluctuation distributions for both structured rod channels is attained. Although, the velocity fluctuation levels depict a similar behavior, the flattened profile of the perforated ring structures in this region can be explained by a more uniform transport of the main flow to the perforated sections. Finally, it can be observed that the outer region of the channel (*iii*), at about a wall distance $0.84 \leq Y_w/H \leq 1.0$, all velocity fluctuation profiles become independent of the artificially structured rod wall, overlapping in a single line within the smooth results, denoting a good agreement within the *roughness sub-layer* concept [132].

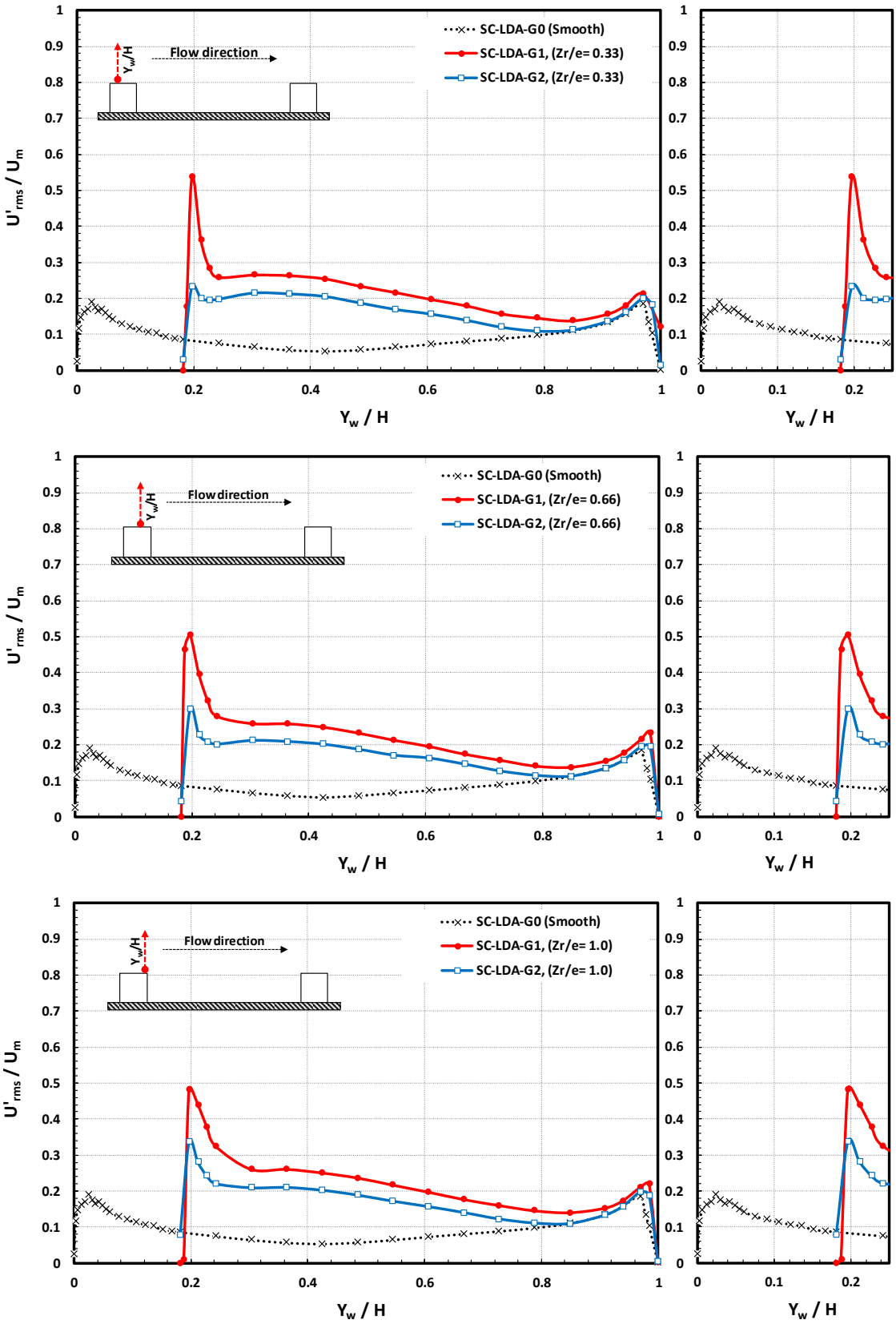

Figure 5.13: Turbulence intensity distributions of the axial velocity components U'_{rms}/U_m for the solid (*G1*) and perforated (*G2*) ring structures, compared to the smooth channel (*G0*) results, for a Reynolds number $Re_i \cong 16477$.

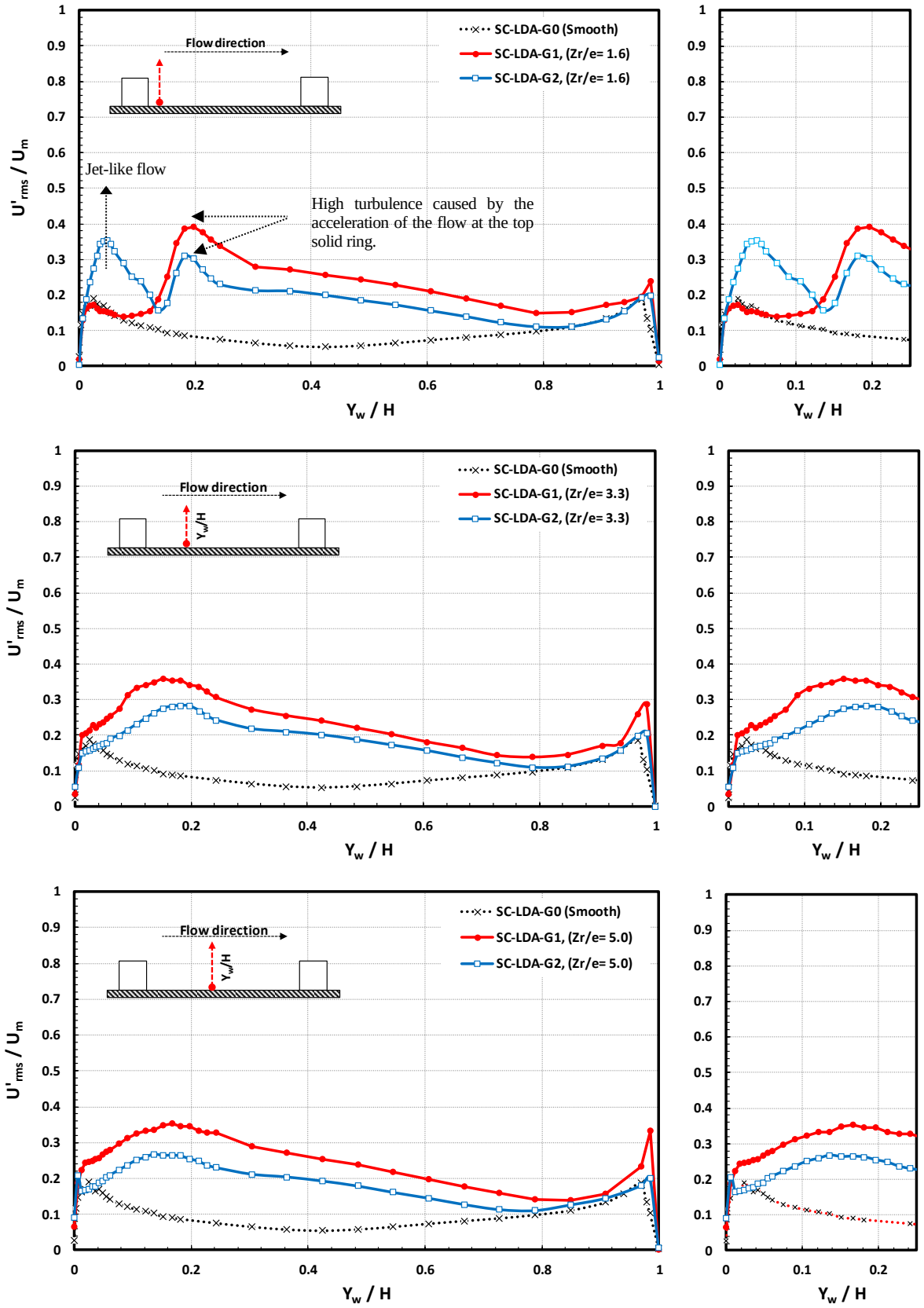

Figure 5.13 (Continuation): Normalized axial velocity fluctuation distributions U'_{rms}/U_m for the solid (*G1*) and perforated (*G2*) ring structures, compared to the smooth channel (*G0*) results, for a Reynolds number $Re_i \cong 16477$.

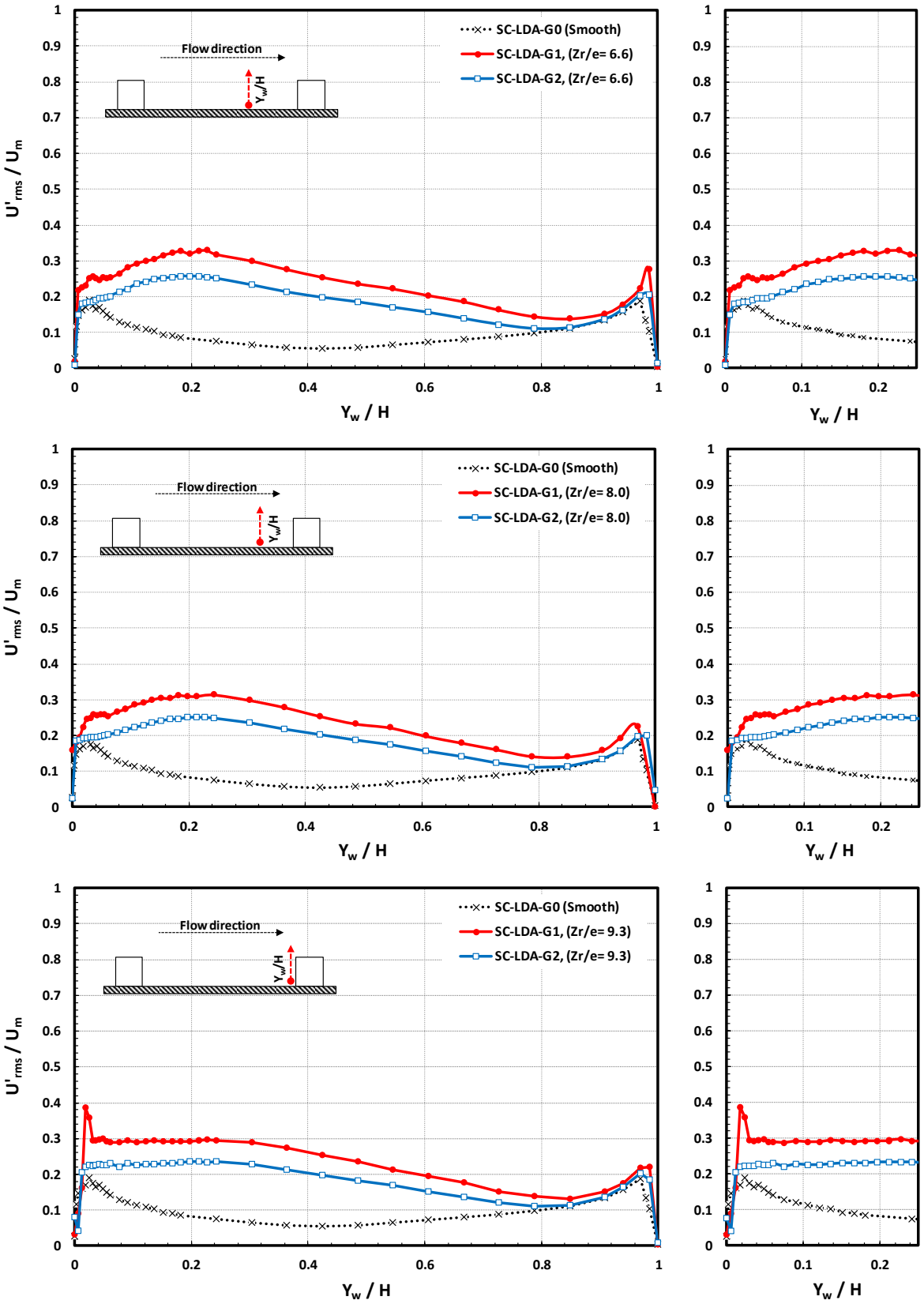

Figure 5.13 (Continuation): Normalized axial velocity fluctuation distributions U'_{rms}/U_m for the solid (*G1*) and perforated (*G2*) ring structures, compared to the smooth channel (*G0*) results, for a Reynolds number $Re_i \cong 16477$.

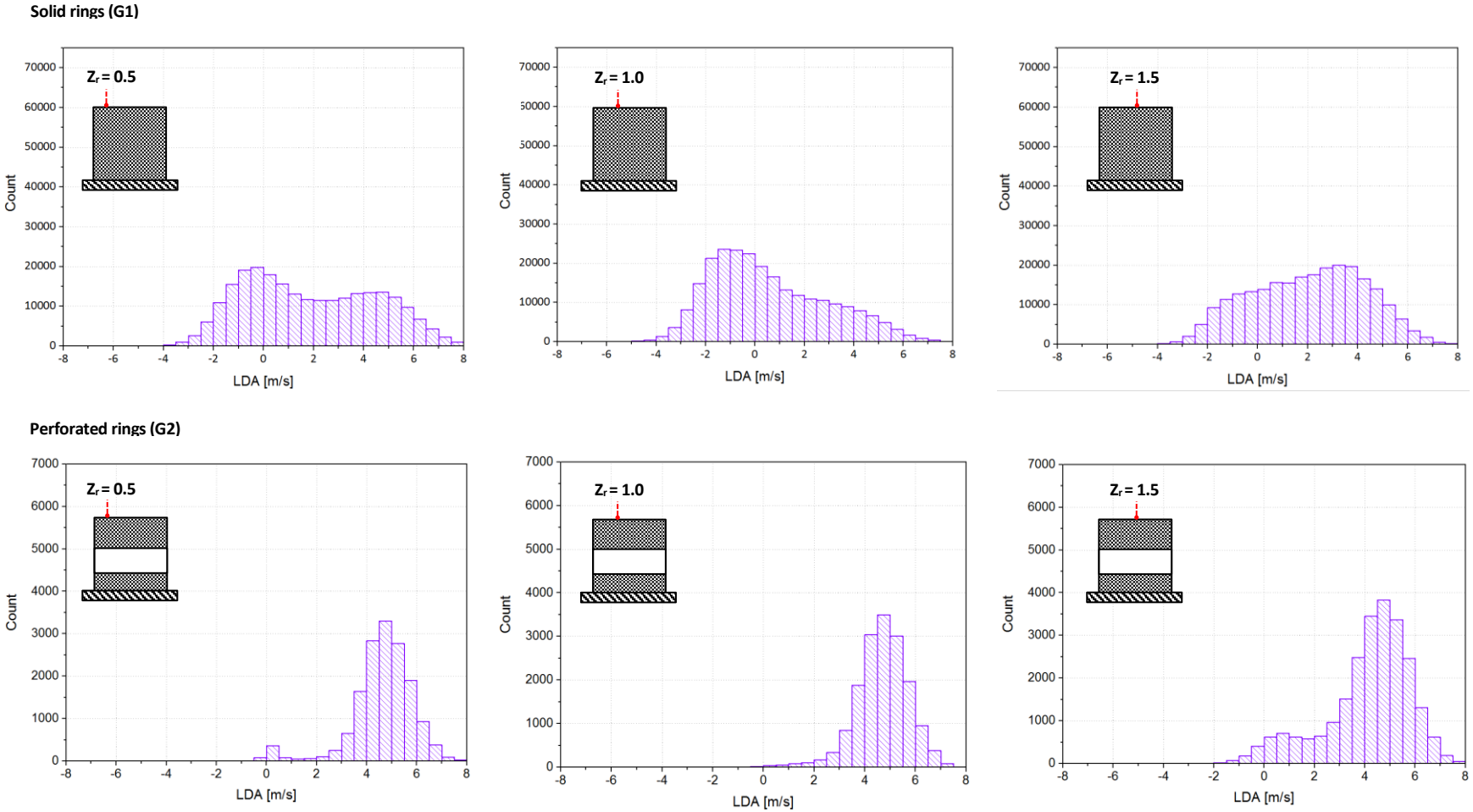

Figure 5.14: Histogram of the time averaged velocity $u_i(t_i)$ at the top of the solid (*G1*) and perforated rings (*G2*) structures at three different axial length positions Z_r.

5.2.2. Friction factor structured rod channel

In this section, the frictional losses $f_{D,r}$ corresponding to the artificially structured rod experiments (L-STAR-G1) and (L-STAR-G2) of the L-STAR facility are discussed. The measurements are carried out for different mass flow rates Re_i and heating conditions q_i^+=0.0015 – 0.003. The local frictional factors are obtained by recording the pressure difference at the test section $\Delta p_{1'2'}$ in terms of Darcy-Weisbach friction factor.

Figure 5.15 shows the local friction factor distribution for both structured rod experiments $f_{D,r(G1)}$ (solid ring structures) and $f_{D,r(G2)}$ (perforated ring structures) under unheated and three different heating rates q_i^+ =0.0015, 0.002 and 0.003, for a total Reynolds number range between $2000 \leq Re_i \leq 70000$. As a reference base line for the structured rod cases, the frictional losses of the smooth rod channel cases $f_{D,s}$ are plotted with a dotted line. It can be noticed, that the friction factors for both solid and perforated structured rods exhibit higher pressure drop values compared to the smooth rod channel under same operating conditions. The ring structures surface increases the turbulent kinetic energy, yielding flow redistribution towards to the center of the flow channel, thereby increasing the pressure losses. Moreover, vortex shedding of the main flow produced by previous surface structures might cause additional energy losses [131].

The local friction factors decrease rapidly for both structured rods as the Reynolds number increases, attaining nearly constant values for $Re_i \geq 40000$; no significant uncertainty magnitudes for both friction factors and Reynolds numbers are obtained at high Re_i. At high Reynolds numbers, the artificial structures tend to project the laminar sub-layer deeper into the turbulent region, decreasing its thickness and transporting the shear stress forces directly to the wall in form of drag forces attaining almost a constant behavior [16, 144]. The region in which the frictional losses become independent of the Reynolds number for any given surface structure shape is known as the *fully rough regime* [26]. The local friction factor results of the solid ring structured rod cases (L-STAR-G1-DP) shows an average increase in the order of 3.2 to 5.9 times; while the perforated ring structured rod cases (L-STAR-G2-DP) exhibit significantly lower friction losses, which are in the order of 2.9 to 4.3 times higher than the smooth rod channel experiments. Comparing the friction factor ratio $f_{D,r(G1)}/f_{D,r(G2)}$, it can be seen that the perforated ring structures show approximately 37% lower friction factors in the whole studied Reynolds number range $2000 \leq Re_i \leq 70000$. The lower friction factor rates of the perforated ring structures are attributed mainly to the lower blockage ratio of the mean flow downstream each ring structure, leading also to weaker recirculation zones and less vortex shedding into the middle part of the channel, as discussed in velocity flow fields analysis.

Furthermore, from Figure 5.15 a-b can be noticed that the local friction factor for the heated cases (L-STAR-G1/G2-TX, q_i^+=0.0015 – 0.003) increases with the increase of q_i^+, as expected from previous results in section 5.1.2, the variation between the unheated and heated cases is about 11% – 21% for the solid (G1) and 6% –19% for the perforated (G2) rings. As well as for the smooth channel cases, the heating effects on the friction factor evaluation are almost negligible by using the derived local

flow conditions $T_{g,15}$ and $p_{1'}$, as shown in Figure 5.15 c. The local friction factors of the structured rod channel cases are compared to recently develop semi-empirical correlations suggested by Rashkovan Eq.[5.16] and Saini Eq.[5.17], for gas cooled channels instrumented with two-dimensional transverse surface structures. Rashkovan et al., 2010 [145, 146] derived a friction factor correlation for annular flow channels with rectangular spaced ribs placed on the inner wall as function of Reynolds number, as well as the main dimensionless geometrical parameters $(e/D_h, P/e, w/e, \alpha)$. The correlation is based on a validated modified $k-\varepsilon$ turbulence model on annular channels. The correlation can be used for a Reynolds number range between $2300 \leq Re \leq 10^5$, relative roughness height $0.02 \leq e/D_h \leq 0.1$, relative roughness width $0.125 \leq w/e \leq 6$ and a relative roughness pitch between $8 \leq P/e \leq 12$. The correlation predicts the friction factor values within ±15% error margin.

$$f_{r_{Rashkovan}} = \left(\frac{w}{e}\right)^{-m_1} \cdot Re^{-m_2} \cdot C_1 \left(\frac{P}{e}\right)^{C_2} exp\left[-C_3\left(\frac{P}{e}\right)\right] \qquad [5.16]$$

where, the constants have a reported value of C_1=0.326, C_2=0.854, C_3=0.114. m_1=0.22, m_2=0.15.

Saini et al., 2002 [75] proposed a correlation for the frictional losses over transverse roughness structures with sharp edges, as a function of geometric and flow parameters $(Re, P/e, e/D_h, \alpha)$ valid for rectangular channels. The correlation is valid for Reynolds numbers $Re \geq 3000$, relative roughness height-to-hydraulic diameter ratio $0.015 \leq e/D \leq 0.08$ and relative roughness pitch $P/e \leq 12$. The correlation produces assessments within an error margin of ±12%. It should be pointed out that the correlation described in Eq.[5.16] and Eq.[5.17] are only suitable for the comparison of the solid ring structure cases (L-STAR-G1).

$$f_{r_{Saini}} = 12.44(Re)^{-0.18} \cdot \left[\left(\frac{e}{D_h}\right)^{-0.99} \cdot \left(\frac{P}{e}\right)^{-0.52} \cdot \left(\frac{\alpha}{10}\right)^{0.49}\right] \qquad [5.17]$$

From Figure 5.15 can be observed that the derived data from both used correlations overestimates the frictional losses for the solid structured rod experiments under unheated condition (L-STAR-G1/G2-DP), while a lower overestimation is seen for the heated experiments (L-STAR-G1/G2-TX). The predicted friction factor values by Rashkovan's equation results in an overestimation of 14.9%, whereas Saini's equation also overestimates the friction factor but exhibit a slightly lower difference of about 10.9%, compared to the experimental data. Although, the uncertainties are relatively larger at lower Reynolds numbers, the frictional losses $f_{D,r}$ for the fully developed flow are in a reasonable agreement within the reported deviation error of Eq.[5.16] and Eq.[5.17]. Additionally, further variation between the experiment and the correlations results might be understandable due to the fact that Eq.[5.16] and Eq.[5.17] have been derived from different channel geometries.

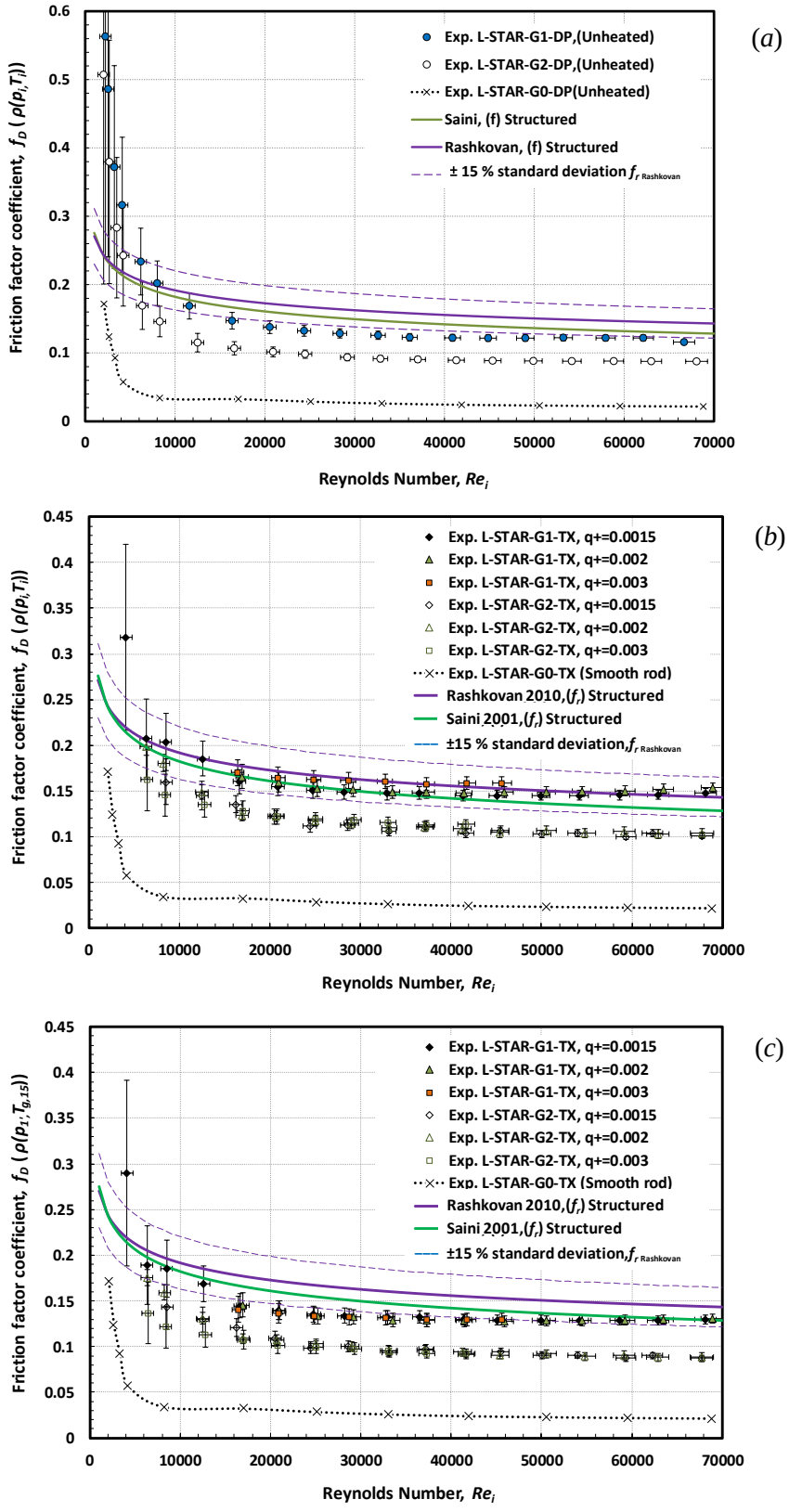

Figure 5.15: Friction factor coefficients for both solid (*G1*) and perforated (*G2*) ring structured channels, (*a*) unheated, (*b*) heated as a function of the inlet conditions T_i, p_i and (*c*) heated as function local $T_{g,15}$, p_1', compared to the smooth channel and correlations proposed by Rashkovan and Saini.

5.2.3. Heat transfer in structured rod channel

In this section, the experimental results for the axial temperature distribution and the heat transfer coefficients in terms of Nusselt number from the structured rod channel experiments are discussed. Additionally, the axial temperature distribution and corresponding Nusselt numbers Nu_i are compared to literature analytical and empirical correlations. Finally, the heat transfer enhancement as function of the frictional factor is evaluated in terms of thermal performance index η.

Wall temperature distribution

Experiments for both structured rod channels are conducted under similar fluid flow and thermal power condition to allow a fair comparison with the smooth rod channel experiments. In addition, the effects of working at higher thermal rates (q_i^+=0.002 and q_i^+=0.003) and similar flow rates Re_i on the cladding surface temperature distribution are investigated, to compared the heat transfer coefficient enhancement at higher thermal loads. The temporal evolution of the cladding temperatures for the solid (L-STAR-G1-TX) and perforated (L-STAR-G2-TX) structured rods at five different axial positions during the heat up transient of the *Base case* scenario (Re_i≅16447 and q_i^+ =0.0015), are presented in Figure 5.16. As a baseline, the wall temperature development of the smooth rod channel is plotted. This figure shows that thermal equilibrium for the structured rod experiments is reached and maintained, after about 0.8 hours. The earlier wall temperature evolution is attributed to faster grow of the thermal boundary layer. Similar evolution is obtained for the perforated rings. By introducing surface structures into a flow, the overall momentum, heat and mass transport is increased, as a result of the structure disturbing the thermal boundary layer [102, 103].

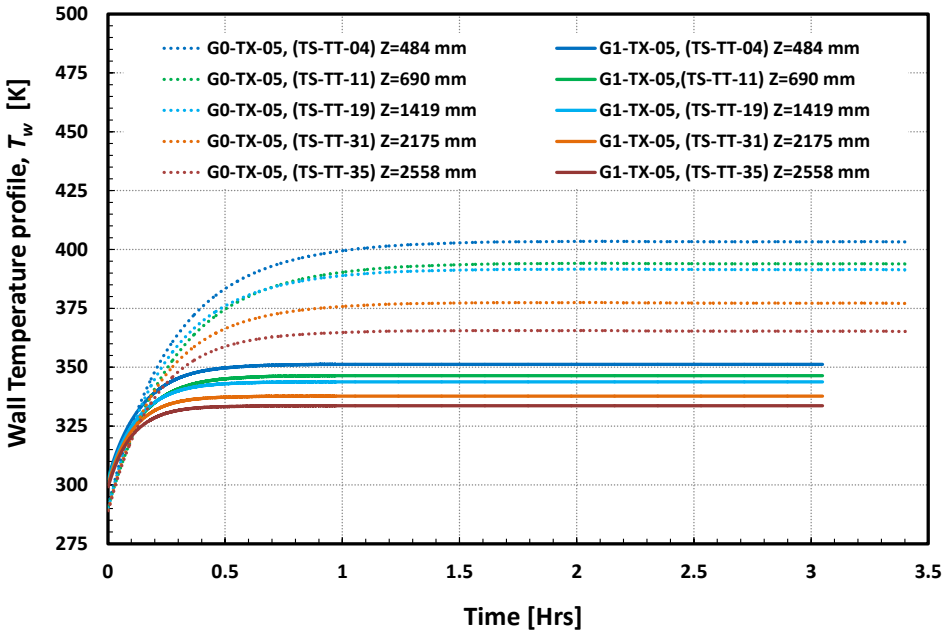

Figure 5.16: Temporal evolution of the axial wall temperature for the solid ring rod at five axial positions during the heat-up transient of the *base case*, Re_i ≅16447 and q_i^+=0.0015, compared to the smooth channel distribution.

Figure 5.17 describes the stationary dimensionless axial cladding temperature profiles $\Theta_{w,i}$ obtained for the solid (*G1*) and perforated (*G2*) ring structured rod channels covering an axial length $Z_0 =$ 0 mm to $Z_1 =$3398 mm at three different heating rates $q_i^+ =$0.0015 – 0.003 for a Reynolds number range $4000 \leq Re_i \leq 70000$. The temperature distribution profiles of the smooth rod channel are also shown as comparison baseline. It can be observed that the axial temperature distribution for both structured rod channels exhibit a similar profile trend, compared to the smooth channel cases. The axial cladding temperature distribution of the rod increase with the distance from the inlet region along the channel as the flow develops, attaining almost a constant temperature distribution at the upstream region of the test section at about axial position 0.14 to 0.29 ($0.5 \text{ m} \leq Z \leq 1.1$ m), where the heat conduction in the rod corresponds almost to the flow gas temperatures.

The measured axial temperature distribution for both structured rod cases exhibit considerably lower temperature distribution values, approximately ~1.9 – 2.1 times lower when compared to the smooth channel experiments. Furthermore, it can be seen that as the Reynolds number increases the slope of the axial temperature distribution between the smooth rod channel and the structured rod channels decreases. This suggests that the cladding temperature distribution depends on a small scale in the dimensionless heating rate q_i^+, but primarily determined by the Reynolds number Re_i. The lower temperature distribution obtained by the structured rod channels is attributed to the increase of the convective turbulent mixing near the structured wall produced by the ring structures, thereby leading to higher heat removal. Slightly variations on the cladding temperature distribution are observed between the solid and the perforated ring structures close to the inlet region at about an axial position 0.5 – 0.8 ($1.6 \text{ m} \leq Z \leq 2.7$ m) for all conducted cases. This difference may be attributed to the lower flow development at this region for the solid ring structures. Nevertheless, the dimensionless temperature distribution curves at the fully developed region exhibit no significant differences, overlapping in single trend line. These results are in very good agreement within the dimensionless temperature distribution concept. Despite the facts, the wall heating rate q_i^+ are increased by a factor of two, the resulting axial temperature distribution of the structured rod cases denotes even lower temperature levels, as those attained for the smooth rod channel conducted at a lower heating rate $q_i^+ =$0.0015.

The axial temperature distribution results exhibit that the artificial structuring of fuel rod elements in Gen-IV GFR could allow working at higher heat flux densities, without exceeding the current temperatures of the smooth cladding design. The measured cladding temperature distribution $T_{w,i}$ and derived bulk gas temperature $T_{g,15}$ for the above mentioned experimental cases in terms of their dimensional form are given in Appendix D. The temperature distribution between two consecutive surface structures can be observed in detail, as indicated in Figure 5.18.

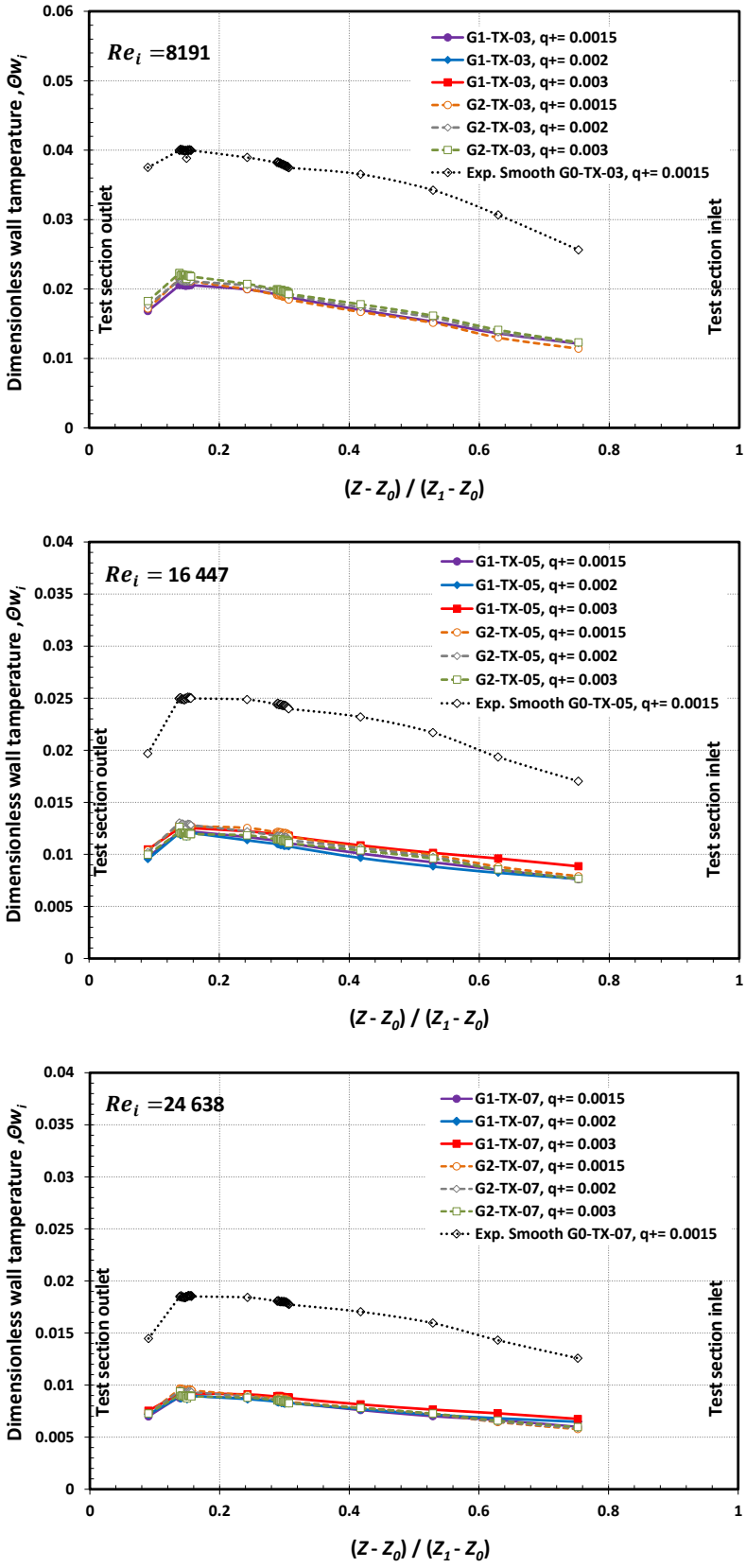

Figure 5.17: Dimensionless axial cladding temperature distribution $\Theta_{w,i}$ for the solid (*G1*) and perforated (*G2*) ring structured channels (e/D_h= 0.084, P/e=10) at three different heating rates q_i^+=0.0015, 0.002, 0.003 and 4000 ≤ Re_i ≤70000.

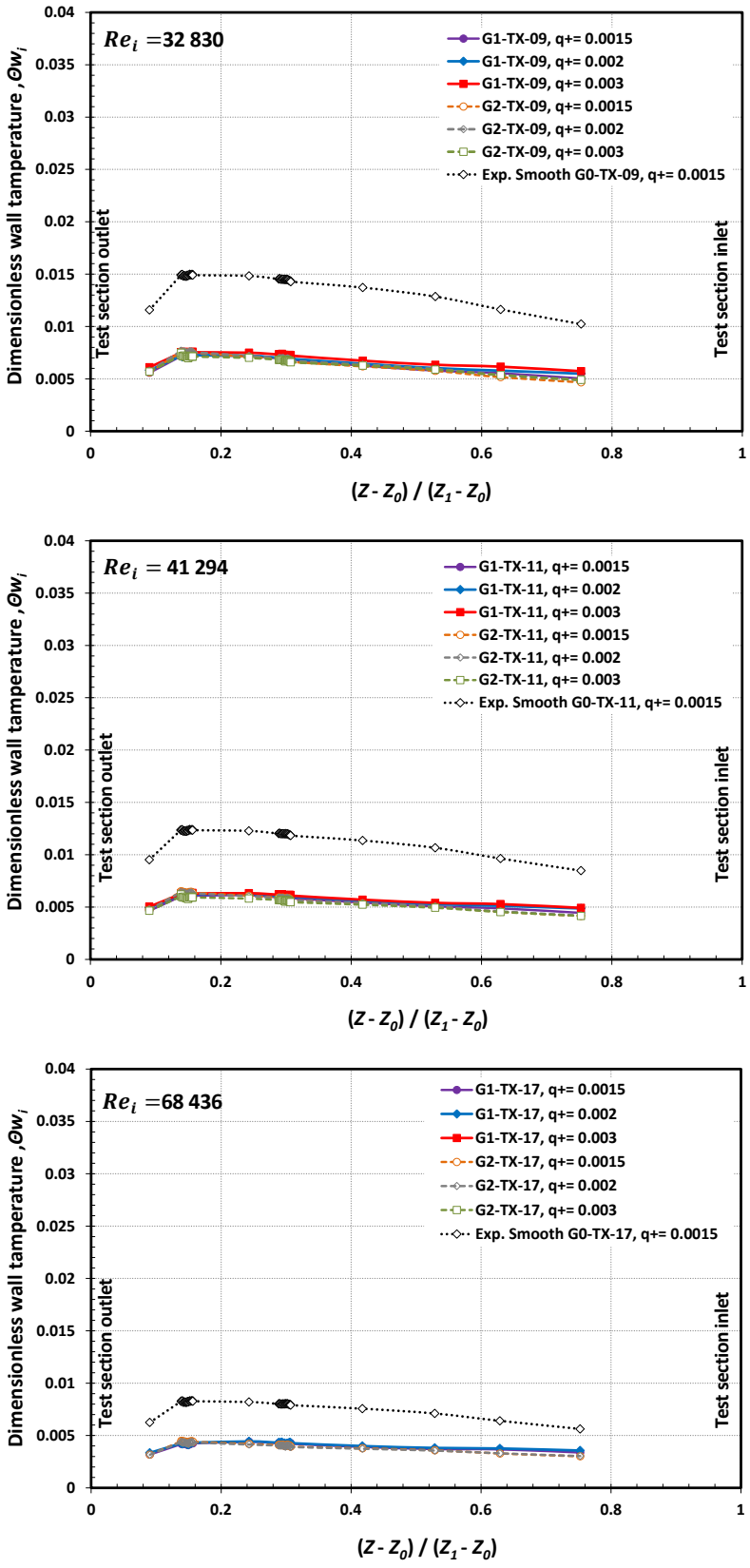

Figure 5.17 (continuation): Dimensionless axial cladding temperature distribution $\Theta_{w,i}$ for the solid (*G1*) and perforated (*G2*) ring structured channels (e/D_h= 0.084, P/e=10) at three different heating rates q_i^+=0.0015, 0.002, 0.003 and 4000 ≤ Re_i ≤70000.

Figure 5.18 shows the cladding temperature distribution between three consecutive ring structure types are measured between the 11th, 12th and 13th rings located at about an axial length Z= 474 mm, 504 mm and 534 mm, for three heating rates q_i^+ and a single Reynolds number $Re_i \cong$ 16447. In addition to the thermocouple measurements, an infrared thermography system by FLIR® has been used as comparison approach for the temperature distribution in this domain. The axial cladding temperature distributions for both measurements show a similar distribution between the ring structures. However, it has to be remarked that the infrared measurements are affected by the emissivity and the tangential radiation effects emitted toward the ambient, which becomes a limiting factor for the accurate surface temperature analysis [147, 148]. An emissivity factor ϵ_{rod} =0.63 (in figure shown as e=0.63) has been used for the infrared thermography measurements. No significant temperature distribution variations are observed between the solid and perforated rings for $q_i^+ = 0.0015$ and q_i^+ =0.002. However, for the highest studied heating rate q_i^+ =0.003 the perforated ring structures exhibit slightly lower temperatures values compared to the solid rings, which can be attributed to the higher turbulence levels close to the vicinity of the wall. For all studied cases, the ring structure surface itself exhibits the lowest temperature levels. Furthermore, it is noticed that the heat transfer enhancement does not actively take place immediately behind or in front of the ring structures, where a slight temperature increase can be observed, as a result of small secondary recirculation zones formed at the back region of the structure wall. Moreover, the cladding temperature distribution between the ring structures at Reynolds numbers Re_i exhibits no significant differences with respect to the described case at $Re_i \cong$ 16447.

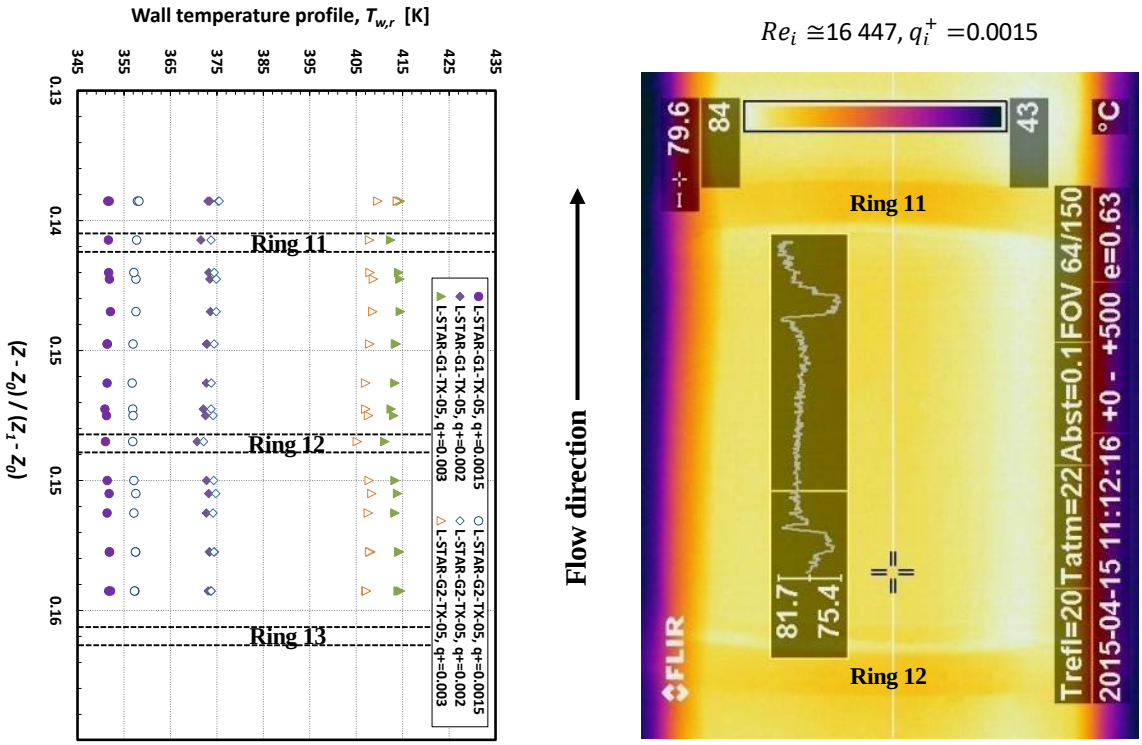

Figure 5.18: Cladding temperature distribution between two consecutive solid (*G1*) and perforated (*G2*) ring structures, as a function the heating rate q_i^+ and Reynolds number Re_i Thermocouple measurements (*left*) and IR thermography (*right*) q_i^+ =0.0015.

Nusselt number structured rod channel

The convective heat transfer enhancement for both structured rod channel experiments in terms of dimensionless Nusselt number Nu_i, as a function of both the non-dimensional heating rate q_i^+ and Reynolds number Re_i are presented in Figure 5.19. The experiments are conducted at heating rates q_i^+=0.0015 – 0.003 and Reynolds number range $2000 \leq Re_i \leq 70000$. The Nusselt numbers are calculated based on the wall heat flux density $\dot{q}_{w5}$ and the local wall temperatures $T_{w,(Z)}$ and derived gas temperature $T_{g,15}$.

The convective heat transfer enhancement for both studied artificially structured rod channels leads to a well-defined heat transfer augmentation compared to the smooth rod channel cases. This general enhancement can be explained due to the fact that the thickness of the laminar sub-layer, which acts as the major resistance component for heat transfer between the solid and the fluid, is reduced. The laminar sub-layer is disrupted by the higher local turbulent mixing produced by the periodical separation and reattachment motions of the artificial surface structures [149]. At lower Reynolds numbers $Re_i \leq 25000$ both structured rod channels exhibit similar enhancement levels. This can be attributed to the lower convective mixing of the flow and thereby lower disturbance of laminar sub-layer. However, as the Reynolds number increases beyond $Re_i \geq 25000$ the perforated ring structures exhibit gradually higher Nusselt number values, up to +8% (for the lowest heating rate q_i^+=0.0015) and +6% (for the highest heating rate q_i^+=0.003) compared to the solid ring cases at similar flow and heating conditions. The higher enhancement levels for the perforated ring structures are attributed to the increase of turbulence levels produced by the multiple jet-like flow system upstream the ring perforations (see Figure 5.11 d), as well as considerable reduction of the recirculation zones in the close vicinity of the wall, thereby preventing the formation of low mixing regions (hot spots) as indicated by velocity distribution measurements in section 5.2.1.

An overall overview on the heat transfer enhancement results of the structured rod channels for all conducted experiments, as well as their comparison with the smooth rod channel and different analytical correlation is given in Figure 5.20. As can be seeing from this figure, the heating rate parameter q_i^+ has a small influence effect by the evaluation of convective heat transfer coefficients, denoting a decrease of the Nusselt number distribution as the heating rate increases from q_i^+ =0.0015 to q_i^+ =0.003. These variations are found to be approximately about ~2% lower for q_i^+ =0.002 and ~13% lower for q_i^+ =0.003, compared to experimental cases conducted at a heating rate of q_i^+=0.0015. A similar variation of ~7% and ~9% are seen for the perforated ring cases. Furthermore, as the Reynolds number increases beyond $Re_i \geq 50000$ the Nusselt number variation between the studied heating rates decreases up to ~3%. The small variation at higher Reynolds numbers may be attributed to the linearization of the gas thermal properties and gas expiation in the test section; similar results have been previously reported in [121]. Furthermore, the use of the inlet gas conditions (i) for the calculation of the Nusselt number Nu_i may exclude possible buoyancy effects.

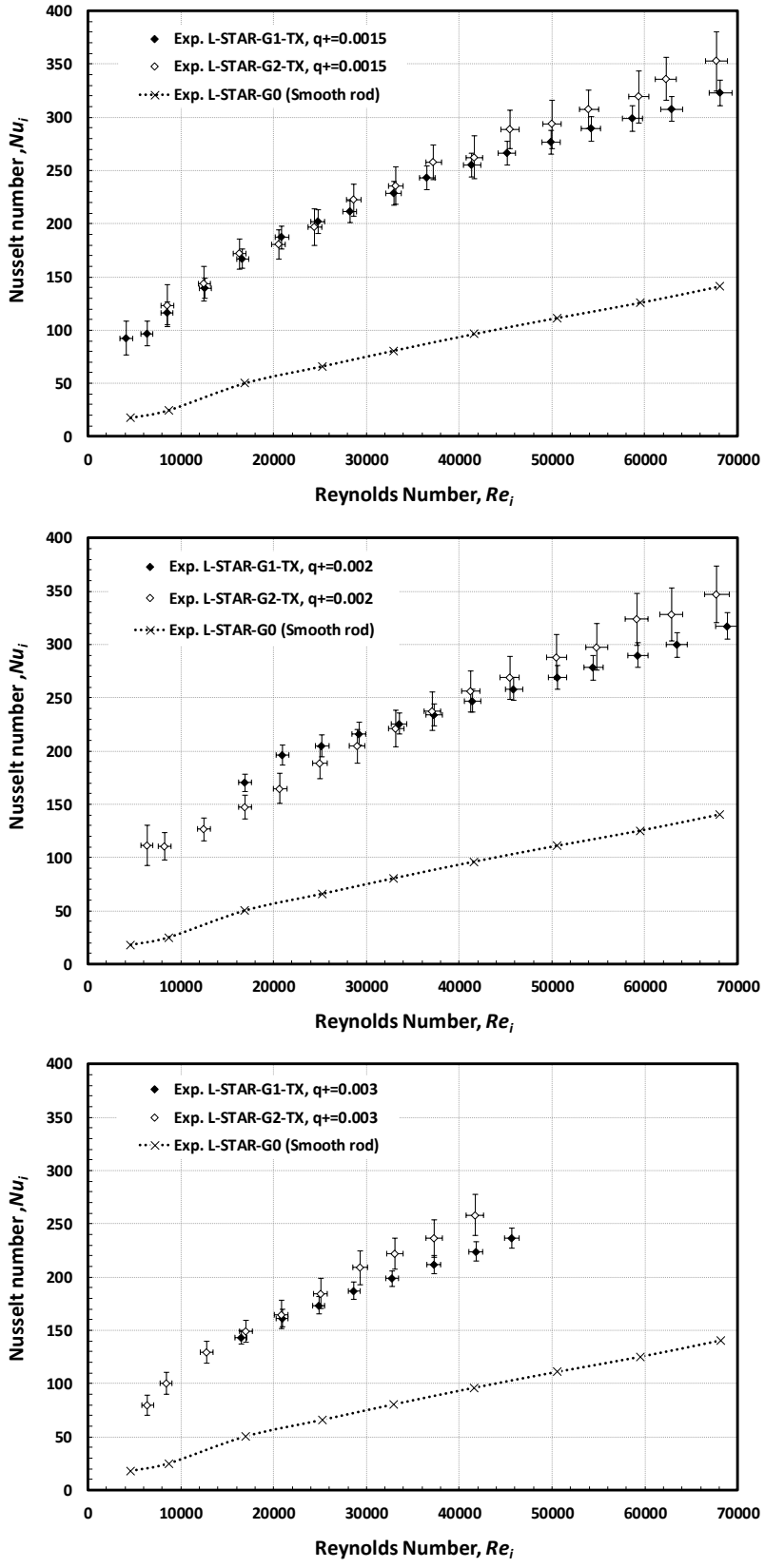

Figure 5.19: Nusselt number distribution for the solid and perforated structured rod channels (e/D_h = 0.084 and P/e=10) at three different heating rates q_i^+, compared to smooth rod channel cases.

The Nusselt number distributions for the solid ring structured rod cases exhibit a heat transfer augmentation on the order of 2.3 to 4.8 times higher compared to the smooth channel. However, the highest Nusselt number enhancement values, on the order of 2.5 to 5.1 times, are obtained by using the perforated ring structures. Based on the augmentation of the convective heat transfer, the perforated structures appear to be a promising option against the solid structures. The convective heat transfer enhancement results of the structured rod channels are compared against analytical correlations proposed by Webb & Eckert, Kader & Yaglom and Han, developed for the heat transfer prediction in internally two-dimensional rib-roughened channels. Webb and Eckert, 1971 [119] developed a correlation Eq. [5.18] for heat transfer and fiction factor for turbulent flow in tubes with repeated artificial structures. The correlations are based on the heat momentum transfer analogy assuming the heat transfer roughness functions $G(e^+)$ and $R(e^+)$ as a function on the flow cross-sectional area. A similar expression for the prediction of the heat transfer in structured cylindrical channels was reported Prasad and Saini, 1988 [150]. The correlation is valid for $0.022 \leq e/D_h \leq 0.05$, $10 \leq P/e \leq 20$, covering a Reynolds number range between $5000 \leq Re \leq 120000$. The correlation predicts the values within ±15% error margin for the friction factor and ±12% for the Nusselt number.

$$Nu_{r_{Webb}} = \frac{(f_r/2) \cdot Re \cdot Pr}{1 + \sqrt{f_r/2} \cdot [G(e^+) \cdot Pr^{0.57} - R(e^+)]} \quad [5.18]$$

where, $G(e^+) = 4.5(e^+)^{0.28}$, $R(e^+) = 0.95 \left(P/e\right)^{0.53}$ and the friction factor f_r is obtained by:

$$\sqrt{(2/f_r)} = 2.5 \ \ln(D_h/2e) - 3.75 + R(e^+) \quad [5.19]$$

and where e^+ refers to the Roughness Reynolds number:

$$e^+ = (e/D_h) \cdot Re \cdot \sqrt{f_r/2} \quad [5.20]$$

Kader and Yaglom, 1977 [151] developed a general equation for the prediction of the heat transfer coefficients between structured wall and fluid flow for fully developed turbulent conditions. The proposed correlation is based on dimensional and similarity considerations estimated from the mean temperature profiles in the vicinity of the wall. The final expression for the heat transfer predictions is described in Eq.[5.20]. The given equation is valid for $0.08 \leq e/D_h \leq 0.18$, $4.0 \leq P/e \leq 40$ and Reynolds number from $3\,000 \leq Re \leq 200\,000$, with a standard deviation of ±15%.

$$Nu_{r_{Kader\ and\ Yaglom}} = \frac{\sqrt{f_r/2} \cdot Re \cdot Pr}{5(e^+)^{0.25} - 3 \ \ln(e/D) + 5.6 - \frac{4.5}{(1 - e/D_h)^2} + 9.5\sqrt{f_r/2}} \quad [5.21]$$

where f_r is the friction factor calculated by Eq.[5.22] as:

$$f_r = \frac{2}{\left[R(e^+) - 2.5\ ln\left(\frac{2e}{D_h}\right) - 2.75\right]^2} \qquad [5.22]$$

Before starting the discussion between the experimental and the selected analytical correlations for the prediction of the heat transfer coefficients, it should be remarked that the analytical correlations are mainly valid for the comparison of the solid ring structure cases. The derived convective Nusselt number coefficients for the solid ring cases are in an acceptable agreement to the experimental data in a Reynolds number range of $4000 \leq Re_i \leq 35000$. In this region the predicted values exhibit a deviation about +15% with respect to the experimental data. For Reynolds numbers higher than $Re_i \geq 35000$, the correlations values show higher deviation errors of about ~25%, manly over predicting the experimental data over the entire range. The discrepancies between experimental data and predicted values can be attributed to experimental uncertainties, but mainly to the fact that the reference correlations are derived for other geometry channel types, which differs from the current studied hexagonal channel. Moreover, recent numerical simulations of the L-STAR facility conducted by Boettcher et al., 2016 [152] and Suikkanen et al., 2014 [153] show that the heat transfer enhancement is additionally deteriorated by the formation of secondary recirculation zones generated at the hexagonal channel edges, as the Reynolds number increases. Based on the comparisons between the obtained experimental data and derived values, the current work can be used to improve the heat transfer predictions of artificially structured hexagonal flow channels.

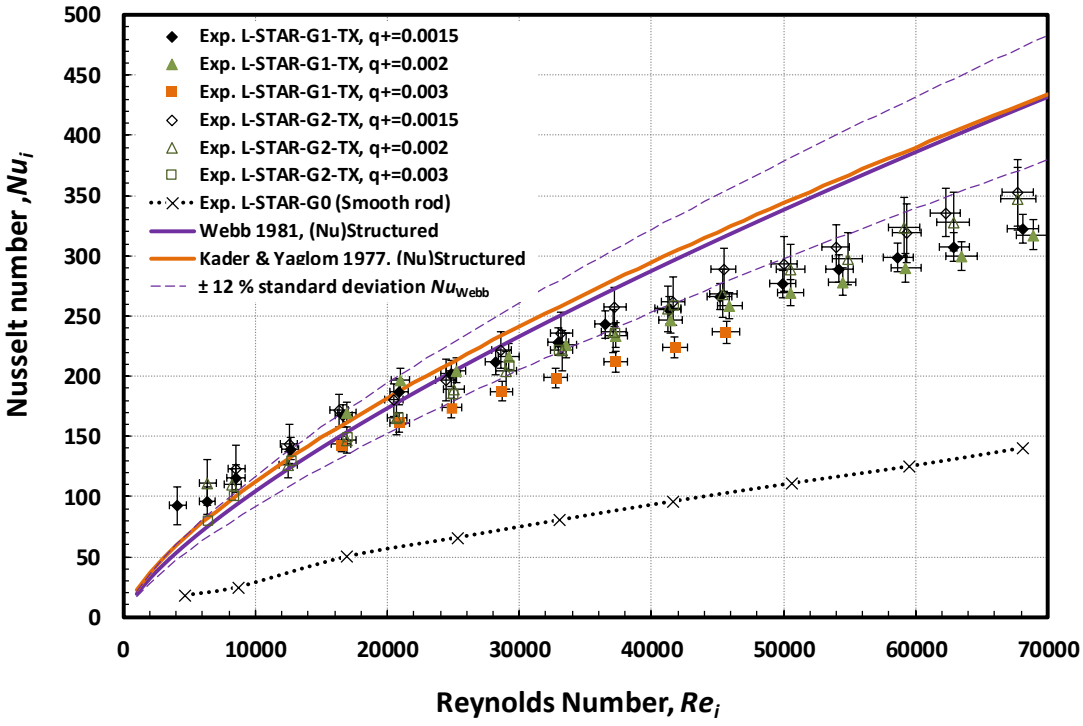

Figure 5.20: Nusselt number distribution for the solid (*G1*) and perforated (*G2*) structured rod channels (e/D_h= 0.084 and P/e=10) at three different heating rates q_i^+=0.0015 – 0.003, as a function Reynolds number and compared to the smooth rod channel (*G0*) and correlations from Webb, Kader & Yaglom.

5.2.4. Thermal performance

Another common way to evaluate the thermal-hydraulic enhancement for the combined effects of the heat transfer and the associated additional pressure losses is provided by using the performance index η. Thermal performance index was firstly proposed by Webb et al., 1981 [119] and is obtained by Eq. [4.17]. This expression considers both the desirable gain in heat transfer, as well as the undesirable increment in friction losses. In addition, this parameter allows an overall comparison of the present study to other experimental and numerical studies having similar rib roughness arrangement. The Nusselt number ratios Nu_r/Nu_s for both solid and perforated ring structured rod channels are found to be around 2.3 to 4.8 and 2.5 to 5.1 times higher than the smooth rod channel. The variation of the friction facto ratios f_r/f_s shows that the solid ring produces considerably higher friction factor values compared to the perforated rings. This supports the implementation of perforated rings on the cladding to considerably reduce the pressure losses in the system. The mean friction factor ratios for the solid (*G1*) and perforated (*G2*) ring structures resulted in an increase of 3.2 to 5.9 and 2.9 to 4.3 with respect to the smooth channel. The plot of thermal-hydraulic performance parameter η as a function of Reynolds number Re_i for both structured rod channels is shown in Figure 5.21. The evaluated thermal performance index is found to vary in a range about 1.3 to 2.8 for the solid (*G1*) and 1.6 to 3.3 for the perforated ring structures (*G2*) up to $Re_i \leq 35000$. For the *base case* scenario ($Re_i \cong 16447$) a thermal performance index about 1.7 to 2.1 times for (*G1*) and 2.0 to 2.3 for (*G2*) is obtained. Subsequently, it can be seen that the evaluated thermal performance index starts to decrease as Reynolds number increases attaining nearly a constant enhancement ratio about 1.3 to 1.6 at the highest Re_i. The lower η values for the solid ring structures are mainly caused by the higher-pressure losses, caused by a stronger separation of the flow to the center of the channel.

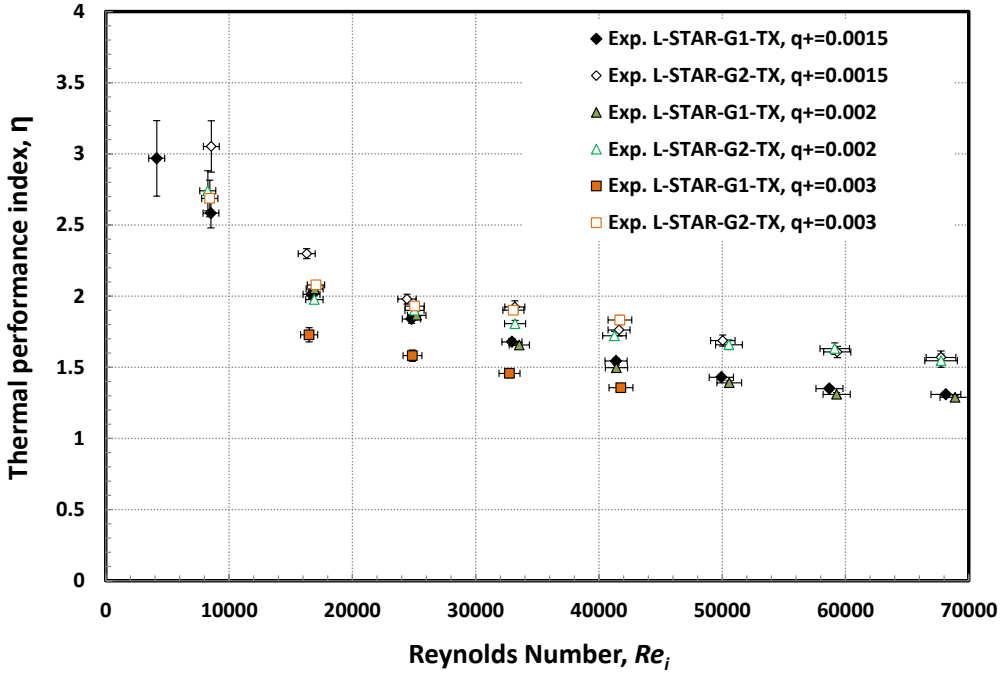

Figure 5.21: Thermal performance index for both structured rod channels at three different heating rates q_i^+=0.0015 – 0.003, as a function of Reynolds number.

5.2.5. Particle deposition

In the field of nuclear safety, the deposition and re-suspension of aerosol and contaminated particles, caused due to abrasive friction between components and gas impurities play a key role in the safety assessment of depressurization accidents in GFR [154]. Therefore, a small description of the particle deposition onto structured rod elements has been carried out. For this purpose, fine TiO_2 particles used for the LDA velocity measurements allowed a qualitative comparison of the particle deposition between the smooth and structured rod channels. The smooth rod channel in Figure 5.22 a, depicts a typical fine homogeneous particle deposition layer all along the cladding. In Figure 5.22 b can be seen that the particle deposition for the solid rings takes mainly place downstream corners of the structures. The particle deposition at this region for the solid ring structures is attributed to the constant impingement of the flow against the solid ring, as the flow separates from the wall. A second deposition region covering at the inner-spacing of the solid rings is observed. The deposits in this region are caused mainly due to the vorticity effects of the primary recirculation zone (*ii*) and the further reattachment of the main flow to the wall (*iii*). Furthermore, a slightly higher particle concentration is exhibited at the top (*i*) of the solid ring structures, caused by the increase of the turbulence levels as the flow separates and crosses at the top the ring structure. For a long-time exposition period, the deposition in these regions may cause a significant geometry change of structures and cladding wall, which might result in lower heat transfer enhancement and increase the pressure losses in the system. The particle deposition for the perforated ring structures shown in Figure 5.22 c, clearly denotes a general lower particle deposition along the cladding wall, compared to both the smooth and solid rings. In contrast to the solid rings, it can be seen that the perforated structures the main deposition regions are found directly at the jet-like flow system (*vi*), caused mainly by the higher turbulence fluctuation at this region. A second small deposition is observed at between the flow-jets.

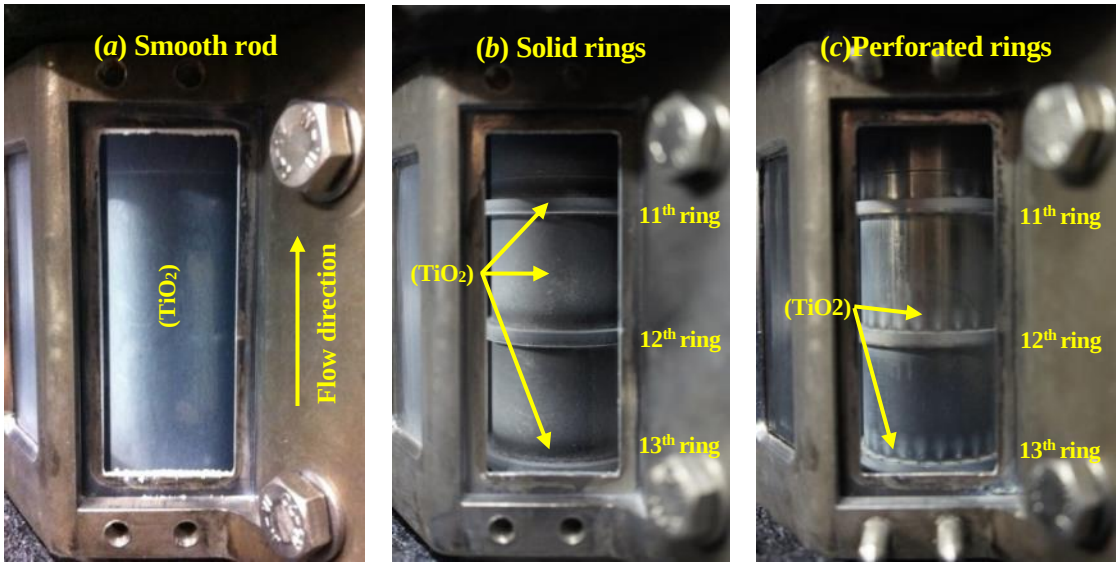

Figure 5.22: Deposition of the TiO_2 particles for (*a*) smooth, (*b*) solid rings and (*c*) perforated ring structures after an eight hours measurement campaign. Constant particle feed of 2310 mg/h.

6. Summary and conclusions

The specific design limitations of innovative gas cooling systems such as the Gen-IV GFR, has led to an increased effort to investigate the heat transfer enhancement between the coolant gas and the fuel rod element. A suitable option is to increase the heat transfer area by means of artificial surface structures placed directly onto the cladding wall of the fuel rod elements, increasing the fluid flow mixing close to the heated wall, thereby increasing the solid-gas heat transfer transport. However, this will at the same time produce an increase of the pressure losses, thereby still representing an optimization problem. This optimization is considered to be a critical design issue for the operational safety performance and behavior of GFR. Furthermore, since both values and their uncertainty have to be precisely known; more detailed experimental investigation is needed.

Therefore, an experimental facility was designed an erected at the INR-KIT. The experimental facility consisted in an annular hexagonal cross-sectional flow channel, with an electrically heated rod element (smooth or structured) placed concentrically in the test section, designed to simulate the flow area of a fuel rod element found in a Gen-IV GFR. The present work has revealed some well-known and some not-well-known insights on convective heat transfer enhancement, frictional losses for smooth and artificially structured channels. Furthermore, the study has provided detailed understanding of the turbulent convective heat transfer augmentation mechanism, capturing the time-averaged axial velocity components and turbulent flow structures with a high spatial resolution across the flow channel. Additionally, optimization between the heat transfer efficiency and the pressure losses in artificially structured channels has been demonstrated by the implementation of modified surface structures in form of perforated rings.

The experimental results are discussed in two parts. In the first part, evaluation and comparison of the experimental characterizing the total loss coefficients, friction factor $f_{D,s}$, heat transfer enhancement coefficients $Nu_{i,s}$ and dimensionless velocity distribution $u^+(y^+)$ for the smooth rod channel are presented. The experimental results are found to be in a very good agreement according to the analytical predictions for nearly all studied cases. Based on these results, the feasibility of the experimental setup, as well as the used methodology for the evaluation of the experimental data is demonstrated.

The second part of the experimental results chapter is devoted to the evaluation and discussion of the structured rod channels experiments. For these experiments, two different types of metallic ring structures (solid *G1* and perforated *G2* rings) with a squared cross-section have been used. The artificial structures are fixed and placed periodically along the heated section with a roughness height ratio $e/D_h = 0.084$, a roughness pitch-to-high ratio $P/e = 10$ and an angle of attack α of 90° degrees with respect to streamwise direction flow. The experimental tests have been conducted at a similar Reynolds number range of $4000 \leq Re_i \leq 70000$ and heating rate $q_i^+ = 0.0015 – 0.003$ as for the smooth channel. The artificial structuring of the cladding results in an increase of the pressure losses, compared to the smooth channel. The pressure losses for both investigated structured rod

channels in terms of the Darcy friction factor f_D are found to be dependent on both Reynolds number and the surface structure type. The friction factors decrease as Reynolds number increases, reaching both nearly a constant value distribution beyond a Reynolds number $Re_i \geq 40000$. The friction factor values for the structured rod experiments are found to be about 3.2 – 5.9 and 2.9 – 4.3 times higher for the solid and perforated ring structures compared to the smooth channel cases. Furthermore, the optimized design of the perforated ring has been found to generate considerably lower frictional losses, about 37% with respect to the solid ring cases. The heating of the test section results in a slight increase of the friction factor values for the studied cases. The variation between the heated and unheated cases for both structured rod channels is about +18.5%. This increase is produced by the variation of the fluid density and viscosity, mainly caused by the temperature variation between inlet and the heated test section. Nevertheless, this effect is neglected by using the derived local bulk gas temperatures $T_{g,15}$ and local pressures $p_{1'}$ at the test section. The results characterizing the friction factor are compared to the reported by Saini et al., 2002 and Rashkovan et al., 2010. The predicted friction factors by both correlations overestimate the experimental data, for the investigated Reynolds numbers. Although, the variation of the predicted values is found to be larger for lower Reynolds numbers $Re_i \leq 10000$, the obtained values at higher Reynolds numbers are in a fair agreement within the reported correlation deviations.

The dimensionless axial temperature distribution for both structured channels cases exhibit significantly lower temperature distribution values, about ~1.9 – 2.1 times lower compared to the smooth channel cases. Another important fact is that due to the increase of the heat flux densities by a factor of two the cladding temperatures levels do not exceed those of the smooth rod channel, conducted at a much lower heating rate $q_i^+ = 0.0015$. Based on these results, it can be assumed that working at higher heat fluxes without exceeding current cladding temperature could be accomplished.

Higher heat transfer enhancement coefficients in terms of Nu_i are attained for both structured rod channels, compared to the smooth channel. The heat transfer coefficient for the solid ring structures resulted in an improvement ratio of 2.3 – 4.8 times higher. However, the highest heat transfer enhancement levels are achieved using the perforated ring structures, showing a heat transfer enhancement of 2.5 – 5.1 higher than the smooth channel. The experimental data for the Nusselt number results are compared against reported correlations by Webb & Eckert, Kader & Yaglom. The experimental data are found to be in acceptable agreement for $Re_i \leq 30000$, whereas as for Reynolds numbers beyond $Re_i \geq 30000$, a deviation of about 25% is obtained. The discrepancies between the experimental results and the predicted values are attributed to experimental uncertainties, as well as applicability of the correlations for hexagonal channels.

A detailed overview of the axial velocities and turbulence intensity distributions with additional focus on close vicinity of the wall has been conducted. The axial velocity distribution for the solid structured channel is dominated by the separation of the flow at the leading edge, giving rise to the formation of several clockwise recirculation zones developing downstream of the structured wall, as well as a high spanwise transport of the main flow to the center of the flow channel. The recirculation zones have

been related to cause a negative effect on the heat transfer enhancement by leading to the formation of local hot spots, which in some cases could exceed the maximum design temperature of the materials [139]. In contrast to the solid ring structures, the perforated ring structures show that the separation of the flow does not fully take place at the leading edge, but rather a high fraction of the main flow passes through the perforations, emerging in form of a multiple jet-like flow system, avoiding the development of recirculation zones downstream the structures. The maximum axial velocities, as well as the reattachment of the flow are found to be similar for both structured channels. The maximum axial velocity is obtained just upstream the center of the flow channel. The velocity distributions of the perforated ring structures are found to be approximately 12% lower at the outer region of the channel, compared to the solid ring cases. The reattachment of the flow is found to take place at about a pitch-to-height ratio $7.5 \leq P/e \leq 8.0$, which is in excellent agreement to the reported values in the literature. Additionally, velocity measurements at the top of the ring structures confirmed the existence of an oscillating flow recirculation at the top of the ring structures. Similar effects were reported by Rau et al., 1998 [136] and Coletti et al., 2014 [137].

The perforated ring structures produce lower turbulence levels compared to the solid rings. This effect is mostly noticed at the top of the perforated ring structures. At this region, the velocity fluctuation levels are recorded to be 1.6 to 2.5 times lower compared to the solid ring cases. Another difference between the solid and the perforated ring is observed at the centerline of the multiple jet-like flow system. The turbulence intensity distributions are characterized by a local increase of the turbulence levels about 2.1 to 2.4 times higher than those obtained for the smooth and solid ring cases. As the flow develops into the center of the flow channel the velocity fluctuations of both structured channels become independent of the artificial structures, overlapping all the measurement point in a single line within the velocity fluctuations of the smooth rod channel, which is in a good agreement within the *roughness sub-layer* concept.

Finally, a qualitative analysis of the particle deposition onto the smooth and structured rod channels is conducted. For the solid ring structures deposition is observed at the downstream face, caused by the constant impingement of the flow, while second deposition is found to take place where the primary recirculation zone is formed. The perforated ring structures show a very low particle deposition compared to the structured solid ring and smooth channels. The main depositions for the perforated structures are observed in a narrow region of the multiple jet-like flow system. The summary and conclusions section are completed with a breakdown of the pros and cons of the studied cases, considered to be promising candidates for the convective heat transfer enhancement and pressure losses optimization of cooled single rod geometries, similar to those found in GFR fuel rod elements. This overview is presented in Table 6.1.

Table 6.1: Pros and Cons of selected test cases

Surface structure type	**Pro and cons**
Perforated ring structures (G2)	+ Highest heat transfer enhancement of around $Nu_{i,r}/Nu_{i,s}$ =2.5 to 5.1 – High pressure losses f_r/f_s = 2.9 to 4.3, (**but** 37% lower than G1) + Highest thermal performance η = 1.6 to 3.3 + Higher turbulence in the vicinity of the wall + Lower particle deposition on the cladding wall + Higher thermal loads are possible without exceeding T_w smooth rod channel – Higher manufacturing costs
Solid ring structures (G1)	+ High heat transfer enhancement of around $Nu_{i,r}/Nu_{i,s}$ =2.3 to 4.8 − Higher pressure losses f_r/f_s = 3.2 to 5.9 − Increased thermal performance η = 1.3 to 2.8 (compared to smooth channel G0). + High turbulence in the vicinity of the wall − Higher particle deposition on the cladding wall + Lower manufacturing costs

References

[1] Simonis,V., Poskas,P and Ragaisis,V., "Enhancement of heat transfer and hydraulic drag in gas-cooled helical channels with artificial roughness on convex wall," *Nuclear Engineering and Design Volume 245,* pp. 153 - 160, April 2012.

[2] Generation IV International Forum (GIF), "A Technology Roadmap for Generation IV Nuclear Energy Systems," Gen IV International Forum, 2002.

[3] Rooijen,W.F.G, "Gas-Cooled Fast Reactor: A Historical Overview and Future Outlook," *Science and Technology of Nuclear Installations,* pp. 1-11, April 2009.

[4] Generation IV International Forum (GIF) , "A Technology Roadmap for Generation IV Nuclear Energy Systems," Generation IV International Forum, 2012.

[5] Jimenez,J., "Turbulent Flows Rough Walls," *Annual Review of Fluid Mechanics, Vol. 36,* pp. 173 - 196, Januar 2004.

[6] Pope,S., Turbulent Flows, Cambridge University Press, 2000.

[7] Reynolds,O., "On the dynamical theory of incomprensible viscous flows and the determination of the criterion.," *Proceedings: Mathematical and Physical Sciences , Vol. 451, No. 1941,* pp. 5 - 47, 1955.

[8] Eswaran,B and Biswas,G., Turbulent Flows: Fundamentals, Experiments and Modeling, CRC Press, 2002.

[9] Tachie,M., Open channel turbulent boundary layers and wall jets on smooth and rough surfaces,PhD thesis, Department of Mechanical Engineering, University of Saskatchewan, Canada, 2001.

[10] Durst,F., Melling,A. and Whitelaw.J., Principles and practice of laser-Doppler anemometry 2nd Edition, Published by Academic Press, 1981.

[11] Shropshire,E.D and Herring,S.J., "Fuel-Cycle and Nuclear Material Disposition Issues Associated with High-Temperature Gas Reactors," *Americas Nuclear Energy Symposium (ANES 2004),Volume 36, Miami, FL (United States),* pp. 1 - 8, October 2004.

[12] Poette,C., Malo,J., Brun-Magaud,V., Morin.F., Dor,I., Mathieu,B., Duhamel,H., Stainsby,R., Mikityuk,K., Gakkai,N, "GFR Demonstrator ALLEGRO design status," *International Congress, Advances in nuclear power plants; (ICAPP 2009),* pp. 1 - 10, 2009.

[13] Stainsby,R., Peers,K., Mitchel,C., Poette,C., Mikityuk,K., Somers,J, "Gas Cooled Fast Reactor Research and Development in the European Union," *Science and Technology of Nuclear Installations,Project Report,* pp. 1 - 7, 14 October 2009.

[14] Bělovský,L., Molnár,J., Gadó,J. and Hatala,B., "Current Status of the Gas Fast Reactor Demonstrator ALLEGRO," *21 St. International Conference Nuclear Energy for New Europe LJUBLJANA,* p. September, 2012.

[15] Arbeiter,F., Krüßmann,R., Gomez,R., Jianu,A., Hering.W. and Aberle.J, "Definition of the L-STAR/SL benchmak activities, Internal Report No.THINS Del. 1.1.03 Rev.1," Karlsruhe

Institute for Technology, Germany, 2012.

[16] Kakac,S., Bhatti,M.S and Shah,R.K., Turbulent and transition convective heat transfer in ducts. Handbook of Single-phase Convective Heat Transfer, New York: John Wiley, 1987.

[17] Arbeiter,F., Untersuchungen von Kühlgasströmungen bei Transitionellen Reynoldszahlen im Einlaufbereich von Minikanälen, Karlsruhe, Germany: Karlsruhe Intitute of Technology, 2009.

[18] Bergles,A., Techniques to augment heat transfer, New York: McaGraw-Hill, 1985.

[19] Dewan,A.,Mahanta,P and Raju,K., "Review of passive heat transfer augmentation techniques," *Proceedings of Institute of Mechanical Engineers (I MECH E) Part A Journal of Power and Energy, 218(7),* pp. 509 - 527, 2004.

[20] Ashrae, Handbook Fundamentals, Atlanta, GA.: American Society of Heating, Refrigeration and Air-Conditioning Engineers, 1997.

[21] Bredberg,J., Turbulence Modelling for Internal Cooling of Gas-Turbine Blades, Dissertation, Göteborg, Sweden : Chalmers University of Technology, 2002.

[22] Webb,R., Eckert,E. and Goldstein,R., "Heat transfer and friction in tubes with repeated-rib roughness," *International Journal of Heat Mass Transfer, Vol.14,* pp. 601 - 617, 1971.

[23] Shamloo,H. and Pirzadeh,B., "Analysis of roughness density and flow submergence effects on turbulence flow characteristics in open channels using a large eddy simulation," *Applied Mathematical Modelling, Volume 39, Issues 3–4,* pp. 1074 -1086, February 2015.

[24] Prandtl,L., "Über Flüssigkeitsbewegung bei sehr kleiner Reibung.," *Verh. III.Intern. Math. Kongr., Heidelberg,* pp. 484 - 491, 1904.

[25] Douglas,J.F., Gasiorek,J.M. and Swaffield,J.A, Fluid Mechanics, Second Ed., Singapore: Longman Singapore Publishers Pty Ltd, 1986.

[26] Schlichting,H., Boundary-Layer Theory 7th Edition, McGraw-Hill, 1979.

[27] Granger.A, Fluid Mechanics, Harcourt College Publishers, 1985.

[28] Ayub.A and Lemckert.J., "A traversing system to measure bottom boundary layer hydraulic properties," *Estuarine, Coastal and Shelf Science, Volume 83, Issue 4,* pp. 425 - 433, August 2009.

[29] Efros,V, "Structure of turbulent boundary layer over a 2D roughness," The Norwegian University of Science and Technology, Trondheim, Norway, 2011.

[30] Coles,D., "The turbulent boundary layer in a compressible fluid," *Technical report, Rand. Rep. R403-PR ARC 24473,* pp. Appendix A: a manual of experimental practice for low-speed-flows, 1962.

[31] Clauser,F., "The turbulent boundary layer," *Advances in Applied Mechanics 4,* pp. 1 - 54, 1954.

[32] Efros,V., "Structure of turbulent boundary layer over a 2-D roughness," Norwegian University of Science and Technology, Trondheim, 2011.

[33] Achie,M., Balachandar,R. and Bergstrom,D., "Rough Wall Turbulent Boundary Layers in Shallow Open Channel Flow," *Journal of Fluids Engineering, Volume 122, Issue 3,* pp. 533-541, February 2000.

[34] Nikuradse,J., "Laws for flow in rough pipes," *VDI Forschungsheft,* p. 361, 1933.

[35] Raupach,M.R, Antonia,R.A. and Rajagopalan,S., "Rough-Wall Turbulent Boundary Layers," *Applied Mechanics Reviews, Volume 44, Issue 1,* pp. 1 - 25, January 1991.

[36] Keirsbulck,L., Labraga,L. ,Mazouz,A. and Tournier,C., "Surface roughness effects on turbulent boundary layer structures," *Journal of Fluids Engineering, Volume 124, Issue 1,* pp. 124 - 135, 15 October 2002.

[37] Clauser,F., "Turbulent boundary layers in adverse pressure gradients," *Journal of Aerospace Science and Technologies 21,* pp. 91 - 109, 1954.

[38] Darcy,H., "Recherches Experimentales Relatives au Mouvement de l'eau dans les tuyax," *Memoires a l'Academie d. Sciences de l'Institute imperial de France,Bd 15,* p. 141, 1858.

[39] Saleh,O., "Fully developed turbulent smooth and rough channel and pipe flows, PhD. Thesis," Technischen Fakulät der Universität Erlangen - Nürnberg, Erlangen, 2005.

[40] Fanning,J.T., "A Practical Treatise on Hydraulic and Water Supply Engineering," Van Nostrand, New York, 1987.

[41] Stanton,T., "The mechanical viscosity of," *Proc. Roy. Soc. London A, Vol. 85,*, p. 366, 1911.

[42] Schiller,L., "Über den Strömungswiderstand von Rohren verschiedenen Querschnitts und Rauhigkeitsgrades," *ZAMM - Journal of Applied Mathematics and Mechanics, Zeitschrift für Angewandte Mathematik und Mechanik,* no. 1 - 13, pp. Volume 3, Issue 1, 1923.

[43] Yarin,L.P., The Pi-Theorem: Applications to Fluid Mechanics and Heat and Mass Transfer, Volume1 of Experimental Fluid Mechanics, Springer, 2012.

[44] Karwa,R., Heat and Mass Transfer, Singapore: Springer , 2017.

[45] Schlichting,H., "Experimental investigation of the problem of surface roughness," *Ing.Archiv, Vol.7, No1, NACA TM 832,* pp. 1 - 34, 1936.

[46] Colebrook,C and White,C., "Experiments with Fluid Friction in Roughened Pipes," *Proceedings of the Royal Society of London. Series A, Mathematical and Physical Sciences,* p. 367–381, 1937.

[47] Cope,W., "The friction and heat-transmission coefficients of rough pipes," *Proc. Instn Mech. Engineers 145 (4th. ed.),* p. 99, 1941.

[48] Sams,E.W., "Experimental investigation of average heat-transfer and friction coefficients for air flowing in circular tubes having square-thread-type roughness," *NASA Technical Report,* pp. 1 - 44, Juny 1952.

[49] Morris,H.M., "Flow in rough conduits," *American Society of Civil Engineers, Vol. 120, Issue 1,* pp. 373 - 398, 1955.

[50] Perry,A and Hoffmann,P., "The development of turbulent thermal layers on flat plates," *International Journal of Heat and Mass Transfer, Vol. 22, Issue 1,* pp. 39 - 46, January 1979.

[51] Nunner,W., "Wärmeübergang und Druckabfall in rauhen Rohren," *VDI Forschungsheft 455,* 1958.

[52] Dipprey,D. and Sabersky,R., "Heat and momentum transfer in smooth and rough tubes at various Prandtl numbers," *International Jourbal of Heat and Mass Transfer, Vol. 6, Issue 4,* pp. 239 - 353, 1963.

[53] Shirai,K., "Investigation and Application of Laser Doppler Velocity Profile Sensors toward Measurements of Turbulent Shear Flows, P.hD Thesis," Fakultät Elektronik und informationtechnik der Technischen Universität Dresden, Dresden, germany, 2009.

[54] Webb,R., "Application of rough surfaces to heat exchanger design," *International Journal of Heat and Mass Transfer, Vol. 15, Issue 9,* pp. 1647 - 1658, September 1972.

[55] Lewis,M.J., "An elementary analysis for predicting the momentum and heat transfer characteristics of a hydraulically rough surface.," *Journal of Heat Transfer, Vol. 97, Issue 2* , pp. 249 - 254, 1975.

[56] Williams,F., Pirie,M. and Warburton.C., "Heat Transfer from Surfaces Roughened by Ribs in Augmentation of Convective Heat Transfer," *Bergles A., Webb R.L., ASME Symposium Volume: Augmentation of Convective Heat and Mass Transfer,* 1970.

[57] Han,J.C., Glicksman,L.R. and Rohsenow,W.M., "An investigation of Heat transfer and Friction For Rib Roughened Surfaces," *International Journal of Heat and Mass Transfer, Vol.21, Issue 8,* pp. 1143 - 1156, August 1978.

[58] Webb,R. and Scott,M, "A parametric analysis of the performance of internally finned tubes for heat exchanger application," *Journal of Heat Transfer, Vol. 102, Issue 1,* pp. 38 - 43, July 1980.

[59] Sparrow,E. and Tao,W., "Enhanced heat transfer in a flat rectangular duct with streamwise-periodic disturbances at one principal wall," *Journal of Heat Transfer, Vol. 105, Issue 4,* pp. 851 - 861, November 1983.

[60] Vilemas,J. and Simonis,V., "Heat transfer and friction of rough ducts carrying gas flow with variable physical properties," *International Journal of Heat and Mass Transfer,Vol. 28, Issue 1,* pp. 59 - 68, January 1985.

[61] Hijikata,K and Mori,Y., "Fundamental study of heat transfer augmentation of tube inside surface by cascade smooth surface-turbulence promoters," *Wärme und Stoffübertragung, Vol. 21, Issue 2,* pp. 115 - 124, March 1987.

[62] Liou,T. and Hwang,J., "Effects of ridge shapes on turbulent heat transfer and friction factor in rectangular channel," *Journal of Heat Transfer, Vol. 114, Issue 1,* pp. 56 - 64, February 1992.

[63] Taslim,M.E. and Wadsworth,C.M., "An Experimental Investigation of the Rib Surface-Averaged Heat Transfer Coefficient in a Rib-Roughened Square Passage," *Journal of Turbomachinery, Vol. 119, Issue 2,* pp. 381 - 390, April 1997.

[64] Rau,G., Çakan,M.,Moeller,D. and Arts,T., "The effect of periodic ribs on the local aerodynamic and heat transfer performance of a straight cooling channel," *Journal of Turbomachinery, Vol.*

120, Issue 2, pp. 368 - 375, April 1998.

[65] Leonardi, S., Mostarda,P., Orlandi,P., and Antonia.R., "Structure of turbulent channel flow with square bars on one wall," *International Journal of Heat and Fluid Flow,Vol. 25, Issue 3,* pp. 384 - 392, June 2003.

[66] Aharwal,K., Gandhi,B. and Sain,J., "Experimental investigation on heat-transfer enhancement due to a gap in an inclined continuous rib arrangement in a rectangular duct of solar air heater," *Renewable Energy, Vol. 33, Issue 4,* pp. 585 - 596, April 2008.

[67] Wilkie,D., "Forced convection heat transfer from surfaces roughened by transverse ribs," in *Third International Heat Transfer Conf. AIChE, Vol. 1*, 1966.

[68] Williams,F and Watts,I., "The development of rough surfaces with improved heat transfer performance and a study of the mechanisms involved," *Proceedings Fourth International Heat Transfer Conference Paris,* 1970.

[69] Rabas.T and Arman.B., „Influence of Prandtl number and effects of disruption shape on the performance of enhanced tubes with the separation and reattachment mechanism," Energy Systems Division, Argonne National Laboratory, 9700 South Cass Avenue, Argonne, Illinois 60439, 1992.

[70] Ichimiy,K., "Effects of Several Roughness Elements on an Insulated Wall for Heat Transfer From the Opposite Smooth Heated Surface in a Parallel Plate Duct," *Journal of Heat Transfer, Vol. 109, Issue 1,* pp. 68 - 73, February 1987.

[71] Krogstad,P. and Antonia,R., "Surface roughness effects in turbulent boundary layers," *Experiments in Fluids,* pp. 450 - 460, October 1999.

[72] Fujita,H., Hirota, M., Yokosawa, H., Hasegawa, M. and Gotoh, I., "Fully developed turbulent flows through rectangular ducts with one roughened wall," *JSME International Journal, Series II: Fluids Engineering, Heat Transfer, Power, Combustion, Thermophysical Properties,* pp. 692 - 701, 1990.

[73] Liou,T.M. and Kao,C.F., "Symmetric and Asymmetric Turbulent Flows in a Rectangular Duct with a Pair of Ribs," *Journal of Fluids Engineering,Vol.110, Issue 4,* pp. 373 - 379, December 1988.

[74] Bates.C.J, and Martin.S.R., "Small-probe-volume laser Doppler anemometry measurements of turbulent flow near the wall of a rib-roughened channel," *Flow Measurement and Instrumentation, Vol. 3, Issue 2,* pp. 81 - 88, 1992.

[75] Bhagoriaa,J.L., Saini,J.S., Solanki,S.C., „Heat transfer coefficient and friction factor correlations for rectangular solar air heater duct having transverse wedge shaped rib roughness on the absorber plate," *Renewable Energy, Vol. 25, Issue 3,* p. 341 – 369, March 2002.

[76] IEE, "Nuclear Reactor Types," The Institution of Electrical Engineers, London, 2005.

[77] Hudina,M. and Noetlinger,H., "Struktur der turbulenten Stömungen in Ringkanälen mit aussen glatten und innen künstlich aufgerauhten Wänden," Swiss Federal Institute for Reactor Research (EIR) , Switzerland, 1983.

[78] Hudina, M., "Rough Surface Heat Transfer and Presure Drop, EIR Bericht Nr.474," EIR,

Würenlingen, Switzerland. , 1962.

[79] Hudina,M., "Investigantions of different artificially roughened surfaces in annular channels, ROHAN experiment-final report, EIR-TM-IN-694," EIR (PSI), Würenlingen, Switzerland., 1977.

[80] Epiney,A., Mikityuk,k. and Chawla,R., "TRACE qualification via analysis of the EIR gas-loop experiments with smooth rods," *Annals of Nuclear Energy, Vol. 37, Issue 6,* pp. 875 - 887, June 2010.

[81] Hudina,H., "Roughening characteristics and choices for the gas-cooled fast breeder reactor," *Nuclear Engineering and Design,Vol. 40, Issue 1,* pp. 133 - 141, January 1977.

[82] Sevatteri,C., "Friction Factors of a Cluster of 19 Rough Rods, KFK 1588," Karlsruhe Institut of Technology, Karlsruhe, Germany., 1972.

[83] Dalle Donne,M., "Wärmeübergang von rauhen Oberflächen, KFK 2397," Karlsruhe Institute of Technology, Karlsruhe, Germany., 1977.

[84] Dalle Donne,M and Meyer,L., "Turbulent convective Heat transfer from rough surfaces with two dimensional rectangular ribs," *International Journal of Heat Mass Transfer, Vol.20, Issue 6,* , pp. 582 - 620, June 1977.

[85] Dalle Donne,M. and Meyer,L., "Convective heat transfer from rough surfaces with two-dimensional ribs transitional and laminar flow, KfK 2566," Karlsruhe Institut of Technology, Karlsruhe, Germany, 1978.

[86] Dalle Donne,M., "Heat transfer in Gas-cooled fast reactors," *Annals of Nuclear Energy, Vol.5, Issues 8–10,* , pp. 439 - 453, 1978.

[87] Dalle Donne,M and Meyer,L., "Heat transfer and friction coefficients for air flow in a smooth annulus, KfK 2831," Karlsruhe Institute of Technology, Karlsruhe, Germany., 1979.

[88] Dalle Donne,M.,Hudina,M.,Haggenberger,M.,Meyer,L. and Rehme,K., "IER, KfK joint heat transfer experiment on single rod roughened with trapezoidal rounded ribs and cooled vy various gases, EIR Bericht Nr.349," Karlsruhe Institute of Technology, Karlsruhe, Germany, 1978.

[89] Meyer,L and Vogel,L., "The Velocity distribution and pressure loss at artificial roughnesses with sharp and rounded edges, KfK 2885," Karlsruhe Institute of Technology, Karlsruhe, Germany., 1979.

[90] Meyer,L., "Turbulent flow in a plane channel having one or two rough walls," *International Journal of Heat and Mass Transfer,Vol. 23, Issue 5,* pp. 591 - 608, May 1980.

[91] Febech,H., Heat transfer and fluid flow in nuclear systems, Pergamon Press Inc., 1981.

[92] Meyer,L. and Neu,W., "Heat transfer and pressure drop at single pins with three-dimensional roughnesses," Karlsruhe Institute of Technology, Karlsruhe, Germany., 1981.

[93] Firth,R.J and Meyer,L., „A comparison of the heat transfer and friction factor performance of four different types of artificially roughened surface,“ *International Journal of Heat and Mass Transfer,Vol. 26, Issue 2,* pp. 175 - 183, February 1983.

[94] European Commission, "Euratom FP7 Research & training projects," http://ec.europa.eu/research/research-eu, 2010.

[95] GoFastR, "FP7 European Gas Cooled Fast Reactor (GoFastR)final report GoFastR-DEL-5-2," AMEC, 2013.

[96] GoFastR, "Seventh Framework Programme EURATOM, FP7-Fission-2009, European Gas Cooled Reactor (GoFastR), Annex I," European Commission, United Kingdom, 2010.

[97] EURATOM, „Seventh Framework Programme EURATOM, Grant Agreement THINS "Thermal-Hydraulics of Innovative Nuclear Systems", Grant agreement No. 249337, Annex I," European Commission, 2010.

[98] Cheng,X., Batta,A., Bandini,G., Roelofs,F., Van Tichelen,K., Gerschenfeld,A., Prasser,M., Papukchiev,U., Hampel,U., Ma,W.M, „European activities on crosscutting thermal-hydraulic phenomena for innovative nuclear systems," *Nuclear Engineering and Design, Vol. 290,* pp. 2 - 12, August 2015.

[99] FP7 EURATOM, "Thermal-Hydraulics of Innovative Nuclear Systems (THINS)," 18 11 2011. [Online]. Available: https://cordis.europa.eu/project/rcn/94432_en.html. [Accessed 11 12 2017].

[100] Jianu,A., "L-Star Water Cooling System Handbook, Internal Report No. N/A.," Karlsruhe Instutute of Technology, Karlsruhe, Germany., 2010.

[101] Arbeiter,F., Aberle,J., Heupel,T., Gomez,R., Hering,W., Jianu,A., Scherrer,S., "Definition of the L-STAR/SL Benschmark Activities, Internal report INR 34/12– NUKLEAR 3450, THINS Del. 1.1.03," Karlsruhe Institute of Technology (KIT), Karlsruhe, Germany., 2013.

[102] Webb,R., Eckert,E. and Goldstein,R., "Heat transfer and friction in tubes with repeated-rib roughness," *International Journal of Heat Mass Transfer, Vol.14, Issue 4,* pp. 601 - 617, April 1971.

[103] Wilkie.D., „Criteria for choice of surface form for gas cooled reactors," *Nuclear Engineering Internstional 16,* pp. 215 - 217, 1971.

[104] Liou,T. and Hwang,J., "Effects of permeble ribs on heat transfer and friction factor in a rectangular channel," *International Gas Turbine and Aeroengine Congress and Exposition,Vol. 3B,* pp. 1 - 7, May 1993.

[105] Mie,G., „Beiträge zur Optik trüber Medien, speziell kolloidaler Metallösungen," *Annalesn der Physik,* Bd. Volume 330, Nr. Issue 3, p. 377 – 445.

[106] Blondel,D., Handbook of Combustion, Volume 5, Wiley-VCH , 2010.

[107] DANTEC Dynamics, "Integrated solutions in Laser Doppler Anemometry," DANTEC Dynamics, 2010. [Online]. Available: https://www.dantecdynamics.com/docs/products-and-services/general-literature/Laser_Doppler_Anemometry_318.pdf. [Accessed 22 July 2016].

[108] Zhang,Z., LDA Application Methods: Laser Doppler Anemometry for Fluid Dynamics, Springer, 2010.

[109] Adrian,R.J., Laser Anemometry In Fluid Mechanics , Second Edition, Taylor & Francis, 1996.

[110] DANTEC Dynamics, "FiberFlow Optics for LDA and PDA," DANTEC Dynamics, 07 02 2007. [Online]. Available: https://www.dantecdynamics.com/docs/products-and-services/fluid-mechanics/lda/PI_FiberFlow_optics_for_LDA_and_PDA_245_v11.pdf. [Accessed 10 January 2017].

[111] Nikon Imaging, "AF-S NIKKOR 85 mm, Use's Manuals," Nikon Imaging, 22 03 2014. [Online]. Available: https://downloadcenter.nikonimglib.com/en/products/303/AF-S_NIKKOR_85mm_f_14G.html. [Accessed 11 January 2017].

[112] DANTEC Dynamics, BSA Flow Software v5 User Manual, DANTEC Dynamics, 2014.

[113] Rohr,C.T., "Investigation on laser light scattering effects relevant for near wall Laser Doppler Anemometer measurements," Karlsruhe Institute of Technology, Karlsruhe,Germany., 2009.

[114] LINOS photonics GmbH, "LINOS Positioning systems," LINOS photonics GmbH, 07 02 2013. [Online]. Available: http://www.qioptiq.com/. [Accessed 05 December 2016].

[115] Arbeiter,F., "Einsatztest des Palas RGB 100 Bürsten-Feststoffdispergierer am L-STAR/Small Loop - Internal Memo," Karlsruhe Institute of Technology, Karlsruhe, Germany., 2008.

[116] Hering,W., Arbeiter,F., Jinau,A., Sengpiel,W., Stratmanns,E. and Zhuang,J, "The L-star project, a new approach to a sophisticated database for heat transfer and pressure loss in gas cooled systems," in *Annual meeting on nuclear technology*, Hamburg, Germany., 2008.

[117] Bergman,T.L., Lavine,A.S., Incropera,F.P. and DeWitt,D.P., Fundamentals of heat and mass transfer, 7th. Edition Incropera, John Wiley & Sons, Inc, 2011.

[118] Rohsenow,W.M.,Hartnet,J.P. and Cho,Y.I., Handbook of heat transfer 3rd. Edition, The McGraw-Hill, 1998.

[119] Webb,R.L., "Performance evaluation criteria for use of enhanced heat transfer surfaces in heat exchanger design," *International Journal of Heat Mass Transfer, Vol. 24, Issue 4,*, pp. 715 - 726, April 1981.

[120] VDI, VDI Heat Atlas, Springer Berlin Heidelberg, 2010.

[121] Arbeiter,F., "Experimental and numerical investigations on minichannel cooling gas thermal-hydraulics," *Proceedings of the ICONE-15. The 15th international conference on nuclear engineering, Nagoya, Japan,* April 2007.

[122] McLaughlin,D.K and Tiederman,W.G., "Biasing correction for individual realization of laser anemometer measurements in turbulent flows," *Physics of Fluids Vol. 16,* pp. 2082 - 2088, 1973.

[123] Jae Hwa,L., Hyung Jin,S., Seung-Hyung,L and Kyoungyoun.Kim, "Structure of the turbulent boundary layer over a rod-roughened wall," *International Journal of Heat and Fluid Flow, Vol. 30, Issue 6,* pp. 1087 - 1098, December 2009.

[124] Chen,H.N., "An Explicit Equation for Friction Factor in Pipe," *Ind. Eng. Chemical fundaments,* pp. 296 - 297, 1979.

[125] Churchill,S.W., "Friction factor equation spansall fluid flow regimes," *Chemical Engineering, Vol.11* , pp. 91 - 92, 1977.

[126] Kline,S.J and McClintock,F.A, "Describing uncertainty in single-sample experiments," *Mechanical Engineering, Vol. 75, No. 1,* pp. 3 - 8, 1953.

[127] Petukhov,B.S and Kirillov,V.V., „The problem of heat exchange in turbulent flow of liquids in tubes (in Russian), Teploenergetika," *Teploenergetika, Vol.4, No.4-5,* pp. 63 - 68, 1958.

[128] Gnielinski,V., "Berechnung des Druckverlustes in glatten konzentrischen Ringspalten bei ausgebildeter laminarer und turbulenter isothermer Strömung," *Chemie Ingenieur Technik, Volume 79, Issue 1 - 2,* p. 91 – 95, 1976.

[129] Ebadian,M.A and Dong,Z.F., Forced Convection, Internal Flow in Ducts, Handbook of Heat Transfer, New York: McGraw-Hill, 1998.

[130] Dittus,F.W and Boelter,L.M.K., "Heat transfer and automobil radiators of the tubular type," *Publications on engineering, Vol.2, University of Berkely,* pp. 443 - 461, 1930.

[131] Karmare,S. and Tikeka,A., "Heat transfer and friction factor correlation for artificiallyroughened duct with metal grit ribs," *International Journal of Heat and Mass Transfer, Vol. 50, Issues 21–22,* p. 4342 – 4351, October 2007.

[132] Pope,S.B., Turbulent Flows, Cambridge University Press, 2000.

[133] von Kármán,T., "The analogy between fluid friction and heat transfer," *Journal of Heat Transfer, Vol. 61,* pp. 131 - 139, 1939.

[134] Prandtl.L., "Eine Beziehung zwischen Wärmetauscher und Strömungswiderstand der Flüssigkeit," *Z.Physik, Vol.11,* pp. 1072 - 1078, 1910.

[135] Reichardt,H., "Vollständige Darstellung der turbulenten Geschwindigkeitsverteilung in glatten Leitungen," *Journal of Applied Mathematics and Mechanics, Vol.31, Issue 7,* pp. 208 - 219, 1951.

[136] Rau,G., Çakan,M., Moeller,D. and Arts,T., "The Effect of Periodic Ribs on the Local Aerodynamic and Heat Transfer Performance of a Straight Cooling Channel," *Journal of Turbomachiner, Vol. 120, Issue 2,* pp. 368 - 375, April 1998.

[137] Coletti,F.Lo Jacono.D., Cresci,I and Arts,T., "Turbulent flow in rib-roughened channel under the effect of Coriolis and rotational buoyancy forces," *Physics of Fluids, Volume 26, Issue 4,* 2014.

[138] Nicholas,D., Pavlos,P., and Karen,A., "Developing and fully developed turbulent flow in ribbed channels," *Experiments in Fluids, Vol. 50, Issue 5,* pp. 1357 - 1371, May 2011.

[139] Casarsa,L. and Arts,T., "Experimental Investigation of the Aerothermal Performance of a High Blockage Rib-Roughened Cooling Channel," *Journal of Turbomachinery, Volume 127, Issue 3,* pp. 580 - 588, 2005.

[140] Bhaganagar,K., Kim.J and Coleman,G., "Effect of Roughness on Wall-Bounded Turbulence," *Flow, Turbulence and Combustion, Vol. 72, Issue 2-4,* pp. 463 - 492, July 2004.

[141] Lee,Seung-Hyung and Sung,Hyung Jin., "Direct numerical simulation of the turbulent boundary layer over a rod-roughened wall," *Journal of Fluid Mechanics, Vol. 584,* pp. 125 - 146, August 2007.

[142] Mills,F.A., Basic Heat and Mass Transfer (2nd edition), Prentice Hall, 1999.

[143] Cukurel,B and Arts,T., "Local Heat Transfer Dependency on Thermal Boundary Condition in Ribbed Cooling Channel Geometries," *Journal of Heat Transferer, Vol. 135, Issue 10,* pp. 1 -11, January 2013.

[144] Jaurker,A.R, Saini.J.S., and Gandhi.B.K., "Heat transfer and friction characteristics of rectangular solar air heater duct using rib-grooved artificial roughness," *Solar Energy, Vol. 80, Issue 8,* pp. 895 - 907, August 2006.

[145] Rashkovan,A., Aharon,J., and Katz,M., "Optimization of rib-roughened annular gas-coolant channels," *Nuclear Engineering and Desig, Vol. 240, Issue 2,* p. 344 – 351, February 2010.

[146] Peretsa,Y., Sherb.E., and Harari,R., "Characterizing the dynamics of a flexible rod wrapped by transverse repeated ribs subjected to axial flow," *Nuclear Engineering and Design, Vol. 269,* pp. 349 - 359, April 2014.

[147] Meinders,E.R., Van der Meer,T.H., and Hanjalic,K., "Local convective heat transfer from an array of wall-monted cubes," *International Journal of Heat Transfer, Vol 41, Issue 2,* pp. 335 - 346, January 1998.

[148] Carlomagno,G.M and Cardone,G., "Infrared thermography for convective heat transfer measurements," *Experiments in Fluids, Volume 49, Issue 6,* p. 1187–1218, December 2010.

[149] Karmare,S.V., and Tikeka,A., "Heat transfer and friction factor correlation for artificially roughened duct with metal grit ribs," *International Journal of Heat and Mass Transfer, Vol.50,Issues 21–22,* p. 4342 – 4351, October 2007.

[150] Prasad,B.N and Saini,J.S, "Effect of artificial roughness on heat transfer and friction factor in a solar air heater," *Solar Energy,Volume 41, Issue 6,* pp. 555 - 560, 1988.

[151] Kader,B.A., and Yaglom,A.M., "Turbulent heat and mass transfer from a wall with parallel roughness ridges," *International Journal of Heat and Mass Transfer, Vol. 20, Issue 4,* no. 345 - 357, pp. 345 - 357, April 1977.

[152] Boettcher,M., and Gomez,R., "CFD studies of heat and momentum transfer at structured rod surface," in *CFD for Nuclear Reactor Safety Applications CFD4NRS-6*, Cambridge, MA, 2016.

[153] Suikkanen,H., "Application and development of numerical methods for the modelling of innovative gas cooled fission reactors," Lappeenranta University of Technology, Finland, 2014.

[154] Barth,T., Lecrivain,G., Jayaraju,S.T., and Hampel,U., "Particle deposition and resuspension in gas-cooled reactors - Activity overview of the two European research projects THINS and ARCHER," *Nuclear Engineering and Design,* pp. 1 - 8, February 2015.

[155] ABB Automation Products GmbH, "Absolute pressure transmitter261AS, Manual," 2016. [Online]. Available: http://new.abb.com/products/measurement-products/pressure/absolute-pressure-transmitters/261as-absolute-pressure-transmitter. [Accessed 03 July 2014].

[156] ABB Automation Products GmbH, „Differential Data Sheet SS/265DS-EN_06, Model 265DS," 2016. [Online]. Available: http://www.abb.com/product/seitp330/c7ea679b4892545dc1256d20002c94c2.aspx. [Zugriff am 03 July 2014].

[157] German Institute for Standardization (DIN), "DIN EN 60584-2-1994 Thermocouples – Part 2: Tolerances (IEC 60584-2:1982 + A1:1989); German version EN 60584-2," German Institute for Standardization (DIN), 1994.

[158] Endress & Hauser, "Endress und Hauser: Technische Information Proline Promass 80/83 F," Endress & Hauser, 2010. [Online]. Available: https://portal.endress.com/wa001/dla/5000275/1921/000/00/TI101DEN_1009.pdf. [Accessed 20 July 2014].

[159] AEG Power Solutions GmbH, "Operating Instructions,Thyristor Power Controller Thyro-A," AEG Power Solutions GmbH, 2014. [Online]. Available: www.aeg-ups.cz/cz/download/1404042102/?at=1. [Accessed 15 January 2017].

[160] Aberle,J., "L-Star/SL Datenerfassung und Steuerung, Interner Bericht Nr./.," Karlsruhe Institute of Technology (KIT), Karlsruhe, Germany., 2011.

[161] Arbeiter,F., Gomez,R. and Scherrer,S., "Preliminary uncertainty assessment for L-STAR/SL wall friction factor and heat transfer measurement, Internal Memo report No. N.A," Institute for Neutron Physics and Reactor Technology (KIT), Karlsruhe, Germany., 2012.

[162] WIAM Metallinfo, „IMA Materialforschung und Anwendungstechnik GmbH," [Online]. Available: www.wiam.de.

Appendix A. Test section instrumentation and heater rod specifications

Test section instrumentation

Pressure and pressure drop measurements

The pressure losses in the experimental facility are acquired by using five absolute pressure transducers "ABB Model 261AS" (SL-PA-01/05)" located before the test section and after test section outlet, as well as between each main component junction (e.g. before the blower and flowmeter), respectively. The absolute pressure transducers have an accuracy of ±0.15 of full-scale, full scale being 0 – 4000 mbar [155]. The pressure drop along the test sections are measured with two differential pressure transducers "ABB Model 265" (TS-DP-1'2' and TS-DP-45) interconnected with a 6 mm outside diameter stainless-steel tube. The differential transducers have reported accuracy of ±0.04% within a full-scale of 0.05 to 0.5 mbar and 0 to 2000 mbar [156], respectively. The transducers are adjusted with a low-pressure calibration system with an accuracy of ±0.025%. Since the ABB transducers signal output varies linearly with the pressure, two measurement points were sufficient for the basic adjustment.

Temperature measurements

An important factor for the correct determination of the convective heat transfer is the accurate capture of the cladding wall and bulk gas temperatures. The bulk gas temperature at the inlet-and outlet of the test section are obtained with both Pt-100 and type-K (Nickel-Chrome/Nickel) thermocouples manufactured at the KIT workshop. According to DIN EN 60584-2-1994 Type-K thermocouples have a design accuracy of ±1.5 °C for temperature range between –40 °C to 333 °C, and $\pm 0.0075 \times |T|$ for temperatures up to 1200 °C [157].The cladding wall temperatures are obtained by micro type-K thermocouples, with a wire diameter of Ø0.5 mm, along forty-eight different axial position along the heater rod assembly. The thermocouples are attached into grooved mini-channels (with an inner diameter of Ø0.5 mm and a deep of Ø0.8 mm) beneath the cladding with the main intention of not disturbing the fluid flow, see Figure 3.8. The thermocouple output signals are supplied to a multiplex Analog to Digital Converter (ADC) "DT9871U TEMPpoint" directly plugged to the main computer.

Flow meter

The gas filled into the facility is put into circulation with a side channel blower. A Coriolis flow meter "Proline Promass 80F DN50" from Endress+Hauser is used for monitoring the flow rate through the test section. The Coriolis flow meter is design to operate at gas temperatures up to 200 °C, pressure rates up to 40 bars, and a maximum throughput up to 70000 kg/h. The flow meter has a specified accuracy of ±0.35% of measured flow rate, taking into consideration the Zero-point stability offset [158].

Electrical heating power

The heating power at the test section is attained by six high performance heating elements type-HLPT Türk +Hillinger. The heater cartridges can be electrically heated up to a maximum design power of 24kW ±10%, capable to provide a maximum wall temperature of about 750 °C. The electrical power is supplied by a three-phase power unit thyristor controller (type AEG Thyro-3A, 400 V-16 A, type HRL1) suitable for two different operation modes: full-wave cycle principle (TAKT) and phase-control principle (VAR) [159]. Two different measurement transducers are used to regulate the supplied electrical power to heater rod. For the TAKT modus a transformator and measurement transducer from the company Ziegler Müller (type Pdr-MU) are used to regulate low power rates (TS-Pist_Low) between 0 kW – 1.6 kW, within an accuracy ± 0.5 %, whereas for higher power rates (TS-Pist_High) between 1.6 kW – 14 kW a Unipower APM380 transducer from the company Ulrich Buhr is used in VAR modus, with a reported accuracy of 2% of the supplied power. Due to the fact that unfortunately not all information on the heater internal structure could be obtained from the manufacturer, a series of investigations were performed to assure that appropriate modelling data is given in this report. X-Ray inspection and infrared thermal imaging of the surface were conducted.

Specifications of the heater rod

Basic specifications provided by the manufacturing company Türk+Hillinger are given in Table 1A:

Maximum Design Temperature	750 °C
Design Power	24 kW ± 10%
Supply voltage (3 phases AC)	400 V
Leakage current	< 0,5 mA
Cartridge heater shell	CrNi steel, Material no. 1.4541
Resistive wires	NiCr 8020, Material no. 2.4869
Insulator between resistive wires and cartridge heater shell	Magnesium oxide, highly compressed
Heater Rod Axial Length	
Heater cartridge length	2712 mm ±1,5%; at least however ±2 mm
Heated zone	2492 mm, divided in 6 sections
Unheated ends	206 mm top, 14 mm bottom
Heater Rod Cross Section	
Heater Core	n.A.
Cartridge heater patrons (Outer Diameter)	31.7 ± 0,3
Cartridge heater patrons wall thickness	2.5 mm
Cladding (Outside Diameter)	35 mm +0.05
Cladding wall thickness	1.5 mm ± 0,3
Thermocouples	K-type, max. temperature 1372 °C

Additional information received from the company:

- The length of each heater zone is 407 mm.
- The gap between each heater zone is 10 mm.
- There are distance plates of 5 mm thickness between each two heater rods made of the ceramic C230
- The voids are filled by compressed MgO powder

The materials of the ceramic support tube or the ceramic glue are not provided by the manufacturer. Led by the aspect that the thermal expansion coefficient of the ceramic support tube should be matched to the stainless-steel heater shell, a selection of market-available ceramic materials was considered, as shown in Table 2A [101].

Ceramic type	**CTE [µm/m/K]**	**Density [kg/m³]**	**Thermal conductivity (30 – 100°C) [W/m/K]**	**Specific heat capacity (30–1000°C) [J/kg/K]**
C230	8 - 10	1800	1.5 - 2.0	800-900
Compressed MgO powder	n.A.	2000 - 2700	3.0 - 5.0	850 - 1050
ZTA (Al2O3+ZrO2)	9 - 11	4000 - 4100	15	800
PSZ (ZrO2)	10 – 13	5000 – 6000	1.5 – 3.0	400 – 550
C820 (MgO)	11 – 13	2500	6 – 10	850 – 1050
C830 (ZrO)	10 – 12	5000	1.2 – 3.5	400 – 500

Table. 3A: Possible ceramic materials and their thermal properties [101].

To match the total mass of 14.6 kg of the finalized rod (with TCs and compression shell), and assuming MgO with 2500 kg/m³ for the gaps, only the heaviest material PSZ with 6000 kg/m³ for the support tube can make the required mass difference. In reference to the detailed heater radial composition as depicted in Figure 9, values for the thermal conductivity of the individual zones are given in Table 3A [101].

	Reference	**Min**	**Max**
Ceramic glue*	4.0	0.3	5.7
Ceramic support	3.0	1.2	15.0
Central filling	4.0	3.0	5.0

* Catalog data from Polytec PT high temperature ceramic glues

Table. 3A: Thermal conductivities (W/m/K) for the ceramic materials of the L-STAR/SL heater rod [101].

X-Ray inspection

X-Ray radioscopy was applied to gain insight in the radial composition of the heater rod. The inspection was performed by the company "DEKRA Materials Testing" (Karlsruhe) before placing the thermocouples. The result was a negative image on photographic film, which was digitized by photographing the film before a lighting screen with a digital camera. The digital image was treated to enhance the contrasts, to distinguish more clearly the objects of interest with different X-Ray absorption in the structure. A section from one evaluated image is shown in Figure 1A [101].

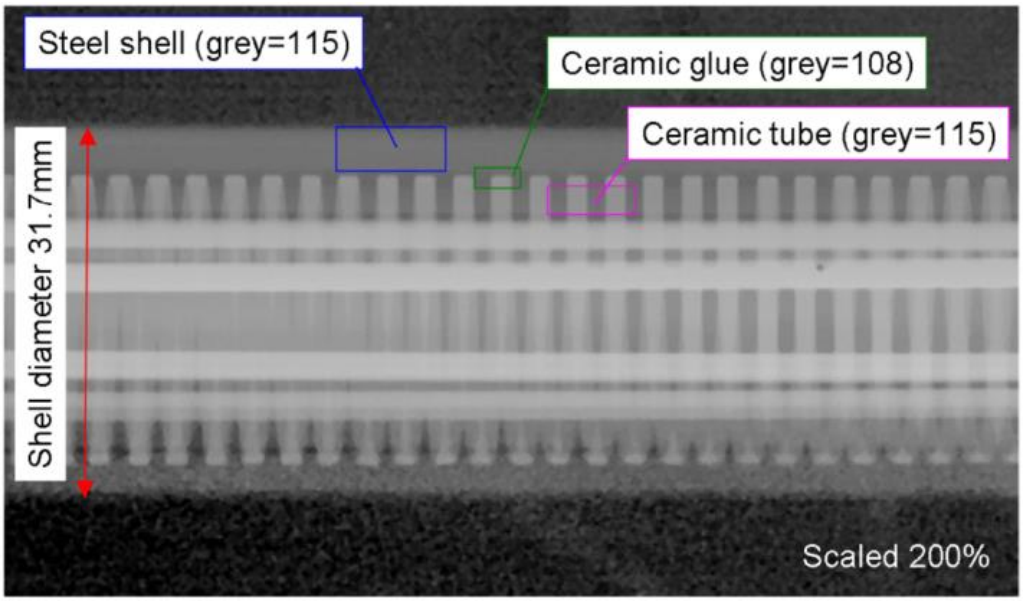

Figure 1A: Image of L-STAR heater rod X-Ray radioscopy, digitally enhanced [101].

Inside the rod, the following objects can be identified: The heater coil, 4 axial wires (current leads to the heater ends) and differently shaded zones, coming from outside: bright (steel), dark (ceramic glue), and bright (ceramic support).

The projection scale was derived from the known outer diameter of 31.7 mm, which corresponds to the grey zone with a width of 185 px (pixels). An uncertainty of ±6 px (3.2%) should be attributed to this value (considering the fuzzy edges), additionally errors due to perspective must be accounted for. Therefore, an uncertainty of ±5% is suggested to apply on the scaling factor. Extra errors apply on each length measurement inside the image, which may be estimated to be ±3 px [101].

The following dimensions were measured (rounded):

- Thickness of ceramic glue layer (containing the coil): 1.35 mm
- Thickness of the ceramic support tube: 2.5 mm
- Pitch of the heater coil (averaged): 3.3 mm/winding
- Width of heater strip: 1.5 mm

IR surface imaging

Imaging the surface of the heater during transient heat-up was used to locate the individual heating zones of the rod. On the outside of the rod, thermally visible markings (shades) were installed at geometrically exactly defined locations, in order to obtain scaling and offset effective between the image coordinate system and the heater coordinate system (especially, the Z coordinate). During a full-power heat-up pulse (400 V), 1-2 seconds after beginning of the heating (to maintain high contrast), an image (640 px x 480 px) was recorded with the FLIR infrared camera, which was installed perpendicular over the center of the region of interest (distance ~1.5 m). A scaling factor of approximately 1 px/mm was obtained. Along the middle of the IR image of the rod, an intensity profile was numerically extracted for each section (see Figure 2A) [101].

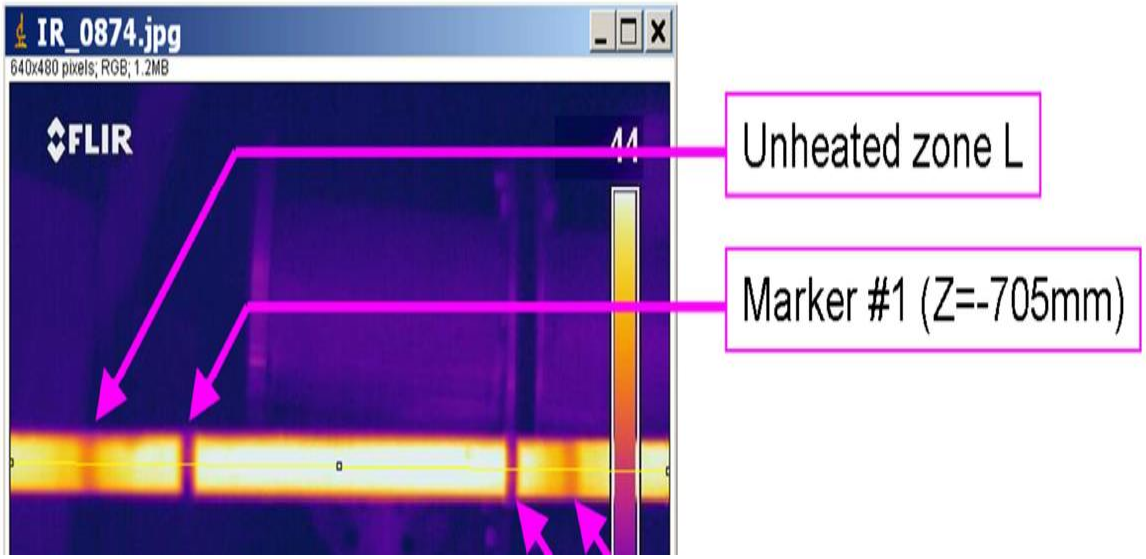

Figure 2A: IR image of heated rod (the example shows heater section 2) with intensity plot showing pronounced local minima due to markers and unheated zones [101].

Z Values[mm]	Manufacturer	Measurement 1	Measurement 2	Decided value
Middle HZ6	409.5	415.0	417.1	**409.5**
Middle UHZ56	618.0	619.4	620.2	**618.0**
Middle HZ5	826.5	826.5	-	**826.5**
Middle UHZ 45	1035.0	1032.8	1034.6	**1035.0**
Middle HZ4	1243.5	1243.1	-	**1243.5**
Middle UHZ 34	1452.0	1451.7	-	**1452.0**
Middle HZ3	1660.5	-	-	**1660.5**
Middle UHZ 23	1869.0	-	-	**1869.0**
Middle HZ2	2077.5	-	-	**2077.5**
Middle UHZ 12	2286.0	-	-	**2286.0**
Middle HZ1	2494.5	-	-	**2494.5**

Table 4A: Axial determination of the heated section of the heater rod assembly [101].

The locations of the minima in the plot were determined by fitting functions (quadratic parabola or the logistic equation) into the locally filtered datasets, with the location of the minimum as free parameter. Usually, the results from the two different fitting functions were as close as 0.5 px or better, giving a measure of error for the exactness of the minimum location. The positioning of the reference markers can be performed within an error of ±0.5 mm. With typical values, the maximum error for the determined z-coordinate values is estimated to be ±2 mm. Additional error must be allowed for optical distortions and other systematic errors, so a total error of ±3 mm seems applicable. This procedure is very well suited to determine the middles of the unheated zones, or respectively the middles of the heated zones, but it is not suited to determine the length of the heated zones with high accuracy. However, the distances between the unheated zones are indicative of the relative length of the heated zones in between. In Table 4A, the determined points are compared with their planned values (given by the manufacturer). The heater zones (HZ) are numbered 1 to 6 ascending from bottom to top. Since only the upper zones are in the densely-instrumented area, the analyses have been performed for heater sections 4 to 6 only [101]. It can be seen that the middles of HZ5 and HZ4 coincide quite exactly (difference < 0.5 mm) with the manufacturer data, and that also the middles of the unheated zones never differ by more than 2.2 mm from the manufacturer data. The middle of HZ6 however differs 5.5…7.6 mm from the measured values and therefore lies out of the tolerance of ±3 mm. Parts of this difference may be attributed to the special situation of HZ6 – without a neighboring heater upstream, it could be imagined that the additional heat drain distorts the temperature field, so that the required symmetry assumption is not applicable. It is therefore tentatively decided to accept the manufacturer data also for the first heater zone [101].

Data acquisition system (DACS)

The relevant operating parameters of the experimental facility are set-up and recorded by means of a Data Acquisition and Controller System (DACS). The data acquisition and control system are based on hardware components and software. The hardware components are mainly composed by a group of data acquisition cards (128- channels multiplex mode reception) installed directly to the main PC. These particular cards can sample up to 64 analog data channels at 300 Hz and 12-bit resolution simultaneously. Additional to the analog inputs, the cards are instrumented with 24 digital input/output lines with a sampling frequency of 150 kHz and 16-bit resolution, which can be used to obtained feedback from external signals. All signals are centrally controlled by a PC running a custom-programmed application based on the software Measure Fondry 5.0 programming environment [160]. This application provided graphical user interface and performed the sequencing data acquisition; preprocessing and logging (output of data files) of the signals. Furthermore, the DACS is additionally instrumented with appropriated signal conditioning hardware such as:

- *Current to voltage converters e.g. for pressure transducers, thermocouples and flow meters.*
- *Low pass-filters (for the Coriolis mass flow meter)*
- *Cold junction compensation and low-level signal amplifiers (temperature, pressure and flowrate)*
- *Effective power meter (for the electric heater of the rod)*

Instrumentation error

To ensure the measurement results of the present experimental study, it is necessary to take into account the uncertainties of all used relevant instrumentation (Coriolis mas flow meter, thermocouples, pressure transducers, etc.), that might influence the results of the dimensionless parameters such as Reynolds number, Friction factor and Nusselt number. An overview of the main instruments with their respective range and associated errors σ is listed in Table 5A.

Variable	Symbol and Unit	Instrument	Range	Instrument Error*
Coriolis flow meter	$\dot{m}_{CFM}$, Kg/s	E+H Promass 80F-DN50 (SL-FL-01)	Up to 2 000 kg/h	$\sigma_m = 0.35\% \cdot \dot{m}_{CFM} + 3.5$ kg/h
Temperatures	$T_{04_{(T_i)}}$ and $T_{05_{(T_o)}}$, K T_{TS}, K	Thermocouples type-K (SL-TT-04 and SL-TT-05) (TS-TT-00…TS-TT-47)	Up to 1 200 °C	$\sigma_T = \pm\max(1.1\text{ K}, 0.004 \cdot (T - 273.15))$
Heater power supply	P_H, kW	Müller-Ziegler Pdr-MU (HZ-LT_IST_LOW)	0 – 1.6 kW	$\sigma_{PH} = \pm 0.5\% \cdot P_H$
		Unipower APM380 (HZ-LT_IST_HIGH)	1.6 kW – 14 kW	$\sigma_{PH} = \pm 2\% \cdot P_H$
Absolut pressure transducer	$p_{4_{(p_i)}}$, Pa	ABB Model 261AS (SL-PA-04)	0 to 4000 mbar	$\sigma_{P4_{(p_i)}} = \pm 0.15\% \times 4000$ mbar
	p_5, Pa	(SL-PA-05)	0 to 3000 mbar	$\sigma_{P5} = \pm 0.15\% \times 3000$ mbar
Differential pressure transducer	$\Delta p_{1'2'}$Pa	ABB Model 265DS (TS-DP-1'2')	-0.05 to 5 mbar	$\sigma_{DP1'2'} = \pm(0.04 + 0.005 \cdot 10 - 0.05)\%$
	Δp_{45} Pa	ABB Model 265DS (TS-DP-45)	0 to 2000 mbar	$\sigma_{DP45} = \pm(0.04 + 0.005 \cdot 60/2 - 0.05)\%$

Table 5A: Instrumentation error of the experimental facility instrumentation

Appendix B. Uncertainty assessment

As a part of this experimental thesis, the evaluation of the instrumentation errors and uncertainty propagation for the experimental key results has been investigated using the Kline & McClintock method [126]. The first section of this appendix discusses the systematic errors. The uncertainty associated with the Systematic errors or "*Bias*", are those that can be reproduced and can in principle by account for. The errors arise mainly from calibration, imperfections of the used instrumentation, incurrent assumption, etc. The second section gives a detailed description of the uncertainty propagation directly affecting the Reynolds number, friction factor, Nusselt number.

For the presented uncertainty analyses, the following uncertainties are assessed [101, 161]:

a) Measurement uncertainties in the primary measured variables, like mass flow (SL-F01), gas temperatures (SL-T04, SL-T05), cladding wall temperatures (TS-TT-{00..47}), heating power (TS-LT_IST), geometry (d_w, L_h) etc. Four classes of uncertainties were considered:

   U1: Instrument nonlinearities, usually specified by the instrument manufacturer or by norms.

   U2: Residual uncertainties from offset corrections. It is assumed, that a certain percentage of the applied offset are uncertain.

   U3: Uncertainties from signal noise and drift. Measured values from one campaign are used.

   U4: Residual uncertainties from systematic deviation corrections rooted in the physical nature of the sensor/measured quantity.

b) Propagation errors to derived (calculated) quantities, like Reynolds number, friction factor and Nusselt Number

The measurement uncertainty contributions for the main variables are calculated as follows:

Mass flow rate (SL-F01), $\dot{m}_{CFM}$ in g/s

Uncertainty contribution	Equation	Value @base case
Instrument error according to manufacturer specification	$\sigma 1_{\dot{m}_{CFM}} = 0.35\% \cdot \dot{m}_{CFM} + (3.5/3600)/1000$	1.06 g/s
Residual uncertainty from offset correction, ~3.5 kg/h	$\sigma 2_{\dot{m}_{CFM}} = ((\text{Offset}/3600) \cdot 0.2)/1000$	0.25 g/s
Uncertainty from signal noise sigma, ~11 kg/h for N=10 000	$\sigma 3_{\dot{m}_{CFM}} = ((\text{Signal noise}/3600)/\sqrt{\text{N}})/1000$	0.03 g/s
not applicable	-	-
Total uncertainty	$\sigma_{\dot{m}_{CFM}} = \sqrt{\sum_{i=1}^{4} \sigma_i^2}$	1.09 g/s

Differential pressure (TS-DP1'2') $\Delta p_{1'2'}$ in Pa

Uncertainty contribution	Equation	Value @base case
Instrument error according to manufacturer specification	$\sigma 1_{\Delta p_{1'2'}} = (0.04\% + 0.005 \cdot 10 - 0.05)\%$	0.4 Pa
Residual uncertainty from offset correction ~ 8 Pa	$\sigma 2_{\Delta p_{1'2'}} = \text{Offset} \cdot 0.2$	1.6 Pa
Uncertainty from signal noise sigma ~2.8 Pa for N=10 000	$\sigma 3_{\Delta p_{1'2'}} = 2.8 / \sqrt{\text{N}}$	0.03 Pa
Residual uncertainties from systematic deviation, manufacturer specification	$\sigma 4_{\Delta p_{1'2'}} = (2 \cdot 0.03 \cdot 0.25)$	0.015 Pa
Total uncertainty	$\sigma_{\Delta p_{1'2'}} = \sqrt{\sum_{i=1}^{4} \sigma_i^2}$	1.6 Pa

Thermocouples in heater rod (TS-TT-{00..47}) in K

Uncertainty contribution	Equation	Value @base case
Instrument error according to manufacturer specification	$\sigma 1_{T_{TS}} = \sqrt{(1.5^2 + 0.2^2)}$	1.51 K
Residual uncertainty from offset correction (~2.0 K)	$\sigma 2_{T_{TS}} = \text{Offset} \cdot 0.2$	0.4 K
Uncertainty from signal noise sigma (0.2 K), N=1 500	$\sigma 3_{T_{TS}} = \text{Signal noise} / \sqrt{\text{N}}$	0.005 K
Systematic deviation due to thermocouple size and position, where: $\sigma \emptyset_{TC} = 0.25$ mm (uncertainty TC size) $\sigma \emptyset_{heater\ shell} = 0.15$ mm (uncertainty related to heater shell diameter)	$\sigma 4_{T_{TS}} = (P_H / A_w / \lambda_{steel}) \cdot (\sigma \emptyset_{TC} + \sigma T_{TS,Z})$	0.1 K
Total uncertainty	$\sigma_{T_{TS}} = \sqrt{\sum_{i=1}^{4} \sigma_i^2}$	1.57 K

Electrical heater power (TS-LT_IST_Low= < 1.6 kW) in W

Uncertainty contribution	Equation	Value @base case
Instrument error according to manufacturer specification, $\dot{Q}_{wr}$ = ~47.91 W	$\sigma 1_{P_H} = P_H \cdot 0.5\% + (\dot{Q}_{wr} \cdot 0.3)$	19.4 W
Residual uncertainty from offset correction, ~0.25 W	$\sigma 2_{P_H} = \text{Offset} \cdot 0.2$	0.05 W
Uncertainty from signal noise sigma, ~42 W for N=10 000	$\sigma 3_{P_H} = \text{Signal noise} / \sqrt{\text{N}}$	0.42 W
Systematic deviation due to in installation location	$\sigma 4_{P_H} = P_H \cdot (0.5\% + 0.2\%) \cdot (*)$	7.1 W
Total uncertainty	$\sigma_{P_H} = \sqrt{\sum_{i=1}^{4} \sigma_i^2}$	20.6 W

Electrical heater power (TS-LT_IST_High > 1.6 kW) in W

Uncertainty contribution	Equation
Instrument error according to manufacturer specification	$\sigma 1_{P_H} = P_H \cdot 2\% + (\dot{Q}_{wr} \cdot 0.3)$
Residual uncertainty from offset correction, ~11 W	$\sigma 2_{P_H} = \text{Offset} \cdot 0.2$
Uncertainty from signal noise sigma, ~250 W for N=10 000	$\sigma 3_{P_H} = \text{Signal noise}/\sqrt{\text{N}}$
Systematic deviation due to in installation location	$\sigma 4_{P_H} = P_H \cdot (0.5\% + 0.2\%) \cdot (*)$
Total uncertainty	$\sigma_{P_H} = \sqrt{\sum_{i=1}^{4} \sigma_i^2}$

(*) Note that the uncertainty is given for the available total heat flux from the rod to the environment (fluid + flow channel wall), which is not proportional to the wall-to-fluid heat flux density needed in the calculation of the Nusselt number according to literature definition [161].

- Based on manual measurements of several surface temperatures and the atmosphere temperature, additional heat losses were estimated to 3.5 W.
- Ohmic losses in the leads are 0.2%, which is in fact very small.

Gas temperature at inlet, SL-TT-04 or T_i in K

Uncertainty contribution	**Equation**	**Value @base case**
Instrument error according to manufacturer specification	$\sigma 1_{T_i} = \sqrt{(1.5^2 + 0.2^2)}$	1.58 K
Residual uncertainty from offset correction (~2.5 K)	$\sigma 2_{T_i} = \text{Offset} \cdot 0.2$	0.50 K
Uncertainty signal noise sigma, ~0.4 K for N=10 000	$\sigma 3_{T_i} = \text{Signal noise}/\sqrt{\text{N}}$	0.004 K
Systematic deviation due to isothermal environment	$\sigma 4_{T_i} = 0$	0
Total uncertainty	$\sigma_{T_i} = \sqrt{\sum_{i=1}^{4} \sigma_i^2}$	1.66 K

Geometrical quantities:

Uncertainties for geometrical quantities are determined by their measurement method and averaging basis [101].

Primary measured variables:

- Heater rod diameter σ_{d_w}: ±0.08 mm
- Hex-tube width-across-flats $\sigma_{h_{hex}}$: ±0.17 mm
- Length of heater segment σ_{L_H}: ±3.5 mm
- Length between pressure ports $\sigma_{\Delta Z_{1'2'}}$: ±1 mm

Derived quantities:

- Hydraulic diameter σ_{D_h}= ±0.25 mm
- Flow cross section σ_{A_c}= ±40 mm²
- Heated surface area per segment (i=1 to 6) σ_{AH_i} = ±7676 mm²

General equations to calculate the propagated uncertainties quantities

The uncertainty propagation magnitudes for the key results are derived by the root-sum-square method proposed by Kline & McClintock, as shown in Eq. 1.B.

$$\sigma R = \sqrt{\sum_{i=1}^{N} \left(\frac{\sigma y}{\sigma x} \cdot \sigma_{xi}\right)^2} \qquad [1.B]$$

The evaluation of the heat transfer in term of Reynolds number Re_i (Eq. [4.7]), Darcy friction factor (Eq.[4.3]) and Nusselt number Nu_i (Eq. [4.9]) are used. For this experimental study following terms were considered for the uncertainty calculations:

Reynolds number:	$Re_i(\dot{m}_{CFM}, D_h, A_C, \mu(T_i))$
Darcy friction factor	$f_D(\dot{m}_{CFM}, \Delta p_{1'2'}, D_h, A_C, \Delta Z_{1'2'})$
Nusselt number	$Nu_i(P_H, T_{TS}, T_g, D_h)$

The uncertainty propagations are then calculated as follows:

Uncertainty Reynolds Number Re_i.

$$\sigma_{Re_i}{}^2 = \left(\frac{D_h}{A_c \cdot \mu_g} \cdot \sigma_{\dot{m}_{CFM}}\right)^2 + \left(\frac{\dot{m}_{CFM} \cdot D_h}{\mu_g{}^2 \cdot A_c} \cdot \sigma_{\mu_g}\right)^2 + \left(\frac{\dot{m}_{CFM}}{A_c \cdot \mu_g} \cdot \sigma_{D_h}\right)^2 + \left(\frac{\dot{m}_{CFM} \cdot D_h}{\mu_g \cdot A_c{}^2} \cdot \sigma_{A_c}\right)^2 \quad [2.B]$$

Uncertainty Darcy friction factor f_D:

$$\sigma_{f_D}{}^2 = \left(\frac{f_D}{\Delta p_{1'2'}} \cdot \sigma\Delta p_{1'2'}\right)^2 + \left(-\frac{2f_D}{\dot{m}_{CFM}} \cdot \sigma_{\dot{m}_{CFM}}\right)^2 + \left(\frac{f_D}{\Delta Z_{1'2'}} \cdot \sigma_{\Delta Z_{1'2'}}\right)^2 + \left(\frac{2f_D}{A_c} \cdot \sigma_{A_c}\right)^2 + \left(-\frac{f_D}{D_h} \cdot \sigma_{D_h}\right)^2 \quad [3.B]$$

Uncertainty Nusselt Number Nu_i:

$$\sigma_{Nu_i}{}^2 = \left(\frac{Nu_i}{P_H} \cdot \sigma_{P_H}\right)^2 + \left(-\frac{Nu_i}{T_w - T_g} \cdot \left(\sigma_{T_w} + \sigma_{T_g}\right)\right)^2 + \left(-\frac{Nu_i}{AH_i} \cdot \sigma_{AH_i}\right)^2 \quad [4.B]$$

Appendix C. Thermophysical properties of dry air and stainless steels

As required in section 4.1, the thermophysical properties of the air were evaluated at their inlet temperatures as well as at their respective pressures. The properties for the air for water were evaluated and adopted by using the data given by the VDI Heat atlas [120] and reported by Arbeiter et al. 2013 [101].

Molar mass

M_{air} =28.96 kg/kmol

R_{air} =287.22 J/Kg/K

Density

For the evaluation of the L-STAR experiments, a constant real gas factor of unity is chosen.

$$\rho_{air}(p,T) = \frac{p}{R_{air} \cdot T}$$

Specific heat capacity at 0.1MPa

$C_{p,air}(0.1\ MPa, T)$ = -3.8799 · 10^{-7} · T^3 + 8.3527 · 10^{-4} · T^2 - 3.5696 · 10^{-1} · T + 1.0491 · 10

T is the Kelvin temperature, $C_{p,air} = J/(kg \cdot K)$

Dynamic viscosity at 0.1MPa

$\mu_{air}(0.1\ MPa, T)$ = -1.5397 · 10^{-11} · T^2 + 5.4773 · 10^{-8} · T + 3.5440 · 10^{-6}

T is the Kelvin temperature, $\mu_{air} = Pa \cdot s$

Heat conductivity at 0.1Mpa

$\lambda_{air}(0.1\ MPa, T)$ = -1.5397 · 10^{-8} · T^2 + 7.9438 · 10^{-5} · T + 3.8280 · 10^{-3}

T is the Kelvin temperature, $\lambda_{air} = W/m \cdot K$

The stainless-steel grades AISI 304 (equivalent to 1.4301 acc. standard DIN EN 10216-5, hexagonal flow channel), 1.4404 (heater rod compression shell) and 1.4571 (heater rod heater cartridge shell) are used in the L-STAR/SL test section. The steel grades 1.4571 and 1.4404 which are used in the heater

rod are identical in their alloying composition for Cr, Ni and Mo, but 1.4571 is additionally alloyed with some Titanium for corrosion stabilization. The WIAM metals database [162] reports the same values for the thermal conductivity for both alloys. The steel grade AISI 304 is alloyed with Cr and Ni only, and has a 7-9% higher thermal conductivity in the relevant (low) temperature range than the above mentioned CrNiMo alloys. Since the relevant heat conduction takes place in the heater rod, the data for the CrNiMo alloys is given as polynoms. The data for 1.4404 from the WIAM metals database in the temperature range 20-400°C has been used. It is suggested to use the same data to model the hexagonal flow channel [101].

Density

$\rho_{air}(p,T) = 7960\ kg/m^3$

Coefficient of linear expansion, referenced to 20°C

$\gamma_{St,20°C}(T) = 4.8183 \cdot 10^{-9} \cdot T^3 - 1.194 \cdot 10^{-5} \cdot T^2 + 1.318 \cdot 10^{-2} \cdot T + 13.158$

T is the Kelvin temperature, $\gamma_{St,20°C} = 10^{-6}/K$, valid 293-973 K

Specific heat capacity

$C_{p,St}(T) = 2.763 \cdot 10^{-6} \cdot T^3 - 4.294 \cdot 10^{-3} \cdot T^2 - 2.333 \cdot T + 86.83$

T is the Kelvin temperature, $C_{p,St} = J/(kg \cdot K)$, valid 293-973 K

Heat conductivity

$\lambda_{St}(T) = -3.467 \cdot 10^{-6} \cdot T^2 + 1.960 \cdot 10^{-2} \cdot T + 7.962$

T is the Kelvin temperature, $\lambda_{St} = W/m \cdot K$, valid 293-973 K

Appendix D. Tables of measurement results

In the following appendix, the experimentally obtained data for the frictional losses, heat transfer, axial wall temperature distribution and velocity distribution for the smooth (L-STAR-G0) and both structured rod channels (L-STAR-G1 and L-STAR-G2), is presented.

Table 1.D: Friction factor results unheated (*top*) and heated (*bottom*) smooth rod channel test (L-STAR-DP-G0), compared against the correlation by Chen and Churchill.

L-STAR-G0	$T_{i(T04)}$	$T_{o(T05)}$	Re_i	σ_{Re_i}	$f_{D,s}$	$\sigma_{f_{D,s}}$	f_{Chen}	$f_{Churchill}$
-DP-1’	290.6	291.6	2083.4	± 651.4	0.172	± 0.135	-	0.031
-DP-2’	290.5	291.4	2654.3	± 651.8	0.124	± 0.079	-	0.039
-DP-3’	290.6	291.3	3320.1	± 652.0	0.092	± 0.049	-	0.043
-DP-01	291.4	292.5	4236.2	± 635.5	0.057	± 0.025	0.039	0.040
-DP-03	291.2	292.2	8595.8	± 642.2	0.034	± 0.008	0.033	0.033
-DP-05	290.5	291.4	17055.6	± 666.3	0.032	± 0.002	0.027	0.027
-DP-07	290.4	290.9	25109.0	± 699.8	0.028	± 0.001	0.025	0.024
-DP-09	290.1	290.6	33027.4	± 741.4	0.026	± 0.001	0.023	0.023
-DP-11	289.9	290.4	41909.8	± 796.7	0.024	± 0.001	0.022	0.022
-DP-13	289.9	290.5	50589.5	± 857.8	0.023	± 0.001	0.021	0.021
-DP-15	291.0	291.6	59545.1	± 924.7	0.022	± 0.001	0.021	0.020
-DP-17	290.3	290.9	68817.4	± 998.9	0.021	± 0.001	0.020	0.019

L-STAR-G0	$T_{i(T04)}$	$T_{o(T05)}$	Re_i	σ_{Re_i}	$f_{D,s}$	$\sigma_{f_{D,s}}$	f_{Chen}	$f_{Churchill}$
-TX-01	288.4	326.9	4631.9	± 635.5	0.069	± 0.026	0.038	0.039
-TX-03	283.5	317.3	8719.9	± 670.2	0.046	± 0.009	0.032	0.032
-TX-05	289.1	325.7	16969.3	± 668.3	0.037	± 0.003	0.027	0.027
-TX-07	289.3	326.0	25300.0	± 702.2	0.035	± 0.002	0.025	0.024
-TX-09	288.9	327.3	33014.6	± 743.1	0.033	± 0.002	0.023	0.023
-TX-11	288.9	327.6	41635.8	± 796.7	0.031	± 0.001	0.022	0.022
-TX-13	290.0	328.6	50610.5	± 858.8	0.029	± 0.001	0.021	0.021
-TX-15	291.0	329.8	59560.7	± 922.9	0.028	± 0.001	0.021	0.020
-TX-17	292.3	332.1	68170.4	± 998.5	0.028	± 0.001	0.020	0.019

Table 2.D: Heat transfer coefficients and relative uncertainties results for the smooth rod channel tests (L-STAR-DP-G0), compared to the correlations by Gnielinski, Petukhov and Dittus-Boelter.

L-STAR-G0	Re_i	δ_{Re_i}	$Nu_{i,s}$	$\delta_{Nu_{i,s}}$	$T_{g,15}$ **[K]**	**Gnielinski**	**Petukhov**	**Dittus &Boelter**
-TX-01	4631.9	± 635.5	17.6	± 1.8	302.04	16.7	15.5	17.9
-TX-03	8719.9	± 670.2	23.1	± 2.5	304.48	28.0	26.8	29.8
-TX-05	16969.3	± 668.3	49.2	± 3.5	316.96	46.8	45.5	50.7
-TX-07	25300.0	± 702.2	65.2	± 4.5	316.46	63.4	62.0	69.8
-TX-09	33014.6	± 743.1	79.9	± 4.1	317.20	77.6	76.1	86.4
-TX-11	41635.8	± 796.7	95.5	± 5.3	317.56	92.6	91.0	104.1
-TX-13	50610.5	± 858.8	110.6	± 5.7	318.62	107.5	105.9	121.7
-TX-15	59560.7	± 922.9	124.9	± 6.1	319.75	121.9	120.1	138.6
-TX-17	68170.4	± 998.5	140.4	± 6.6	322.02	135.2	133.4	154.4

Table 3.D: Axial cladding wall temperature distribution for the smooth rod channel experiments (L-STAR-TX-G0) at a dimensionless heat up ratio q_i^+ =0.0015.

$Z_{TC,i}$ [m]	TC	TX01	TX02	TX03	TX04	TX05	TX06	TX07	TX08	TX09	TX10	TX11	TX12	TX13	TX14	TX15	TX16	TX17
0.074	TT03	-	-	-	-	-	-	-	-	-	-	-	-	-	-	-	-	-
0.307	TT07	-	-	358.7	-	382.2	-	388.4	-	396.7	-	402.1	-	407.2	-	412.1	-	418.3
0.472	TT00	-	-	387.7	-	407.3	-	416.1	-	427.8	-	435.9	-	443.4	-	450.3	-	459.5
0.472	TT02	-	-	387.8	-	407.3	-	415.7	-	427.6	-	435.6	-	443.0	-	449.9	-	458.9
0.478	TT24	-	-	388.1	-	407.6	-	416.5	-	428.2	-	436.3	-	443.8	-	450.8	-	460.0
0.484	TT04	-	-	387.8	-	407.0	-	415.6	-	427.0	-	434.8	-	442.0	-	448.8	-	457.6
0.483	TT06	-	-	387.7	-	406.9	-	415.4	-	426.8	-	434.6	-	441.8	-	448.5	-	457.3
0.489	TT28	-	-	388.0	-	407.0	-	415.7	-	427.1	-	434.9	-	442.1	-	448.9	-	457.7
0.494	TT08	-	-	387.5	-	406.7	-	415.2	-	426.5	-	434.3	-	441.4	-	448.1	-	456.8
0.494	TT10	-	-	387.6	-	407.0	-	415.5	-	426.9	-	434.7	-	441.9	-	448.6	-	457.4
0.500	TT32	-	-	387.7	-	406.7	-	415.2	-	426.5	-	434.3	-	441.4	-	448.1	-	456.8
0.504	TT12	-	-	387.6	-	407.2	-	415.7	-	427.1	-	434.9	-	442.1	-	448.8	-	457.6
0.505	TT14	-	-	387.7	-	407.5	-	416.1	-	427.5	-	435.5	-	442.7	-	449.6	-	458.5
0.509	TT36	-	-	384.7	-	407.1	-	415.7	-	427.1	-	435.0	-	442.1	-	448.8	-	457.6
0.515	TT16	-	-	387.7	-	407.6	-	416.3	-	427.8	-	435.9	-	443.2	-	450.1	-	459.2
0.517	TT18	-	-	388.0	-	407.9	-	416.7	-	428.3	-	436.4	-	443.9	-	450.9	-	460.1
0.520	TT40	-	-	387.6	-	407.5	-	416.2	-	427.9	-	435.9	-	443.2	-	450.1	-	459.2
0.526	TT20	-	-	387.9	-	407.8	-	416.5	-	428.2	-	436.3	-	443.7	-	450.8	-	459.9
0.526	TT22	-	-	387.9	-	407.5	-	416.3	-	427.9	-	436.0	-	443.4	-	450.4	-	459.5
0.532	TT44	-	-	387.8	-	407.7	-	416.5	-	428.2	-	436.3	-	443.8	-	450.8	-	460.0
0.532	TT23	-	-	387.7	-	407.4	-	416.1	-	427.6	-	435.7	-	443.1	-	450.0	-	459.1
0.690	TT11	-	-	381.3	-	400.1	-	407.1	-	417.0	-	423.5	-	429.5	-	435.3	-	442.9
0.826	TT15	-	-	385.0	-	406.8	-	415.4	-	426.9	-	434.8	-	442.0	-	448.9	-	457.8
0.982	TT01	-	-	383.0	-	404.7	-	412.9	-	424.1	-	431.8	-	438.7	-	445.3	-	454.1
0.983	TT26	-	-	383.3	-	404.8	-	413.1	-	424.3	-	432.0	-	438.9	-	445.5	-	454.2

Table 3.D (continuation): Axial cladding wall temperature distribution for the smooth rod channel experiments (L-STAR-TX-G0) at a dimensionless heat up ratio $q_i^+ = 0.0015$.

$Z_{TC,i}$ [m]	TC	TX01	TX02	TX03	TX04	TX05	TX06	TX07	TX08	TX09	TX10	TX11	TX12	TX13	TX14	TX15	TX16	TX17
0.988	TT25	-	-	383.2	-	405.1	-	413.3	-	424.5	-	432.2	-	439.1	-	445.7	-	454.5
0.993	TT05	-	-	382.8	-	404.4	-	412.6	-	423.8	-	431.5	-	438.3	-	444.9	-	453.6
0.995	TT30	-	-	-	-	-	-	-	-	-	-	-	-	-	-	-	-	-
0.999	TT29	-	-	382.9	-	404.6	-	412.6	-	424.0	-	431.7	-	438.5	-	445.1	-	453.8
1.005	TT09	-	-	382.5	-	404.3	-	412.6	-	423.8	-	431.6	-	438.5	-	445.2	-	454.0
1.005	TT34	-	-	382.4	-	404.6	-	412.8	-	424.0	-	431.7	-	438.6	-	445.2	-	453.9
1.012	TT33	-	-	382.4	-	404.1	-	412.4	-	423.6	-	431.4	-	438.4	-	445.0	-	453.8
1.016	TT13	-	-	382.2	-	404.3	-	412.7	-	423.9	-	431.8	-	438.8	-	445.5	-	454.4
1.016	TT38	-	-	382.1	-	404.2	-	412.5	-	423.8	-	431.6	-	438.6	-	445.3	-	454.2
1.021	TT37	-	-	382.0	-	404.0	-	412.4	-	423.7	-	431.5	-	438.5	-	445.2	-	454.1
1.026	TT17	-	-	381.9	-	404.1	-	412.5	-	423.8	-	431.6	-	438.7	-	445.5	-	454.4
1.026	TT42	-	-	381.8	-	404.0	-	412.3	-	423.6	-	431.5	-	438.5	-	445.3	-	454.2
1.031	TT41	-	-	381.5	-	403.7	-	412.0	-	423.3	-	431.1	-	438.2	-	445.0	-	453.8
1.038	TT21	-	-	381.5	-	403.4	-	411.7	-	422.9	-	430.7	-	437.7	-	444.4	-	453.3
1.037	TT46	-	-	381.4	-	403.1	-	411.3	-	422.5	-	430.2	-	437.1	-	443.8	-	452.6
1.043	TT45	-	-	381.1	-	402.9	-	411.1	-	422.3	-	430.1	-	437.0	-	443.8	-	452.6
1.044	TT47	-	-	381.0	-	402.6	-	410.7	-	421.8	-	429.4	-	436.3	-	442.9	-	451.6
1.419	TT19	-	-	378.5	-	398.9	-	406.0	-	416.5	-	423.9	-	430.1	-	436.7	-	444.9
1.798	TT27	-	-	372.4	-	391.7	-	398.5	-	408.6	-	415.6	-	421.5	-	427.7	-	435.6
2.138	TT31	-	-	362.9	-	380.7	-	387.3	-	397.1	-	403.5	-	408.8	-	413.7	-	421.5
2.558	TT35	-	-	349.4	-	369.6	-	375.5	-	384.1	-	389.7	-	394.5	-	398.9	-	405.8
2.928	TT39	-	-	-	-	-	-	-	-	-	-	-	-	-	-	-	-	-
3.320	TT43	-	-	-	-	-	-	-	-	-	-	-	-	-	-	-	-	-

Table 4.D: Friction factors results for the unheated solid ring structured rod channel (L-STAR-DP-G1), compared correlations developed by Rashkovan and Saini.

Case G1	$\dot{m}_{CFM}$ [g/s]	$T_{i(T04)}$ [K]	P_i [Pa]	$\Delta p_{1'2'}$ [Pa]	Δp_{45} [Pa]	P_H [W]	Re_i	σ_{Re_i}	$f_{D_{s,(G1)}}$	$\sigma_{f_{Ds,(G1)}}$	$f_{Rashkovann}$	f_{Saini}
-DP-1’	3.49	295.12	150899.2	3.23	27.14	-	2246.0	±632.7	0.563	±0.323	0.240	0.238
-DP-2’	3.97	295.62	150395.0	3.63	30.70	-	2551.4	±632.2	0.486	±0.245	0.235	0.233
-DP-3’	5.04	296.65	150255.2	4.50	39.17	-	3231.8	±631.3	0.372	±0.148	0.227	0.223
-DP-01	6.40	295.44	150772.8	6.13	57.18	-	4117.3	±630.1	0.316	±0.099	0.219	0.214
-DP-02	9.61	295.27	150737.3	10.19	93.62	-	6181.4	±634.9	0.234	±0.049	0.206	0.199
-DP-03	12.46	295.36	149947.9	14.91	135.84	-	8015.0	±640.1	0.202	±0.033	0.198	0.190
-DP-04	18.01	295.21	150370.2	25.94	234.60	-	11590.1	±653.9	0.169	±0.019	0.187	0.177
-DP-05	25.42	295.52	150489.7	45.08	402.20	-	16349.1	±677.8	0.147	±0.012	0.178	0.167
-DP-06	31.96	295.53	150657.5	66.61	588.46	-	20549.9	±703.4	0.138	±0.009	0.172	0.160
-DP-07	37.89	295.50	151041.5	89.74	786.03	-	24368.7	±730.7	0.132	±0.008	0.168	0.155
-DP-09	44.08	295.49	150766.1	118.26	1028.94	-	28351.2	±762.8	0.129	±0.007	0.164	0.151
-DP-09	50.71	295.55	151573.4	152.26	1316.55	-	32608.5	±800.6	0.126	±0.006	0.161	0.147
-DP-10	56.16	295.36	151621.9	182.26	1570.78	-	36131.7	±834.7	0.123	±0.006	0.158	0.145
-DP-11	63.60	295.59	152197.9	231.64	1983.43	-	40892.7	±883.1	0.122	±0.005	0.155	0.141
-DP-12	69.75	295.47	152466.1	277.08	2360.39	-	44860.2	±926.2	0.122	±0.005	0.153	0.139
-DP-13	76.26	295.88	153103.2	330.15	2798.87	-	48996.1	±972.4	0.122	±0.005	0.151	0.137
-DP-14	83.21	297.61	154266.0	394.37	3318.44	-	53233.2	±1020.3	0.122	±0.004	0.149	0.135
-DP-15	90.63	297.88	155381.4	463.41	3886.24	-	57942.9	±1077.0	0.122	±0.004	0.147	0.133
-DP-16	97.28	298.29	155210.0	535.37	4476.55	-	62130.7	±1128.7	0.122	±0.004	0.146	0.131
-DP-17	104.3	298.03	154191.9	588.04	4957.89	-	66673.4	±1186.6	0.116	±0.004	0.144	0.129

Table 5.D: Friction factors results for the unheated perforated ring structured rod channel (L-STAR-DP-G2), compared to correlations developed by Rashkovan and Saini.

Case G2	$\dot{m}_{CFM}$ [g/s]	$T_{i(T04)}$ [K]	P_i [Pa]	$\Delta p_{1'2'}$ [Pa]	Δp_{45} [Pa]	P_H [W]	Re_i	σ_{Re_i}	$f_{D_{s,(G2)}}$	$\sigma_{f_{Ds,(G2)}}$	$f_{Rashkovann}$	f_{Saini}
-DP-1’	3.13	289.92	150921.2	2.31	22.93	-	2042.7	±645.44	0.507	±0.306	0.243	0.242
-DP-2’	4.11	290.50	150748.6	2.98	28.71	-	2675.4	±645.03	0.380	±0.178	0.234	0.231
-DP-3’	5.39	290.69	150500.3	3.84	37.68	-	3510.8	±645.65	0.283	±0.103	0.224	0.220
-DP-01	6.52	291.94	150086.5	4.84	46.96	-	4231.0	±639.82	0.243	±0.074	0.218	0.213
-DP-02	9.74	289.99	152010.8	7.39	75.29	-	6352.5	±644.46	0.169	±0.035	0.205	0.198
-DP-03	12.81	292.52	150055.3	11.28	113.16	-	8301.2	±650.79	0.146	±0.022	0.197	0.188
-DP-04	19.32	292.90	150077.0	20.25	205.38	-	12508.0	±666.62	0.115	±0.014	0.185	0.175
-DP-05	25.54	291.39	151096.1	32.45	330.66	-	16596.3	±686.15	0.107	±0.010	0.178	0.166
-DP-06	32.24	292.02	151141.2	49.20	499.57	-	20912.8	±713.10	0.102	±0.007	0.172	0.160
-DP-07	37.72	291.83	151205.4	65.21	661.11	-	24482.7	±738.85	0.098	±0.006	0.168	0.155
-DP-09	44.96	291.71	151343.1	88.06	890.75	-	29189.2	±774.39	0.094	±0.005	0.163	0.150
-DP-09	50.66	292.00	151485.5	109.36	1104.36	-	32867.1	±808.74	0.092	±0.005	0.160	0.147
-DP-10	57.04	291.73	151710.4	136.63	1376.26	-	37031.0	±849.71	0.091	±0.004	0.157	0.144
-DP-11	63.66	291.88	151980.4	167.81	1687.43	-	41311.2	±890.41	0.089	±0.004	0.155	0.141
-DP-12	69.99	292.32	152283.5	201.25	2019.38	-	45371.3	±931.18	0.089	±0.004	0.153	0.139
-DP-13	77.02	292.56	152685.5	242.31	2426.59	-	49897.0	±982.97	0.088	±0.004	0.151	0.136
-DP-14	83.70	292.88	153085.2	284.80	2847.24	-	54183.1	±1033.36	0.088	±0.003	0.149	0.134
-DP-15	90.94	293.02	153587.8	335.33	3344.51	-	58848.9	±1089.17	0.088	±0.003	0.147	0.132
-DP-16	97.61	293.89	154066.5	384.91	3837.10	-	63024.7	±1149.06	0.088	±0.003	0.145	0.131
-DP-17	104.7	291.34	156468.9	432.16	4447.12	-	68063.8	±1213.51	0.088	±0.003	0.144	0.129

Table 6.D: Friction factor and Nusselt number results for the solid ring structured rod channel experiments (L-STAR-TX-G1) at a dimensionless heat up ratio $q_i^+ = 0.001$, with their respective uncertainties values.

Case G1	$\dot{m}_{CFM}$ [g/s]	$T_{i(T04)}$ [K]	$T_{o(T05)}$ [K]	P_i [Pa]	$\Delta p_{1'2'}$ [Pa]	Δp_{45} [Pa]	P_H [W]	$\dot{Q}_{wr}$ [W]	$T_{g,15}$ [K]	Re_i	σ_{Re_i}	$f_{D_r,(G1)}$	$\sigma_{f_{Dr,(G1)}}$	$Nu_{i,r(G1)}$	$\sigma_{Nu_i,r(G1)}$
-TX-01	6.32	289.29	320.87	149804.8	5.92	50.95	254.4	27.21	316.4	4130.1	±645.2	0.318	±0.102	85.18	±15.69
-TX-02	9.79	291.80	323.90	150736.9	9.29	79.03	382.0	36.32	319.5	6355.9	±640.8	0.208	±0.043	96.56	±11.63
-TX-03	13.13	291.77	324.64	149352.3	16.57	137.32	511.9	38.41	320.1	8525.4	±647.3	0.204	±0.031	116.09	±10.71
-TX-04	19.46	291.42	327.39	150029.5	32.84	264.76	755.3	45.04	320.1	12641.7	±664.5	0.185	±0.019	139.58	±9.37
-TX-05	25.60	290.37	327.83	149843.6	48.94	391.46	1030.6	47.91	320.5	16679.8	±687.6	0.160	±0.013	167.02	±9.26
-TX-06	32.25	292.35	330.43	149690.4	75.61	597.62	1298.6	54.05	322.6	20906.4	±710.6	0.155	±0.010	186.98	±10.56
-TX-07	38.22	292.03	330.31	150314.8	102.35	799.17	1538.9	60.16	322.4	24793.4	±739.0	0.150	±0.009	201.83	±10.77
-TX-09	43.56	292.79	332.21	150309.6	131.97	1019.53	1776.7	67.58	323.6	28205.2	±765.4	0.149	±0.008	211.58	±10.41
-TX-09	50.83	292.44	332.16	149014.0	178.60	1371.97	2070.0	73.83	323.3	32941.2	±807.9	0.147	±0.007	228.53	±11.18
-TX-10	56.82	295.53	334.41	150171.8	223.75	1711.73	2265.9	78.53	325.8	36537.6	±838.8	0.148	±0.007	243.20	±11.21
-TX-11	63.95	292.97	333.13	150400.2	275.02	2087.52	2597.4	82.42	323.9	41387.8	±891.6	0.145	±0.006	254.80	±11.05
-TX-12	69.87	293.55	333.51	150298.5	327.33	2475.66	2821.9	86.42	324.3	45154.4	±931.7	0.145	±0.006	266.01	±11.19
-TX-13	77.20	293.24	333.42	150472.3	398.82	3001.03	3124.1	91.40	324.1	49932.2	±986.1	0.145	±0.006	276.68	±11.30
-TX-14	83.82	293.31	333.44	150591.1	468.77	3516.69	3378.6	90.90	324.1	54200.8	±1036.2	0.145	±0.005	288.95	±11.42
-TX-15	90.84	293.65	333.92	150329.2	551.05	4116.43	3667.5	97.58	324.5	58694.2	±1090.4	0.146	±0.005	298.71	±11.63
-TX-16	97.36	293.59	334.21	150407.8	632.74	4703.44	3933.4	101.85	324.5	62912.6	±1142.8	0.146	±0.005	307.48	±11.63
-TX-17	105.53	293.84	334.81	149713.9	752.21	5562.53	4306.5	109.74	325.1	68149.7	±1209.2	0.148	±0.005	322.70	±12.08

Table 7.D: Friction factor and Nusselt number results for the solid ring structured rod channel experiments (L-STAR-TX-G1) at a dimensionless heat up ratio $q_i^+ = 0.002$, with their respective uncertainties values.

Case G1	$\dot{m}_{CFM}$ [g/s]	$T_{i(T04)}$ [K]	$T_{o(T05)}$ [K]	P_i [Pa]	$\Delta p_{1'2'}$ [Pa]	Δp_{45} [Pa]	P_H [W]	$\dot{Q}_{wr}$ [W]	$T_{g,15}$ [K]	Re_i	σ_{Re_i}	$f_{D_r,(G1)}$	$\sigma_{f_{Dr,(G1)}}$	$Nu_{i,r(G1)}$	$\sigma_{Nu_i,r(G1)}$
-TX-01	n/a	n/a	n/a	n/a	n/a	n/a	n/a	n/a	n/a	n/a	n/a	n/a	n/a	n/a	n/a
-TX-02	n/a	n/a	n/a	n/a	n/a	n/a	n/a	n/a	n/a	n/a	n/a	n/a	n/a	n/a	n/a
-TX-03	n/a	n/a	n/a	n/a	n/a	n/a	n/a	n/a	n/a	n/a	n/a	n/a	n/a	n/a	n/a
-TX-04	n/a	n/a	n/a	n/a	n/a	n/a	n/a	n/a	n/a	n/a	n/a	n/a	n/a	n/a	n/a
-TX-05	26.16	292.78	339.63	150143.5	53.17	414.00	1350.6	73.11	332.8	16937.9	±685.8	0.166	±0.013	170.20	±8.33
-TX-06	32.42	292.65	340.70	150243.2	78.46	604.47	1697.7	82.90	332.6	20996.5	±711.1	0.160	±0.011	196.62	±9.46
-TX-07	38.60	289.24	340.95	149997.8	105.34	803.29	2023.3	89.88	329.8	25217.0	±746.5	0.153	±0.009	204.60	±10.44
-TX-09	44.79	290.22	342.31	150815.7	140.45	1061.52	2359.7	98.10	330.1	29192.1	±777.5	0.152	±0.008	216.31	±10.47
-TX-09	51.08	287.28	343.88	149843.7	177.67	1329.12	2696.0	106.42	327.8	33537.0	±820.3	0.149	±0.007	225.51	±9.79
-TX-10	56.98	288.19	343.38	149822.2	221.07	1643.82	3037.7	115.10	328.7	37326.8	±855.7	0.148	±0.007	234.14	±10.46
-TX-11	63.30	288.61	343.16	149838.8	272.25	2011.32	3390.0	122.92	329.6	41419.7	±897.2	0.148	±0.006	247.00	±10.68
-TX-12	70.21	288.80	344.04	150255.0	333.59	2450.54	3731.7	130.22	329.9	45921.9	±945.7	0.148	±0.006	258.20	±10.80
-TX-13	77.44	289.38	344.66	150081.8	407.44	2978.53	4116.1	138.51	330.2	50571.1	±997.8	0.149	±0.006	269.22	±11.10
-TX-14	83.50	289.86	345.42	150086.6	475.28	3461.40	4457.8	146.20	330.7	54468.3	±1043.0	0.150	±0.005	278.24	±11.33
-TX-15	91.05	290.61	345.21	149945.6	566.81	4108.48	4847.5	151.69	331.3	59278.2	±1100.6	0.150	±0.005	289.78	±11.60
-TX-16	97.71	291.49	345.31	149982.1	659.37	4761.30	5189.2	160.91	332.2	63474.6	±1152.0	0.152	±0.005	299.62	±11.82
-TX-17	106.21	292.06	345.70	151619.0	777.85	5594.59	5605.6	167.71	333.01	68892.5	±1220.5	0.154	±0.005	317.54	±12.21

Table 8.D: Friction factor and Nusselt number results for the solid ring structured rod channel experiments (L-STAR-TX-G1) at a dimensionless heat up ratio $q_i^+ = 0.003$, with their respective uncertainties values.

Case G1	$\dot{m}_{CFM}$ [g/s]	$T_{i(T04)}$ [K]	$T_{o(T05)}$ [K]	P_i [Pa]	$\Delta p_{1'2'}$ [Pa]	Δp_{45} [Pa]	P_H [W]	$\dot{Q}_{wr}$ [W]	$T_{g,15}$ [K]	Re_i	σ_{Re_i}	$f_{D_{r,}(G1)}$	$\sigma_{f_{Dr,(G1)}}$	$Nu_{i,r(G1)}$	$\sigma_{Nu_i,r(G1)}$
-TX-01	-	-	-	-	-	-	-	-	-	-	-	-	-	-	-
-TX-02	-	-	-	-	-	-	-	-	-	-	-	-	-	-	-
-TX-03	-	-	-	-	-	-	-	-	-	-	-	-	-	-	-
-TX-04	-	-	-	-	-	-	-	-	-	-	-	-	-	-	-
-TX-05	25.35	290.88	365.93	150420.0	50.82	385.78	2064.3	140.29	350.6	16493.0	±699.4	0.170	±0.014	143.46	±6.47
-TX-06	32.12	290.62	368.43	150461.1	78.96	588.29	2582.8	153.63	350.1	20910.0	±734.0	0.165	±0.011	161.40	±7.88
-TX-07	38.25	291.16	371.00	150173.8	110.53	813.86	3087.0	176.80	351.0	24870.7	±769.1	0.162	±0.010	173.55	±7.93
-TX-09	44.10	291.33	373.77	150183.3	145.88	1062.52	3597.7	196.79	352.0	28661.0	±807.1	0.161	±0.009	187.14	±8.11
-TX-09	50.45	291.75	375.50	150277.4	189.43	1367.75	4097.2	211.28	352.3	32748.5	±851.5	0.160	±0.008	198.44	±7.65
-TX-10	57.21	290.43	375.13	150541.5	237.67	1703.67	4644.3	227.74	351.2	37265.4	±906.9	0.158	±0.007	212.00	±8.62
-TX-11	64.16	290.50	375.89	150550.4	299.42	2132.23	5182.1	242.30	351.1	41784.4	±963.6	0.158	±0.007	223.89	±8.87
-TX-12	70.53	292.94	378.48	150691.1	364.67	2608.86	5719.8	262.66	353.8	45647.3	±1010.9	0.159	±0.006	236.80	±9.25

Table 9.D: Friction factor and Nusselt number results for the perforated ring structured rod channel experiments (L-STAR-TX-G2) at a dimensionless heat up ratio $q_i^+ = 0.0015$, with their respective uncertainties values.

Case G2	$\dot{m}_{CFM}$ [g/s]	$T_{i(T04)}$ [K]	$T_{o(T05)}$ [K]	P_i [Pa]	$\Delta p_{1'2'}$ [Pa]	Δp_{45} [Pa]	P_H [W]	$\dot{Q}_{wr}$ [W]	$T_{g,15}$ [K]	Re_i	σ_{Re_i}	$f_{D_{r,}(G2)}$	$\sigma_{f_{Dr,(G2)}}$	$Nu_{i,r(G2)}$	$\sigma_{Nu_i,r(G2)}$
-TX-01	-	-	-	-	-	-	-	-	-	-	-	-	-	-	-
-TX-02	-	-	-	-	-	-	-	-	-	-	-	-	-	-	-
-TX-03	13.22	293.09	324.22	150348.6	13.15	124.05	520.0	41.71	327.8	8556.2	±645.7	0.160	±0.025	123.06	±19.49
-TX-04	19.40	293.60	325.46	150810.7	25.56	229.54	772.5	48.48	330.2	12536.0	±669.0	0.145	±0.015	143.73	±16.51
-TX-05	25.31	294.99	329.34	151322.7	40.72	365.34	1025.4	54.84	332.0	16295.4	±687.1	0.136	±0.009	171.46	±13.87
-TX-06	32.02	296.91	331.36	150974.3	59.15	525.36	1288.7	63.34	327.4	20521.6	±701.6	0.122	±0.008	180.40	±13.46
-TX-07	37.63	291.75	329.21	150369.1	73.46	677.33	1523.0	63.00	333.7	24427.9	±736.7	0.111	±0.007	196.66	±17.04
-TX-09	44.87	298.73	334.00	150923.6	107.47	950.27	1783.8	74.77	326.4	28627.1	±761.3	0.112	±0.006	222.04	±15.14
-TX-09	51.06	291.35	329.24	149955.4	128.09	1166.91	2020.1	70.90	326.9	33181.0	±811.5	0.106	±0.005	235.66	±17.46
-TX-10	57.30	291.38	327.52	150616.7	167.22	1459.50	2291.6	74.63	328.1	37231.4	±850.7	0.546	±0.005	257.34	±16.26
-TX-11	64.32	292.92	331.09	149159.3	200.11	1814.33	2552.6	82.89	327.5	41633.9	±894.3	0.103	±0.004	262.08	±20.30
-TX-12	70.04	291.65	328.48	150470.3	241.90	2084.32	2818.0	81.19	328.9	45478.7	±937.4	0.107	±0.004	288.62	±17.81
-TX-13	77.40	293.34	332.02	149826.9	286.50	2581.97	3090.0	89.99	329.0	50049.4	±987.4	0.103	±0.004	293.44	±22.61
-TX-14	83.35	292.84	330.67	151472.6	330.68	2822.73	3373.6	90.53	328.2	53964.8	±1033.9	0.104	±0.004	307.35	±18.36
-TX-15	91.53	292.33	332.01	150456.6	384.32	3444.96	3670.5	95.36	331.0	59334.9	±1099.5	0.100	±0.004	319.00	±24.27
-TX-16	96.71	294.93	332.72	151609.0	443.83	3739.63	3903.8	99.04	329.9	62284.5	±1133.8	0.104	±0.004	335.64	±20.13
-TX-17	104.81	293.44	333.36	151176.2	504.58	4496.18	4262.9	103.73	329.8	67750.5	±1204.5	0.101	±0.003	352.34	±27.60

Table 10.D: Friction factor and Nusselt number results for the perforated ring structured rod channel experiments (L-STAR-TX-G2) at a dimensionless heat up ratio $q_i^+ = 0.002$, with their respective uncertainties values.

Case G2	$\dot{m}_{CFM}$ [g/s]	$T_{i(T04)}$ [K]	$T_{o(T05)}$ [K]	P_i [Pa]	$\Delta p_{1'2'}$ [Pa]	Δp_{45} [Pa]	P_H [W]	$\dot{Q}_{wr}$ [W]	$T_{g,15}$ [K]	Re_i	σ_{Re_i}	$f_{D_{r,}(G2)}$	$\sigma_{f_{Dr,(G2)}}$	$Nu_{i,r(G2)}$	$\sigma_{Nu_i,r(G2)}$
-TX-01	-	-	-	-	-	-	-	-	-	-	-	-	-	-	-
-TX-02	9.79	291.51	331.26	151194.3	8.85	83.32	510.6	44.84	328.9	6359.6	±643.7	0.199	±0.041	111.30	±14.31
-TX-03	12.77	292.73	334.86	149463.3	13.90	125.61	679.4	53.26	331.3	8270.1	±649.9	0.181	±0.028	110.51	±12.86
-TX-04	19.30	292.61	338.75	149968.5	26.03	228.45	1026.3	67.14	331.7	12500.3	±673.5	0.149	±0.016	126.56	±10.72
-TX-05	25.96	290.30	338.61	150259.3	38.74	350.40	1348.3	74.05	328.9	16912.2	±703.5	0.124	±0.010	147.41	±10.92
-TX-06	31.82	290.52	340.39	150014.9	57.68	518.96	1688.5	83.49	330.2	20720.3	±732.8	0.122	±0.008	164.97	±13.76
-TX-07	38.45	290.55	340.17	150301.8	80.91	725.33	2018.6	87.99	330.0	25037.1	±771.8	0.118	±0.007	188.80	±15.11
-TX-09	44.57	290.82	341.36	150341.7	105.75	940.93	2345.0	95.00	330.5	29001.9	±811.7	0.115	±0.006	204.60	±15.85
-TX-09	51.13	291.70	343.69	150421.6	132.52	1176.70	2703.9	102.56	331.7	33199.8	±856.9	0.109	±0.005	221.22	±17.01
-TX-10	57.20	291.62	344.19	150590.9	167.83	1481.86	3067.5	109.53	332.3	37145.4	±903.8	0.111	±0.005	237.28	±17.75
-TX-11	63.78	293.12	345.87	150307.3	204.55	1806.02	3403.8	114.85	333.7	41260.3	±953.2	0.108	±0.005	255.97	±19.16
-TX-12	70.24	293.10	345.79	151589.2	236.95	2084.36	3691.1	118.50	333.1	45441.8	±1008.1	0.104	±0.004	268.78	±19.98
-TX-13	77.67	290.77	344.34	150065.6	295.67	2592.95	4166.4	124.06	331.7	50545.7	±1081.1	0.107	±0.004	288.37	±21.33
-TX-14	83.88	288.94	342.91	151679.2	329.27	2872.18	4481.5	128.30	329.8	54842.2	±1144.5	0.104	±0.004	297.82	±21.86
-TX-15	91.65	294.23	347.64	150059.9	408.46	3570.35	4851.3	132.87	334.7	59127.4	±1198.5	0.105	±0.004	323.78	±24.52
-TX-16	97.05	292.59	346.92	150113.7	443.69	3854.65	5188.9	139.84	333.5	62872.8	±1256.1	0.103	±0.004	328.33	±24.61
-TX-17	104.87	293.64	348.41	149964.1	523.29	4518.26	5648.7	146.51	334.9	67754.9	±1327.7	0.104	±0.003	347.27	±26.40

Table 11.D: Friction factor and Nusselt number results for the perforated ring structured rod channel experiments (L-STAR-TX-G2) at a dimensionless heat up ratio $q_i^+ = 0.003$, with their respective uncertainties values.

Case G2	$\dot{m}_{CFM}$ [g/s]	$T_{i(T04)}$ [K]	$T_{o(T05)}$ [K]	P_i [Pa]	$\Delta p_{1'2'}$ [Pa]	Δp_{45} [Pa]	P_H [W]	$\dot{Q}_{wr}$ [W]	$T_{g,15}$ [K]	Re_i	σ_{Re_i}	$f_{D_{r,}(G2)}$	$\sigma_{f_{Dr,(G2)}}$	$Nu_{i,r(G2)}$	$\sigma_{Nu_i,r(G2)}$
-TX-01	n/a	n/a	n/a	n/a	n/a	n/a	n/a	n/a	n/a	n/a	n/a	n/a	n/a	n/a	n/a
-TX-02	9.84	289.35	355.70	150959.6	7.26	65.70	762.4	86.57	343.4	6428.0	±647.5	0.162	±0.034	79.67	±9.73
-TX-03	12.90	289.18	357.66	150611.0	11.19	101.58	1022.1	96.10	345.7	8427.6	±655.0	0.145	±0.023	100.29	±10.11
-TX-04	19.65	290.29	359.43	149890.8	24.41	218.10	1536.5	113.53	347.2	12804.9	±675.8	0.135	±0.014	129.64	±10.24
-TX-05	26.29	292.22	362.70	149526.7	41.77	362.46	2021.8	130.70	348.8	17048.3	±701.6	0.128	±0.010	149.31	±10.17
-TX-06	32.17	292.62	367.97	150111.4	59.11	508.78	2556.1	152.91	351.4	20835.8	±730.7	0.122	±0.008	164.95	±13.41
-TX-07	38.52	290.97	366.25	149992.3	82.71	708.46	3013.6	159.59	349.3	25053.6	±771.5	0.120	±0.007	184.68	±14.30
-TX-09	45.09	291.30	367.23	149220.5	112.57	958.98	3569.4	172.19	350.6	29303.4	±814.3	0.118	±0.006	209.09	±15.83
-TX-09	51.03	292.67	370.31	150943.8	139.68	1186.7	4054.4	186.61	352.3	33053.7	±853.9	0.116	±0.006	221.72	±14.41
-TX-10	57.15	289.83	369.42	149135.3	170.61	1442.6	4583.5	197.80	350.2	37282.0	±908.3	0.112	±0.005	236.25	±17.30
-TX-11	64.26	291.87	370.09	149252.1	217.95	1842.9	5095.7	204.35	351.7	41700.7	±960.8	0.113	±0.005	258.40	±18.95
-TX-12	-	-	-	-	-	-	-	-	-	-	-	-	-	-	-

Table 12.D: Axial cladding wall temperature distribution for the solid ring structured rod channel experiments (L-STAR-TX-G1) at a dimensionless heat up ratio $q_i^+ = 0.0015$.

$Z_{TC,i}$ [m]	TC	TX01	TX02	TX03	TX04	TX05	TX06	TX07	TX08	TX09	TX10	TX11	TX12	TX13	TX14	TX15	TX16	TX17
0.074	TT03	-	-	-	-	-	-	-	-	-	-	-	-	-	-	-	-	-
0.307	TT07	325.1	330.5	332.4	337.2	339.2	343.1	344.6	347.7	349.0	351.7	352.4	353.7	355.4	356.4	358.3	359.7	361.5
0.472	TT00	331.3	338.7	341.4	348.3	351.5	356.6	359.0	363.1	365.3	368.2	370.0	371.9	374.4	375.9	378.4	380.4	383.0
0.472	TT02	331.5	338.9	341.7	348.6	351.8	356.9	357.9	363.5	365.8	368.8	370.6	372.6	375.1	376.7	379.2	381.3	383.9
0.478	TT24	330.1	337.4	340.1	347.0	350.1	355.1	357.5	361.6	363.7	366.7	368.4	370.3	372.7	374.2	376.7	378.6	381.2
0.484	TT04	331.5	338.9	341.7	348.6	351.8	357.0	359.4	363.5	365.8	368.7	370.6	372.5	375.0	376.6	379.1	381.2	383.8
0.483	TT06	331.5	338.8	341.6	348.5	351.7	356.8	359.2	363.3	365.6	368.5	370.4	372.3	374.8	376.3	378.8	380.9	383.5
0.489	TT28	331.7	339.0	341.8	348.8	352.1	357.2	359.7	363.9	366.3	369.3	371.3	373.2	375.8	377.5	380.1	382.2	385.0
0.494	TT08	331.3	338.6	341.3	348.2	351.4	356.5	358.9	363.1	365.4	368.3	370.2	372.1	374.6	376.2	378.7	380.8	383.4
0.494	TT10	331.4	338.7	341.4	348.2	351.4	356.4	358.8	362.9	365.2	368.0	369.9	371.8	374.2	375.7	378.3	380.3	382.9
0.500	TT32	331.3	338.6	341.3	348.2	351.3	356.4	358.8	362.9	365.2	368.1	370.0	371.9	374.3	375.9	378.4	380.4	383.0
0.504	TT12	331.2	338.5	341.1	347.9	350.9	355.8	358.0	362.0	364.2	367.0	368.7	370.4	372.8	374.2	376.6	378.5	380.9
0.505	TT14	331.3	338.6	341.2	348.1	351.2	356.2	358.5	362.6	364.9	367.7	369.5	371.4	373.8	375.2	377.7	379.7	382.2
0.509	TT36	329.8	337.1	339.7	346.5	349.5	354.5	356.7	360.7	362.9	365.7	367.4	369.1	371.4	372.8	375.2	377.1	379.5
0.515	TT16	331.2	338.5	341.3	348.2	351.4	356.5	358.8	363.0	365.3	368.1	369.9	371.8	374.2	375.7	378.2	380.1	382.6
0.517	TT18	331.5	338.8	341.6	348.5	351.8	356.9	359.3	363.5	365.8	368.8	370.6	372.5	374.9	376.5	379.0	381.0	383.6
0.520	TT40	331.2	338.5	341.2	348.1	351.4	356.5	358.9	363.1	365.4	368.3	370.1	372.0	374.4	375.9	378.5	380.4	383.0
0.526	TT20	331.4	338.8	341.6	348.6	351.8	357.1	359.6	363.8	366.3	369.3	371.2	373.1	375.7	377.3	379.9	382.0	384.7
0.526	TT22	331.5	338.8	341.6	348.6	351.9	357.1	359.6	363.9	366.2	369.2	371.2	373.1	375.7	377.3	379.9	381.9	384.6
0.532	TT44	331.5	338.9	341.7	348.7	352.1	357.4	359.9	364.2	366.7	369.7	371.7	373.7	376.3	377.9	380.5	382.6	385.3
0.532	TT23	331.3	338.6	341.4	348.4	351.7	356.8	359.3	363.6	365.9	368.9	370.8	372.8	375.3	376.9	379.5	381.5	384.2
0.690	TT11	328.7	335.4	337.7	341.0	344.4	349.1	351.4	355.4	357.4	360.6	362.2	364.0	366.4	368.0	370.5	372.5	374.9
0.826	TT15	330.0	337.4	340.4	344.8	349.0	354.7	357.7	362.4	365.3	368.8	371.3	373.6	376.7	378.7	381.8	384.2	387.3
0.982	TT01	328.5	335.8	338.7	342.9	347.2	352.8	355.8	360.3	363.1	366.5	368.8	371.1	374.0	376.0	379.0	381.3	384.3
0.983	TT26	328.3	335.6	338.5	343.3	347.6	353.2	356.2	360.8	363.5	367.0	369.4	371.7	374.7	376.7	379.7	382.1	385.2

Table 12.D (continuation): Axial cladding wall temperature distribution for the solid ring structured rod channel experiments (L-STAR-TX-G1) at a dimensionless heat up ratio $q_i^+ = 0.0015$.

$Z_{TC,i}$ [m]	TC	TX01	TX02	TX03	TX04	TX05	TX06	TX07	TX08	TX09	TX10	TX11	TX12	TX13	TX14	TX15	TX16	TX17
0.988	TT25	328.3	335.4	338.3	342.9	347.1	352.6	355.4	359.9	362.5	366.0	368.1	370.3	373.2	375.1	378.0	380.2	383.2
0.993	TT05	328.1	335.4	338.4	343.2	347.5	353.2	356.2	360.8	363.6	367.1	369.5	371.8	374.8	376.7	379.7	382.1	385.2
0.995	TT30	-	-	-	-	-	-	-	-	-	-	-	-	-	-	-	-	-
0.999	TT29	328.3	335.5	338.5	343.3	346.7	353.3	355.7	360.9	363.7	367.2	369.6	371.9	374.9	376.9	379.9	382.3	385.4
1.005	TT09	327.9	335.1	338.0	342.7	346.9	352.5	355.4	359.8	362.5	365.9	368.1	370.3	373.1	375.0	377.8	380.1	383.0
1.005	TT34	327.9	335.1	338.0	342.5	346.7	352.1	354.9	359.3	362.0	365.2	367.4	369.5	372.3	374.1	376.9	379.1	381.9
1.012	TT33	327.9	335.1	338.0	342.7	346.9	352.5	355.4	359.9	362.6	366.0	368.3	370.5	373.4	375.3	378.2	380.6	383.5
1.016	TT13	327.8	335.0	337.8	342.4	346.5	352.0	354.8	359.2	361.8	365.1	367.3	369.4	372.2	374.0	376.7	378.9	381.7
1.016	TT38	327.8	334.9	337.8	342.4	346.5	352.0	354.8	359.2	361.9	365.2	367.3	369.5	372.2	374.0	376.8	379.0	381.8
1.021	TT37	327.7	334.8	337.6	342.1	346.2	351.6	354.3	358.7	361.3	364.5	366.6	368.7	371.4	373.1	375.9	378.0	380.7
1.026	TT17	327.7	334.9	337.8	342.5	346.7	352.3	355.2	359.7	362.4	365.8	368.0	370.2	373.1	375.0	377.8	380.1	383.0
1.026	TT42	327.6	334.7	337.6	342.3	346.6	352.1	355.1	359.5	362.3	365.7	367.9	370.2	373.0	374.9	377.8	380.1	382.9
1.031	TT41	327.5	334.6	337.5	342.1	346.4	351.9	354.9	359.3	362.1	365.5	367.7	370.0	372.8	374.7	377.6	379.9	382.8
1.038	TT21	327.5	334.6	337.6	342.3	346.6	352.2	355.3	359.9	362.7	366.3	368.7	371.0	374.1	376.1	379.1	381.5	384.6
1.037	TT46	327.4	334.5	337.4	342.1	346.4	352.1	355.1	359.7	362.6	366.2	368.6	370.9	373.9	376.0	379.0	381.5	384.5
1.043	TT45	327.3	334.5	337.4	342.1	346.4	352.1	355.2	359.8	362.7	366.3	368.7	371.0	374.1	376.2	379.2	381.7	384.8
1.044	TT47	327.2	334.2	337.1	341.8	346.0	351.6	354.6	359.1	361.9	365.5	367.8	370.1	373.1	375.1	378.0	380.4	383.4
1.419	TT19	323.1	329.9	332.7	337.2	341.0	345.8	349.2	353.2	355.9	359.8	362.4	364.4	367.5	369.4	372.0	374.1	376.9
1.798	TT27	319.8	325.9	328.7	332.7	336.8	341.5	344.8	348.6	351.2	355.3	357.7	359.8	362.9	364.9	367.5	369.7	372.6
2.138	TT31	315.9	321.4	324.6	328.2	333.2	338.2	342.0	346.2	348.6	352.8	355.3	357.5	360.9	363.2	366.0	368.9	371.9
2.558	TT35	312.8	317.8	321.0	324.1	328.6	333.6	337.2	341.1	343.5	347.5	349.7	351.9	355.1	357.3	359.9	362.6	365.6
2.928	TT39	-	-	-	-	-	-	-	-	-	-	-	-	-	-	-	-	-
3.320	TT43	-	-	-	-	-	-	-	-	-	-	-	-	-	-	-	-	-

Table 13.D: Axial cladding wall temperature distribution for the solid ring structured rod channel experiments (L-STAR-TX-G1) at a dimensionless heat up ratio $q_i^+ = 0.002$.

$Z_{TC,i}$ [m]	TC	TX01	TX02	TX03	TX04	TX05	TX06	TX07	TX08	TX09	TX10	TX11	TX12	TX13	TX14	TX15	TX16	TX17
0.074	TT03	-	-	-	-	-	-	-	-	-	-	-	-	-	-	-	-	-
0.307	TT07	-	-	349.7	-	356.2	359.3	362.7	365.4	366.3	369.6	372.4	375.1	377.2	379.6	381.8	384.5	386.4
0.472	TT00	-	-	363.2	-	373.1	377.8	380.2	383.1	385.5	389.8	393.5	397.3	400.1	403.1	406.0	409.4	412.3
0.472	TT02	-	-	363.4	-	373.4	378.2	379.2	383.7	386.0	390.4	394.3	398.1	401.0	404.1	407.0	410.5	413.5
0.478	TT24	-	-	361.7	-	370.2	376.2	378.7	381.6	383.8	388.1	391.8	395.5	398.2	401.2	404.0	407.4	410.3
0.484	TT04	-	-	362.9	-	373.5	378.2	380.7	383.6	386.0	390.3	394.2	397.9	400.8	403.8	406.7	410.3	413.2
0.483	TT06	-	-	362.6	-	373.3	378.0	380.5	383.4	385.7	390.1	393.9	397.6	400.4	403.5	406.4	409.9	412.8
0.489	TT28	-	-	362.8	-	373.6	378.4	381.1	384.1	386.5	390.9	394.8	398.7	401.6	404.8	407.8	411.4	414.5
0.494	TT08	-	-	362.8	-	372.8	377.6	380.1	383.1	385.4	389.7	393.5	397.3	400.2	403.2	406.1	409.7	412.6
0.494	TT10	-	-	362.5	-	372.8	377.5	380.0	382.9	385.1	389.4	393.1	396.8	399.6	402.6	405.5	408.9	411.8
0.500	TT32	-	-	362.2	-	372.7	377.4	380.0	382.9	385.2	389.4	393.2	396.9	399.8	402.8	405.7	409.2	412.1
0.504	TT12	-	-	362.1	-	372.1	376.6	379.1	381.8	383.9	388.0	391.6	395.1	397.7	400.6	403.3	406.6	409.2
0.505	TT14	-	-	362.4	-	372.5	377.2	379.6	382.5	384.6	388.8	392.5	396.1	398.9	401.8	404.6	408.0	410.7
0.509	TT36	-	-	360.5	-	369.4	375.3	377.8	380.5	382.6	386.7	390.3	393.8	396.4	399.3	402.0	405.2	407.9
0.515	TT16	-	-	362.2	-	372.8	377.5	380.0	382.9	385.1	389.4	393.1	396.7	399.4	402.4	405.2	408.5	411.3
0.517	TT18	-	-	362.6	-	373.2	378.0	380.6	383.5	385.7	390.1	393.9	397.5	400.3	403.3	406.2	409.6	412.4
0.520	TT40	-	-	362.1	-	372.7	377.5	380.1	383.0	385.3	389.6	393.4	397.1	399.9	402.9	405.7	409.1	411.9
0.526	TT20	-	-	362.3	-	373.4	378.3	380.9	383.9	386.4	390.8	394.7	398.6	401.5	404.6	407.6	411.1	414.0
0.526	TT22	-	-	362.2	-	373.4	378.3	381.0	383.9	386.5	390.9	394.8	398.7	401.5	404.6	407.6	411.1	414.0
0.532	TT44	-	-	361.9	-	373.6	378.6	381.4	384.4	387.0	391.5	395.5	399.4	402.4	405.6	408.6	412.2	415.2
0.532	TT23	-	-	361.8	-	373.1	378.0	380.7	383.7	386.2	390.6	394.5	398.3	401.2	404.3	407.3	410.8	413.7
0.690	TT11	-	-	355.7	-	362.4	366.7	370.2	373.6	376.0	380.2	384.0	387.6	390.5	393.6	396.5	399.8	402.3
0.826	TT15	-	-	358.3	-	368.3	373.8	377.7	381.8	385.4	390.4	395.0	399.4	403.0	406.6	410.2	414.1	417.1
0.982	TT01	-	-	355.7	-	366.0	371.4	375.2	379.4	382.6	387.4	391.8	396.2	399.6	403.1	406.5	410.4	413.5
0.983	TT26	-	-	355.8	-	366.4	371.9	375.7	379.9	383.1	388.0	392.5	396.8	400.3	403.8	407.3	411.2	414.5

Table 13.D (continuation): Axial cladding wall temperature distribution for the solid ring structured rod channel experiments (L-STAR-TX-G1) at a dimensionless heat up ratio $q_i^+ = 0.002$.

$Z_{TC,i}$ [m]	TC	TX01	TX02	TX03	TX04	TX05	TX06	TX07	TX08	TX09	TX10	TX11	TX12	TX13	TX14	TX15	TX16	TX17
0.988	TT25	-	-	355.9	-	365.7	371.0	374.7	378.7	381.8	386.5	390.8	395.0	398.3	401.7	405.0	408.8	411.9
0.993	TT05	-	-	355.4	-	366.4	371.9	375.7	380.0	383.3	388.2	392.6	397.0	400.5	404.0	407.4	411.4	414.7
0.995	TT30	-	-	-	-	-	-	-	-	-	-	-	-	-	-	-	-	-
0.999	TT29	-	-	355.6	-	365.2	372.0	374.8	380.1	383.3	388.3	392.7	397.1	400.5	404.1	407.6	411.5	414.8
1.005	TT09	-	-	355.4	-	365.6	371.0	374.7	378.9	381.9	386.6	390.9	395.1	398.4	401.8	405.0	408.8	411.9
1.005	TT34	-	-	355.6	-	365.2	370.5	374.2	378.2	381.1	385.8	390.0	394.0	397.2	400.5	403.7	407.3	410.3
1.012	TT33	-	-	355.0	-	365.6	371.0	374.7	378.9	382.0	386.8	391.1	395.4	398.7	402.1	405.5	409.3	412.4
1.016	TT13	-	-	354.9	-	365.0	370.3	374.0	378.0	381.0	385.6	389.8	393.8	397.0	400.3	403.5	407.1	410.0
1.016	TT38	-	-	354.7	-	365.0	370.3	374.0	378.0	381.0	385.7	389.9	394.0	397.2	400.5	403.6	407.3	410.2
1.021	TT37	-	-	355.0	-	364.6	369.8	373.5	377.5	380.3	384.9	389.0	393.0	396.1	399.4	402.5	406.0	408.9
1.026	TT17	-	-	355.0	-	365.3	370.7	374.6	378.7	381.8	386.6	390.9	395.1	398.4	401.8	405.1	408.8	411.8
1.026	TT42	-	-	354.9	-	365.1	370.5	374.4	378.5	381.7	386.5	390.8	395.0	398.4	401.8	405.1	408.9	411.9
1.031	TT41	-	-	354.8	-	364.8	370.2	374.1	378.3	381.4	386.2	390.5	394.7	398.1	401.5	404.8	408.6	411.5
1.038	TT21	-	-	354.5	-	365.1	370.6	374.8	378.9	382.3	387.3	391.8	396.2	399.8	403.4	407.0	410.9	414.0
1.037	TT46	-	-	354.2	-	364.9	370.5	374.5	378.7	382.1	387.1	391.6	396.0	399.5	403.2	406.7	410.7	413.8
1.043	TT45	-	-	353.7	-	364.9	370.4	374.5	378.8	382.2	387.1	391.7	396.1	399.7	403.3	406.9	410.9	414.1
1.044	TT47	-	-	353.5	-	364.4	369.8	373.9	378.1	381.3	386.1	390.6	394.9	398.4	401.9	405.3	409.3	412.4
1.419	TT19	-	-	348.2	-	357.0	362.3	367.8	371.8	375.0	379.4	384.0	388.1	391.5	394.9	398.8	401.9	404.6
1.798	TT27	-	-	343.1	-	351.5	356.7	362.4	366.4	369.2	373.6	378.2	382.3	385.7	389.2	393.2	396.5	399.5
2.138	TT31	-	-	336.3	-	347.5	353.1	358.9	362.6	365.9	370.7	375.5	379.9	383.7	387.5	390.9	395.0	398.1
2.558	TT35	-	-	331.02	-	343.69	349.10	355.40	358.85	362.00	366.59	371.15	375.30	378.96	382.67	385.96	389.80	392.50
2.928	TT39	-	-	-	-	-	-	-	-	-	-	-	-	-	-	-	-	-
3.320	TT43	-	-	-	-	-	-	-	-	-	-	-	-	-	-	-	-	-

Table 14.D: Axial cladding wall temperature distribution for the solid ring structured rod channel experiments (L-STAR-TX-G1) at a dimensionless heat up ratio $q_i^+ = 0.003$.

$Z_{TC,i}$ [m]	TC	TX01	TX02	TX03	TX04	TX05	TX06	TX07	TX08	TX09	TX10	TX11	TX12	TX13	TX14	TX15	TX16	TX17
0.074	TT03	-	-	-	-	-	-	-	-	-	-	-	-	-	-	-	-	-
0.307	TT07	-	-	-	-	393.8	397.5	403.2	408.6	412.6	414.6	417.7	422.1	-	-	-	-	-
0.472	TT00	-	-	-	-	414.0	420.0	427.6	434.8	440.4	444.1	448.6	454.3	-	-	-	-	-
0.472	TT02	-	-	-	-	414.4	420.5	425.1	435.6	441.3	445.1	449.8	455.6	-	-	-	-	-
0.478	TT24	-	-	-	-	412.6	418.3	425.9	433.1	438.7	442.3	446.8	452.4	-	-	-	-	-
0.484	TT04	-	-	-	-	414.4	420.5	428.1	435.4	441.1	444.9	449.5	455.2	-	-	-	-	-
0.483	TT06	-	-	-	-	414.1	420.2	427.8	435.0	440.7	444.5	449.0	454.7	-	-	-	-	-
0.489	TT28	-	-	-	-	414.5	420.7	428.4	435.9	441.7	445.6	450.4	456.3	-	-	-	-	-
0.494	TT08	-	-	-	-	413.6	419.5	427.1	434.3	440.0	443.7	448.3	453.9	-	-	-	-	-
0.494	TT10	-	-	-	-	413.4	419.3	426.7	433.8	439.4	443.0	447.5	453.0	-	-	-	-	-
0.500	TT32	-	-	-	-	413.3	419.2	426.8	434.0	439.7	443.4	448.0	453.6	-	-	-	-	-
0.504	TT12	-	-	-	-	412.5	418.1	425.3	432.2	437.5	440.9	445.1	450.4	-	-	-	-	-
0.505	TT14	-	-	-	-	413.1	418.8	426.2	433.2	438.6	442.2	446.5	451.9	-	-	-	-	-
0.509	TT36	-	-	-	-	411.3	416.8	424.1	431.0	436.4	439.8	444.0	449.3	-	-	-	-	-
0.515	TT16	-	-	-	-	413.4	419.2	426.7	433.8	439.3	442.9	447.3	452.7	-	-	-	-	-
0.517	TT18	-	-	-	-	413.9	419.9	427.4	434.6	440.2	443.9	448.4	453.9	-	-	-	-	-
0.520	TT40	-	-	-	-	413.3	419.3	426.8	434.1	439.7	443.4	447.8	453.4	-	-	-	-	-
0.526	TT20	-	-	-	-	414.2	420.3	428.0	435.4	441.2	445.0	449.7	455.4	-	-	-	-	-
0.526	TT22	-	-	-	-	414.3	420.4	428.1	435.5	441.3	445.2	449.8	455.6	-	-	-	-	-
0.532	TT44	-	-	-	-	414.5	420.8	428.7	436.2	442.2	446.1	450.8	456.7	-	-	-	-	-
0.532	TT23	-	-	-	-	414.0	420.2	427.9	435.3	441.1	444.9	449.5	455.3	-	-	-	-	-
0.690	TT11	-	-	-	-	403.7	409.2	416.3	422.0	427.4	430.8	435.2	440.7	-	-	-	-	-
0.826	TT15	-	-	-	-	411.0	417.9	426.4	433.5	440.1	444.8	450.3	456.8	-	-	-	-	-
0.982	TT01	-	-	-	-	408.1	415.0	423.4	430.4	436.8	441.2	446.6	453.1	-	-	-	-	-
0.983	TT26	-	-	-	-	408.5	415.5	423.9	430.9	437.4	441.9	447.4	453.9	-	-	-	-	-

Table 14.D (continuation): Axial cladding wall temperature distribution for the solid ring structured rod channel experiments (L-STAR-TX-G1) at a dimensionless heat up ratio $q_i^+ = 0.003$.

$Z_{TC,i}$ [m]	TC	TX01	TX02	TX03	TX04	TX05	TX06	TX07	TX08	TX09	TX10	TX11	TX12	TX13	TX14	TX15	TX16	TX17
0.988	TT25	-	-	-	-	-	407.6	414.3	422.4	429.2	435.5	439.7	444.9	-	-	-	-	-
0.993	TT05	-	-	-	-	-	408.6	415.7	424.1	431.2	437.8	442.4	447.9	-	-	-	-	-
0.995	TT30	-	-	-	-	-	-	-	-	-	-	-	-	-	-	-	-	-
0.999	TT29	-	-	-	-	-	407.1	415.7	423.1	431.2	437.8	442.4	447.9	-	-	-	-	-
1.005	TT09	-	-	-	-	-	407.6	414.4	422.6	429.5	435.8	440.2	445.4	-	-	-	-	-
1.005	TT34	-	-	-	-	-	407.1	413.7	421.7	428.4	434.6	438.8	443.9	-	-	-	-	-
1.012	TT33	-	-	-	-	-	407.6	414.4	422.6	429.5	435.9	440.4	445.6	-	-	-	-	-
1.016	TT13	-	-	-	-	-	406.8	413.4	421.4	428.0	434.2	438.4	443.4	-	-	-	-	-
1.016	TT38	-	-	-	-	-	406.7	413.3	421.4	428.1	434.2	438.5	443.5	-	-	-	-	-
1.021	TT37	-	-	-	-	-	406.3	412.7	420.7	427.2	433.3	437.4	442.2	-	-	-	-	-
1.026	TT17	-	-	-	-	-	407.2	414.0	422.2	429.0	435.4	439.7	444.9	-	-	-	-	-
1.026	TT42	-	-	-	-	-	407.0	413.8	422.0	428.9	435.2	439.6	444.8	-	-	-	-	-
1.031	TT41	-	-	-	-	-	406.6	413.4	421.5	428.4	434.7	439.1	444.3	-	-	-	-	-
1.038	TT21	-	-	-	-	-	406.9	414.0	422.3	429.4	436.0	440.6	446.0	-	-	-	-	-
1.037	TT46	-	-	-	-	-	406.7	413.7	422.1	429.2	435.7	440.3	445.8	-	-	-	-	-
1.043	TT45	-	-	-	-	-	406.7	413.7	422.2	429.3	435.8	440.4	445.9	-	-	-	-	-
1.044	TT47	-	-	-	-	-	406.1	413.0	421.3	428.2	434.7	439.1	444.4	-	-	-	-	-
1.419	TT19	-	-	-	-	-	397.6	404.7	412.1	418.9	425.1	429.2	434.6	-	-	-	-	-
1.798	TT27	-	-	-	-	-	390.6	397.4	404.7	411.3	417.4	421.5	427.0	-	-	-	-	-
2.138	TT31	-	-	-	-	-	385.3	394.4	399.4	407.6	413.7	418.4	424.0	-	-	-	-	-
2.558	TT35	-	-	-	-	-	377.9	386.7	391.4	399.2	405.2	409.5	414.8	-	-	-	-	-
2.928	TT39	-	-	-	-	-	-	-	-	-	-	-	-	-	-	-	-	-
3.320	TT43	-	-	-	-	-	-	-	-	-	-	-	-	-	-	-	-	-

Table 15.D: Axial cladding wall temperature distribution for the perforated ring structured rod channel experiments (L-STAR-TX-G2) at a dimensionless heat up ratio $q_i^+ = 0.0015$.

$Z_{TC,i}$ [m]	TC	TX01	TX02	TX03	TX04	TX05	TX06	TX07	TX08	TX09	TX10	TX11	TX12	TX13	TX14	TX15	TX16	TX17
0.074	TT03	-	-	-	-	-	-	-	-	-	-	-	-	-	-	-	-	-
0.307	TT07	-	-	334.8	341.2	345.9	351.7	346.0	356.4	347.2	353.3	352.4	356.7	355.2	362.4	357.4	365.6	360.2
0.472	TT00	-	-	345.2	352.5	357.9	365.2	363.5	371.4	366.8	370.0	374.1	375.1	378.7	382.5	383.0	387.7	387.5
0.472	TT02	-	-	345.4	352.8	358.2	365.5	363.7	371.8	367.0	370.4	374.4	375.6	379.1	383.1	383.3	388.3	387.9
0.478	TT24	-	-	345.3	352.4	356.4	364.9	363.5	371.0	366.7	369.4	374.0	374.3	378.6	381.5	382.8	386.7	387.3
0.484	TT04	-	-	345.1	352.3	357.6	364.8	363.2	370.8	366.4	369.2	373.6	374.1	378.1	381.3	382.3	386.5	386.7
0.483	TT06	-	-	344.9	351.9	357.1	364.2	362.6	370.1	365.7	368.3	372.8	373.0	377.2	380.1	381.2	385.1	385.5
0.489	TT28	-	-	345.1	352.3	357.5	364.7	363.2	370.6	366.4	369.0	373.6	373.8	378.2	381.0	382.3	386.0	386.8
0.494	TT08	-	-	-	-	-	-	-	-	-	-	-	-	-	-	-	-	-
0.494	TT10	-	-	344.8	351.8	356.9	364.0	362.7	369.7	365.8	367.9	372.9	372.6	377.4	379.6	381.4	384.5	385.7
0.500	TT32	-	-	344.5	351.7	356.7	363.8	362.1	369.5	365.1	367.6	372.0	372.3	376.4	379.2	380.4	384.2	384.7
0.504	TT12	-	-	344.5	351.7	356.9	363.9	362.0	369.6	365.0	367.7	371.9	372.4	376.2	379.3	380.2	384.2	384.3
0.505	TT14	-	-	344.7	351.8	356.9	364.0	362.4	369.8	365.6	367.9	372.6	372.6	377.0	379.6	381.0	384.5	385.2
0.509	TT36	-	-	344.5	351.8	355.6	363.9	362.0	369.6	365.0	367.7	371.9	372.4	376.2	379.3	380.1	384.2	384.3
0.515	TT16	-	-	344.6	351.9	357.1	364.3	362.6	370.2	365.9	368.5	373.1	373.3	377.6	380.5	381.7	385.5	386.0
0.517	TT18	-	-	344.9	352.2	357.5	364.7	363.2	370.7	366.5	369.2	373.8	374.0	378.4	381.3	382.6	386.4	387.0
0.520	TT40	-	-	344.6	351.9	357.1	364.3	362.6	370.3	365.9	368.6	373.1	373.5	377.7	380.6	381.7	385.8	386.1
0.526	TT20	-	-	344.7	352.2	357.5	364.7	363.0	370.8	366.4	369.3	373.7	374.2	378.4	381.5	382.6	386.7	387.2
0.526	TT22	-	-	344.6	352.2	357.4	364.7	362.9	370.8	366.3	369.3	373.6	374.3	378.3	381.6	382.6	386.9	387.1
0.532	TT44	-	-	344.4	352.1	357.3	364.5	362.3	370.6	365.6	369.0	372.8	373.9	377.3	381.2	381.4	386.4	385.8
0.532	TT23	-	-	344.3	352.0	357.2	364.4	362.4	370.5	365.7	368.9	372.9	373.8	377.5	381.1	381.7	386.4	386.2
0.690	TT11	-	-	339.5	347.5	352.5	359.2	354.4	364.8	356.9	362.9	363.3	367.5	367.3	374.4	370.7	379.5	374.5
0.826	TT15	-	-	341.6	350.7	356.5	364.0	358.8	370.7	362.1	369.8	369.2	375.0	373.7	382.7	377.6	388.3	381.9
0.982	TT01	-	-	339.6	348.5	354.3	361.7	356.6	368.5	359.6	367.6	366.8	373.1	371.3	380.9	375.4	386.3	379.8
0.983	TT26	-	-	339.7	348.6	354.5	361.8	356.7	368.6	359.7	367.7	366.9	373.1	371.5	380.9	375.5	386.2	379.9

Table 15.D (continuation): Axial cladding wall temperature distribution for the perforated ring structured rod channel experiments (L-STAR-TX-G2) at a dimensionless heat up ratio $q_i^+ = 0.0015$.

$Z_{TC,i}$ [m]	TC	TX01	TX02	TX03	TX04	TX05	TX06	TX07	TX08	TX09	TX10	TX11	TX12	TX13	TX14	TX15	TX16	TX17
0.988	TT25	-	-	339.9	348.8	354.6	362.0	356.9	368.8	359.9	367.9	367.1	373.4	371.7	381.1	375.7	386.4	380.1
0.993	TT05	-	-	339.4	348.3	354.1	361.5	356.5	368.3	359.5	367.4	366.6	372.8	371.1	380.5	375.0	385.6	379.4
0.995	TT30	-	-	-	-	-	-	-	-	-	-	-	-	-	-	-	-	-
0.999	TT29	-	-	339.6	348.5	354.4	361.8	356.7	368.6	359.8	367.7	366.9	373.1	371.5	380.9	375.5	386.0	379.8
1.005	TT09	-	-	339.4	348.3	354.2	361.7	356.5	368.6	359.6	367.8	366.8	373.3	371.3	381.2	375.3	386.3	379.7
1.005	TT34	-	-	339.6	348.5	354.3	361.8	356.7	368.6	359.8	367.7	366.9	373.1	371.5	380.9	375.4	385.9	379.8
1.012	TT33	-	-	339.1	347.9	353.8	361.1	355.8	367.8	358.7	366.9	365.7	372.1	370.1	379.8	373.9	384.8	378.2
1.016	TT13	-	-	339.0	347.9	353.7	361.1	355.7	367.8	358.6	366.9	365.5	372.3	369.9	380.0	373.7	384.9	377.9
1.016	TT38	-	-	338.9	347.8	353.6	360.9	355.5	367.6	358.4	366.7	365.2	372.0	369.5	379.6	373.2	384.4	377.4
1.021	TT37	-	-	339.2	348.1	354.0	361.4	356.2	368.3	359.4	367.6	366.5	373.1	371.0	380.9	375.0	385.8	379.3
1.026	TT17	-	-	339.1	348.1	354.0	361.5	356.2	368.5	359.5	367.9	366.7	373.5	371.3	381.4	375.3	386.4	379.7
1.026	TT42	-	-	339.0	348.0	353.9	361.4	356.2	368.5	359.5	367.9	366.7	373.6	371.3	381.5	375.4	386.6	379.9
1.031	TT41	-	-	338.9	347.9	353.9	361.4	356.1	368.5	359.3	368.0	366.6	373.8	371.2	381.8	375.3	386.7	379.7
1.038	TT21	-	-	338.7	347.6	353.5	360.9	355.6	367.8	358.9	367.0	366.0	372.7	370.6	380.5	374.7	385.7	379.1
1.037	TT46	-	-	338.5	347.3	353.1	360.4	355.2	367.2	358.2	366.3	365.3	371.8	369.8	379.5	373.8	384.8	378.1
1.043	TT45	-	-	338.1	346.9	352.5	359.8	354.4	366.5	357.4	365.4	364.3	370.8	368.7	378.3	372.5	383.5	376.7
1.044	TT47	-	-	337.9	346.7	352.4	359.7	354.2	366.3	357.1	365.2	364.1	370.6	368.5	378.0	372.3	383.3	376.5
1.419	TT19	-	-	333.6	341.8	347.4	354.5	350.0	361.7	352.8	360.7	360.1	366.3	364.7	373.9	368.8	379.5	373.1
1.798	TT27	-	-	329.8	338.0	343.7	350.9	345.4	358.2	348.6	357.3	355.9	363.0	360.6	370.7	364.7	376.5	369.1
2.138	TT31	-	-	324.6	332.9	338.2	345.3	339.6	352.2	342.7	351.3	350.0	357.3	354.5	364.8	358.1	371.2	362.6
2.558	TT35	-	-	320.8	328.6	333.7	340.5	334.6	347.3	337.8	346.2	345.0	352.2	349.2	359.5	352.6	365.6	356.9
2.928	TT39	-	-	-	-	-	-	-	-	-	-	-	-	-	-	-	-	-
3.320	TT43	-	-	-	-	-	-	-	-	-	-	-	-	-	-	-	-	-

Table 16.D: Axial cladding wall temperature distribution for the perforated ring structured rod channel experiments (L-STAR-TX-G2) at a dimensionless heat up ratio $q_i^+ = 0.002$.

$Z_{TC,i}$ [m]	TC	TX01	TX02	TX03	TX04	TX05	TX06	TX07	TX08	TX09	TX10	TX11	TX12	TX13	TX14	TX15	TX16	TX17
0.074	TT03	-	341.7	348.8	355.4	356.9	361.4	362.2	364.7	368.2	370.6	372.7	373.3	374.3	374.2	378.0	379.4	381.8
0.307	TT07	-	353.2	360.5	369.8	375.3	381.8	384.1	388.2	393.2	397.0	400.4	401.7	404.4	405.4	409.7	412.4	416.0
0.472	TT00	-	353.4	360.8	370.1	375.5	382.0	384.3	388.4	393.4	397.3	400.6	401.9	404.7	405.7	410.0	412.8	416.4
0.472	TT02	-	351.8	360.4	368.0	373.9	380.2	382.5	386.5	391.5	395.2	398.5	399.9	402.5	403.5	407.8	410.5	414.1
0.478	TT24	-	352.9	360.3	369.4	374.9	381.3	383.6	387.6	392.5	396.3	399.5	400.8	403.4	404.4	408.6	411.3	414.8
0.484	TT04	-	352.7	359.9	368.9	374.4	380.7	382.9	386.8	391.6	395.3	398.4	399.7	402.2	403.1	407.2	409.8	413.2
0.483	TT06	-	353.0	360.2	369.3	374.8	381.3	383.6	387.6	392.5	396.3	399.5	400.8	403.5	404.5	408.7	411.4	414.9
0.489	TT28	-	-	-	-	-	-	-	-	-	-	-	-	-	-	-	-	-
0.494	TT08	-	352.7	359.8	368.7	374.4	380.8	382.9	386.9	391.8	395.5	398.6	399.9	402.4	403.4	407.4	410.1	413.4
0.494	TT10	-	352.4	359.6	368.5	373.8	380.1	382.1	386.0	390.8	394.4	397.4	398.8	401.2	402.2	406.3	408.8	412.2
0.500	TT32	-	352.4	359.7	368.7	373.8	380.1	382.1	386.0	390.7	394.3	397.3	398.6	400.9	401.9	405.8	408.4	411.7
0.504	TT12	-	352.6	359.8	368.7	374.2	380.6	382.7	386.6	391.4	395.1	398.1	399.5	401.8	402.9	406.7	409.5	412.7
0.505	TT14	-	350.8	359.7	367.1	372.3	378.4	380.5	384.3	389.0	392.7	395.6	396.9	399.3	400.3	404.2	406.8	410.1
0.509	TT36	-	352.4	359.8	368.9	374.3	380.8	383.0	387.1	391.9	395.7	398.7	400.2	402.6	403.7	407.7	410.5	413.8
0.515	TT16	-	352.7	360.1	369.3	374.7	381.3	383.6	387.8	392.6	396.6	399.6	401.2	403.6	404.8	408.8	411.6	415.1
0.517	TT18	-	352.3	359.8	368.9	374.1	380.6	382.9	387.0	391.8	395.6	398.7	400.1	402.7	403.8	407.8	410.6	414.0
0.520	TT40	-	352.4	360.0	369.2	374.5	381.1	383.4	387.6	392.6	396.5	399.7	401.2	403.8	405.0	409.0	411.9	415.5
0.526	TT20	-	352.4	360.0	369.2	374.3	380.9	383.3	387.5	392.4	396.4	399.5	401.1	403.6	404.9	408.9	411.9	415.5
0.526	TT22	-	352.1	359.9	369.1	373.8	380.2	382.5	386.6	391.4	395.2	398.3	399.8	402.2	403.3	407.3	410.2	413.7
0.532	TT44	-	352.1	359.9	369.0	373.8	380.3	382.6	386.8	391.6	395.5	398.6	400.2	402.6	403.8	407.8	410.7	414.3
0.532	TT23	-	346.6	355.1	363.3	365.5	371.1	372.7	376.2	380.4	383.8	386.5	387.7	389.5	390.4	394.2	396.7	399.7
0.690	TT11	-	348.8	358.0	367.4	369.9	376.2	378.4	382.4	387.1	390.9	393.9	395.5	397.7	398.9	402.8	405.6	408.9
0.826	TT15	-	346.2	355.4	364.6	367.0	373.1	375.4	379.4	384.1	387.8	391.0	392.6	394.9	396.1	400.1	402.9	406.4
0.982	TT01	-	346.4	348.8	355.4	356.9	361.4	362.2	364.7	368.2	370.6	372.7	373.3	374.3	374.2	378.0	379.4	381.8
0.983	TT26	-	341.7	360.5	369.8	375.3	381.8	384.1	388.2	393.2	397.0	400.4	401.7	404.4	405.4	409.7	412.4	416.0

Table 16.D (continuation): Axial cladding wall temperature distribution for the perforated ring structured rod channel experiments (L-STAR-TX-G2) at a dimensionless heat up ratio $q_i^+ = 0.002$.

$Z_{TC,i}$ [m]	TC	TX01	TX02	TX03	TX04	TX05	TX06	TX07	TX08	TX09	TX10	TX11	TX12	TX13	TX14	TX15	TX16	TX17
0.988	TT25	-	346.5	355.6	364.8	367.2	373.3	375.7	379.6	384.3	388.1	391.3	392.8	395.1	396.3	400.4	403.1	406.6
0.993	TT05	-	346.0	355.2	364.3	366.7	372.9	375.2	379.2	383.8	387.6	390.7	392.2	394.5	395.6	399.7	402.4	405.9
0.995	TT30	-		-	-	-	-	-	-	-	-	-	-	-	-	-	-	-
0.999	TT29	-	346.3	355.4	364.5	367.0	373.2	375.5	379.5	384.2	388.0	391.1	392.7	395.0	396.2	400.3	403.0	406.5
1.005	TT09	-	346.0	355.1	364.3	366.8	373.0	375.3	379.4	384.0	387.8	390.9	392.5	394.8	396.1	400.1	402.9	406.3
1.005	TT34	-	346.2	355.3	364.5	367.0	373.2	375.5	379.5	384.2	388.0	391.1	392.7	394.9	396.1	400.2	403.0	406.4
1.012	TT33	-	345.7	354.8	363.8	366.2	372.2	374.4	378.3	382.8	386.6	389.5	391.1	393.2	394.5	398.4	401.1	404.5
1.016	TT13	-	345.6	354.7	363.8	366.0	372.2	374.2	378.3	382.6	386.5	389.2	391.0	392.9	394.2	398.0	400.8	404.1
1.016	TT38	-	345.5	354.6	363.6	365.9	372.1	374.0	378.2	382.3	386.3	388.8	390.7	392.3	393.8	397.4	400.2	403.4
1.021	TT37	-	345.7	354.8	364.0	366.5	372.7	374.9	379.1	383.6	387.5	390.4	392.2	394.3	395.6	399.5	402.4	405.8
1.026	TT17	-	345.6	354.8	364.0	366.5	372.8	375.0	379.2	383.8	387.8	390.7	392.5	394.6	396.1	400.0	402.9	406.3
1.026	TT42	-	345.5	354.7	363.9	366.4	372.7	375.0	379.3	383.8	387.8	390.8	392.6	394.8	396.2	400.2	403.1	406.6
1.031	TT41	-	345.4	354.6	363.8	366.3	372.6	374.8	379.0	383.6	387.6	390.6	392.4	394.6	395.9	399.9	402.8	406.3
1.038	TT21	-	345.3	354.4	363.5	365.8	372.1	374.3	378.5	383.0	387.0	390.0	391.8	393.9	395.3	399.2	402.2	405.7
1.037	TT46	-	345.0	354.1	363.1	365.4	371.5	373.7	377.8	382.2	386.1	389.1	390.8	392.9	394.2	398.1	401.0	404.4
1.043	TT45	-	344.5	353.6	362.5	364.6	370.7	372.8	376.8	381.1	384.9	387.8	389.5	391.4	392.7	396.5	399.3	402.7
1.044	TT47	-	344.4	353.5	362.4	364.4	370.4	372.5	376.5	380.8	384.7	387.5	389.2	391.2	392.4	396.2	399.1	402.4
1.419	TT19	-	339.0	348.0	356.5	359.4	365.2	367.3	371.3	375.9	379.3	382.8	384.1	386.6	387.8	391.8	394.3	397.7
1.798	TT27	-	334.4	343.2	351.5	353.8	359.6	361.9	366.0	370.4	374.0	377.4	379.0	381.3	382.6	386.9	389.3	392.9
2.138	TT31	-	328.5	336.5	344.7	346.1	351.9	354.5	358.7	362.8	366.6	369.8	372.0	373.4	374.7	379.7	382.2	385.6
2.558	TT35	-	323.6	331.5	339.1	340.2	345.8	348.4	352.5	356.5	360.1	363.2	365.3	366.6	367.8	372.7	375.0	378.3
2.928	TT39	-		-	-	-	-	-	-	-	-	-	-	-	-	-	-	-
3.320	TT43	-		-	-	-	-	-	-	-	-	-	-	-	-	-	-	-

Table 17.D: Axial cladding wall temperature distribution for the perforated ring structured rod channel experiments (L-STAR-TX-G2) at a dimensionless heat up ratio $q_i^+ = 0.003$.

$Z_{TC,i}$ [m]	TC	TX01	TX02	TX03	TX04	TX05	TX06	TX07	TX08	TX09	TX10	TX11	TX12	TX13	TX14	TX15	TX16	TX17
0.074	TT03	-	-	-	-	-	-	-	-	-	-	-	-	-	-	-	-	-
0.307	TT07	-	372.3	375.9	381.6	388.2	396.2	397.0	399.2	404.6	405.7	407.6	410.1	-	-	-	-	-
0.472	TT00	-	389.3	395.0	404.3	409.6	420.8	423.4	428.0	435.6	438.9	442.2	442.3	-	-	-	-	-
0.472	TT02	-	389.4	395.1	404.5	413.8	425.0	427.6	432.2	439.8	443.2	446.5	443.6	-	-	-	-	-
0.478	TT24	-	387.5	393.2	402.5	408.1	419.0	421.6	426.1	433.7	436.9	440.2	440.4	-	-	-	-	-
0.484	TT04	-	388.6	394.2	403.4	408.7	419.6	422.2	426.7	434.1	437.3	440.6	443.2	-	-	-	-	-
0.483	TT06	-	388.2	393.8	402.9	408.0	418.7	421.2	425.4	432.8	435.8	439.0	442.7	-	-	-	-	-
0.489	TT28	-	388.4	394.0	403.2	408.6	419.6	422.2	426.7	434.2	437.5	440.8	444.3	-	-	-	-	-
0.494	TT08	-	-	-	-	-	-	-	-	-	-	-	-	-	-	-	-	-
0.494	TT10	-	388.1	393.7	402.8	407.9	418.7	421.2	425.4	432.7	435.9	439.0	441.0	-	-	-	-	-
0.500	TT32	-	387.5	393.1	402.1	407.0	417.8	420.1	424.3	431.6	434.7	437.7	441.6	-	-	-	-	-
0.504	TT12	-	387.6	393.1	402.1	407.0	417.7	420.0	424.0	431.2	434.3	437.1	438.4	-	-	-	-	-
0.505	TT14	-	387.9	393.5	402.6	407.6	418.4	420.8	425.0	432.2	435.4	438.1	439.9	-	-	-	-	-
0.509	TT36	-	385.6	391.2	400.2	405.2	415.9	418.3	422.4	429.6	432.7	435.5	437.3	-	-	-	-	-
0.515	TT16	-	387.6	393.3	402.6	407.8	418.8	421.2	425.7	432.9	436.3	439.2	440.7	-	-	-	-	-
0.517	TT18	-	387.9	393.7	403.1	408.4	419.5	422.1	426.8	434.0	437.5	440.5	441.9	-	-	-	-	-
0.520	TT40	-	387.4	393.0	402.3	407.6	418.6	421.2	425.7	433.0	436.4	439.4	441.4	-	-	-	-	-
0.526	TT20	-	387.6	393.3	402.8	408.1	419.3	421.9	426.7	434.1	437.6	440.8	443.4	-	-	-	-	-
0.526	TT22	-	387.5	393.2	402.6	407.9	419.0	421.6	426.5	433.9	437.4	440.6	443.6	-	-	-	-	-
0.532	TT44	-	387.0	392.6	401.9	407.1	418.2	420.6	425.2	432.4	435.8	438.8	444.7	-	-	-	-	-
0.532	TT23	-	387.1	392.7	402.0	407.2	418.3	420.8	425.5	432.8	436.2	439.4	443.3	-	-	-	-	-
0.690	TT11	-	379.4	384.0	391.9	399.9	409.4	411.1	414.7	421.0	423.5	426.0	428.7	-	-	-	-	-
0.826	TT15	-	382.2	387.7	397.0	406.1	416.9	419.0	423.7	430.5	433.8	436.7	444.8	-	-	-	-	-
0.982	TT01		378.3	383.9	393.3	402.3	412.8	415.1	419.6	426.6	429.8	433.0	441.1	-	-	-	-	-
0.983	TT26		378.4	383.9	393.3	402.3	412.8	415.1	419.6	426.5	429.6	432.9	441.9	-	-	-	-	-

Table 17.D (continuation): Axial cladding wall temperature distribution for the perforated ring structured rod channel experiments (L-STAR-TX-G2) at dimensionless heat up ratio $q_i^+ = 0.003$.

$Z_{TC,i}$ [m]	TC	TX01	TX02	TX03	TX04	TX05	TX06	TX07	TX08	TX09	TX10	TX11	TX12	TX13	TX14	TX15	TX16	TX17
0.988	TT25	-	378.4	383.9	393.4	402.5	412.9	415.3	419.8	426.8	429.9	433.2	439.2	-	-	-	-	-
0.993	TT05	-	377.9	383.4	392.9	401.9	412.4	414.8	419.2	426.2	429.3	432.5	442.4	-	-	-	-	-
0.995	TT30	-	-	-	-	-	-	-	-	-	-	-	-	-	-	-	-	-
0.999	TT29	-	378.1	383.6	393.1	402.2	412.7	415.1	419.6	426.6	429.8	433.1	442.4	-	-	-	-	-
1.005	TT09	-	377.8	383.4	392.9	402.0	412.5	414.9	419.5	426.4	429.7	432.8	439.6	-	-	-	-	-
1.005	TT34	-	378.1	383.6	393.1	402.2	412.7	415.1	419.7	426.6	429.8	433.0	437.9	-	-	-	-	-
1.012	TT33	-	377.3	382.8	392.2	401.0	411.4	413.6	418.0	424.7	427.9	430.8	439.9	-	-	-	-	-
1.016	TT13	-	377.2	382.7	392.1	400.9	411.3	413.3	417.8	424.2	427.5	430.2	437.5	-	-	-	-	-
1.016	TT38	-	377.0	382.5	391.9	400.6	411.1	413.0	417.6	423.7	427.0	429.6	437.6	-	-	-	-	-
1.021	TT37	-	377.2	382.8	392.4	401.4	411.9	414.2	418.9	425.5	428.9	431.9	436.2	-	-	-	-	-
1.026	TT17	-	377.1	382.8	392.4	401.5	412.1	414.4	419.2	425.9	429.3	432.3	439.1	-	-	-	-	-
1.026	TT42	-	377.1	382.7	392.3	401.4	412.1	414.4	419.2	426.0	429.4	432.6	439.1	-	-	-	-	-
1.031	TT41	-	376.9	382.5	392.2	401.2	411.8	414.1	418.9	425.6	429.0	432.1	438.5	-	-	-	-	-
1.038	TT21	-	376.7	382.2	391.7	400.7	411.2	413.5	418.2	425.0	428.3	431.5	440.5	-	-	-	-	-
1.037	TT46	-	376.3	381.8	391.2	400.1	410.5	412.7	417.2	424.0	427.2	430.2	440.3	-	-	-	-	-
1.043	TT45	-	375.6	381.0	390.3	399.1	409.4	411.4	415.8	422.4	425.5	428.4	440.5	-	-	-	-	-
1.044	TT47	-	375.4	380.8	390.0	398.7	409.0	411.0	415.5	422.1	425.1	428.1	438.8	-	-	-	-	-
1.419	TT19	-	368.1	373.7	383.3	392.0	402.2	404.6	409.2	415.7	418.6	422.1	428.9	-	-	-	-	-
1.798	TT27	-	360.2	365.9	375.7	384.5	394.4	397.0	401.7	408.3	411.1	414.8	421.4	-	-	-	-	-
2.138	TT31	-	350.7	356.2	365.9	374.5	384.4	387.0	391.3	398.0	401.6	404.7	411.3	-	-	-	-	-
2.558	TT35	-	342.2	347.7	357.5	365.9	375.3	377.9	382.3	388.8	392.3	395.3	401.8	-	-	-	-	-
2.928	TT39	-	-	-	-	-	-	-	-	-	-	-	-	-	-	-	-	-
3.320	TT43	-	-	-	-	-	-	-	-	-	-	-	-	-	-	-	-	-

Table 18.D: Mean axial velocity results for the Smooth rod channel experiments (L-STAR-G0-LDA)

X_w [mm]	Y_w [mm]	Z_r [mm]	P_i [Bar]	T_i [°C]	$\dot{m}_{CFM}$ [kg/h]	U_m [m/s]	$U_{s(G0)}$ [m/s]	$U_{s.rms(G0)}$ [m/s]	$U_{s(G0)}/U_m$ [m/s]
0	0	15	1.52	13.95	92.43	4.65	0.00	0.160	0.000
0	0.05	15	1.52	13.97	92.41	4.64	0.59	0.542	0.126
0	0.1	15	1.51	14.08	92.64	4.68	1.25	0.687	0.268
0	0.2	15	1.51	14.08	92.68	4.68	2.17	0.757	0.464
0	0.3	15	1.52	14.09	93.01	4.67	2.75	0.794	0.589
0	0.4	15	1.52	13.99	92.53	4.66	3.27	0.883	0.703
0	0.5	15	1.52	14.09	93.01	4.67	3.61	0.815	0.772
0	0.6	15	1.52	14.08	92.64	4.66	3.79	0.765	0.814
0	0.7	15	1.52	14.05	92.54	4.64	3.94	0.790	0.849
0	0.8	15	1.52	14.08	92.30	4.63	4.07	0.734	0.880
0	0.9	15	1.52	14.08	93.38	4.70	4.14	0.697	0.881
0	1	15	1.52	14.07	93.07	4.68	4.22	0.663	0.901
0	1.25	15	1.52	14.10	92.85	4.67	4.39	0.605	0.939
0	1.5	15	1.52	14.17	93.39	4.70	4.56	0.566	0.971
0	1.75	15	1.53	14.16	93.24	4.67	4.66	0.530	0.999
0	2	15	1.52	14.05	92.91	4.67	4.73	0.499	1.015
0	2.25	15	1.52	14.05	92.61	4.64	4.84	0.475	1.042
0	2.5	15	1.53	13.89	93.93	4.68	5.01	0.431	1.073
0	2.75	15	1.51	13.97	91.80	4.63	5.03	0.414	1.087
0	3	15	1.53	13.88	92.97	4.65	5.09	0.400	1.095
0	4	15	1.51	13.99	91.88	4.64	5.25	0.346	1.133
0	5	15	1.51	14.07	91.94	4.65	5.38	0.299	1.158
0	6	15	1.51	14.07	91.67	4.63	5.45	0.262	1.178
0	7	15	1.51	14.11	91.96	4.64	5.48	0.248	1.191
0	8	15	1.51	14.10	91.68	4.63	5.45	0.264	1.177
0	9	15	1.52	14.17	91.99	4.64	5.38	0.298	1.159
0	10	15	1.51	14.26	91.49	4.62	5.31	0.337	1.148
0	11	15	1.52	14.29	91.08	4.60	5.09	0.371	1.109
0	12	15	1.51	14.31	91.12	4.61	4.95	0.407	1.073
0	13	15	1.52	14.36	92.16	4.63	4.72	0.452	1.021
0	14	15	1.51	14.35	90.75	4.59	4.44	0.505	0.968
0	15	15	1.51	14.42	90.71	4.59	4.02	0.610	0.878
0	15.5	15	1.51	15.04	92.74	4.71	3.74	0.741	0.795
0	16	15	1.51	14.47	90.30	4.57	2.30	0.850	0.504
0	16.15	15	1.52	14.69	89.87	4.54	1.69	0.606	0.373
0	16.25	15	1.51	14.66	89.91	4.56	1.09	0.472	0.239
0	16.5	15	1.51	14.76	89.26	4.53	0.00	0.012	0.000

Table 19.D: Mean axial velocity results for the Solid ring structures experiments (L-STAR-G1-LDA)

X_w [mm]	Y_w [mm]	Z_r [mm]	P_i [Bar]	T_i [°C]	$\dot{m}_{CFM}$ [kg/h]	U_m [m/s]	$U_{r(G1)}$ [m/s]	$U_{r.rms(G1)}$ [m/s]	$U_{r(G1)}/U_m$ [m/s]
0	3.0	0	1.50	27.64	90.46	4.82	0.01	0.04	0.002
0	3.1	0	1.50	27.83	91.54	4.87	2.81	1.03	0.577
0	3.2	0	1.51	27.75	92.20	4.88	4.60	1.53	0.942
0	3.3	0	1.51	27.98	91.99	4.87	4.78	1.35	0.983
0	3.4	0	1.50	26.57	92.26	4.89	4.79	1.23	0.979
0	3.5	0	1.51	27.93	91.76	4.86	4.87	1.25	1.001
0	3.75	0	1.50	26.57	92.27	4.89	5.18	1.29	1.059
0	4.0	0	1.49	25.20	88.71	4.73	5.22	1.30	1.105
0	5.0	0	1.50	25.40	88.85	4.70	5.44	1.32	1.156
0	6.0	0	1.50	24.90	87.75	4.64	5.76	1.29	1.242
0	7.0	0	1.49	25.00	86.69	4.61	6.05	1.22	1.311
0	8.0	0	1.49	25.20	88.71	4.73	6.36	1.16	1.346
0	9.0	0	1.50	25.40	88.85	4.70	6.59	1.07	1.401
0	10.0	0	1.50	25.50	88.93	4.71	6.75	0.98	1.433
0	11.0	0	1.50	26.70	88.31	4.70	6.83	0.88	1.454
0	12.0	0	1.50	26.70	88.30	4.70	6.88	0.79	1.465
0	13.0	0	1.50	26.70	87.51	4.65	6.87	0.71	1.476
0	14.0	0	1.50	26.80	88.57	4.71	6.74	0.67	1.431
0	15.0	0	1.50	26.90	87.65	4.66	6.33	0.76	1.357
0	15.5	0	1.50	26.90	87.78	4.67	5.92	0.86	1.267
0	16.0	0	1.50	26.90	88.21	4.69	4.95	1.03	1.055
0	16.25	0	1.50	27.10	87.63	4.67	3.57	1.02	0.765
0	16.5	0	1.50	27.10	87.48	4.66	0.00	0.01	0.000
0	3.0	0.5	1.51	28.37	91.41	4.85	0.04	0.14	0.009
0	3.1	0.5	1.51	28.38	91.41	4.86	1.41	1.24	0.291
0	3.2	0.5	1.51	28.37	92.69	4.92	3.09	2.57	0.627
0	3.3	0.5	1.51	28.49	92.14	4.90	3.79	2.27	0.774
0	3.4	0.5	1.51	28.45	91.74	4.87	4.91	1.94	1.008
0	3.5	0.5	1.51	28.57	91.76	4.88	5.19	1.59	1.064
0	3.75	0.5	1.50	27.30	87.32	4.65	5.55	1.26	1.193
0	4.0	0.5	1.50	27.32	89.40	4.76	5.68	1.26	1.192
0	5.0	0.5	1.50	27.31	89.31	4.76	5.77	1.30	1.212
0	6.0	0.5	1.50	27.53	89.71	4.78	6.03	1.28	1.261
0	7.0	0.5	1.50	27.43	89.11	4.75	6.27	1.21	1.320
0	8.0	0.5	1.50	27.41	89.27	4.75	6.53	1.13	1.373
0	9.0	0.5	1.50	23.39	87.80	4.63	6.69	1.03	1.446
0	10.0	0.5	1.50	22.95	89.03	4.68	6.87	0.96	1.469
0	11.0	0.5	1.50	22.67	89.45	4.68	6.98	0.87	1.491
0	12.0	0.5	1.50	22.63	89.11	4.67	7.00	0.78	1.500
0	13.0	0.5	1.50	22.70	90.49	4.74	6.99	0.68	1.475
0	14.0	0.5	1.50	22.83	90.97	4.77	6.80	0.67	1.425
0	15.0	0.5	1.50	22.71	90.44	4.73	6.36	0.76	1.344
0	15.5	0.5	1.50	22.78	90.86	4.76	5.93	0.86	1.246
0	16.0	0.5	1.50	22.72	90.68	4.75	4.94	1.07	1.041
0	16.25	0.5	1.50	22.71	90.77	4.75	3.40	1.16	0.716
0	16.50	0.5	1.50	22.72	90.99	4.76	0.00	0.01	0.000
0	3.0	1.0	1.49	21.117	89.45	4.68	0.00	0.00	0.000
0	3.1	1.0	1.49	21.117	89.45	4.68	-0.11	0.83	-0.023
0	3.25	1.0	1.49	21.121	89.24	4.67	4.28	2.51	0.916
0	3.5	1.0	1.49	21.114	88.75	4.65	5.39	1.69	1.160
0	3.75	1.0	1.49	21.178	88.92	4.66	5.55	1.32	1.192
0	4.0	1.0	1.49	21.118	88.70	4.65	5.59	1.2	1.203

Table 19.D (continuation): Mean axial velocity results for the Solid ring structures experiments (L-STAR-G1-LDA)

X_w [mm]	Y_w [mm]	Z_r [mm]	P_i [Bar]	T_i [°C]	$\dot{m}_{CFM}$ [kg/h]	U_m [m/s]	$U_{r(G1)}$ [m/s]	$U_{r.rms(G1)}$ [m/s]	$U_{r(G1)}/U_m$ [m/s]
0	5.0	1.0	1.49	21.11	88.72	4.65	5.59	1.23	1.203
0	6.0	1.0	1.49	21.12	88.44	4.64	5.78	1.22	1.246
0	7.0	1.0	1.50	21.11	88.91	4.64	6.00	1.18	1.293
0	8.0	1.0	1.49	21.11	88.21	4.62	6.25	1.08	1.354
0	9.0	1.0	1.49	21.12	89.06	4.67	6.47	1.01	1.386
0	10.0	1.0	1.50	21.11	89.38	4.66	6.61	0.92	1.417
0	11.0	1.0	1.49	21.12	88.42	4.62	6.73	0.83	1.457
0	12.0	1.0	1.49	21.04	88.85	4.65	6.78	0.73	1.460
0	13.0	1.0	1.49	21.01	88.00	4.61	6.74	0.67	1.463
0	14.0	1.0	1.49	21.01	88.83	4.64	6.59	0.64	1.419
0	15.0	1.0	1.49	21.10	88.04	4.61	6.19	0.72	1.344
0	15.5	1.0	1.49	21.10	87.38	4.57	5.80	0.82	1.269
0	16.0	1.0	1.49	21.01	88.13	4.61	4.96	0.98	1.076
0	16.25	1.0	1.49	21.11	88.84	4.64	0.53	0.56	0.114
0	3.0	1.5	1.51	17.02	91.52	4.67	0.00	0.00	0.000
0	3.1	1.5	1.51	17.51	91.66	4.43	-0.08	0.03	-0.018
0	3.25	1.5	1.51	17.04	91.57	4.68	3.34	3.03	0.714
0	3.5	1.5	1.51	17.54	89.92	4.59	5.16	2.43	1.123
0	3.75	1.5	1.50	17.35	91.38	4.68	5.76	1.81	1.230
0	4.0	1.5	1.50	17.07	90.93	4.66	5.96	1.47	1.280
0	5.0	1.5	1.51	17.42	91.11	4.65	5.98	1.36	1.287
0	6.0	1.5	1.50	17.62	90.47	4.64	6.17	1.37	1.330
0	7.0	1.5	1.51	17.39	89.46	4.57	6.37	1.33	1.395
0	8.0	1.5	1.51	16.99	91.84	4.69	6.54	1.26	1.394
0	9.0	1.5	1.51	17.73	92.21	4.72	6.77	1.18	1.435
0	10	1.5	1.51	17.39	91.11	4.65	6.90	1.08	1.484
0	11	1.5	1.51	17.70	90.47	4.62	7.04	0.97	1.523
0	12	1.5	1.51	17.68	90.65	4.63	7.09	0.87	1.530
0	13	1.5	1.51	17.12	89.64	4.58	7.08	0.78	1.546
0	14	1.5	1.51	17.42	90.65	4.63	6.87	0.76	1.482
0	15	1.5	1.51	17.48	89.64	4.58	6.48	0.88	1.415
0	16	1.5	1.51	17.54	91.29	4.67	6.29	0.89	1.348
0	16.25	1.5	1.51	17.09	90.19	4.59	4.45	1.27	0.969
0	16.5	1.5	1.50	17.25	91.66	4.69	0.00	0.01	0.000
0	3.0	2.0	1.48	18.82	87.31	4.58	0.00	0.00	0.000
0	3.1	2.0	1.48	18.82	87.31	4.58	1.27	2.13	0.278
0	3.25	2.0	1.50	20.90	88.43	4.61	4.08	2.32	0.886
0	3.5	2.0	1.50	20.82	88.46	4.61	4.89	1.82	1.062
0	3.75	2.0	1.50	20.82	88.39	4.60	5.28	1.48	1.147
0	4.0	2.0	1.50	20.82	88.79	4.62	5.44	1.29	1.177
0	5.0	2.0	1.50	20.82	88.48	4.61	5.63	1.19	1.222
0	6.0	2.0	1.50	20.82	87.91	4.58	5.81	1.18	1.269
0	7.0	2.0	1.50	20.82	88.16	4.59	6.05	1.14	1.319
0	8.0	2.0	1.49	20.80	88.35	4.61	6.24	1.07	1.354
0	9.0	2.0	1.50	20.80	88.50	4.61	6.45	0.98	1.399
0	10	2.0	1.50	20.82	88.50	4.61	6.58	0.90	1.426
0	11	2.0	1.50	20.76	88.59	4.61	6.69	0.80	1.453
0	12	2.0	1.50	20.72	88.08	4.58	6.73	0.72	1.469
0	13	2.0	1.50	20.77	88.76	4.62	6.7	0.65	1.451
0	14	2.0	1.50	20.81	88.09	4.58	6.54	0.63	1.427
0	15	2.0	1.50	20.81	87.96	4.58	6.15	0.71	1.343

Table 19.D (continuation): Mean axial velocity results for the Solid ring structures experiments (L-STAR-G1-LDA)

X_w [mm]	Y_w [mm]	Z_r [mm]	P_i [Bar]	T_i [°C]	$\dot{m}_{CFM}$ [kg/h]	U_m [m/s]	$U_{r(G1)}$ [m/s]	$U_{r.rms(G1)}$ [m/s]	$U_{r(G1)}/U_m$ [m/s]
0	15.5	2.0	1.50	20.82	89.02	4.63	5.81	0.82	1.254
0	16.0	2.0	1.50	20.82	89.48	4.66	4.84	1	1.040
0	16.25	2.0	1.50	20.70	88.97	4.62	3.37	1.08	0.729
0	16.5	2.0	1.50	20.70	89.5	4.65	0.00	0.00	0.000
0	3.0	2.5	1.50	18.92	88.06	4.55	0.00	0.00	0.000
0	3.1	2.5	1.50	18.92	88.06	4.55	1.36	2.11	0.299
0	3.25	2.5	1.51	18.82	89.74	4.61	3.11	2.26	0.675
0	3.5	2.5	1.48	18.73	89.43	4.67	4.19	2.04	0.897
0	3.75	2.5	1.49	18.62	89.95	4.68	4.81	1.68	1.029
0	4.0	2.5	1.49	18.63	89.55	4.66	5.09	1.43	1.091
0	5.0	2.5	1.48	18.63	88.89	4.65	5.44	1.17	1.171
0	6.0	2.5	1.48	18.55	88.82	4.64	5.63	1.15	1.213
0	7.0	2.5	1.48	18.52	88.11	4.60	5.87	1.12	1.275
0	8.0	2.5	1.48	18.60	88.00	4.60	6.07	1.04	1.319
0	9.0	2.5	1.48	18.42	88.42	4.62	6.34	0.98	1.373
0	10	2.5	1.48	18.42	88.26	4.60	6.49	0.89	1.411
0	11	2.5	1.48	18.42	88.38	4.60	6.60	0.79	1.434
0	12	2.5	1.49	18.42	89.59	4.65	6.62	0.74	1.422
0	13	2.5	1.48	18.42	90.06	4.69	6.69	0.65	1.425
0	14	2.5	1.48	18.42	89.78	4.68	6.53	0.62	1.395
0	15	2.5	1.49	18.42	89.39	4.65	6.13	0.71	1.319
0	15.5	2.5	1.48	18.40	89.71	4.68	5.76	0.80	1.231
0	16	2.5	1.48	18.42	89.70	4.68	4.88	0.99	1.044
0	16.25	2.5	1.48	18.33	89.07	4.64	3.61	0.98	0.778
0	16.5	2.5	1.48	18.31	88.69	4.62	0.00	0.05	0.000
0	3.0	3.0	1.48	21.81	90.59	4.78	0.00	0.00	0.000
0	3.1	3.0	1.48	21.81	90.59	4.78	0.01	0.05	0.002
0	3.25	3.0	1.49	22.22	91.1	4.81	2.91	2.32	0.605
0	3.5	3.0	1.49	22.28	91.00	4.78	4.27	2.10	0.893
0	3.75	3.0	1.49	22.30	90.28	4.75	4.81	1.80	1.013
0	4.0	3.0	1.49	22.39	89.52	4.71	5.18	1.53	1.100
0	5.0	3.0	1.49	22.39	89.20	4.68	5.65	1.22	1.206
0	6.0	3.0	1.49	22.18	87.65	4.61	5.89	1.20	1.278
0	7.0	3.0	1.49	22.19	87.29	4.59	6.14	1.15	1.338
0	8.0	3.0	1.49	22.29	86.82	4.56	6.32	1.08	1.385
0	9.0	3.0	1.49	22.40	86.79	4.57	6.49	0.99	1.421
0	10	3.0	1.50	22.39	90.36	4.71	6.78	0.93	1.439
0	11	3.0	1.49	22.34	89.46	4.69	6.89	0.83	1.469
0	12	3.0	1.50	22.40	89.36	4.68	6.90	0.75	1.474
0	13	3.0	1.49	22.40	88.97	4.67	6.87	0.68	1.471
0	14	3.0	1.49	22.35	88.39	4.64	6.72	0.65	1.449
0	15	3.0	1.51	22.40	92.15	4.78	6.41	0.73	1.341
0	15.5	3.0	1.50	22.45	90.82	4.75	6.07	0.82	1.279
0	16	3.0	1.51	22.48	91.34	4.75	5.22	1.00	1.098
0	16.25	3.0	1.50	22.48	90.73	4.74	4.12	1.04	0.868
0	16.5	3.0	1.50	22.58	90.43	4.72	0.00	0.01	0.000
0	0	5.0	1.49	23.57	89.46	4.72	0.00	0.09	0.000
0	0.1	5.0	1.49	23.29	89.09	4.71	-0.13	0.61	-0.028
0	0.2	5.0	1.49	23.12	90.56	4.77	-0.42	0.77	-0.088
0	0.3	5.0	1.49	23.34	90.10	4.75	-0.45	0.81	-0.095
0	0.4	5.0	1.49	23.12	88.45	4.66	-0.48	0.80	-0.103

Table 19.D (continuation): Mean axial velocity results for the Solid ring structures experiments (L-STAR-G1-LDA)

X_w [mm]	Y_w [mm]	Z_r [mm]	P_i [Bar]	T_i [°C]	$\dot{m}_{CFM}$ [kg/h]	U_m [m/s]	$U_{r(G1)}$ [m/s]	$U_{r.rms(G1)}$ [m/s]	$U_{r(G1)}/U_m$ [m/s]
0	0.5	5.0	1.50	22.96	90.56	4.75	-0.51	0.77	-0.107
0	0.6	5.0	1.49	23.39	89.46	4.71	-0.54	0.72	-0.115
0	0.7	5.0	1.49	23.38	89.46	4.71	-0.58	0.73	-0.123
0	0.8	5.0	1.49	23.12	89.37	4.71	-0.58	0.71	-0.123
0	0.9	5.0	1.49	23.39	90.01	4.74	-0.57	0.7	-0.120
0	1	5.0	1.49	23.45	89.09	4.70	-0.54	0.68	-0.115
0	1.25	5.0	1.49	23.22	91.02	4.79	-0.53	0.67	-0.111
0	1.5	5.0	1.49	23.42	90.19	4.76	-0.43	0.67	-0.090
0	1.75	5.0	1.49	23.22	88.18	4.64	-0.31	0.68	-0.067
0	2	5.0	1.49	23.28	90.93	4.79	-0.09	0.74	-0.019
0	2.25	5.0	1.49	23.25	91.11	4.80	0.32	0.90	0.067
0	2.5	5.0	1.49	23.28	90.93	4.79	1.02	1.20	0.213
0	2.75	5.0	1.49	23.22	88.18	4.64	2.01	1.60	0.433
0	3	5.0	1.49	23.42	90.19	4.76	2.97	1.84	0.624
0	3.25	5.0	1.49	23.25	90.01	4.74	3.72	1.86	0.785
0	3.5	5.0	1.49	22.80	89.92	4.73	4.29	1.78	0.907
0	3.75	5.0	1.49	23.36	89.46	4.72	4.67	1.68	0.990
0	4.0	5.0	1.49	23.38	89.09	4.70	4.98	1.59	1.059
0	5.0	5.0	1.49	23.34	90.01	4.75	5.56	1.32	1.170
0	6.0	5.0	1.49	23.18	89.28	4.70	5.85	1.27	1.245
0	7.0	5.0	1.49	23.57	90.93	4.79	6.12	1.22	1.278
0	8.0	5.0	1.49	23.54	89.83	4.74	6.36	1.15	1.341
0	9.0	5.0	1.49	23.29	89.19	4.70	6.52	1.07	1.388
0	10	5.0	1.49	23.28	89.64	4.73	6.67	0.99	1.411
0	11	5.0	1.49	23.29	88.82	4.69	6.75	0.89	1.439
0	12	5.0	1.49	23.48	88.09	4.64	6.82	0.79	1.470
0	13	5.0	1.50	23.35	90.56	4.75	6.77	0.71	1.425
0	14	5.0	1.49	23.28	90.01	4.74	6.57	0.72	1.387
0	15	5.0	1.49	23.20	90.01	4.74	5.98	0.82	1.262
0	15.5	5.0	1.49	23.29	89.28	4.71	5.56	0.84	1.181
0	16	5.0	1.49	23.51	89.00	4.70	4.92	0.92	1.047
0	16.25	5.0	1.49	23.12	87.36	4.60	3.87	1.10	0.842
0	16.5	5.0	1.49	23.26	89.55	4.73	0.00	0.07	0.000
0	0.0	10	1.50	19.33	88.36	4.57	0.00	0.16	0.000
0	0.1	10	1.50	19.94	88.73	4.59	-0.91	0.54	-0.198
0	0.2	10	1.50	19.73	89.00	4.59	-0.79	0.92	-0.171
0	0.3	10	1.50	19.91	89.28	4.62	-0.77	0.95	-0.166
0	0.4	10	1.50	19.47	90.38	4.67	-0.59	1.00	-0.126
0	0.5	10	1.51	19.09	89.00	4.58	-0.59	1.05	-0.128
0	0.6	10	1.50	19.87	92.39	4.78	-0.50	1.06	-0.104
0	0.7	10	1.51	19.18	91.84	4.73	-0.40	1.09	-0.084
0	0.8	10	1.51	19.23	91.75	4.73	-0.32	1.12	-0.067
0	0.9	10	1.50	19.59	91.29	4.72	-0.19	1.16	-0.040
0	1.0	10	1.50	18.98	90.83	4.69	-0.10	1.19	-0.021
0	1.25	10	1.50	19.93	89.55	4.64	0.36	1.27	0.077
0	1.5	10	1.50	19.08	89.46	4.61	0.65	1.44	0.141
0	1.75	10	1.50	19.23	88.09	4.54	1.08	1.51	0.237
0	2.0	10	1.50	19.79	88.36	4.57	1.53	1.56	0.334
0	2.25	10	1.51	19.73	89.46	4.62	2.00	1.61	0.433
0	2.5	10	1.50	19.69	89.00	4.60	2.48	1.65	0.538
0	2.75	10	1.50	19.91	90.83	4.70	2.94	1.66	0.625

Table 19.D (continuation): Mean axial velocity results for the Solid ring structures experiments (L-STAR-G1-LDA)

X_w [mm]	Y_w [mm]	Z_r [mm]	P_i [Bar]	T_i [°C]	$\dot{m}_{CFM}$ [kg/h]	U_m [m/s]	$U_{r(G1)}$ [m/s]	$U_{r.rms(G1)}$ [m/s]	$U_{r(G1)}/U_m$ [m/s]
0	3.0	10	1.50	19.15	89.92	4.63	3.37	1.64	0.727
0	3.25	10	1.50	19.85	91.20	4.71	3.77	1.61	0.800
0	3.5	10	1.50	19.78	89.55	4.63	4.13	1.56	0.892
0	3.75	10	1.50	19.78	90.01	4.65	4.40	1.50	0.945
0	4.0	10	1.50	19.03	90.93	4.69	4.63	1.44	0.987
0	5.0	10	1.51	19.00	90.19	4.64	5.20	1.27	1.120
0	6.0	10	1.50	19.96	89.19	4.62	5.55	1.18	1.202
0	7.0	10	1.50	19.81	89.19	4.61	5.81	1.11	1.260
0	8.0	10	1.50	20.01	90.10	4.66	6.05	1.03	1.299
0	9.0	10	1.50	19.27	89.74	4.63	6.26	0.94	1.352
0	10	10	1.50	20.16	89.83	4.67	6.43	0.85	1.376
0	11	10	1.50	19.81	89.46	4.62	6.56	0.76	1.420
0	12	10	1.50	19.75	90.28	4.66	6.58	0.67	1.411
0	13	10	1.51	19.82	89.55	4.61	6.51	0.64	1.412
0	14	10	1.51	19.99	90.19	4.65	6.22	0.68	1.337
0	15	10	1.50	18.97	89.55	4.62	5.69	0.79	1.230
0	15.5	10	1.50	19.88	89.64	4.64	5.31	0.83	1.143
0	16	10	1.50	19.35	90.74	4.69	4.25	1.22	0.906
0	16.25	10	1.51	20.02	90.38	4.67	1.24	1.34	0.265
0	16.5	10	1.50	19.88	89.19	4.61	0.00	0.00	0.000
0	0.0	15	1.50	16.62	89.74	4.59	0.00	0.30	0.000
0	0.1	15	1.50	16.44	89.19	4.57	0.32	0.85	0.070
0	0.2	15	1.50	16.63	90.74	4.65	0.60	1.04	0.129
0	0.3	15	1.50	16.54	89.92	4.61	0.75	1.12	0.162
0	0.4	15	1.50	17.24	89.46	4.60	0.84	1.13	0.182
0	0.5	15	1.49	17.27	90.38	4.68	0.89	1.16	0.190
0	0.6	15	1.50	16.71	90.56	4.65	0.98	1.18	0.210
0	0.7	15	1.49	16.82	91.47	4.71	1.03	1.21	0.218
0	0.8	15	1.49	17.18	91.11	4.72	1.12	1.25	0.237
0	0.9	15	1.49	16.85	89.19	4.60	1.19	1.26	0.258
0	1.0	15	1.50	17.56	90.01	4.64	1.28	1.29	0.275
0	1.25	15	1.49	17.79	89.83	4.64	1.51	1.38	0.325
0	1.5	15	1.49	17.79	89.83	4.64	1.77	1.45	0.381
0	1.75	15	1.49	16.98	90.56	4.67	2.01	1.51	0.430
0	2.0	15	1.49	16.98	90.83	4.68	2.29	1.56	0.489
0	2.25	15	1.49	17.73	91.84	4.76	2.56	1.59	0.537
0	2.5	15	1.49	17.08	90.56	4.66	2.86	1.62	0.613
0	2.75	15	1.49	16.91	89.09	4.59	3.14	1.62	0.684
0	3.0	15	1.49	17.08	90.65	4.68	3.55	1.62	0.759
0	3.25	15	1.49	17.18	90.56	4.67	3.68	1.61	0.788
0	3.5	15	1.49	17.17	91.20	4.70	3.91	1.56	0.831
0	3.75	15	1.49	17.12	91.57	4.72	4.14	1.54	0.877
0	4.0	15	1.49	17.24	89.09	4.59	4.34	1.50	0.945
0	5.0	15	1.49	17.14	90.65	4.67	4.93	1.35	1.055
0	6.0	15	1.49	17.15	89.09	4.59	5.35	1.25	1.164
0	7.0	15	1.49	17.29	89.28	4.60	5.67	1.17	1.232
0	8.0	15	1.49	17.24	90.56	4.67	5.91	1.11	1.266
0	9-0	15	1.49	17.17	90.56	4.67	6.13	1.02	1.313
0	10	15	1.49	17.27	90.83	4.69	6.32	0.92	1.347
0	11	15	1.50	17.66	90.28	4.65	6.45	0.82	1.386
0	12	15	1.49	17.76	89.64	4.63	6.51	0.74	1.406

Table 19.D (continuation): Mean axial velocity results for the Solid ring structures experiments (L-STAR-G1-LDA)

X_w [mm]	Y_w [mm]	Z_r [mm]	P_i [Bar]	T_i [°C]	$\dot{m}_{CFM}$ [kg/h]	U_m [m/s]	$U_{r(G1)}$ [m/s]	$U_{r.rms(G1)}$ [m/s]	$U_{r(G1)}/U_m$ [m/s]
0	13	15	1.49	17.72	90.28	4.66	6.48	0.66	1.390
0	14	15	1.50	17.88	90.83	4.69	6.30	0.65	1.343
0	15	15	1.48	17.67	90.93	4.73	5.88	0.74	1.243
0	16	15	1.49	17.82	90.38	4.67	3.72	1.09	0.797
0	16.25	15	1.49	17.82	91.57	4.73	0.07	0.32	0.014
0	16.5	15	1.49	18.08	90.19	4.66	0.00	0.01	0.000
0	0	20	1.49	17.55	90.74	4.68	0.15	0.09	0.032
0	0.1	20	1.49	17.54	90.38	4.66	0.79	1.02	0.169
0	0.2	20	1.46	17.06	90.10	4.74	1.39	1.07	0.293
0	0.3	20	1.49	18.33	90.01	4.67	1.49	1.08	0.319
0	0.4	20	1.50	17.35	90.47	4.66	1.53	1.17	0.328
0	0.5	20	1.50	17.12	89.19	4.57	1.62	1.17	0.354
0	0.6	20	1.48	17.55	89.00	4.64	1.71	1.16	0.368
0	0.7	20	1.49	16.90	90.83	4.69	1.76	1.15	0.375
0	0.8	20	1.48	17.41	89.19	4.64	1.81	1.17	0.390
0	0.9	20	1.48	17.48	90.10	4.69	1.87	1.18	0.398
0	1	20	1.48	17.49	89.64	4.67	1.89	1.18	0.404
0	1.25	20	1.49	17.51	90.65	4.68	2.05	1.24	0.437
0	1.5	20	1.50	17.57	89.46	4.61	2.22	1.30	0.481
0	1.75	20	1.49	17.52	89.28	4.61	2.37	1.35	0.513
0	2	20	1.49	17.62	90.28	4.67	2.53	1.40	0.541
0	2.25	20	1.49	17.42	90.74	4.69	2.74	1.43	0.584
0	2.5	20	1.49	17.64	89.46	4.62	2.92	1.46	0.631
0	2.75	20	1.50	17.55	89.74	4.63	3.13	1.49	0.676
0	3	20	1.50	17.93	89.92	4.64	3.32	1.52	0.715
0	3.25	20	1.49	18.06	91.11	4.72	3.52	1.51	0.746
0	3.5	20	1.50	17.80	90.01	4.63	3.71	1.52	0.801
0	3.75	20	1.50	17.88	89.09	4.59	3.91	1.51	0.851
0	4	20	1.49	17.94	90.47	4.68	4.07	1.49	0.869
0	5	20	1.49	17.83	89.74	4.64	4.71	1.39	1.016
0	6	20	1.49	18.00	89.64	4.64	5.14	1.28	1.108
0	7	20	1.49	17.78	90.56	4.68	5.47	1.19	1.169
0	8	20	1.49	17.77	91.75	4.74	5.75	1.12	1.213
0	9	20	1.49	17.86	89.74	4.64	6.01	1.03	1.295
0	10	20	1.49	17.97	90.28	4.66	6.21	0.95	1.331
0	11	20	1.49	18.03	88.36	4.57	6.33	0.85	1.386
0	12	20	1.49	18.10	89.92	4.66	6.42	0.76	1.378
0	13	20	1.49	17.97	90.93	4.70	6.42	0.68	1.364
0	14	20	1.49	17.97	90.93	4.70	6.31	0.65	1.341
0	15	20	1.50	17.87	90.56	4.66	5.95	0.71	1.276
0	15.5	20	1.50	17.88	89.55	4.61	5.59	0.82	1.213
0	16	20	1.50	17.81	89.19	4.59	4.71	1.02	1.026
0	16.25	20	1.50	17.97	88.55	4.56	3.41	1.26	0.748
0	16.5	20	1.50	17.83	88.63	4.56	0.00	0.02	0.000
0	0	24	1.51	17.17	90.93	4.64	0.45	0.74	0.097
0	0.1	24	1.51	17.40	91.29	4.66	1.45	0.84	0.311
0	0.2	24	1.50	16.36	91.47	4.69	1.73	0.91	0.369
0	0.3	24	1.50	16.30	91.66	4.70	1.77	1.05	0.376
0	0.4	24	1.502	16.44	89.09	4.57	1.88	1.12	0.411
0	0.5	24	1.504	16.302	90.28	4.62	1.95	1.15	0.422
0	0.6	24	1.503	16.211	88.73	4.54	2.01	1.17	0.442

Table 19.D (continuation): Mean axial velocity results for the Solid ring structures experiments (L-STAR-G1-LDA)

X_w [mm]	Y_w [mm]	Z_r [mm]	P_i [Bar]	T_i [°C]	$\dot{m}_{CFM}$ [kg/h]	U_m [m/s]	$U_{r(G1)}$ [m/s]	$U_{r.rms(G1)}$ [m/s]	$U_{r(G1)}/U_m$ [m/s]
0	0.7	24	1.50	16.48	89.37	4.59	2.05	1.17	0.447
0	0.8	24	1.50	16.33	89.00	4.56	2.11	1.18	0.462
0	0.9	24	1.50	16.33	89.37	4.58	2.17	1.19	0.473
0	1.0	24	1.49	16.31	91.47	4.71	2.23	1.20	0.473
0	1.25	24	1.50	16.30	90.93	4.66	2.35	1.24	0.504
0	1.5	24	1.50	16.37	90.56	4.65	2.48	1.27	0.533
0	1.5	24	1.50	16.44	90.38	4.63	2.48	1.27	0.535
0	1.75	24	1.50	16.45	89.92	4.61	2.63	1.32	0.569
0	2.0	24	1.50	16.59	90.01	4.62	2.76	1.35	0.596
0	2.25	24	1.50	16.19	89.74	4.61	2.94	1.38	0.638
0	2.5	24	1.50	16.68	89.83	4.62	3.06	1.41	0.663
0	2.75	24	1.49	16.79	90.65	4.67	3.22	1.42	0.689
0	3.0	24	1.49	16.76	88.91	4.58	3.39	1.43	0.740
0	3.25	24	1.49	16.65	90.83	4.67	3.54	1.45	0.757
0	3.5	24	1.49	16.71	90.93	4.68	3.71	1.45	0.792
0	4.0	24	1.49	16.86	89.00	4.59	4.07	1.44	0.887
0	4.0	24	1.50	16.74	90.65	4.66	4.01	1.45	0.860
0	5.0	24	1.50	16.79	90.56	4.65	4.61	1.39	0.991
0	6.0	24	1.50	16.82	90.19	4.63	5.06	1.29	1.094
0	7.0	24	1.50	17.18	90.93	4.68	5.43	1.19	1.160
0	8.0	24	1.49	16.51	91.84	4.72	5.71	1.10	1.209
0	9.0	24	1.50	16.31	89.64	4.60	5.96	1.02	1.296
0	10	24	1.50	16.27	90.28	4.63	6.18	0.92	1.334
0	11	24	1.49	16.22	89.83	4.62	6.31	0.83	1.367
0	12	24	1.50	16.30	89.55	4.59	6.36	0.74	1.384
0	13	24	1.50	16.33	90.56	4.65	6.36	0.66	1.368
0	14	24	1.50	16.07	90.47	4.63	6.18	0.65	1.334
0	15	24	1.49	16.33	91.10	4.68	5.77	0.74	1.233
0	15.5	24	1.50	16.79	88.82	4.57	5.23	0.88	1.144
0	16	24	1.50	16.54	91.38	4.69	3.58	1.06	0.763
0	16.5	24	1.50	16.48	90.19	4.63	0.00	0.01	0.000
0	0	28	1.50	16.18	90.83	4.64	0.00	0.15	0.000
0	0.1	28	1.50	16.18	90.10	4.61	-0.01	0.42	-0.002
0	0.2	28	1.50	16.27	91.02	4.65	-0.15	0.75	-0.032
0	0.3	28	1.50	16.10	90.65	4.63	-0.28	1.79	-0.060
0	0.4	28	1.50	15.35	89.64	4.57	0.48	1.64	0.104
0	0.5	28	1.50	15.47	89.09	4.55	0.80	1.34	0.175
0	0.6	28	1.50	15.40	90.28	4.61	0.96	1.35	0.208
0	0.7	28	1.50	13.61	89.92	4.55	1.08	1.35	0.237
0	0.8	28	1.50	15.38	89.28	4.55	1.20	1.36	0.263
0	0.9	28	1.50	15.57	90.01	4.60	1.22	1.34	0.265
0	1.0	28	1.50	15.63	90.47	4.62	1.43	1.34	0.309
0	1.25	28	1.50	15.49	90.93	4.64	1.67	1.34	0.359
0	1.5	28	1.50	15.72	90.19	4.61	1.88	1.35	0.408
0	1.75	28	1.50	15.75	90.56	4.62	2.09	1.34	0.451
0	2.0	28	1.50	15.52	90.47	4.61	2.28	1.34	0.494
0	2.25	28	1.50	15.72	89.64	4.58	2.49	1.35	0.543
0	2.5	28	1.50	16.05	90.10	4.61	2.73	1.35	0.592
0	2.75	28	1.50	16.08	90.19	4.61	2.95	1.34	0.639
0	3.0	28	1.50	16.24	90.19	4.61	3.17	1.35	0.686
0	4.0	28	1.50	16.11	90.56	4.63	3.98	1.36	0.858

Table 19.D (continuation): Mean axial velocity results for the Solid ring structures experiments (L-STAR-G1-LDA)

X_w [mm]	Y_w [mm]	Z_r [mm]	P_i [Bar]	T_i [°C]	$\dot{m}_{CFM}$ [kg/h]	U_m [m/s]	$U_{r(G1)}$ [m/s]	$U_{r.rms(G1)}$ [m/s]	$U_{r(G1)}/U_m$ [m/s]
0	5.0	28	1.50	16.24	90.65	4.64	4.64	1.34	0.999
0	6.0	28	1.50	16.25	90.83	4.65	5.12	1.27	1.101
0	7.0	28	1.50	16.30	89.74	4.60	5.53	1.17	1.202
0	8.0	28	1.50	16.27	90.65	4.64	5.80	1.09	1.249
0	9.0	28	1.50	16.22	90.56	4.64	6.04	0.99	1.302
0	10	28	1.50	16.21	90.65	4.64	6.23	0.90	1.343
0	11	28	1.50	16.22	89.83	4.60	6.36	0.81	1.383
0	12	28	1.50	16.27	90.93	4.65	6.43	0.71	1.381
0	13	28	1.50	16.33	90.01	4.61	6.43	0.64	1.394
0	14	28	1.50	16.16	91.66	4.69	6.28	0.62	1.339
0	15	28	1.50	16.30	89.46	4.58	5.91	0.69	1.289
0	15.5	28	1.50	16.07	90.01	4.60	5.54	0.80	1.205
0	16	28	1.50	16.24	89.09	4.56	4.56	0.99	0.999
0	16.25	28	1.50	16.30	89.83	4.60	3.19	1.01	0.693
0	16.5	28	1.50	16.27	89.64	4.59	0.00	0.02	0.000

Table 20.D: Mean axial velocity results for the perforated ring structures experiments (L-STAR-G2-LDA)

X_w [mm]	Y_w [mm]	Z_r [mm]	P_i [Bar]	T_i [°C]	$\dot{m}_{CFM}$ [kg/h]	U_m [m/s]	$U_{r(G2)}$ [m/s]	$U_{r.rms(G2)}$ [m/s]	$U_{r(G2)}/U_m$ [m/s]
0	3.0	0.0	1.53	16.25	91.80	4.63	0.013	0.118	0.003
0	3.25	0.0	1.51	16.03	92.17	4.69	4.281	0.955	0.912
0	3.5	0.0	1.51	16.07	91.91	4.68	4.295	0.974	0.917
0	3.75	0.0	1.52	16.06	93.12	4.72	4.292	0.991	0.909
0	4.0	0.0	1.52	16.01	92.70	4.70	4.331	1.009	0.922
0	5.0	0.0	1.52	16.06	92.65	4.70	4.612	1.035	0.980
0	6.0	0.0	1.51	15.97	92.07	4.68	4.948	1.014	1.057
0	7.0	0.0	1.51	16.00	92.35	4.69	5.229	0.959	1.114
0	8.0	0.0	1.51	16.04	91.60	4.66	5.470	0.888	1.173
0	9.0	0.0	1.51	16.04	91.70	4.67	5.700	0.811	1.221
0	10.0	0.0	1.51	16.00	91.52	4.65	5.879	0.732	1.264
0	11.0	0.0	1.52	16.04	92.24	4.68	6.043	0.646	1.290
0	12.0	0.0	1.51	15.85	92.13	4.68	6.106	0.567	1.305
0	13.0	0.0	1.52	15.95	92.05	4.67	6.100	0.513	1.305
0	14.0	0.0	1.52	15.85	91.90	4.66	5.965	0.521	1.279
0	15.0	0.0	1.52	15.85	91.23	4.63	5.595	0.633	1.209
0	15.5	0.0	1.52	15.95	92.38	4.67	5.203	0.754	1.113
0	16.0	0.0	1.52	15.94	91.79	4.64	4.218	0.969	0.908
0	16.25	0.0	1.52	15.97	92.29	4.67	3.170	0.885	0.679
0	16.5	0.0	1.52	15.94	91.74	4.64	0.000	0.023	0.000
0	3.0	0.5	1.52	15.40	94.47	4.76	0.005	0.171	0.001
0	3.25	0.5	1.52	15.35	92.50	4.67	4.557	1.153	0.975
0	3.5	0.5	1.52	15.28	92.18	4.67	4.587	0.914	0.983
0	3.75	0.5	1.52	15.28	92.04	4.66	4.519	0.928	0.969
0	4.0	0.5	1.52	15.25	93.15	4.71	4.510	0.971	0.958
0	5.0	0.5	1.52	15.31	93.02	4.69	4.649	1.037	0.991
0	6.0	0.5	1.52	15.20	92.74	4.68	4.921	1.014	1.051
0	7.0	0.5	1.52	15.25	92.50	4.67	5.167	0.989	1.106
0	8.0	0.5	1.52	15.19	92.56	4.68	5.426	0.906	1.159
0	9.0	0.5	1.52	15.19	92.48	4.68	5.639	0.821	1.206
0	10	0.5	1.52	15.10	92.43	4.68	5.827	0.750	1.246
0	11	0.5	1.52	15.08	92.54	4.68	5.996	0.658	1.281
0	12	0.5	1.51	15.19	91.98	4.66	6.065	0.584	1.302
0	13	0.5	1.52	15.13	92.97	4.69	6.072	0.521	1.295
0	14	0.5	1.52	15.09	93.10	4.69	5.944	0.517	1.267
0	15	0.5	1.52	15.08	92.56	4.67	5.571	0.620	1.193
0	15.5	0.5	1.52	15.08	92.50	4.67	5.215	0.736	1.117
0	16	0.5	1.52	15.08	92.60	4.67	4.297	0.900	0.920
0	16.25	0.5	1.52	15.13	92.37	4.67	3.109	0.887	0.666
0	16.5	0.5	1.52	15.08	92.71	4.68	0.000	0.009	0.000
0	3.0	1.0	1.51	15.70	90.53	4.60	0.003	0.132	0.001
0	3.25	1.0	1.51	15.69	90.55	4.61	4.549	1.075	0.987
0	3.5	1.0	1.51	15.69	90.36	4.60	4.629	0.919	1.006
0	3.75	1.0	1.51	15.69	90.49	4.60	4.600	0.897	1.001
0	4.0	1.0	1.51	15.69	90.58	4.60	4.601	0.909	1.001
0	5.0	1.0	1.52	15.69	90.37	4.58	4.691	0.985	1.024
0	6.0	1.0	1.52	15.69	90.45	4.58	4.944	0.974	1.079
0	7.0	1.0	1.52	15.68	90.62	4.59	5.196	0.943	1.132
0	8.0	1.0	1.52	15.68	90.37	4.58	5.428	0.859	1.185
0	9.0	1.0	1.51	15.68	90.38	4.59	5.630	0.778	1.227
0	10	1.0	1.52	15.68	91.92	4.66	5.884	0.731	1.263

Table 20.D (continuation): Mean axial velocity results for the perforated ring structures experiments (L-STAR-G2-LDA).

X_w [mm]	Y_w [mm]	Z_r [mm]	P_i [Bar]	T_i [°C]	$\dot{m}_{CFM}$ [kg/h]	U_m [m/s]	$U_{r(G2)}$ [m/s]	$U_{r.rms(G2)}$ [m/s]	$U_{r(G2)}/U_m$ [m/s]
0	11	1.0	1.52	15.68	91.70	4.64	6.011	0.649	1.295
0	12	1.0	1.52	15.68	92.32	4.67	6.113	0.563	1.308
0	13	1.0	1.52	15.68	91.90	4.65	6.100	0.511	1.311
0	14	1.0	1.52	15.68	91.17	4.61	5.931	0.518	1.286
0	15	1.0	1.52	15.67	91.62	4.64	5.575	0.633	1.202
0	15.5	1.0	1.52	15.68	91.56	4.64	5.176	0.745	1.116
0	16	1.0	1.52	15.68	91.17	4.61	4.165	0.922	0.903
0	16.25	1.0	1.52	15.68	91.51	4.63	2.727	0.846	0.588
0	16.5	1.0	1.51	15.68	92.84	4.71	0.005	0.074	0.001
0	3.0	1.5	1.52	16.00	91.91	4.64	0.071	0.141	0.015
0	3.25	1.5	1.52	15.94	92.01	4.65	4.022	1.651	0.865
0	3.5	1.5	1.52	15.92	91.84	4.65	4.557	1.187	0.981
0	3.75	1.5	1.52	15.92	91.51	4.63	4.713	0.996	1.017
0	4.0	1.5	1.52	15.93	91.28	4.63	4.731	0.965	1.023
0	5.0	1.5	1.52	15.83	91.58	4.64	4.837	0.979	1.043
0	6.0	1.5	1.51	15.86	91.10	4.63	5.046	0.995	1.091
0	7.0	1.5	1.51	15.91	90.38	4.60	5.305	0.947	1.154
0	8.0	1.5	1.51	15.82	90.44	4.60	5.547	0.894	1.205
0	9.0	1.5	1.51	16.00	90.37	4.60	5.727	0.807	1.246
0	10	1.5	1.51	15.92	90.41	4.60	5.920	0.730	1.288
0	11	1.5	1.51	15.92	90.47	4.60	6.034	0.652	1.312
0	12	1.5	1.52	16.00	90.89	4.60	6.126	0.573	1.332
0	13	1.5	1.52	15.91	91.78	4.65	6.112	0.518	1.315
0	14	1.5	1.52	15.91	91.61	4.63	5.984	0.516	1.293
0	15	1.5	1.52	15.88	90.59	4.59	5.619	0.621	1.225
0	15.5	1.5	1.52	15.91	90.74	4.60	5.259	0.733	1.143
0	16	1.5	1.52	15.91	91.07	4.62	4.379	0.914	0.948
0	16.25	1.5	1.52	15.80	91.24	4.62	3.156	0.900	0.683
0	16.5	1.5	1.52	15.81	91.09	4.60	0.001	0.029	0.000
0	3.0	1.5	1.52	16.00	91.91	4.64	0.071	0.141	0.015
0	3.25	1.5	1.52	15.94	92.01	4.65	4.022	1.651	0.865
0	3.5	1.5	1.52	15.92	91.84	4.65	4.557	1.187	0.981
0	3.75	1.5	1.52	15.92	91.51	4.63	4.713	0.996	1.017
0	4.0	1.5	1.52	15.93	91.28	4.63	4.731	0.965	1.023
0	3.0	2.0	1.51	15.69	91.55	4.66	0.008	0.202	0.002
0	3.25	2.0	1.51	15.68	91.20	4.64	4.112	1.388	0.887
0	3.5	2.0	1.51	15.66	91.37	4.65	4.492	1.055	0.967
0	3.75	2.0	1.51	15.66	91.01	4.63	4.576	0.966	0.988
0	4.0	2.0	1.51	15.66	90.90	4.62	4.633	0.930	1.002
0	5.0	2.0	1.51	15.67	90.93	4.62	4.779	0.978	1.034
0	6.0	2.0	1.51	15.66	91.41	4.65	5.015	0.970	1.079
0	7.0	2.0	1.51	15.66	90.77	4.61	5.257	0.929	1.139
0	8.0	2.0	1.51	15.66	90.79	4.62	5.474	0.865	1.185
0	9.0	2.0	1.51	15.59	90.76	4.62	5.667	0.788	1.228
0	10	2.0	1.52	16.00	92.07	4.66	6.005	0.758	1.288
0	11	2.0	1.52	15.81	91.59	4.63	6.136	0.675	1.326
0	12	2.0	1.52	15.81	92.34	4.66	6.230	0.590	1.338
0	13	2.0	1.52	15.70	92.04	4.64	6.217	0.532	1.339
0	14	2.0	1.52	15.70	93.01	4.69	6.088	0.525	1.297
0	15	2.0	1.52	15.56	92.78	4.68	5.716	0.629	1.220
0	15.5	2.0	1.52	15.59	92.76	4.69	5.359	0.738	1.143
0	16	2.0	1.52	15.48	93.90	4.74	4.450	0.919	0.939
0	16.25	2.0	1.52	15.47	94.44	4.76	3.200	0.924	0.672
0	16.5	2.0	1.52	15.39	94.44	4.76	0.000	0.027	0.000
0	3.0	2.5	1.51	14.86	92.31	4.67	0.001	0.126	0.000
0	3.25	2.5	1.51	14.86	91.14	4.61	3.841	1.387	0.833

Table 20.D (continuation): Mean axial velocity results for the perforated ring structures experiments (L-STAR-G2-LDA).

X_w [mm]	Y_w [mm]	Z_r [mm]	P_i [Bar]	T_i [°C]	$\dot{m}_{CFM}$ [kg/h]	U_m [m/s]	$U_{r(G2)}$ [m/s]	$U_{r.rms(G2)}$ [m/s]	$U_{r(G2)}/U_m$ [m/s]
0	3.5	2.5	1.51	14.86	91.06	4.61	4.227	1.128	0.917
0	3.75	2.5	1.51	14.86	91.34	4.62	4.393	0.965	0.950
0	4.0	2.5	1.52	14.86	91.31	4.62	4.442	0.916	0.962
0	5.0	2.5	1.51	14.86	90.77	4.60	4.602	0.958	1.001
0	6.0	2.5	1.51	14.86	90.92	4.60	4.837	0.957	1.051
0	7.0	2.5	1.52	14.85	91.00	4.60	5.093	0.911	1.108
0	8.0	2.5	1.52	14.85	90.81	4.59	5.297	0.849	1.154
0	9.0	2.5	1.51	16.12	90.45	4.60	5.553	0.773	1.207
0	10	2.5	1.52	16.81	89.24	4.54	5.717	0.701	1.260
0	11	2.5	1.52	17.42	89.70	4.58	5.846	0.625	1.277
0	12	2.5	1.51	18.06	89.58	4.59	5.896	0.547	1.286
0	13	2.5	1.52	16.81	90.77	4.59	6.057	0.500	1.318
0	15	2.5	1.52	17.24	89.79	4.57	5.539	0.614	1.213
0	15.5	2.5	1.52	18.14	90.87	4.63	5.197	0.730	1.122
0	16	2.5	1.52	19.78	90.12	4.61	4.368	0.893	0.947
0	16.25	2.5	1.52	20.44	89.21	4.58	2.758	0.840	0.602
0	16.5	2.5	1.52	20.85	89.40	4.59	0.038	0.216	0.008
0	3.0	3.0	1.51	15.72	92.03	4.67	0.020	0.362	0.004
0	3.25	3.0	1.51	15.73	91.37	4.64	3.650	1.560	0.787
0	3.5	3.0	1.52	15.73	91.65	4.64	4.178	1.300	0.900
0	3.75	3.0	1.52	15.72	91.89	4.65	4.403	1.126	0.947
0	4.0	3.0	1.51	15.71	90.68	4.61	4.533	1.016	0.984
0	5.0	3.0	1.51	15.71	90.95	4.62	4.774	0.966	1.033
0	6.0	3.0	1.51	15.71	90.83	4.62	5.018	0.970	1.086
0	7.0	3.0	1.51	15.71	90.96	4.62	5.286	0.934	1.145
0	8.0	3.0	1.52	15.71	90.81	4.60	5.498	0.869	1.195
0	9.0	3.0	1.52	15.71	91.26	4.62	5.688	0.794	1.231
0	10	3.0	1.52	15.70	91.47	4.63	5.882	0.725	1.271
0	11	3.0	1.52	15.70	91.14	4.61	5.992	0.646	1.300
0	12	3.0	1.52	15.72	91.81	4.64	6.064	0.567	1.306
0	13	3.0	1.52	15.69	91.06	4.61	6.070	0.510	1.317
0	14	3.0	1.52	15.70	92.07	4.67	5.920	0.509	1.269
0	15	3.0	1.51	15.70	91.23	4.63	5.573	0.616	1.203
0	15.5	3.0	1.51	15.69	91.20	4.65	5.211	0.728	1.121
0	16	3.0	1.51	15.69	90.87	4.62	4.291	0.912	0.928
0	16.25	3.0	1.52	15.70	90.94	4.61	3.065	0.868	0.665
0	16.5	3.0	1.51	15.69	91.15	4.63	0.000	0.014	0.000
0	0	5.0	1.51	18.92	91.30	4.71	0.00	0.02	0.00
0	0.1	5.0	1.51	18.92	91.66	4.71	-0.10	0.63	-0.02
0	0.2	5.0	1.51	18.81	91.53	4.71	-0.19	0.88	-0.04
0	0.3	5.0	1.51	18.81	91.47	4.70	0.05	1.11	0.01
0	0.4	5.0	1.51	18.81	90.93	4.69	0.43	1.29	0.09
0	0.5	5.0	1.51	18.80	91.01	4.69	0.85	1.45	0.18
0	0.6	5.0	1.51	18.07	92.18	4.74	1.25	1.63	0.26
0	0.7	5.0	1.51	18.05	91.92	4.72	1.59	1.65	0.34
0	0.8	5.0	1.52	18.05	92.84	4.74	1.99	1.67	0.42
0	0.9	5.0	1.51	17.96	91.78	4.72	2.39	1.62	0.51
0	1.0	5.0	1.51	17.99	91.58	4.71	2.67	1.52	0.57
0	1.25	5.0	1.51	17.81	90.48	4.64	3.05	1.34	0.66
0	1.5	5.0	1.52	17.73	93.26	4.76	3.22	1.20	0.68
0	1.75	5.0	1.52	17.75	92.33	4.71	2.60	1.12	0.55
0	2.0	5.0	1.51	17.86	90.72	4.66	1.56	0.93	0.33
0	2.25	5.0	1.52	17.72	91.59	4.67	1.07	0.73	0.23
0	2.5	5.0	1.52	17.61	90.29	4.60	1.20	0.81	0.26
0	2.75	5.0	1.52	17.67	89.88	4.58	1.99	1.19	0.43
0	3.0	5.0	1.52	17.61	90.57	4.62	2.98	1.43	0.65

Table 20.D (continuation): Mean axial velocity results for the perforated ring structures experiments (L-STAR-G2-LDA).

X_w [mm]	Y_w [mm]	Z_r [mm]	P_i [Bar]	T_i [°C]	$\dot{m}_{CFM}$ [kg/h]	U_m [m/s]	$U_{r(G2)}$ [m/s]	$U_{r.rms(G2)}$ [m/s]	$U_{r(G2)}/U_m$ [m/s]
0	3.25	5.0	1.52	17.58	89.74	4.58	3.70	1.38	0.81
0	3.5	5.0	1.52	17.50	91.36	4.66	4.28	1.26	0.92
0	3.75	5.0	1.52	17.50	92.00	4.69	4.47	1.15	0.95
0	4.0	5.0	1.52	17.50	91.88	4.69	4.58	1.08	0.98
0	5.0	5.0	1.51	17.44	93.59	4.78	4.97	1.02	1.04
0	6.0	5.0	1.51	17.32	93.17	4.77	5.26	1.01	1.10
0	7.0	5.0	1.51	17.27	93.13	4.77	5.54	0.95	1.16
0	8.0	5.0	1.51	17.30	92.58	4.75	5.71	0.88	1.20
0	9.0	5.0	1.50	17.21	91.24	4.69	5.92	0.81	1.26
0	10.0	5.0	1.52	17.19	92.21	4.69	6.06	0.73	1.29
0	11.0	5.0	1.52	17.20	92.07	4.67	6.18	0.65	1.32
0	12.0	5.0	1.52	17.19	92.07	4.67	6.23	0.57	1.33
0	13.0	5.0	1.52	17.19	92.00	4.67	6.22	0.52	1.33
0	14.0	5.0	1.52	17.31	92.06	4.67	6.07	0.52	1.30
0	15.0	5.0	1.52	17.29	92.46	4.70	5.72	0.62	1.22
0	15.5	5.0	1.52	17.18	93.22	4.73	5.35	0.73	1.13
0	16.0	5.0	1.52	17.27	92.92	4.72	4.56	0.91	0.97
0	16.25	5.0	1.52	17.29	93.01	4.72	3.44	0.94	0.73
0	16.5	5.0	1.52	17.29	93.09	4.73	0.00	0.11	0.00
0	0	10	1.53	17.17	92.22	4.66	-0.015	0.260	-0.003
0	0.1	10	1.52	17.08	93.56	4.75	-0.107	0.522	-0.023
0	0.2	10	1.52	17.02	93.16	4.72	-0.212	0.708	-0.045
0	0.3	10	1.52	16.97	92.69	4.70	-0.179	0.734	-0.038
0	0.4	10	1.53	17.00	93.49	4.72	-0.127	0.750	-0.027
0	0.5	10	1.53	17.01	93.27	4.72	-0.058	0.769	-0.012
0	0.6	10	1.52	16.98	92.78	4.71	0.011	0.788	0.002
0	0.7	10	1.52	16.95	92.65	4.69	0.063	0.804	0.013
0	0.8	10	1.52	16.93	92.13	4.67	0.110	0.822	0.024
0	0.9	10	1.53	16.93	92.20	4.67	0.184	0.836	0.039
0	1.0	10	1.52	16.93	91.82	4.65	0.277	0.882	0.060
0	1.25	10	1.53	16.91	91.86	4.64	0.502	0.928	0.108
0	1.5	10	1.52	16.91	91.57	4.64	0.775	0.997	0.167
0	1.75	10	1.52	16.91	91.47	4.63	1.076	1.069	0.232
0	2.0	10	1.52	16.92	90.66	4.60	1.413	1.135	0.307
0	2.25	10	1.52	16.91	90.38	4.58	1.791	1.203	0.391
0	2.5	10	1.52	16.91	90.08	4.56	2.182	1.254	0.478
0	2.75	10	1.52	16.91	90.15	4.57	2.573	1.283	0.563
0	3.0	10	1.52	16.91	89.51	4.53	2.944	1.282	0.649
0	3.25	10	1.52	17.00	87.49	4.44	3.283	1.250	0.739
0	3.5	10	1.52	16.71	89.23	4.51	3.673	1.208	0.814
0	3.75	10	1.52	16.71	90.40	4.58	3.946	1.163	0.861
0	4.0	10	1.53	16.68	90.33	4.57	4.121	1.108	0.902
0	5.0	10	1.52	16.68	90.37	4.57	4.565	0.998	0.998
0	6.0	10	1.52	16.70	89.94	4.56	4.868	0.957	1.068
0	7.0	10	1.52	16.62	90.30	4.59	5.175	0.922	1.129
0	8.0	10	1.52	16.70	91.14	4.62	5.459	0.866	1.182
0	9.0	10	1.52	16.62	91.05	4.61	5.675	0.794	1.232
0	10.0	10	1.52	16.61	90.25	4.57	5.858	0.717	1.282
0	11.0	10	1.52	16.69	90.78	4.60	5.997	0.635	1.305
0	12.0	10	1.52	16.65	90.43	4.58	6.070	0.560	1.326
0	13.0	10	1.52	16.69	90.65	4.59	6.042	0.504	1.317
0	14.0	10	1.52	16.62	90.24	4.57	5.909	0.514	1.293
0	15.0	10	1.52	16.61	89.92	4.56	5.559	0.616	1.220
0	15.5	10	1.52	16.68	89.82	4.56	5.163	0.723	1.133
0	16.0	10	1.52	16.65	90.01	4.56	4.237	0.901	0.929
0	16.25	10	1.52	16.66	89.61	4.54	3.530	0.940	0.777

Table 20.D (continuation): Mean axial velocity results for the perforated ring structures experiments (L-STAR-G2-LDA).

X_w [mm]	Y_w [mm]	Z_r [mm]	P_i [Bar]	T_i [°C]	$\dot{m}_{CFM}$ [kg/h]	U_m [m/s]	$U_{r(G2)}$ [m/s]	$U_{r.rms(G2)}$ [m/s]	$U_{r(G2)}/U_m$ [m/s]
0	16.25	10	1.52	16.66	89.61	4.54	3.530	0.940	0.777
0	16.5	10	1.52	16.65	90.01	4.56	0.000	0.000	0.000
0	0	15	1.52	16.60	89.07	4.53	0.001	0.405	0.000
0	0.1	15	1.51	16.68	90.77	4.63	0.259	0.954	0.056
0	0.2	15	1.51	16.60	90.80	4.62	0.375	0.756	0.081
0	0.3	15	1.51	16.60	90.81	4.63	0.497	0.777	0.107
0	0.4	15	1.52	16.59	90.29	4.59	0.565	0.779	0.123
0	0.5	15	1.52	16.68	90.29	4.59	0.612	0.807	0.133
0	0.6	15	1.52	16.60	90.14	4.58	0.687	0.806	0.150
0	0.7	15	1.52	16.59	90.54	4.59	0.771	0.858	0.168
0	0.8	15	1.52	16.59	90.71	4.60	0.842	0.879	0.183
0	0.9	15	1.52	16.59	90.34	4.58	0.917	0.929	0.200
0	1.0	15	1.52	16.67	90.21	4.58	1.004	0.955	0.219
0	1.25	15	1.52	16.67	90.12	4.57	1.208	1.016	0.264
0	1.5	15	1.52	16.67	89.83	4.57	1.442	1.081	0.316
0	1.75	15	1.52	16.67	89.91	4.56	1.694	1.141	0.372
0	2.0	15	1.52	16.67	90.17	4.57	1.965	1.182	0.430
0	2.25	15	1.52	16.67	89.55	4.55	2.229	1.217	0.490
0	2.5	15	1.50	16.22	89.26	4.58	2.597	1.208	0.567
0	2.75	15	1.50	16.28	89.03	4.57	2.867	1.209	0.627
0	3.0	15	1.50	16.13	89.36	4.58	3.127	1.203	0.682
0	3.25	15	1.50	16.22	88.95	4.57	3.381	1.163	0.740
0	3.5	15	1.50	16.19	89.01	4.56	3.597	1.131	0.788
0	3.75	15	1.50	16.22	89.41	4.59	3.782	1.086	0.823
0	4.0	15	1.50	16.27	89.27	4.59	3.891	1.054	0.848
0	5.0	15	1.50	16.17	88.61	4.56	4.357	0.963	0.956
0	6.0	15	1.50	16.11	88.09	4.53	4.664	0.922	1.029
0	7.0	15	1.50	16.19	88.47	4.55	5.005	0.874	1.100
0	8.0	15	1.50	16.25	91.42	4.69	5.470	0.836	1.166
0	9.0	15	1.50	16.21	91.62	4.71	5.719	0.755	1.215
0	10.0	15	1.49	16.17	91.22	4.70	5.897	0.678	1.254
0	11.0	15	1.49	16.21	90.64	4.67	6.012	0.591	1.287
0	12.0	15	1.51	16.22	91.46	4.67	6.068	0.525	1.298
0	13.0	15	1.51	16.21	90.97	4.65	5.983	0.509	1.287
0	14.0	15	1.51	16.21	91.45	4.67	5.699	0.585	1.219
0	15.0	15	1.51	16.13	90.76	4.63	4.793	0.667	1.034
0	15.5	15	1.50	16.12	91.59	4.70	3.212	0.681	0.684
0	16.0	15	1.50	16.31	90.68	4.65	2.198	0.732	0.472
0	16.25	15	1.50	16.43	91.38	4.68	0.947	0.937	0.202
0	16.5	15	1.51	16.49	92.28	4.68	0.000	0.026	0.001
0	0	20	1.51	16.35	91.76	4.68	0.000	0.038	0.000
0	0.1	20	1.51	16.41	92.06	4.68	0.350	0.695	0.075
0	0.2	20	1.51	16.43	91.11	4.65	1.206	0.839	0.259
0	0.3	20	1.51	16.60	91.35	4.67	1.295	0.854	0.278
0	0.4	20	1.51	16.61	91.41	4.67	1.409	0.859	0.302
0	0.5	20	1.51	16.61	91.31	4.66	1.483	0.861	0.318
0	0.6	20	1.52	16.60	91.22	4.64	1.527	0.879	0.329
0	0.7	20	1.51	16.60	90.98	4.64	1.553	0.903	0.334
0	0.8	20	1.52	16.52	91.98	4.66	1.614	0.909	0.346
0	0.9	20	1.52	16.54	92.11	4.68	1.669	0.917	0.357
0	1.0	20	1.52	16.55	92.08	4.67	1.718	0.940	0.368
0	1.25	20	1.52	16.52	91.99	4.65	1.864	0.985	0.401
0	1.5	20	1.52	16.62	91.83	4.65	2.003	1.030	0.430
0	1.75	20	1.53	16.61	92.02	4.65	2.161	1.091	0.465
0	2.0	20	1.52	16.61	91.73	4.65	2.374	1.117	0.511
0	2.25	20	1.52	16.61	91.41	4.62	2.552	1.149	0.552

Table 20.D (continuation): Mean axial velocity results for the perforated ring structures experiments (L-STAR-G2-LDA).

X_w [mm]	Y_w [mm]	Z_r [mm]	P_i [Bar]	T_i [°C]	$\dot{m}_{CFM}$ [kg/h]	U_m [m/s]	$U_{r(G2)}$ [m/s]	$U_{r.rms(G2)}$ [m/s]	$U_{r(G2)}/U_m$ [m/s]
0	2.5	20	1.52	16.61	92.09	4.66	2.728	1.168	0.586
0	2.75	20	1.52	16.60	92.15	4.66	2.912	1.181	0.624
0	3.0	20	1.52	16.60	92.17	4.67	3.087	1.199	0.661
0	3.25	20	1.52	16.67	92.12	4.66	3.260	1.191	0.700
0	3.5	20	1.52	16.68	91.88	4.65	3.436	1.193	0.738
0	3.75	20	1.52	16.67	91.70	4.64	3.603	1.175	0.777
0	4.0	20	1.52	16.67	91.29	4.63	3.733	1.158	0.807
0	5.0	20	1.52	16.67	91.16	4.62	4.261	1.072	0.922
0	6.0	20	1.52	16.67	91.46	4.63	4.661	0.983	1.007
0	7.0	20	1.52	16.67	91.92	4.65	4.982	0.917	1.071
0	8.0	20	1.52	16.67	91.51	4.64	5.270	0.856	1.136
0	9.0	20	1.52	16.66	91.97	4.65	5.484	0.789	1.179
0	10.0	20	1.52	16.66	91.02	4.61	5.687	0.716	1.234
0	11.0	20	1.52	16.66	91.62	4.64	5.849	0.642	1.260
0	12.0	20	1.53	16.66	91.21	4.61	5.936	0.562	1.287
0	13.0	20	1.52	16.66	90.85	4.60	5.961	0.508	1.295
0	14.0	20	1.52	16.71	90.79	4.60	5.822	0.519	1.265
0	15.0	20	1.52	16.74	90.79	4.60	5.463	0.626	1.188
0	15.5	20	1.52	16.77	90.56	4.59	5.123	0.745	1.117
0	16.0	20	1.52	16.77	91.15	4.62	4.239	0.934	0.917
0	16.25	20	1.52	16.76	90.42	4.59	3.043	0.939	0.663
0	16.5	20	1.52	16.76	89.39	4.53	0.005	0.066	0.001
0	0	24	1.50	19.05	94.36	4.88	0.004	0.117	0.001
0	0.1	24	1.51	21.39	91.15	4.74	1.105	0.873	0.233
0	0.2	24	1.50	21.84	90.92	4.74	1.270	0.890	0.268
0	0.3	24	1.51	22.22	90.92	4.74	1.435	0.907	0.303
0	0.4	24	1.52	17.36	92.02	4.69	1.525	0.900	0.325
0	0.5	24	1.52	16.93	91.67	4.67	1.581	0.904	0.339
0	0.6	24	1.52	16.74	91.83	4.67	1.655	0.915	0.354
0	0.7	24	1.52	16.61	92.31	4.70	1.700	0.917	0.362
0	0.8	24	1.51	16.50	92.00	4.69	1.778	0.927	0.379
0	0.9	24	1.51	16.49	91.65	4.67	1.883	0.929	0.403
0	1.0	24	1.51	16.44	91.64	4.66	1.928	0.945	0.414
0	1.25	24	1.52	16.39	91.69	4.66	2.053	0.968	0.441
0	1.5	24	1.51	16.39	91.03	4.63	2.179	1.000	0.470
0	1.75	24	1.51	16.31	91.26	4.65	2.309	1.035	0.497
0	2.0	24	1.51	16.30	91.19	4.64	2.453	1.064	0.528
0	2.25	24	1.51	16.30	91.44	4.66	2.589	1.101	0.556
0	2.5	24	1.51	16.30	91.17	4.65	2.743	1.113	0.590
0	2.75	24	1.51	16.30	91.60	4.66	2.898	1.144	0.621
0	3.0	24	1.52	16.29	92.05	4.68	3.058	1.154	0.654
0	3.25	24	1.52	16.29	92.07	4.67	3.193	1.169	0.683
0	3.5	24	1.52	16.32	92.00	4.67	3.351	1.172	0.718
0	3.75	24	1.52	16.29	92.06	4.67	3.501	1.170	0.750
0	4.0	24	1.52	16.29	92.22	4.68	3.662	1.163	0.783
0	5.0	24	1.52	16.29	92.04	4.67	4.195	1.098	0.898
0	6.0	24	1.52	16.29	91.87	4.67	4.608	1.020	0.988
0	7.0	24	1.52	16.29	92.00	4.67	4.957	0.946	1.061
0	8.0	24	1.52	16.29	92.02	4.67	5.255	0.872	1.124
0	9.0	24	1.52	16.29	92.12	4.68	5.505	0.814	1.177
0	10.0	24	1.52	16.29	92.33	4.69	5.733	0.736	1.223
0	11.0	24	1.51	16.29	91.99	4.68	5.891	0.657	1.259
0	12.0	24	1.51	16.29	91.75	4.67	5.983	0.578	1.282
0	13.0	24	1.51	16.29	91.48	4.65	5.996	0.520	1.289